

University of Alberta
Department of Civil &
Environmental Engineering



Structural Engineering Report

Structural Behaviour of Textile and Steel Reinforced Ceramic Composite Slabs

by
Samson T. Tassew
and
Adam S. Lubell

September, 2014

**Structural Behaviour of Textile and Steel Reinforced Ceramic
Composite Slabs**

by

Samson Takele Tassew

and

Adam S. Lubell

Department of Civil and Environmental Engineering
University of Alberta

September 2014

Abstract

Magnesium potassium phosphate cement (MPPC) is an innovative chemically bonded cement formed by the reaction of magnesium oxide and monopotassium phosphate. Concrete produced using a MPPC binder can exhibit faster strength gain and results in lower overall environmental impacts from greenhouse gas emissions and embodied energy compared to concretes produced with Portland cement binders. This research had two parts: the first part was to develop and characterize lightweight structural ceramic concretes made from MPPC binders and various aggregates, and to study the uniaxial tensile response of composite made of these ceramic concretes and glass textile reinforcements. The second part of the study developed an innovative structural system using these ceramic concretes, reinforcing steel and glass textile reinforcements.

Laboratory tests were performed to develop and characterize the rheological and mechanical properties of an innovative ceramic concrete that contained or omitted chopped glass fibers. Results indicated that ceramic concrete could be formulated with rheological and mechanical properties suitable for structural applications. The produced concretes exhibited rapid strength gain and had 28-day compressive strengths between 17 and 55 MPa for densities between 1600 and 2200 kg/m³, respectively. The addition of chopped glass fiber into ceramic concrete increased the flexural strength and direct shear strength.

The uniaxial tensile response of textile reinforced ceramic concrete with and without additional chopped glass fibers were also investigated. The test results indicated that the textile reinforcement increased the ultimate load-bearing capacity and ductility of the specimens. The addition of short glass fibres in textile reinforced concrete increased the first-crack stress and the axial tensile strength.

The flexural behaviour of six composite slabs made of ceramic concrete reinforced with longitudinal steel bars and glass textile reinforcements were examined. The test results of the slabs indicated that ceramic concrete composites are suitable for structural applications. However, some further studies on durability are needed prior to field applications.

A numerical model was developed using MATLAB® to study the flexural behaviour of the slabs. The full-member model was developed based on equilibrium and strain compatibility, accounting for the non-linear material behaviour. The developed model was in good agreement with the experimental results.

Preface

This report is based on the doctoral thesis of the first author, completed under the direction of the second author.

Portions of this report are derived from scientific articles that have been published in various scientific journals or conference proceedings:

- Chapter 3 is based on the article: Samson T. Tassew and Adam S. Lubell, “Properties of Phosphate-based Cements with High Fly Ash Content,” *American Concrete Institute (ACI) Special Publication: SP-294 Advances in Green Binder System, American Concrete Institute*, SP294-5, 1-16.
- Chapter 4 is based on the article: Samson T. Tassew and Adam S. Lubell, “Mechanical Properties of Lightweight Ceramic Concrete,” *Materials and Structures Journal*, vol. 45, issue 4, 561-574.
- Chapter 5 is based on the article: Samson Tassew and Adam Lubell, “Textile Reinforced Ceramic Composite for Structural Infill Slab Application,” *Proceedings of 34th IABSE Symposium, Venice, Italy*, A-0317, 1-8.
- Chapter 6 is based on the article: S. T. Tassew, and A. S. Lubell, “Mechanical Properties of Glass Fiber Reinforced Ceramic Concrete,” *Construction and Building Materials Journal*, vol. 51, issue 31, 215-224.

Acknowledgements

Financial support for this study was provided by the Natural Sciences and Engineering Research Council of Canada (NSERC), C-Bond Technology and Canada School for Energy and Environment.

Donation of materials by Stalite, Argex, Buildex, St. Gobain Technical Fabrics, Nippon Electric Glass America, Lafarge North America and BASF are gratefully acknowledged

The authors also thank the support of Dr. Gilbert Grondin at the University of Alberta who provided technical assistance and advice for some of the laboratory work reported. The technical support from laboratory staff is also acknowledged, including Rizaldy Mariano Greg Miller, Cameron West and Michael Leitch.

Table of Contents

Chapter 1	1
Introduction	1
1.1 General.....	1
1.2 Research Objectives and Scope	4
1.3 Research Significance.....	7
1.4 Structure of the Report.....	8
1.5 References.....	12
Chapter 2	14
Background	14
2.1 Introduction.....	14
2.2 Magnesium Potassium Phosphate Ceramic Binders and Mortars	14
2.3 Lightweight Concrete.....	19
2.4 Textile Reinforcement	21
2.5 Discontinuous Short Fibers as Concrete Reinforcement	25
2.6 Use of Ceramic Concrete for Structural Applications	28
2.7 Summary.....	28
2.8 References.....	29
Chapter 3	33
Mechanical Properties of Magnesium Potassium Phosphate Cement and Mortars	33
3.1 Introduction.....	33
3.2 Materials and Experimental Procedure.....	35
3.2.1 Materials and Mix Preparations	35
3.2.1.1 Magnesium Potassium Phosphate Cement	35
3.2.1.2 Sand Aggregate Ceramic Mortar	36
3.2.2 Test Procedures.....	38
3.3 Results and Discussions.....	39
3.3.1 Result for Magnesium Potassium Phosphate Binder	39

3.3.1.1	Setting Time.....	39
3.3.1.2	Influence of Mixing Time on Compressive Strength	40
3.3.1.3	Influence of Fly Ash Loading on Density.....	41
3.3.1.4	Effect of Water to Binder Ratio and Fly Ash Loading on Compressive Cube Strength.....	41
3.3.1.5	Relationship Between Compressive Strength and Density.....	43
3.3.1.6	Compressive Strength Development.....	44
3.3.1.7	Modulus of Elasticity	46
3.3.1.8	Flexural Strength.....	46
3.3.2	Results for Sand Aggregate Ceramic Mortars	47
3.3.2.1	Influence of Binder to Sand Ratio on Density	47
3.3.2.2	Influence of Binder to Sand Ratio on Compressive Strength...	48
3.3.2.3	Compressive Strength Development.....	50
3.3.2.4	Modulus of Elasticity	52
3.3.2.5	Flexural Strength.....	52
3.3.2.6	Effect of Fly Ash Type on Compressive Strength	53
3.4	Conclusions.....	54
3.5	References.....	55
Chapter 4		57
Mechanical Properties of Lightweight Ceramic Concrete.....		57
4.1	Introduction.....	57
4.2	Experimental Program	59
4.2.1	Materials	59
4.2.1.1	Magnesium Potassium Phosphate Binder	59
4.2.1.2	Lightweight Aggregate	60
4.2.2	Specimen Preparation	61
4.2.3	Test Set-up	63
4.2.3.1	Fresh Property Test.....	63
4.2.3.2	Compressive Strength Test	64
4.2.3.3	Flexure Test	65
4.2.3.4	Direct Shear Test.....	65

4.3	Results and Discussion	66
4.3.1	Fresh Ceramic Concrete Properties	66
4.3.1.1	Slump Flow Test.....	66
4.3.1.2	Setting Time.....	67
4.3.2	Hardened Ceramic Concrete Properties.....	68
4.3.2.1	Density	68
4.3.2.2	Compression Strength.....	69
4.3.2.3	Stress-strain Relation and Modulus of Elasticity.....	74
4.3.2.4	Flexural Strength.....	77
4.3.2.5	Direct Shear Strength.....	79
4.4	Conclusions.....	81
4.5	References.....	82
Chapter 5	85
Proof of Concept Study of Textile Reinforced Ceramic Composite for	Structural Infill Slab Applications	85
5.1	Introduction.....	85
5.2	Materials	87
5.2.1	Concrete	87
5.2.1.1	Mix Proportions	89
5.2.1.2	Mix Procedures	89
5.2.1.3	Test Procedure	90
5.2.1.4	Results.....	91
5.2.2	Fabric Reinforcement.....	93
5.3	Panels	94
5.3.1	Specimen Preparation	94
5.3.2	Test Procedure and Test Set-up	95
5.3.3	Results and Ongoing Work.....	96
5.4	Conclusions.....	96
5.5	References.....	97
Chapter 6	98
Mechanical Properties of Glass Fiber Reinforced Ceramic Concrete.....		98

6.1	Introduction.....	98
6.2	Experimental Program	101
6.2.1	Materials and Mix Design.....	101
6.2.2	Mixing Procedures and Specimen Preparation.....	104
6.2.3	Test Procedures.....	105
6.2.3.1	Workability	105
6.2.3.2	Compressive Strength.....	106
6.2.3.3	Flexure Test	107
6.2.3.4	Direct Shear Test.....	108
6.3	Results and Discussion	108
6.4.1	Fresh Properties of GFRCC	108
6.4.2	Hardened Properties of GFRCC	109
6.4.2.1	Density	109
6.4.2.2	Compression	110
6.4.2.2.1	Cube Compression Strength.....	110
6.4.2.2.2	Cylinder Compression Response	110
6.4.2.3	Flexure	114
6.4.2.4	Direct Shear	119
6.4.3	Outlook and Implications Towards Member design.....	121
6.4	Conclusions.....	122
6.5	References.....	123
Chapter 7		127
Uniaxial Tensile Behaviour of Textile Reinforced Ceramic Concrete.....		127
7.1	Introduction.....	127
7.2	Materials	130
7.2.1	Ceramic Concrete.....	130
7.2.2	Textile Reinforcement	132
7.3	Specimen Preparation	134
7.3.1	Cube, Cylinder and Prism Specimens.....	134
7.3.2	Dog-bone Shaped Specimens	135
7.4	Test Methods.....	137
7.4.1	Hardened GFRCC Properties.....	137

7.4.1.1	Compression Tests	137
7.4.1.2	Splitting Tensile Test	138
7.4.1.3	Third-point Loading Bending Test	139
7.4.2	Uniaxial Tensile Test of Textile Reinforced Ceramic Concrete.	140
7.5	Experimental Results	141
7.5.1	Hardened GFRCC Properties.....	141
7.5.1.1	Air-dried Density	141
7.5.1.2	Compressive Strength	141
7.5.1.3	Splitting Tensile Strength	145
7.5.1.4	Flexure Tensile Strength.....	145
7.5.2	Uniaxial Tensile Test of Textile Reinforced Ceramic Concrete.	147
7.5.3	Comparison of Test Method Influence on Tensile Strength.....	156
7.6	Conclusions.....	157
7.7	References.....	159
Chapter 8	162
Experimental Study on Reinforced Ceramic Concrete Slabs.....	162
8.1	Introduction.....	162
8.2	Slab Configurations	164
8.3	Materials	167
8.3.1	Ceramic Concretes	168
8.3.2	Textile Fabric	171
8.3.3	Steel Reinforcement.....	172
8.4	Slab Specimen Fabrication	174
8.4.1	Formwork and Reinforcing Material Preparation.....	174
8.4.2	Mixing Concrete, Casting and Curing of Slab Specimens	175
8.4.2.1	Mix Procedure.....	175
8.4.2.2	Casting Slab Specimens.....	176
8.5	Test Set-up, Instrumentation and Procedure.....	178
8.5.1	Test Set-up	178
8.5.2	Instrumentation	181
8.5.3	Test Procedures.....	186

8.6	Test Results and Discussion.....	187
8.6.1	Load-Deflection Behaviour	187
8.6.2	Failure Modes	191
8.6.3	Moment-Curvature Responses.....	193
8.6.4	Strain Response.....	195
8.6.4.1	Concrete Strain.....	195
8.6.4.2	Reinforcing Steel Strain.....	197
8.6.4.3	Strain Distribution Through the Slab Depth.....	199
8.6.5	Ductility	200
8.6.6	Cracking Pattern and Crack Widths.....	202
8.7	Implication of Test Results	208
8.8	Conclusions.....	209
8.9	References.....	211
Chapter 9	214
Modeling the Flexural Behaviour of Reinforced Ceramic Concrete Slabs .	214	
9.1	Introduction.....	214
9.2	Slab Configurations	216
9.3	Material Models.....	218
9.3.1	Glass Fiber Reinforced Ceramic Concrete (GFRCC).....	218
9.3.2	Textile Reinforcement	223
9.3.3	Reinforcing Steel	224
9.4	Non-linear Analysis Model for Flexural Behaviour	226
9.4.1	Moment Curvature Response.....	228
9.4.2	Deflection and Slope Computation.....	232
9.5	Model Implementation.....	235
9.5.1	Analysis Using Computer Program	237
9.6	Comparison Between Experimental and Model Results	241
9.6.1	Comparison of Moment-Curvature Response	241
9.6.2	Comparisons of Concrete Strain	243
9.6.3	Comparison of Reinforcement Strain	244
9.6.4	Comparison of Load-Deflection Response.....	246

9.7	Parametric Study.....	248
9.7.1	Effect of f_c' and ρ on Moment-Curvature Response.....	249
9.7.2	Effect of f_c' and ρ on Neutral Axis Depth.....	252
9.7.3	Effect of f_c' and ρ on Curvature Ductility.....	252
9.8	Conclusions.....	254
9.9	References.....	255
Chapter 10		258
Conclusions and Recommendations.....		258
10.1	Summary.....	258
10.2	Conclusions.....	261
10.2.1	Magnesium Potassium Phosphate Binder and Mortar	261
10.2.2	Mechanical Properties of LWCC.....	262
10.2.3	Mechanical Properties of GFRCC	263
10.2.4	Uniaxial Tensile Behaviour of Textile Reinforced Ceramic Concrete	264
10.2.5	Flexural Behaviour of Reinforced Ceramic Concrete Slabs.....	265
10.3	Recommendations and Future Works.....	267
Bibliography		269
Appendix A		278
Tables and Plots		278
A.1	Introduction.....	278
A.2	Magnesium Potassium Phosphate Cement and Mortar	279
A.3	Lightweight Ceramic Concrete	285
A.4	Textile Reinforced Ceramic Concrete Panels	298
A.5	Glass Fiber Reinforced Ceramic Concrete	299
A.6	Uniaxial Tensile Behaviour of Textile Reinforced Ceramic Concrete	305
A.7	Reinforced Ceramic Concrete Slabs	313

List of Tables

Table 3.1- Chemical composition of Fly Ash	35
Table 3.2- Average 28 day mechanical properties of the B5 and B7 binders.....	47
Table 3.3- Average SCM properties	53
Table 4.1- Chemical composition of Fly Ash	60
Table 4.2- Physical properties of lightweight aggregates	61
Table 4.3- Mix proportion of lightweight aggregates ceramic composite	62
Table 4.4- Setting time of different ceramic concrete.....	68
Table 4.5- Effect of curing time on cube compressive strength and summary of cylinder compressive, flexure and shear test results	70
Table 5.1- Chemical composition of Fly Ash	88
Table 5.2- Textile fabric properties.....	93
Table 5.3- Detail of panels	95
Table 6.1- Chemical composition of Fly Ash	101
Table 6.2- Mix proportion of ceramic concretes.....	104
Table 6.3- Summary of test results.....	112
Table 7.1- Mix proportion of ceramic composite	131
Table 7.2- Characteristics of chopped glass fiber	132
Table 7.3- Cube compressive strength (f_{cu}) of ceramic concrete at 28 days.....	142
Table 7.4- Compressive strength ($f_{ct, t}$), flexural strength ($f_{ct, r}$) and splitting tensile strength ($f_{ct, st}$) of glass fiber reinforced ceramic concrete ($V_f=1.5\%$)...	143
Table 7.5- Axial tensile strength, $f_{ct, t}$ (MPa) from dog-bone specimens	148
Table 8.1- Slab geometry and ceramic concrete material properties	166
Table 8.2- Mix proportion of GFRCC	168
Table 8.3- GFRCC properties (Average).....	170

Table 8.4- Reinforcing steel properties	174
Table 8.5- List of instrumentation for each specimen.....	182
Table 8.6- Test results at different loading stages.....	189
Table 8.7- Curvature-ductility of tested slabs	201
Table 8.8- Displacement-ductility index.....	202
Table 8.9- Load and maximum flexural crack width at service and peak load conditions.....	205
Table 8.10- Number of flexural cracks and average crack spacing	206
Table 9.1- Slab geometry and concrete material properties.....	217
Table 9.2- Summary of GFRCC compression stress-strain curve parameters...	221
Table 9.3- Textile tensile stress-strain parameters.....	224
Table 9.4- Reinforcing steel stress-strain parameters	225
Table 9.5- Summary of experimental and model results	242
Table 9.6- Slab geometry and concrete material properties used for parametric study.....	249

List of Figures

Figure 1.1- Partial depth and full depth precast panels.....	2
Figure 1.2- Project structure.....	6
Figure 1.3- Report structure.....	9
Figure 2.1- Synthetic aggregates.....	20
Figure 2.2- Schematic representation of different concrete reinforcing systems	21
Figure 2.3- Examples of textile reinforcements made of AR-glass.....	22
Figure 2.4- Pedestrian bridge made of textile reinforced concrete in Albstadt, Germany (Hegger et al., 2011)	23
Figure 2.5- Facade of the extension of the testing hall of the Institute of Structural Concrete, Aachen University, Germany (Hegger and Voss, 2008).....	23
Figure 2.6- Stay-in-place formwork element made of TRC (Brameshuber et al., 2004).....	23
Figure 2.7- Examples of chopped glass fibers	26
Figure 3.1- Mix process	36
Figure 3.2- Particle size distribution of sands.....	37
Figure 3.3- Specimen identification.....	37
Figure 3.4- Test setups for compressions and prism test	39
Figure 3.5- Influence of retarder type on the binder setting times.....	40
Figure 3.6- Influence of mixing time on 7-day cube compressive strength	40
Figure 3.7- Average density vs. fly ash loading by mass of binder	41
Figure 3.8- Influence of fly ash loading and water/binder ratio on average compressive strength.....	43
Figure 3.9- Relationship between binder average compressive strength and average density.....	44
Figure 3.10- Compressive strength development with time of B5 and B7	45
Figure 3.11- Compressive stress-strain response of B5 and B7	46
Figure 3.12- Influence of binder to sand ratio on the density of sand ceramic mortars for w/b =0.2	48
Figure 3.13- Influence of b/S ratio on average compressive strength for 0.20 w/b ratio	49
Figure 3.14- Relationship between average compressive strength and average density for 0.20 w/b ratio	49
Figure 3.15- Early strength development.....	50
Figure 3.16- Compressive strength development with time	51
Figure 3.17- Compressive stress-strain response of sand ceramic mortars with B5 binders for b/S ratio of 1.5	52
Figure 3.18- Influence of fly ash type on compressive strength.....	54
Figure 4.1- Particle size distribution of lightweight aggregates	61
Figure 4.2- Compressive test configurations	64
Figure 4.3- Test set-up for prisms.....	65
Figure 4.4- Results of slump flow tests.....	67

Figure 4.5- Effect of mix proportions on the density of hardened ceramic concrete	69
Figure 4.6- Compressive strength of cubes for LWCC at ages of 7 and 28 days	71
Figure 4.7- Influence of water/binder ratio on compressive strength of LWCC using different aggregate types	73
Figure 4.8- Relation between compressive strength and density for different aggregates	73
Figure 4.9- Density to strength ratios of lightweight concrete with different aggregate for $a/b=0.67$	74
Figure 4.10- Stress-strain relation of B concrete for $a/b=0.67$	75
Figure 4.11- Effect of water/binder ratio on modulus of elasticity for LWCC using different types of aggregates	75
Figure 4.12- Relation between modulus of elasticity and compressive strength.	76
Figure 4.13- Flexural strength of Type B concrete	77
Figure 4.14- Influence of water/binder ratio on modulus of rupture for LWCC using different aggregate types	78
Figure 4.15- Relation between modulus of rupture and compressive strength....	78
Figure 4.16- Shear strength of B concrete	80
Figure 4.17- Effect of water/binder ratio on shear strength for LWCC using different types of aggregates.....	80
Figure 4.18- Relation between shear strength and compressive strength	80
Figure 5.1- Cross-section configuration of prototype panel	87
Figure 5.2- Finished prototype and cross-sections.....	87
Figure 5.3- Particle size distribution of sand and LECA aggregates	88
Figure 5.4- Test set-up for material characterization	91
Figure 5.5- 7 days compressive strength.....	91
Figure 5.6- Compressive strength development	92
Figure 5.7- Stress-strain responses.....	93
Figure 5.8- Textile types and orientation	93
Figure 5.9- Panels cross-sections	94
Figure 5.10- Flexural test setup.....	95
Figure 5.11- Load deflection response.....	95
Figure 6.1- Particle size distribution of aggregates.....	102
Figure 6.2- Glass fiber and geometry.....	103
Figure 6.3- Compressive test configurations	106
Figure 6.4- Test set-up for prisms.....	107
Figure 6.5- Influence of fiber volume fraction on flow	109
Figure 6.6- Influence of fiber volume fraction on density.....	109
Figure 6.7- Influence of fiber volume fraction on compressive stress to displacement relationship of cube samples.....	110
Figure 6.8- Influence of fiber volume fraction on compressive stress-strain relation	111
Figure 6.9- Relationship between compression toughness index and fiber volume fraction	114
Figure 6.10- Influence of fiber volume fraction on load-displacement under flexure	115

Figure 6.11- Effect of fibers on flexural strength	117
Figure 6.12- Relationship between flexural toughness and fiber volume fraction	118
Figure 6.13- Influence of fiber volume fraction on load-displacement under shear	119
Figure 6.14- Effect of fibers on shear strength	120
Figure 6.15- Relationship between shear toughness and fiber volume fraction	121
Figure 7.1- Textile fiber and geometry	133
Figure 7.2- Average tensile stress-strain curve for textile fabric	134
Figure 7.3- Dog-bone specimen geometry	135
Figure 7.4- Dog-bone specimen preparation stage	136
Figure 7.5- Compression test set-up	138
Figure 7.6- Splitting cylinder and bending test set-up	139
Figure 7.7- Uniaxial tensile test set-up	141
Figure 7.8- Average stress-strain curves in uniaxial compression	143
Figure 7.9- Compressive, flexural and splitting strengths of GFRCC	144
Figure 7.10- Average flexural stress versus mid-span displacement curves of GFRCC	146
Figure 7.11- Average axial stress-strain of ceramic concrete	148
Figure 7.12- Average axial stress-strain of ceramic concrete reinforced with 1.5% short fibers and without textile fabric	149
Figure 7.13- Typical cracking pattern of tensile test specimens	149
Figure 7.14- Typical observed crack pattern at failure of textile reinforced concrete: (a) transverse crack; (b) Longitudinal or splitting cracks	151
Figure 7.15- Average axial stress-strain of ceramic concrete reinforced with one layer of textile only	153
Figure 7.16- Average axial stress-strain of ceramic concrete reinforced with one layer of textile and 1.5% short fibers	154
Figure 7.17- Average axial stress-strain of ceramic concrete reinforced with two layers of textile and 1.5% short fibers	156
Figure 7.18- Relation of compressive strength and tensile strengths of GFRCC ($V_f=1.5\%$)	157
Figure 8.1- Dimensions of reinforcement details for test specimens	165
Figure 8.2- Cross-sections for the test slab	165
Figure 8.3- Detail of test specimens identification	166
Figure 8.4- Average compressive stress-strain curves for all the slab samples	170
Figure 8.5- Slab reinforcement materials	172
Figure 8.6- Reinforcement tensile test set-up	173
Figure 8.7- Average tensile stress-strain curve of reinforcing steel	173
Figure 8.8- Form work and reinforcement layout	175
Figure 8.9- Slab specimen preparation process	178
Figure 8.10- Textile reinforced layer preparation and surface scraping	178
Figure 8.11- Schematic of the test set-up for slab specimens	179
Figure 8.12- General views of the test set-up and instrumentations	180
Figure 8.13- Detail of support systems	181
Figure 8.14- Schematic view of instrumentation for slab specimen	183

Figure 8.15- West side view and digital camera system set-up	185
Figure 8.16- Effect of concrete type and f_c' on load-deflection behaviour	188
Figure 8.17- Effect of reinforcement configuration on load-deflection behaviour	190
Figure 8.18- Typical observed failure modes for slabs.....	192
Figure 8.19- Moment-curvature response.....	194
Figure 8.20- Load versus extreme fiber compressive concrete strain at mid-span	196
Figure 8.21- Load versus reinforcing steel strain at mid-span.....	198
Figure 8.22- Strain distribution through depth of slab at mid-span	200
Figure 8.23- Effect of concrete type and f_c' on load-crack width behaviour.....	203
Figure 8.24- Effect of reinforcement configuration on load-crack width behaviour	204
Figure 8.25- Test specimen crack patterns after failure.....	207
Figure 8.26- Schematic of crack patterns after failure.....	208
Figure 9.1- Dimensions and reinforcement details for test specimens	217
Figure 9.2- Comparison of predicted with experimental compressive stress-strain curves for GFRCC	220
Figure 9.3- Idealized tensile stress-strain curves for GFRCC	221
Figure 9.4- Idealized tensile stress-strain curves for textile reinforced ceramic concrete	223
Figure 9.5- Tensile stress-strain behaviour of steel reinforcement.....	226
Figure 9.6- Strain, stress and force distribution considered for moment-curvature analysis.....	228
Figure 9.7- Slope and deflection diagrams of slab.....	233
Figure 9.8- Program flow chart.....	236
Figure 9.9- Analysis program process	237
Figure 9.10- Illustrative output figures from the analysis program (S03L).....	239
Figure 9.11- Convergence study of the computer program	241
Figure 9.12- Measured and predicted moment-curvature comparison	243
Figure 9.13- Measured and predicted load versus extreme fiber compressive concrete strain comparison at mid-span.....	244
Figure 9.14- Measured and predicted load versus mid-span steel strain comparison.....	245
Figure 9.15- Measured and predicted mid-span load-deflection comparison....	247
Figure 9.16- Effect of f_c' on moment-curvature response predicted by model..	250
Figure 9.17- Effect of ρ on moment-curvature response predicted by model ...	251
Figure 9.18- Effect of f_c' and ρ on neutral axis depth at peak load	252
Figure 9.19- Effect of f_c' on μ_c	253
Figure 9.20- Effect of ρ on μ_c	254

List of Abbreviations and Notations

Abbreviations

- B = LWCC made by using coated expanded shale aggregates
- BA = LWCC made by using crushed bottom ash
- BC = LWCC made by using crushed expanded shale aggregates
- CBPC = Chemically Bonded Phosphate Ceramic
- CV = Coefficient of variation
- DIC = Digital image correlation
- FB = GFRCC ($V_f=1.5\%$) made by using coated expanded shale aggregates
- FLL = GFRCC ($V_f=1.5\%$) made by made by combining fine and coarse expanded clay aggregates
- FS = GFRCC ($V_f=1.5\%$) made by using sand
- GFRCC = Glass fiber reinforced ceramic concrete
- MPPC = Magnesium potassium phosphate cement
- L = LWCC made by using fine expanded clay aggregates
- LL = LWCC made by combining fine and coarse expanded clay aggregates
- LECA = Lightweight expanded clay aggregates
- LVDT = Linear variable differential transducer
- LWC = Lightweight concrete
- LWCC = Lightweight ceramic concrete
- PC = Portland cement
- RB = Reinforcing steel
- RT = Textile reinforcement
- S = LWCC made by using expanded slate aggregates
- SCM = Sand ceramic mortar
- TRC = Textile reinforced concrete

Notations

A	= area of concrete section (mm ²)
a	=depth of notch (mm)
A_{ci}	= area of concrete strip section (mm ²)
A_f	= area of textile reinforcement (mm ²)
A_s	= area of reinforcing steel (mm ²)
b	= width of slab or prism (mm)
D	= diameter of cylinder specimen (mm)
d	= location of steel reinforcement from top fiber (mm)
d_c	= location of steel reinforcement from bottom fiber (mm)
d_f	= depth of textile reinforcement from bottom fiber (mm)
dh	= depth of slab section strip (mm)
d_p	= depth of prism sample (mm)
dx	= slab strip width (mm)
E_b	= modulus of elasticity of binder (GPa)
E_c	= modulus of elasticity of LWCC or GFRCC (GPa)
E_{f1}	= first slope of of bi-linear stress-strain (MPa)
E_{f2}	= second slope of bi-linear stress-strain (MPa)
E_m	= modulus of elasticity of SCM (GPa)
E_s	= modulus of elasticity of reinforcing steel (GPa)
f_c	= cylinder compressive strength of LWCC (MPa)
f_c	= ceramic concrete compressive stress at any strain ε (MPa)
$f_{c,b}$	= cylinder compressive strength of binder (MPa)
$f_{c,m}$	= compressive strength of SCM (MPa)
f_c'	= cylinder compressive strength of GFRCC (MPa)
F_{cci}	= concrete compression force for element i (kN)
f_{cci}	= stress in the concrete of element i in compression (MPa)
f_{cct}	= axial tensile stress of GFRCC at any strain ε (MPa)

f_{cr}	= cracking stress of GFRCC (MPa)
f_{ct}	= axial tensile strength of GFRCC (MPa)
$f_{ct,r}$	= flexural tensile strength of GFRCC (MPa)
$f_{ct,st}$	= splitting tensile strength of GFRCC (MPa)
$f_{ct,t}$	= axial tensile strength of dog-bone specimen (MPa)
f_{ctI}	= axial tensile softening stress of GFRCC (MPa)
F_{cti}	= concrete tension force for element i (kN)
f_{cti}	= stress in the concrete of element i in tension (MPa)
f_{cu}	= cube compressive strength of GFRCC (MPa)
F_f	= force in the textile reinforcement (kN)
f_f	= stress in the textile reinforcement (MPa)
f_r	= modulus of rupture of LWCC (MPa)
$f_{r,b}$	= modulus of rupture of binder (MPa)
$f_{r,m}$	= modulus of rupture of SCM (MPa)
F_s	= force in the steel reinforcement (kN)
f_s	= stress in the steel reinforcement (MPa)
f_{uf}	= textile ultimate stress (MPa)
f_{us}	= steel ultimate stress (MPa)
f_y	= yield stress in the steel reinforcement (MPa)
f_{yf}	= textile stress corresponds to ϵ_{yf} (MPa)
f_{τ}	= shear strength of LWCC (MPa)
h	= total thickness of the slab (mm)
I_{tc}	= compression toughness index
L	= total span length (mm)
L_{AB}	= distance between two points along the span (mm)
l_c	= length of cylinder specimen (mm)
L_f	= length of fiber (mm)
L_p	= distance between applied loads (mm)

L_{pr}	= span length of prism (mm)
M	= bending moment (kN-m)
M_u	= peak bending moment (kN-m)
M_y	= yield bending moment (kN-m)
N_L	= number of textile layers
P	= applied load (kN)
P_s	= service load (kN)
P_u	= peak load (kN)
P_y	= yeild load (kN)
R^2	= Coefficient of determination
T_{δ_r}	= flexural toughness (J)
T_τ	= shear toughness (J)
V_f	= volume of fiber (%)
w	= crack width (mm)
w_s	= crack width at service load (mm)
w_u	= crack width at peak load (mm)
y	= distance from neutral axis to center of the strip (mm)
y_c	= distance from neutral axis to concrete strip in compression (mm)
y_f	= distance from neutral axis to centroid of textile reinforcement (mm)
y_{mc}	= distance from neutral axis to concrete total compression force (mm)
y_{mt}	= distance from neutral axis to concrete total tension force (mm)
y_o	= depth of neutral axis (mm)
y_s	= distance from neutral axis to centroid of tension steel reinforcement (mm)
y_t	= distance from neutral axis to concrete strip in tension (mm)
β_a, β_b	= compression material parameter
γ_b	=density of binder (kg/m ³)
γ_c	= density of LWCC or GFRCC (kg/m ³)
δ_r	= displacement corresponding to modulus of rupture of LWCC or GFRCC (mm)

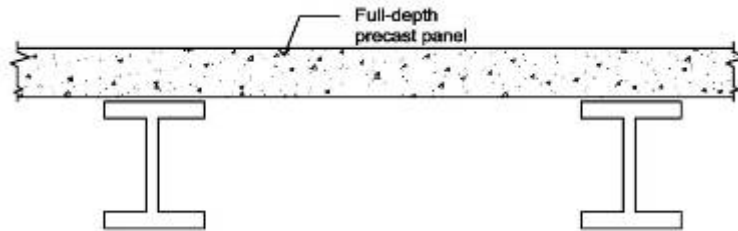
δ_{τ}	= displacement corresponding to maximum shear of LWCC or GFRCC (mm)
Δ	= slab deflection (mm)
Δ_s	= service load deflection (mm)
Δ_u	= peak load deflection (mm)
Δ_y	= yield load deflection (mm)
ε_b	= strain corresponding to maximum stress for binder (mm/mm)
ε_c	= strain corresponding to maximum stress of LWCC in compression (mm/mm)
ε_{cc}	= strain in extreme concrete compression fiber (mm/mm)
ε_{cci}	= strain in concrete strip in compression of element i (mm/mm)
ε_{co}	= value of strain at the peak compression stress of GFRCC (mm/mm)
ε_{ct}	= strain in extreme concrete tension fiber (mm/mm)
ε_{ct1}	= axial tensile softening strain of GFRCC (mm/mm)
ε_{ctu}	= axial ultimate tensile strain of GFRCC (mm/mm)
ε_{cu}	= ultimate concrete strain at extreme compression fiber (mm/mm)
ε_f	= strain in textile reinforcement (mm/mm)
ε_m	= strain corresponding to maximum stress for binder (mm/mm)
ε_s	= reinforcing steel strain (mm/mm)
ε_{uf}	= ultimate textile strain (mm/mm)
ε_{us}	= ultimate tensile strain in reinforcing steel (mm/mm)
ε_{yf}	= textile strain at end of first gradient (mm/mm)
ε_{ys}	= yield strain in reinforcing steel (mm/mm)
θ	= slab slope (rad)
μ_c	= curvature-ductility index
μ_c	= displacement-ductility index
ρ	= reinforcement ratio (%)
ϕ	= curvature (1/m)
ϕ_y	= yield curvature (1/m)
ϕ_u	= ultimate curvature (1/m)

Introduction

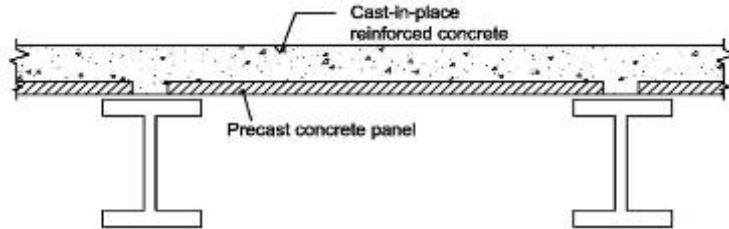
1.1 General

Prefabricated reinforced concrete slabs have been used for building slabs and bridge deck constructions. They may be constructed using full-depth precast panels or using a partial-depth precast system (e.g., Biswas, 1986). Full-depth precast panels are normally constructed under controlled conditions away from the final structure and then brought to the site for final installation. Thus, the method provides good quality control of the construction and will allow minimization of the total time required for at-site construction. The main disadvantage of this method is that each structural concrete element requiring transport is typically very heavy. Full depth precast panels are schematically shown in Figure 1.1(a). In the partial-depth system, the precast panels act as stay in place formwork for additional cast-in-place concrete as shown in Figure 1.1(b). The panels also contribute to the overall structural response of the final slab. This method offers several advantages compared to conventional forming, including elimination of the field labour required to remove the forms after the deck concrete cures. The disadvantage is increased delay in construction compared to a full-depth precast system to allow for the on-site placing and curing of the additional concrete. While reinforced concrete precast panel systems have been widely applicable for building slabs, building cladding panels and bridge deck

constructions, they have unfavourable characteristics due to high self-weight, slow strength gain of concrete and long-term durability problems. Thus, there is a clear need to consider alternative construction materials that are lightweight, rapid to build and durable.



(b) Partial depth precast panel



(b) Partial depth precast panel

Figure 1.1- Partial depth and full depth precast panels

The traditional concretes used for construction of slabs in buildings and bridges are typically made using Portland cement (PC) and various sand and gravel aggregates. While widely used as a concrete binder, PC has several detrimental characteristics including high permeability, high density, slow curing and rate of strength gain (Wagh, 2004; Wagh et al., 1997). In addition, the production of 1 tonne of PC requires about 1.5 tonnes of raw materials, and at the same time generates about 1 tonne of carbon dioxide (CO₂). At the same time, the energy required for the production of 1 tonne of PC is about 5.8 million BTU (e.g., Wagh, 2004). Therefore, the production of PC has very high environmental impacts due to CO₂ emissions, resource and energy consumption (Li et al., 2004).

In recent years, phosphate cements have gained attention as an alternative to PC and these can be used to produce so-called chemically bonded phosphate ceramics

(CBPC) (Wagh et al., 1997; Ding and Li, 2005; Qiao et al., 2010). CBPCs can be formulated to cure rapidly, have high early strength, and have good durability, including chemical attack resistance and deicer scaling resistance (e.g., Wagh, 2004). The production of CBPC consumes 30-50% of the energy required for cement production (e.g., Wagh, 2004). Furthermore, because high fly ash loading can be used (over 40 % by mass of the paste), which is about twice that commonly used for PC (Wagh, 2004) and the raw materials for CBPC require different production techniques than PC, the overall environmental impacts from CO₂ emissions and energy consumption are greatly reduced.

Aggregates typically constitute about 70 to 80% by volume of concrete. Due to its large volume the physical characteristics of the aggregate will, therefore, have a pronounced influence on the properties of lightweight PC concrete (Chi et al., 2003). Lightweight concretes made with low-density aggregates can have strengths comparable to normal weight concretes, yet typically have 25% to 35% lower unit density (www.escsi.org). When used as part of a structural system, this reduction in density (or self weight) results in many advantages: reduction in substructure cost, ability to provide longer spans, improved seismic structural response due to a lower structural mass (e.g., Chandra and Berntsson, 2002). Lightweight aggregates can originate from natural resources or they can be manufactured. The main natural resource for lightweight aggregates is volcanic material. Manufactured or synthetic aggregates are typically produced by a thermal process to expand and harden the base materials by the rotary kiln process (e.g., Chandra and Berntsson, 2002). Common manufactured aggregates include lightweight expanded clay (LECA), expanded shale and expanded slate aggregate.

The use of textile reinforcement to produce a composite material known as textile reinforced concrete (TRC) is a recent innovation. In contrast to steel reinforcement, textile reinforcement can match almost any geometric shape, due to the very small diameter of the reinforcement fibres, making it possible to produce very thin and lightweight concrete elements (e.g., Bruckner, 2006). Furthermore, no minimum thickness of concrete cover is needed to prevent

corrosion of the textile reinforcement, because the fibers are non-corrosive unlike steel (e.g., Bruckner, 2006).

This research project developed a novel textile reinforced ceramic composite slab system and examined the structural behaviour of these ceramic composite slabs for building and bridge deck components. Both experimental and numerical techniques are used. To properly understand the performance of these composite systems, the mechanical properties of ceramic concrete produced with MPPC binder and aggregates (sand and lightweight aggregates), are established. No prior research has been reported in the literature concerning the structural behaviour of lightweight ceramic composite systems with textile reinforcement. This research provides a solid technical foundation to allow use of this novel composite system in practice for structural applications. The research also leads to enhanced understanding of ceramic concrete mix designs that promote efficient usage of the constituent materials while obtaining targeted rheological and mechanical properties. The research contributes to the general understanding of composite design and analysis methods for structural applications.

1.2 Research Objectives and Scope

The long-term objectives of this research are to develop design guidelines for ceramic composite slabs reinforced with textile fabric and reinforcing steel, and to use this system in field applications. Understanding the structural behaviour of textile reinforced ceramic composite slabs is therefore an important first step to meet these objectives. To achieve the long-term goal, the following short-term objectives of this research are established:

1. To establish a viable mix design through establishing trends of MPPC binders and ceramic concretes made using MPPC binders and different aggregates (sand and lightweight aggregates), and then to develop a quantitative understanding of key parameters used in the later structural application.

2. To study the uniaxial tensile behaviour of textile reinforced ceramic concrete.
3. To study the structural behaviour of slab systems manufactured using ceramic concretes, textile reinforcement and reinforcing steel.
4. To develop a nonlinear numerical model to investigate the flexural response up to failure.

In order to achieve these short-term objectives, the research program was divided into two main parts: Material Development and Characterization, and Structural Application. The research program organization is shown in Figure 1.2.

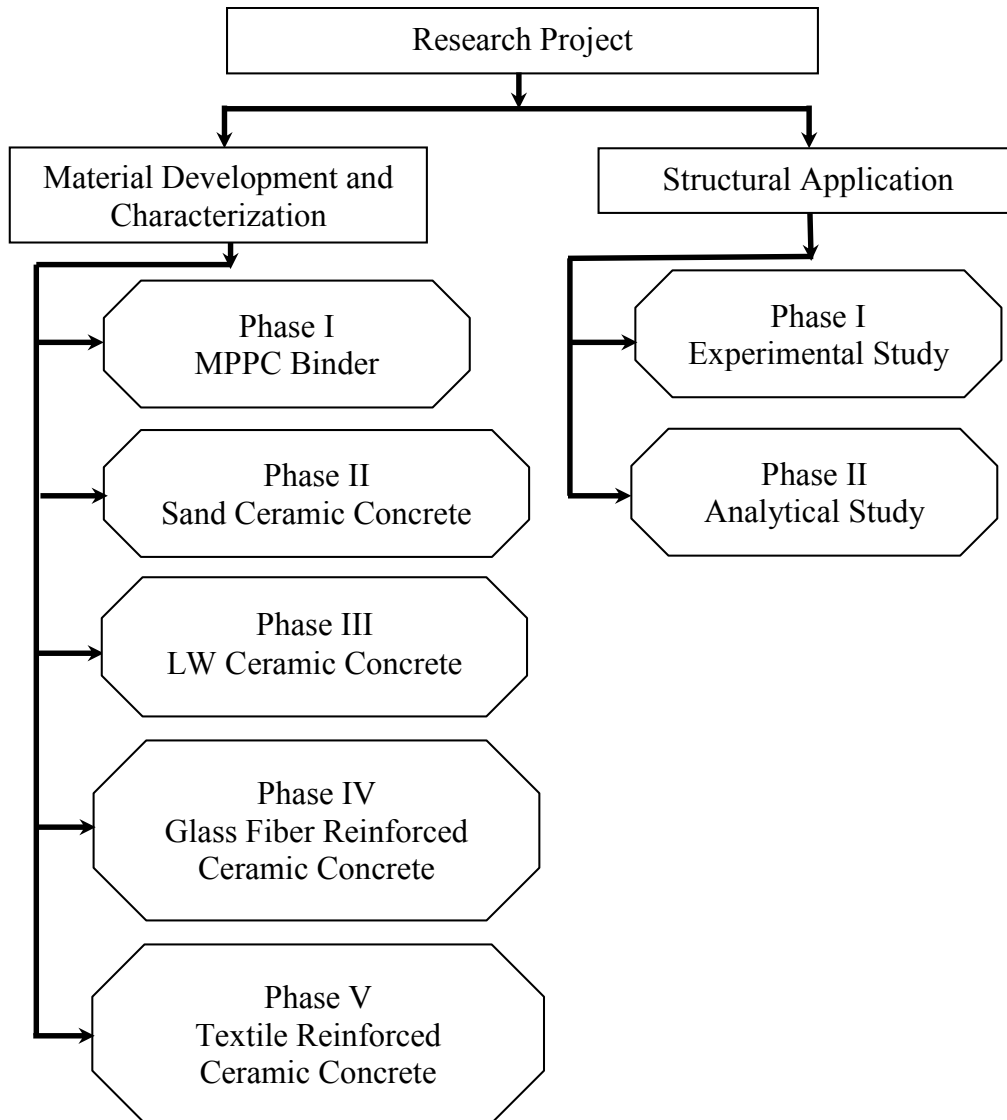


Figure 1.2- Project structure

The first part of the research project on Material Development and Characterization was divided into five phases. In Phase I, the research aimed to develop and characterize MPPC binder that incorporate a high fly ash loading to minimize the quantity of reactive components which are of higher unit cost. For the second Phase II, using the developed binders and sand aggregates, the research aimed to develop a composite material termed as sand ceramic concrete (SCC) having a minimum compressive strength of 50 MPa. Phase III aimed to produce and characterize a lightweight ceramic concrete (LWCC) using the developed MPPC binder and various lightweight aggregates with a target

minimum compressive strength of 20 MPa. Phase IV aimed to develop fiber reinforced ceramic concrete using the developed ceramic concrete and chopped glass fibers. Phase V targeted to examine the uniaxial tensile behaviour of ceramic concrete reinforced with textile reinforcements.

The second part of the research project on Structural Application contained two phases. Phase I consisted of an experimental study of slabs. Using glass fiber reinforced ceramic concrete from the first part of the research project, reinforcing steel and textile reinforcement, a total of 6 full-scale slabs, 200 x 150 x 2200 mm, were produced and tested. In Phase II, a numerical model was developed to predict the load deflection response of the slabs up to failure and validated using experimental results from phase I.

1.3 Research Significance

This research project adds to the knowledge and understanding of the subject of glass fiber and textile reinforced ceramic concretes for structural slab applications. The results are expected to be significant in terms of the following:

- (a) The magnesium phosphate ceramic binder used in the research incorporates fly ash at high loading. Therefore, it allows a decreased environmental impact from both CO₂ emissions and energy use during binder production compared to Portland cement binders. This research will help to further promote mix designs with efficient usage of the constituent materials. The results of this study indicated that lightweight ceramic concrete produced using magnesium phosphate binder and various lightweight aggregates attained mechanical properties similar to Portland cement concrete and hence this study allow use of these lightweight ceramic concrete for a wide range of applications.
- (b) The research aims to quantify the structural behaviour of glass fiber and textile reinforced ceramic composites. The combination of materials and

their configuration is novel, and allows tailored performance to the application.

- (c) The research provided experimental result of six large-scale ceramic concrete slab specimens reinforced by reinforcing steel and textile reinforcement. The study focused on typical design parameters including reinforcement ratio and material properties for the ceramic composites. The new information gathered in this research provided a solid technical foundation for general understanding of these composites behaviour for future use in structural application.
- (d) A nonlinear numerical model to simulate the flexural behaviour of fiber and textile reinforced ceramic composites was developed. This model allowed examining the typical design parameters including reinforcement ratio and material properties influence on the flexural properties of ceramic composites. This model is a general model and can further be refined for use in modeling similar composites from constituent materials with different mechanical properties.

1.4 Structure of the Report

As described in Section 1.2 this research project contained two main parts that included different phases. Those phases were completed and compiled into 10 different chapters as shown in Figure 1.3. Chapters 3, 4, 5 and 6 have been published as conference or journal articles. The content in the remaining chapters (i.e. 7, 8 and 9) are under preparation as future journal articles.

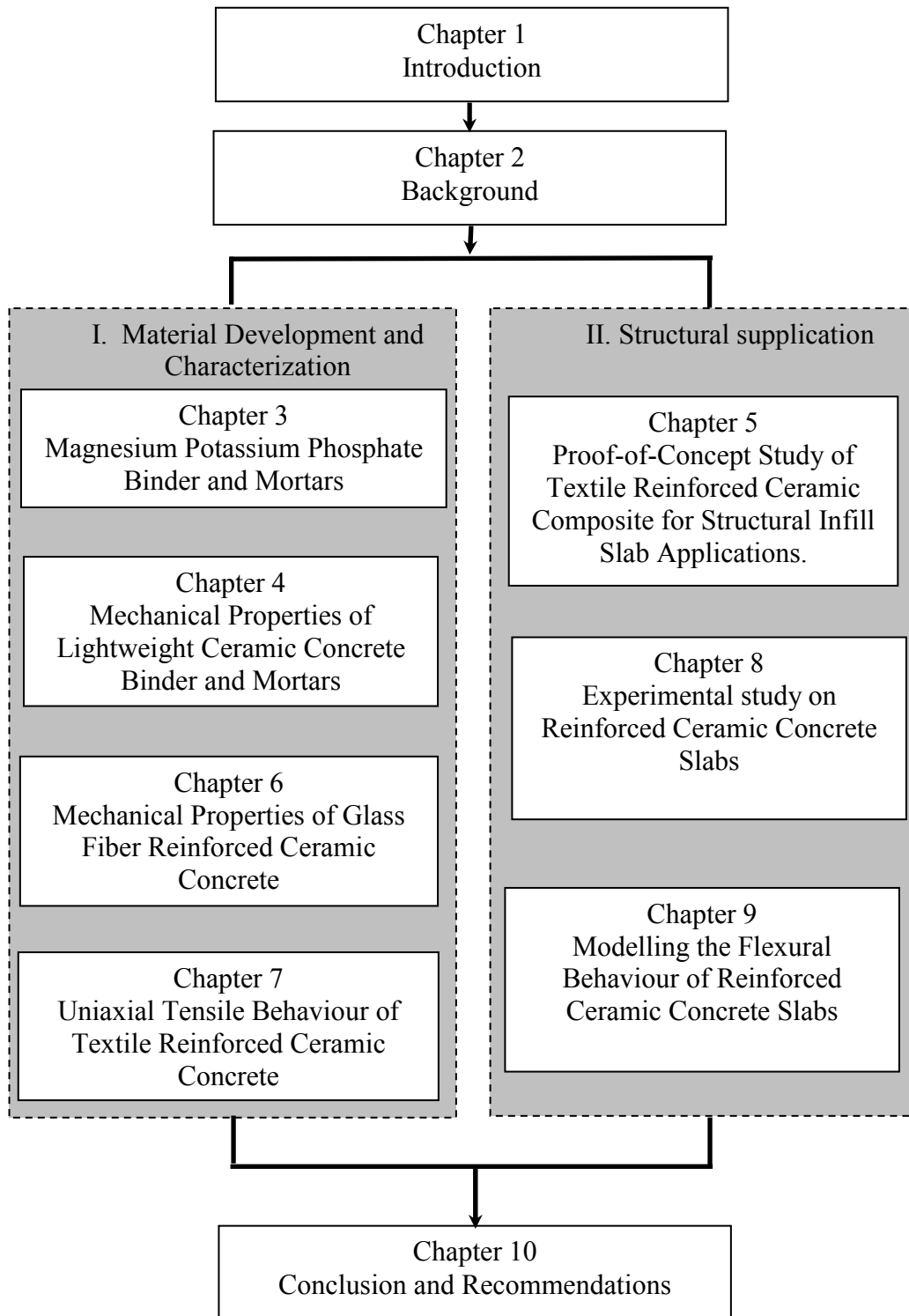


Figure 1.3- Report structure

Chapter 1 presents an introduction to this study including the objective and scopes, research significance and the structure of the report.

Chapter 2 provides a review of magnesium potassium phosphate concretes and their application in structural engineering. Background information on lightweight concrete, textile reinforced concrete, and fiber reinforced concrete relevant to this research area are also presented.

Chapter 3 contains the results of the experimental investigation carried out to study the mechanical properties of the magnesium potassium phosphate binder. The influences of water/binder ratio, fly ash content and mixing time on the compressive strength are examined. The relationship between compressive strength and density are presented. The influence of curing time on compressive strength is also presented, along with information on the setting time of the binder. In addition, results from a study of sand ceramic concrete composed of magnesium potassium phosphate binders and sand aggregates are presented. The influences from the sand to binder ratio and from the size distribution of the sand on the compressive strength at different ages are discussed.

The fresh and hardened properties of lightweight ceramic concrete made using magnesium potassium phosphate binders and different lightweight aggregates are described in Chapter 4. Six different lightweight aggregates were used. Six groups of mixes were produced using combinations of coarse and fine lightweight expanded clay aggregates (LECA), fine LECA only, expanded slate, expanded shale coated, expanded shale crushed and bottom ash. Three different water/binder ratios and three aggregate to binder mass ratios were used. The influence of these ratios on the compressive strength and the density are discussed. The influence of aggregate type on the modulus of elasticity, flexural strength and direct shear strength are also presented. Relationships were developed between the compressive strength and the flexural strength, shear strength and modulus of elasticity.

Chapter 5 reports on a proof-of-concept study for a structural infill slab system using textile reinforced ceramic composites. The ceramic concrete developed in Chapter 3 and 4 was used. Using ceramic concrete and flexible fiberglass reinforcing fabrics, small-scale specimens representing full-depth precast structural elements as well as partial-depth precast panels suitable for use as a stay-in-place formwork solution were produced and evaluated for strength and stiffness. The influences of the panel thickness and the fabric type on load carrying capacity are presented. The influences of the fabric on the pre- and post-cracking behaviour of the panels are discussed.

The influence of short fibers on the mechanical properties of glass fiber reinforced ceramic concrete (GFRCC) is discussed in Chapter 6. Mechanical properties of GFRCC mixes are studied by using two types of ceramic concrete adapted from Chapter 3 and 4: LECA ceramic concrete and sand ceramic concrete, and using chopped glass fibers. Fiber volume fractions between 0 and 2% are examined.

Chapter 7 discusses the behaviour of textile-reinforced ceramic concrete under direct uniaxial tension. Three ceramic concrete types developed in Chapters 3 and 4 and three types of glass fiber reinforced ceramic concretes from Chapter 6 are used. Various parameters including the addition of short fibers and number of textile layers on direct uniaxial tensile properties are discussed.

The experimental study of six full-scale slab specimens is presented in Chapter 8. The slabs were made using GFRCC, textile reinforcements and reinforcing steel. The parameters considered in the study include the ceramic concrete compressive strength as well as the amount of steel reinforcement and textile reinforcement. This chapter discusses the fabrication of specimens, details of the test set-up and instrumentation, the test procedures and the test results.

Chapter 9 presents a numerical study of the six slab specimens. The procedures used to develop a computer program using MATLAB® programming language based on the non-linear slab analysis approach is explained. The developed program is used to generate moment-curvature, load-deflection, load-concrete

strain and load-steel strain curves for the six slab specimens. These results are compared with the experimental results from Chapter 8.

Finally, summaries of the main conclusions regarding the overall experimental and analytical study are presented in Chapter 10. Recommendations for future investigations are also presented.

1.5 References

Advantages of Structural Lightweight Aggregate Concrete. Expanded Clay, Shale and Slate Institute, www.escsi.org. Last accessed on April, 2013.

Biswas, M. (1986). Precast Bridge Deck Design Systems. *PCI Journal*, 31(2): 40-90.

Bruckner, A., Ortlepp, R. and Curbach, M. (2006). Textile Reinforced Concrete for Strengthening in Bending and Shear. *Materials and Structures*, 39(8): 741-748.

Chandra, S. and Berntsson, L. (2002). *Lightweight Aggregate Concrete*, Noyes Publications, New York, USA, 167-229.

Chi, J. M., Huang, R., Yang, C.C. and Chang J.J. (2003). Effect of aggregate properties on the strength and stiffness of lightweight concrete, *Cement and Concrete Composites*, 25(2): 197-205.

Ding, Z. and Li, Z. (2005). High-early-strength magnesium phosphate cement with fly ash. *ACI Materials Journal*, 102(6): 357-381.

Hegger, J., Will N., Bruckermann, S. and Voss, S. (2006). Loading-bearing behaviour and simulation of textile-reinforced concrete. *Materials and Structures*, 39(8): 765–776.

Li, Z. Ding, Z. and Zhang, Y. (2004). Development of sustainable cementitious materials. Proceedings of International Workshop on Sustainable Development and Concrete Technology, Beijing, China, 55–76.

Qiao, F., Chau, C. K. and Li, Z. (2010). Property evaluation of magnesium phosphate cement mortar as patch repair material. *Construction and Building Materials*, 24: 695-700.

Wagh, A. S. (2004). *Chemically bonded phosphate ceramics: Twenty-first century material with diverse applications*. Elsevier Ltd., Amsterdam. 1-283.

Chapter 1: Introduction

Wagh, A. S., Jeong, S. Y. and Singh, D. (1997). High-strength ceramic (cement) using industrial by-product and slag. Proc. of Int. Conf. On High-Strength concrete, Kona, HI, 541-553.

Background

2.1 Introduction

This chapter presents background information relevant to this overall study including prior research related to magnesium potassium phosphate cement, lightweight concrete, textile reinforcement and the use of discontinuous short fibers as concrete reinforcement.

2.2 Magnesium Potassium Phosphate Ceramic Binders and Mortars

Chemically bonded ceramics are inorganic solids formed and consolidated by chemical reactions similar to cements but their structure is highly crystalline like ceramics (Roy, 1997). When phosphates are used to form chemically bonded ceramics, they are termed as chemically bonded phosphate ceramics (CBPCs) (Wagh, 2004). Traditional ammonium-phosphate cement based mortars produced by reacting magnesium oxide and ammonium hydrogen phosphate or ammonium dihydrogen phosphate are the most developed CBPCs and widely used as fast setting grouts or as rapid repair materials for roads, industrial floors and airport runways (e.g., Abdelrazig et al. 1988). However, widespread use of mortars based on ammonium-phosphate is limited because of the chemical reaction process will emit ammonia gas during mixing and curing (Wagh 2004). This can lead to

corrosion of mixing containers and unpleasant odours (e.g., Ding 2005). Recently developed potassium phosphate-based CBPC circumvented this limitation (Wagh et al., 1997).

Wagh et al. (Wagh, 2004; Wagh et al., 1997) developed CBPCs, which are produced through the acid-base reaction between calcined magnesium oxide (MgO) and monopotassium phosphate (KH₂PO₄) in an aqueous solution. The reaction between these compounds is given by:



The reaction product (MgKPO₄·6H₂O) functions as a binder called magnesium potassium phosphate cement (MPPC) here after that can be used as the matrix material to host inorganic materials such as ash, waste slag, or various natural or manufactured aggregates.

Both MPPC and Portland cement (PC) are formed by chemical reactions at room temperature, and both need water to activate the reactions. However, MPPCs are formed by either ionic or covalent bonds, while the hydration process in PCs relies on weaker Van der Waals forces (Wagh, 2004).

Several benefits of MPPC binders compared to PC binders have been reported (Wagh, 2004; Wagh et al., 1997). MPPC is more stable in acidic and high temperature environments. MPPC has a faster curing rate. While PCs are typically porous, MPPC can have significantly lower porosity. MPPC products exhibit porosity of 5-9% while PC products have porosity of approximately 20% (Wagh, 2004). MPPC can be blended with fly ash at higher loadings than conventional Portland cements. As a result of these advantages, MPPC are finding many applications. MPPC matrix composites are especially useful in extremely cold climates and in corrosive environments. These include use as a structural material in permafrost regions, as construction materials for low cost housing, as oil-field drilling cements and as road repair materials that set in very cold environments (Wagh, 2004).

Previous research has demonstrated that the mechanical and bonding properties of MPPC are enhanced by inclusion of fly ash (FA) (Wagh, 2004; Wagh et al, 1997; Ding and Li, 2005a). Wagh et al. (1997) reported that pure MPPC has a typical compressive strength of 20-25 MPa. When Class C FA is added at 60% by mass loading of dry binder, the compressive strength can increase to 80-85 MPa for some mix compositions. The gain in strength results from formation of silico-phosphate bonds demonstrating that the FA actively participates in the chemical reaction process (Wagh et al., 1997). According to Wagh, the compression strength is optimal when the FA loading is between 50 and 60% (Wagh et al., 1997).

Ding and Li (2005a) reported that the compressive strength for MPPC mortar depends on the fly ash content and the specimen age. Two kinds of hard burnt magnesia were used in the study: Magnesia containing either 89.6% magnesium oxide or 71.6% magnesium oxide and termed M9 and M7 respectively. The study showed that the MPPC mortars with 30%-50% FA exhibited higher strengths than samples prepared without FA. The highest compressive strength occurred for samples with 40% FA. M9 mortar with FA content of 40% had a compressive strength of 65-70 MPa. Ding and Li (2005a) also concluded that inclusion of FA improves the modulus of elasticity of MPPC mortar. The elastic modulus of MPPC using M9 material and with 0% and 40% fly ash determined at an age of 7 days were 27.5 and 31.9 GPa, respectively. Ding and Li (2005a) reported that the particles of FA fill the voids of MPPC and strongly bond together with the hydrates of the MPPC.

FA is a by product from coal-fired thermal power stations and thus MPPC with FA can result in substantially lower environmental impact and energy consumption during production than PC binders. MPPC can use FA at over 40% by mass of the paste while PC products typically incorporate a maximum of 15-20% FA in them (Wagh, 2004).

Ding and Li (2005*b*) studied the effect of the mixing water content on the properties of hardened MPPC mortars. The study showed that the compressive strength and modulus of elasticity of the MPPC mortar both decreased with an increase of the water to binder (w/b) ratio at ages of 3, 7 and 28 days. For example, for M9 mortar the compressive strength of 75-80 MPa was obtained for a w/b ratio of 0.16. The strength reduced to 45-50 MPa when the w/b ratio was increased to 0.21 for the M9 series mortars. Note that according to the reaction in Equation 2.1, the w/b ratio should be approximately 0.51 for a complete reaction of pure MPPC, with some variation depending on the FA content where the FA reacts with the phosphate compound. Nevertheless, the actual w/b values reported in Ding and Li (2005*b*) suggest that for small w/b ratio mixes there is insufficient water for a complete reaction but a maximum compressive strength is still achieved.

Ding and Li (2005*b*) investigated the influence of the fine aggregate type and quantity on the compressive strength of MPPC mortars. Qiao et al. (2010) also examined the influence of the sand to binder mass ratio on compressive strength. Both studies concluded that the compressive strength of MPPC mortar decreases as the aggregate content increases, regardless of the curing age and the type of sand. An increase in sand content causes a reduction in the paste volume fraction, thereby increasing the portion of paste in the interfacial region. This causes weaker bonding links in the mortar, which can lead to lower compressive strengths (Ding and Li, 2005*b*). Both studies reported that the highest compressive strengths were obtained when the sand to binder ratio was 1:1 among the various ratios considered.

The setting time of MPPC is very short. To obtain sufficient working time for practical applications, a retarder admixture can be used. The additives can take the form of either a coating agent or a water getter (Yang and Wu, 1999; Singh, 2001; Qiao et al., 2009). A coating agent such as boric acid works by coating and therefore isolating particles of one of the reactive components (typically the MgO) from complete exposure or contact by the other reactant (usually the

phosphate compound). A suitable water getter such as lignosulphonate serves to keep the water from quickly reacting with the phosphate. Singh et al. (2001) recommended that retarder admixture values between 0.5-3.5 weight percent are suitable.

Yang and Wu (1999) studied the setting time of a phosphate binder produced using magnesium oxide and mono-ammonium phosphate. The setting time could be controlled between several minutes and one hour by adjusting the added quantity of Borax, with the relationship also dependent on the amount of MgO in the mix. The setting time and overall reaction rate is also highly influenced by the fineness of the MgO, with shortened setting times occurring as the specific surface area of MgO is increased (Yang and Wu, 1999). The recommended specific surface area of the magnesium oxide powder should be in the range from 0.30 to 0.55 m²/g (Singh et al., 2001). Material with higher specific surface area than this range results in an accelerated reaction rate, leading to overheating due to the exothermic reaction process. Yang and Wu (1999) indicated that the setting time is lengthened with increased addition of Borax (B). It is also observed that a 5% mass ratio of Borax to MgO (B/M) could retard the setting time to 10-15 and 3-5 min for 0.126 m²/g and 0.350 m²/g surface area, respectively. These results indicate that a greater quantity of Borax is required as the specific surface area of MgO increases to keep a constant setting time.

Qiao et al. (2009) studied the effect of the magnesia composition (i.e. MgO content) on the strength and setting time by fixing the Borax to magnesia weight ratio at 5% and combining two kinds of magnesia: magnesia with 84% of MgO (MH) and with 76.8% of MgO (ML). The results showed that with an increase in the MH content the setting time is reduced and the strength is increased. For example, usage of MH at 50% content of the total magnesia resulted in setting time and strength of 20-25 min and 40-50 MPa respectively.

2.3 Lightweight Concrete

According to ACI 213R-03 (2009), structural lightweight concretes have 28-day compressive strengths in excess of 17 MPa and dry density in the range of 1680 to 1920 kg/m³ compared to normal weight concrete with a density in the range of 2240 to 2400 kg/m³.

Structural lightweight concretes produced using lightweight aggregate have been used successfully for many structural applications including building and bridge components (Chandra and Berstsson, 2002). Structural lightweight concrete offers design flexibility and substantial cost savings for the overall structure through a reduction in the self weight (i.e. dead load) (www.escsi.org). This reduced weight can allow smaller member sizes with lower reinforcing steel requirements and can potentially allow decreased story heights. The reduced weight can also permit longer spans if the member size remains constant, lower foundation costs are often possible, and the seismic structural response can be improved. Furthermore, the use of lightweight concrete can enhance fire ratings allowing thinner sections (Chandra and Berstsson, 2002).

One method to produce structural lightweight concrete is to replace normal weight aggregate by lightweight aggregate. Lightweight aggregates can originate from natural resources or they can be manufactured. The most common natural lightweight aggregate is from volcanic material. Manufactured or synthetic aggregates are typically produced by a thermal rotary kiln process to expand and harden the base materials (e.g., Chandra and Berstsson, 2002). Common manufactured aggregates that are used for structural lightweight concrete applications include lightweight expanded clay (LECA), expanded shale and expanded slate aggregate (see Figure 2.1).



Figure 2.1- Synthetic aggregates

Aggregates normally constitute about 70-80% by volume of a concrete mix. Due to its large volume the physical characteristics of the aggregate will, therefore, have a pronounced influence on the compressive strength and elastic modulus of lightweight Portland cement concrete (Chi et al., 2003; Ke et al., 2009; Lo et al., 2007). The Chi et al. (2003) investigated the influence of the volume fraction of lightweight aggregates on the compressive strength and elastic modulus for three aggregate types which differed by their saturated surface dry density, particle size and particle strength. The Chi et al. (2003) results demonstrate that both the compressive strength and elastic modulus decrease with an increase in volume fraction of lightweight aggregates. The physical properties of the lightweight aggregates are key factors affecting the compressive strength and elastic modulus of the concretes.

The compressive strength and modulus of elasticity of lightweight Portland cement concrete are also influenced by the water/binder ratio. Chi et al. (2003) reported that both the compressive strength and the elastic modulus of concrete decrease with an increase in the water to binder ratio.

Lo et al. (2007) reported that at ages of 7, 28 and 56 days, the compressive strength of Portland cement lightweight concrete decreases as the water/binder ratio increases. This influence of water/cement ratio (w/c) on the 28-day strength was studied for three grades of lightweight expanded clay aggregates having maximum aggregate sizes of 25, 15, and 5 mm. They reported that the mix with a maximum aggregate size of 15 mm achieved a higher strength than the mixes

with 5 and 25 mm aggregates due to the higher crushing strength of the 15 mm aggregate. They concluded that the strength of lightweight aggregate concrete depends on the aggregate strength, the hardened cement paste properties and the bonding of the aggregates to the cement paste in the interfacial zone.

While many prior studies have examined lightweight concretes made with Portland cement, no prior studies have investigated the properties of lightweight ceramic concretes produced using MPPC binders and manufactured lightweight aggregates.

2.4 Textile Reinforcement

Concrete is a brittle material and has low tensile strength. Usually steel reinforcement is used to resist tensile stresses. Similar to steel reinforcement, high strength textile fabric is able to resist tensile stresses after the concrete cracks. Schematic representations of the three common types of concrete reinforcing systems are shown in Figure 2.2.

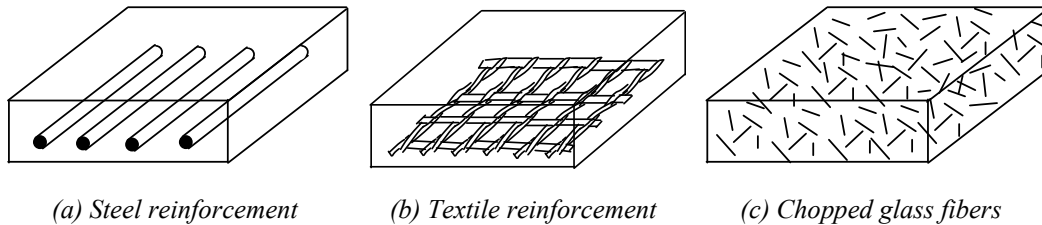


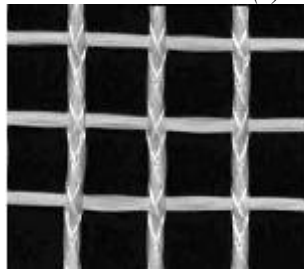
Figure 2.2- Schematic representation of different concrete reinforcing systems

In recent years, several research projects have focused on the development of cementitious composites reinforced with textile fabrics (e.g., Hegger et al., 2006; Bruckner et al. 2006; Bosche et al., 2008; Bruckner et al., 2008; Triantafillou and Papanicolaou, 2005; Peled, 2007). Textile reinforced concrete (TRC) is a composite material consisting of one or more layers of a textile fabric mesh and a fine-grained concrete. Commonly used textile materials include alkali-resistant glass (AR-glass) and carbon (e.g., Figure 2.3). Due to the corrosion resistance of the fiber materials, a large concrete cover is not required for corrosion protection (Hegger et al., 2006), and thus allows the development of thinner, lightweight

elements (Bruckner et al., 2006). Use of textile reinforcement has several additional advantages compared to conventional steel reinforcement including the ability for the textile to be formed to match complex geometric shapes (see Figure 2.3). Textile fabrics are lightweight, thereby providing easier handling and rapid placement to speed the overall construction process.



(a) Roll of textile reinforcement



(b) Bosche, 2008



(c) Hegger et al., 2011

Figure 2.3- *Examples of textile reinforcements made of AR-glass*

TRC can be used both for new structures as well as for strengthening of existing structures. Application of TRC for new structures includes bridge deck construction (e.g. Hegger et al. 2011) or building wall panel construction (e.g., Hegger and Voss, 2008; Hegger et al., 2012). Prior works have also considered application of TRC for strengthening of structural elements including slabs, beams and columns (e.g., Bruckner et al., 2006; Bosche et al., 2008). Figure 2.4 shows a textile reinforced pedestrian bridge constructed over a road in Albstadt, Germany (Hegger et al., 2011). Application of TRC for the outer wall construction of the Institute of Structural Concrete, Aachen University is shown in Figure 2.5 (Hegger and Voss, 2008). Figure 2.6 shows the cross-section of a TRC panel used as a stay-in-place formwork element (Brameshuber et al., 2004).



Figure 2.4- Pedestrian bridge made of textile reinforced concrete in Albstadt, Germany (Hegger et al., 2011)

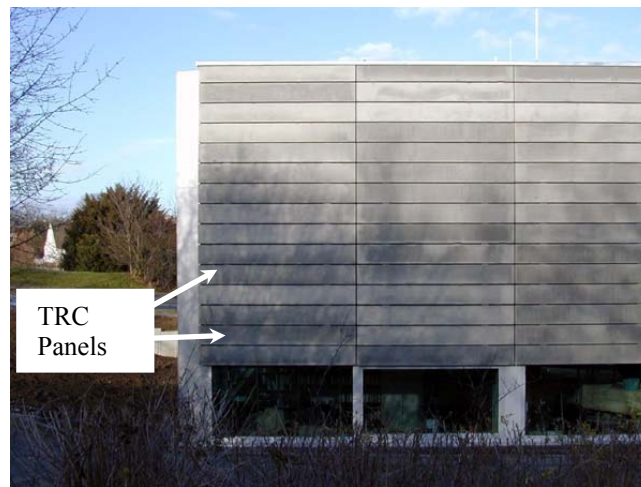


Figure 2.5- Facade of the extension of the testing hall of the Institute of Structural Concrete, Aachen University, Germany (Hegger and Voss, 2008)

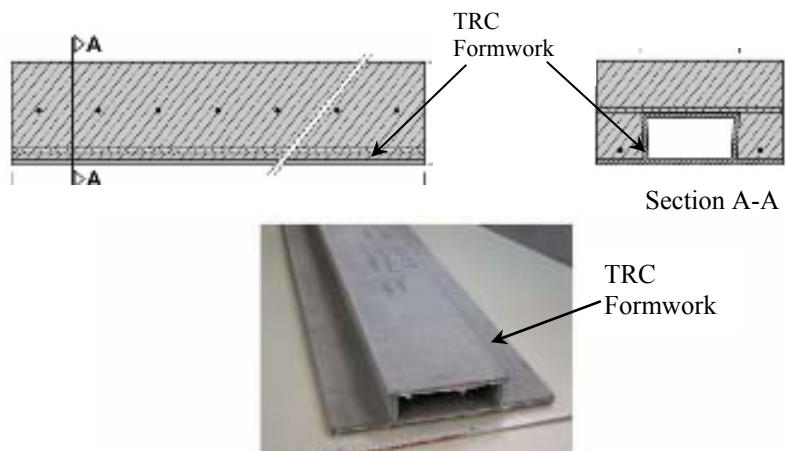


Figure 2.6- Stay-in-place formwork element made of TRC (Brameshuber et al., 2004)

Reinforced concrete flexural elements strengthened by TRC have been reported to show noticeable improvements to both the load-bearing behaviour as well as the serviceability (e.g., Bruckner et al., 2006). However, the strengthening effect of TRC depends on the load-bearing behaviour of TRC, which is influenced by the material properties of the textile fabric used (Bosche et al., 2008), the amount of the textile reinforcements and the properties of the concrete matrix (Hegger et al., 2006).

Bruckner et al. (2006) reported that strengthening slabs with TRC noticeably improved the ultimate load carrying capacity as well as the stiffness. The study reported that the load-displacement response of the strengthened slab was much stiffer than the non-strengthened control slab due to a larger moment of inertia of the strengthened slab in both the un-cracked state and after the occurrence of multiple cracks.

Bosche et al. (2008) also demonstrated that TRC is a viable means to increase the ultimate load capacity of flexural components and reported that the strengthening effect depends on the material properties of the textiles used. Two different types of AR-glass textiles were considered in the study: textiles referred to as NWM3-022-00 (with an ultimate capacity 400-500 MPa and strain of about 24 mm/m) and NWM4-011-03 (an ultimate capacity of 350-400 MPa and strain of about 19 mm/m). The study showed that the increase in capacity of the slab strengthened with textile NWM4-011-03 (improved textile, see Figure 2.3 (b)) was distinctly higher than the slabs strengthened with textile NWM3-022-00. The results showed that cracking started at a considerably higher load level for the strengthened slab. This was attributed to the higher effective concrete tensile strength of the TRC layer and, to the increased section modulus of the strengthened specimens.

Recently, research has established the effective use of MPPC-based binding agent with fiber-reinforced polymer (FRP) to strengthen reinforced concrete slabs (Obregon-Salinas et. al, 2011). This study showed that MPPC-based binder was

effective to externally bond the FRP to the concrete slab and increased the flexural strength of the slab. The study also reported that MPPC-based binder combined with FRP strengthening system could provide a high resistance to fire.

Although various researchers have reported on the behaviour of textile reinforced concrete made using Portland cement-based binders, no prior research is available for textile reinforced MPPC-based concretes used as a preliminary structural element.

2.5 Discontinuous Short Fibers as Concrete Reinforcement

One way of reinforcing concrete is by using randomly distributed short fibers (see Figure 2.2(c)). The main role of short fibers is to control the cracks from widening and propagating in the concrete, by bridging the cracks and transferring loads across the cracks, thus improving the toughness or energy absorption capacity of the composite matrix (Bentur and Mindess, 1990; Balaguru and Shah, 1992; Brandt, 2008). There are different commercially available types of short fibers including steel, glass, carbon, etc. Depending on the type of fiber used, fiber reinforced concrete has a wide range of applications such as precast panels, pavements, shotcrete, dams, seismic-resistant structures, etc. (e.g., Bentur and Mindess, 1990).

Glass fiber reinforced concrete is a composite material made of fine aggregate concrete and glass fibers. Glass fiber reinforced concrete has several applications including building cladding panels, stay in place formwork and the construction of many architectural details (Mobasher, 2011).

Typical discontinuous short glass fibers are shown in Figure 2.7. Glass fibers are a relatively lightweight material and have high tensile strength. Typical glass fibers have a tensile strength of 2070 MPa (more than three times that of steel fibers), a modulus of elasticity of 76 GPa and a specific gravity of 2.7 (about one-third that of steel fibers) (e.g., www.negamerica.com).



Figure 2.7- *Examples of chopped glass fibers*

Prior studies have been conducted to investigate the performance of cementitious composites, which incorporated randomly distributed short fibers into the cement matrix (e.g., Fanella and Naaman, 1985; Mirza and Soroushian 1999; Ali et al., 1975; Choi and Yuan, 2005).

Ali et al. (2009) reported that the bending strengths of cement composites were increased by 4 to 5 times when 6 Vol.-% of short glass fibers were used.

Fanella and Naaman (1985) have studied the behaviour of fiber reinforced concrete under compression. They used steel, glass and polypropylene fibers with volume fractions of 1, 2 and 3%. They reported that, except for steel fibers, adding fibers to a concrete does not alter the compressive strength. They also reported that the glass and polypropylene fibers used typically failed by tensile rupture whereas the steel fibers exhibited pullout failure modes.

Mirza and Soroushian (1999) studied the flexural strength, ductility and restrained shrinkage cracking of lightweight concrete incorporating glass fibers at volume fractions from 0.125 up to 0.75%. They reported that addition of glass fibers promoted multiple cracking and reduced crack widths, and also improved the flexural strength and ductility of lightweight concrete.

Choi and Yuan (2005) studied the splitting tensile strength and the compressive strength of glass fiber reinforced concrete using 1% and 1.5% short glass fiber by volume. They reported that the addition of glass fibers to concrete increased the

splitting tensile strength of concrete by approximately 20-50%. The splitting tensile strength of glass fiber reinforced concrete ranged from 9% to 13% of its compressive strength.

The beneficial influence on the mechanical properties of TRC from adding distributed short glass fibers have been reported in prior research. (e.g., Hinzen and Brameshuber, 2009; Barhum and Mechtcherine, 2012). All TRC studies used PC binders.

Hinzen and Brameshuber (2009) reported the enhancement potential of the tensile load-bearing capacity of textile reinforced concrete by also adding short fibers. They reported that the load at first cracking increased considerably after addition of 2.0 Vol-% glass fibres. Further, they reported that the addition of two different short fibers (1.5 Vol-% glass fibres and 1.0 Vol-% Aramid fibers) increased the stress at first cracking by approximately 40% and improved the post-cracking behaviour.

Barhum and Mechtcherine (2012) studied TRC samples with 4 layers of textile reinforcement with 0.5% by volume short glass fibers and TRC samples with two layers of textile reinforcement with 1% by volume short glass fibers. They reported that the addition of short glass fibres to TRC increased the first-crack stress value by a factor of 1.5. However, a moderate increase (1.1 to 1.5 times) in the tensile strength of the TRC was observed when short fibers were used. Furthermore, they reported that the addition of the short fibers improved the overall bond developed between the textile and the cement matrix.

It has also been reported that adding discontinuous short fibers can improve the performance of MPPC-based composites (e.g., Wagh, 2004; Jeong and Wagh, 2003). For example, the addition of 3 Wt.-% glass fibers in MPPC with 60% fly ash loading enhanced the flexural strength from 6.3 MPa to 9.1 MPa and 11.9 MPa for mixes using 6 mm and 13 mm fiber lengths, respectively (Wagh, 2004). Similarly, the fracture toughness improved significantly compared to mixes without fibers (Wagh, 2004).

2.6 Use of Ceramic Concrete for Structural Applications

There is no prior research available that has examined the application of ceramic concrete, and especially ceramic concrete containing coarse aggregates and/or lightweight aggregates. Some previous research has demonstrated the application of glass fiber reinforced phosphate cements in thin building elements such as sandwich panels (Cuypers, 2002). However, the ceramic binders in these studies (Cuypers, 2002) differed from that proposed for the current research project. Only a few publications (e.g., Ding and Li 2005*b*; Qiao et al 2010) have reported on studies using MPPC based mortars but applications of these mortars were typically focussed on use as a rapid and durable repair material for structural rehabilitation rather than large-scale reinforced structural elements.

2.7 Summary

This chapter provided background information on MPPC binders, PC based lightweight concrete, textile reinforcement and use of discontinuous short fibres as concrete reinforcement.

There are prior studies that have investigated the mechanical properties of MPPC based concrete made from MPPC binder and sand aggregates. However no prior research has examined the mechanical or rheological properties of MPPC-based concretes made using MPPC binder and lightweight aggregates that contained or omitted chopped glass fibers.

Although a great deal of research has been reported on the performance of fiber reinforced concretes and textile reinforced concrete using PC-based binders, no prior investigations have examined the structural response of lightweight MPPC-based concretes with chopped glass fibers and/or glass textile reinforcement. This research project aims first to understand the mechanical properties of concretes made with MPPC binder and various aggregates (sand and lightweight coarse

aggregates). The project then aims to investigate the structural behaviour of slabs produced using these composites and textile reinforcement.

2.8 References

- ACI Committee 213 (2009). Guide for Structural Lightweight-Aggregate Concrete (ACI 213R-03), ACI manual of Concrete Practice (Part 1), American Concrete Institute, Farmington Hills, MI, 1-20.
- Advantages of Structural Lightweight Aggregate Concrete. Expanded Clay, Shale and Slate Institute, www.escsi.org. Last accessed on April, 2013.
- Ali, M. A. Majumdar, A. J. and Singh, B. (1975). Properties of glass fiber reinforced cement-the effect of fiber length and content. *Journal of Material Science*, 10: 1732-40.
- Balaguru, P. N. and Shah, S. P. (1992). Fiber reinforced cement composites. McGraw Hill Inc. publishers, New York, 70-90.
- Barhum, R. and Mechtcherine, V. (2012). Effect of short, dispersed glass and carbon fibres on the behaviour of textile-reinforced concrete under tensile loading. *Journal of Engineering Fracture Mechanics*, 92: 56-71.
- Bentur, A. and Mindess, S. (1990). Fibre reinforced cementitious composites, Elsevier Applied Science, London, 1-10.
- Bosche, A., Jesse F., Ortlepp, R., Weiland, S. and Curbach, M. (2008). Textile-Reinforced Concrete for Flexural Strength of RC-Structures-Part 1: Structural Behaviour and Design Model. American Concrete Institute, Farmington Hills, MI, ACI SP-251: 19-40.
- Bramshuber, W., Koster, M., Hegger, J., Voss, S., Gries, T., Barle, M., Reinhardt, H. W. and Kruger, M. (2004). Integrated Formwork Elements Made of Textile Reinforced Concrete. American Concrete Institute, MI, ACI SP-224: 45-54.
- Brandt, A.M. (2008). Fibre reinforced cement-based (FRC) composites after over 40 years of development in building and civil engineering. *Journal of Composite Structures*, 86(1): 3-9.
- Bruckner, A., Ortlepp, R. and Curbach, M. (2006). Textile reinforced concrete for strengthening in bending and shear. *Materials and Structures*, 39(8): 741-748.

Chapter 2: Background

- Bruckner, A., Ortlepp, R. and Curbach, M. (2008). Anchoring of shear strengthening for T-beams made of textile reinforced concrete (TRC). *Materials and Structures*, 41(2): 407–418.
- Chandra, S. and Berntsson, L. (2002). Lightweight aggregate concrete. Noyes Publications, New York, USA, 167-229.
- Chi, J. M., Huang, R., Yang, C.C. and Chang, J.J. (2003). Effect of aggregate properties on the strength and stiffness of lightweight concrete. *Cement and Concrete Composites*, 25(2): 197-205.
- Choi, Y. and Yuan, R. L. (2005). Experimental relationship between splitting tensile strength and compressive strength of GFRC and PFRC. *Cement and Concrete Research*, 35(8): 1587–1591.
- Cuypers, H. (2002). Analysis and design of Sandwich Panels with Brittle Matrix Composite Faces for Building Applications. PhD thesis, Vrije Universiteit Brussel, 1-235.
- Ding, Z. and Li, Z. (2005a). High-early-strength magnesium phosphate cement with fly ash. *ACI Material Journal*, 102(6): 357-381.
- Ding, Z. and Li, Z. (2005b). Effect of aggregate and water content on the properties of magnesium phospho-silicate cement. *Cement and Concrete Composites*, 27(1): 11-18.
- Fanella, D. A. and Naaman, A. E. (1985). Stress-strain properties of fiber reinforced mortar in compression. *ACI Journal*, 82(4): 475-583.
- Hegger, J. and Voss, S. (2008). Investigations on the bearing behaviour and application potential of textile reinforced concrete. *Engineering Structures*, 30(7): 2050-2056.
- Hegger, J., Kulas, C. and Horstmann, M. (2012). Spatial textile reinforcement structures for ventilated and sandwich facade elements. *Advances in Structural Engineering*, 15 (4): 665-675.
- Hegger, J., Kulas, C., Raupach, M. and Buttner, T. (2011). Tragverhalten und Dauerhaftigkeit einer schlanken Textilbetonbrücke. *Beton und Stahlbetonbau*, 106(2): 72- 80.
- Hegger, J., Will, N., Bruckermann, S. and Voss, S. (2006). Loading-bearing behaviour and simulation of textile-reinforced concrete. *Materials and Structures*, 39(8): 765–776.

Chapter 2: Background

- Hinzen, M. and Brameshuber, W. (2009). Improvement of serviceability and strength of Textile Reinforced Concrete by using short fibres. Proceeding of 4th colloquium on textile reinforced structures (CTRS4), Dresden, 261–272.
- Jeong, S. and Wagh, A. (2003). Cementing the gap between ceramics, cement, and polymers. *Material Technology*, 3: 162-168.
- Ke, Y., Beaucour, A. L., Ortola, S., Dumontent, H. and Cabrillac, R. (2009). Influence of volume fraction and characteristics of lightweight aggregates on the mechanical properties of concrete. *Construction and Building Materials*, 23(8): 2821-2828.
- Lo, T., Tang, W.C. and Cui, H. Z. (2007). The effect of aggregate properties on lightweight concrete. *Building and Environment*, 42(8): 3025-3029.
- Mirza, F. A. and Soroushian, P. (1999). Effects of Alkali-Resistant Glass Fiber Reinforced on Crack Temperature Resistance of Lightweight Concrete. *Cement and Concrete Composite*, 24(2): 223-227.
- Mobasher, B. (2011). Mechanics of fiber and textile reinforced cement composites. CRC Press, 14-15.
- Nippon Electric Glass America. <http://www.negamerica.com>. Last accessed on April, 2013.
- Obregon-Salinas, A. J., Rizkalla, S. H. and Zia, P. (2011). American Concrete Institute, MI, ACI SP275-17: 1-12.
- Peled, A. (2007). Confinement of damaged and non-damaged structural concrete with FRP and TRC sleeves. *ASCE Journal of Composite Construction*, 11(5): 514–522.
- Qiao, F., Chau, C. K., Li, Z. (2010). Property evaluation of magnesium phosphate cement mortar as patch repair material. *Construction and Building Materials*, 24: 695-700.
- Qiao, F., Lin, W., Chau, C. K., Li, Z. (2009). Property assessment of magnesium phosphate cement. *Key Engineering Material*, 400-402: 115-120.
- Roy, D. (1997). New strong cement materials: chemically bonded ceramics. *Science*, 235: 651–658.
- Singh, D., Wagh, A. S., and Jeong, S. Y. (2001). Pumpable/Injectable Phosphate-Bonded Ceramics. U.S. patent US 6,204,214, B1.

Chapter 2: Background

- Triantafillou, T. C. and Papanicolaou, C. G. (2005). Textile reinforced mortar (TRM) versus FRP as strengthening material of concrete structures. American Concrete Institute, Farmington Hills, MI, ACI SP-230: 99-118.
- Wagh, A. S. (2004). Chemically bonded phosphate ceramics: Twenty-first century material with diverse application. Elsevier Limited, Amsterdam, 1-10, 19-25, 37-41, 97-110 and 157-175.
- Wagh, A. S., Jeong, S. Y. and Singh, D. (1997). High-strength ceramic (cement) using industrial by-product and slag. *Proceeding of International Conference on High-Strength Concrete*, Kona, HI, 542-553
- Yang, Q. and Wu, X. (1999). Factors influencing properties of phosphate cement-based binder for rapid repair of concrete. *Cement and Concrete Research*, 29(3): 389-396.

Mechanical Properties of Magnesium Potassium Phosphate Cement and Mortars¹

3.1 Introduction

Wagh et al. (Wagh, 2004; Wagh et al., 1997) developed a Chemically Bonded Phosphate Ceramic (CBPC) cement by reacting calcined magnesium oxide (MgO) and monopotassium phosphate (KH₂PO₄) in an aqueous solution. CBPC is formed by the following acid-base reaction:



The reaction product, herein termed magnesium potassium phosphate cement (MPPC) is a binder that can be used as the matrix material to host inorganic waste materials.

It has been previously reported that the compressive strength of MPPC is enhanced by inclusion of fly ash (Wagh, 2004; Wagh et al, 1997; Ding and Li, 2005a). Wagh et al. (2004) reported that pure MPPC has a typical compressive strength of 20-25 MPa. When Class C fly ash is added at 60% loading (i.e. mass

¹ Parts of this chapter have been published. Reference: Samson T. Tassew and Adam S. Lubell., "Properties of phosphate-based cements with high Fly Ash content". American Concrete Institute (ACI) Special Publication: SP-294 Advances in Green Binder System, American Concrete Institute, SP294-5, 2013, 1-16.

fraction of the dry ingredients), the compressive strength can increase to 80-85 MPa.

Prior research has examined the properties of MPPC mortars produced using sand aggregates. Ding et al. (2010b) and Qiao et al. (2010) found that increasing the sand to binder ratio decreased the compressive strength. Ding et al. (2010b) reported that an increase in the water to binder ratio reduces both the compressive strength and the elastic modulus of sand mortar made using magnesium phosphate binders. However, no detailed study is available that has systematically examined influences on the mechanical properties of MPPC binders made with fly ash but without aggregates. This study was conducted to establish the influence of mix composition on the properties of MPPC binders and sand mortars. The research reported in this chapter examines the physical and mechanical properties of MPPC binders with different fly ash loading and sand mortars made with MPPC binders.

This chapter reports on two main phases of the study. In the first phase, mix development for different magnesium phosphate binders was completed and the mixes were characterized for rheological and mechanical properties. Test results are presented for magnesium phosphate binders with different proportions of the constituent materials. From these candidate mixes, two were selected for further study: a mix resulting in high compressive strength and a mix resulting in a comparatively lower strength but having lower unit cost. Laboratory testing of these two mixes was conducted to investigate important relationships between the mix composition, the preparation techniques and the resulting mechanical properties of compressive strength, elastic modulus and modulus of rupture. The study also examined the workability and setting times of the mixes, and influences on the properties due to variations in the mixing time.

The focus of the second phase of the study was to investigate the mechanical properties of sand ceramic mortar (SCM) produced using the MPPC binders developed in the first phase. Mechanical properties of interest included the stress-

strain response and strength in compression, modulus of rupture, modulus of elasticity, and density. A primary objective was to evaluate the influence of the sand to binder mass ratio on these properties. Influences of the sand grading, strength development with age and the fly ash type (Class C and Class F) on compressive strength were also investigated.

3.2 Materials and Experimental Procedure

3.2.1 Materials and Mix Preparations

3.2.1.1 Magnesium Potassium Phosphate Cement

Calcined magnesium oxide (MgO) was used in this study. Manufacturer supplied data indicated that the material was 97% MgO by weight and had a specific surface area of 0.3 m²/g with minimum 95% of particles passing the 200 mesh size. Fertilizer grade KH₂PO₄ used in this study was obtained from a local farm supply warehouse. Most mixes were prepared with Class C fly ash (FA) but some sand mortar mixes were also prepared with Class F fly ash. The chemical composition of the FA is given in Table 3.1.

Table 3.1- Chemical composition of Fly Ash

Fly Ash Type	Mass fraction of the sample (%)						
	MgO	CaO	SiO ₂	Fe ₂ O ₃	Al ₂ O ₃	SO ₃	Na ₂ O
Class C	1.22	10.97	55.53	3.62	23.24	0.24	2.83

To prepare the MPPC binders, mass ratios of MgO:KH₂PO₄=1:3.4 were used, similar to that indicated by the molar ratios in Equation 3.1. Fly ash (FA) loadings of 40 to 80% of total dry binder ingredients (i.e. MgO+KH₂PO₄+FA) were considered in this study. MPPC binders formed using fly ash loadings of 40, 50, 60, 70 and 80%, were denoted as BC4, BC5, BC6, BC7 and BC8, respectively. For these mixes, the water to binder ratio was varied from 0.16 to 0.26, where the binder mass was taken as the total mass of MgO+KH₂PO₄+FA. MPPC binders with 0.2 water binder (*w/b*) ratio and weight ratio of MgO:KH₂PO₄:FA = 1:3.4:4.4 and 1:3.4:10.3 was denoted as B5 and B7, respectively.

To control the reaction rate and retard the setting time, different admixtures were investigated. Borax at up to 4% by mass of the MgO and a commercially available lignosulphonate admixture at up to 6.6% by mass of the MgO were examined. The Borax was in powder form and the lignosulphonate was a liquid.

For each mix design studied, the MgO, KH_2PO_4 and FA were dry-mixed together for approximately 5 min using a 20 l capacity portable mixer with a mixing bucket speed of 60 RPM. The water was mixed with the retarder and poured into a bowl. The dry mix was then added gradually and the entire batch was mixed together for 5 to 10 min using a 5 l Hobart planetary mixer with a mixing speed of 28.5 RPM. The mixes were then carefully placed into plastic molds using a scoop and vibrated for 45 seconds using a vibrating table. The samples were removed from the molds after 3 hrs and then stored in the ambient laboratory environment ($25 \pm 2^\circ\text{C}$ with a relative humidity of $50 \pm 5\%$) until testing. The mixing sequence is illustrated in Figure 3.1.

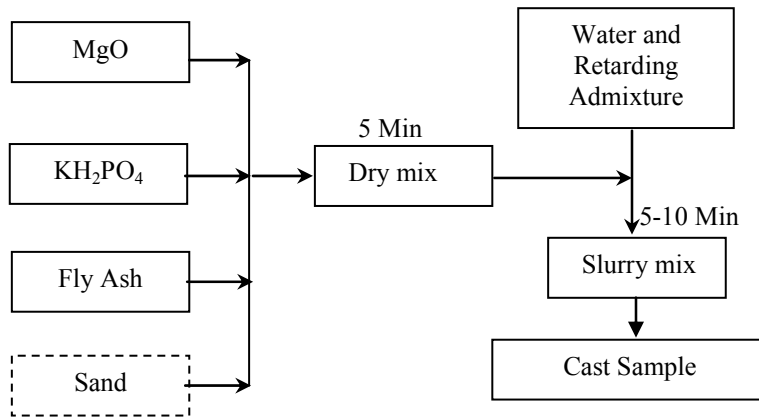


Figure 3.1- Mix process

3.2.1.2 Sand Aggregate Ceramic Mortar

Binder types B5 and B7 described in Section 3.2.1.1 were selected to prepare the sand ceramic mortars in the second phase of this study. Quartz sand aggregates in three different particle size gradations were examined in this study. Each sand had maximum particle size of 1.25 mm. The gradation curves are shown in Figure 3.2. The fineness modulus of sand 1, sand 2 and sand 3 were 3.84, 3.4 and 3, respectively. The specific gravity of the sand was 2.65 in all cases.

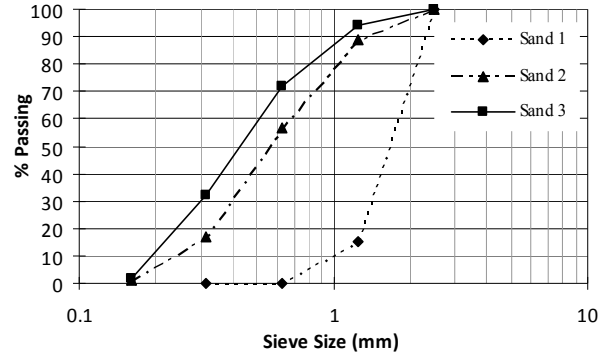


Figure 3.2- Particle size distribution of sands

Different binder to sand (b/S) mass ratios of 1, 1.5, 2, 2.5 and 3 were considered wherein binder refers to the combined mass of $MgO+KH_2PO_4+FA$. The water to binder mass (w/b) ratio of all mixes was kept constant at 0.2 except for mixes using sand 3 where a w/b ratio of 0.22 was used. The higher w/b ratio was required in this case to obtain adequate workability. The mixing procedure of the sand ceramic mortar was similar to section 3.2.1.1 whereby the sand was introduced during the dry mixing of the binder. The mix preparation sequence is illustrated in Figure 3.1.

The nomenclature to identify the mix design is illustrated in Figure 3.3. The naming convention had three components: the first letter indicated the b/S ratio with a letter M indicated for b/S ratio of 1.5 (a letter MC for b/S of 1, 1.5, 2, 2.5 or 3) ratios; the first number represents the binder type; the second number represents the sand type. For example MC51 was sand ceramic mortar having b/S ratio of 1, 1.5, 2, 2.5 or 3 with 50% fly ash binder (B5) and containing Sand 1.

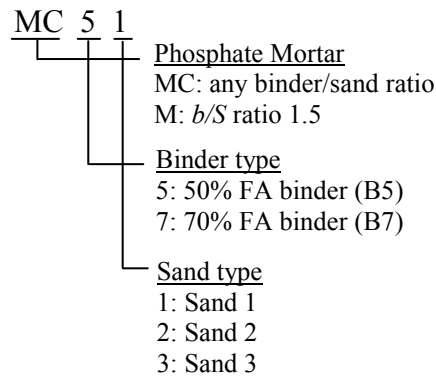


Figure 3.3- Specimen identification

3.2.2 Test Procedures

Setting time was measured using a Vicat needle apparatus, according to ASTM C191.

The cube compressive strength was determined using 50×50×50 mm cubes according to ASTM C39. The tests were completed using a Forney testing machine with capacity of 3100 kN as shown in Figure 3.4(a), at a loading rate of 0.25 MPa/s. To establish the strength development with time, cube compression tests were conducted at ages of 2, 7, and 24 hrs; and 3, 7 and 28 days after casting.

The modulus of elasticity was evaluated from uniaxial compression tests on 100x200 mm cylinders in accordance with ASTM C469. Displacement controlled tests were conducted in a stiff MTS frame with capacity of 2600 kN (Figure 3.4(b)) at a machine stroke rate of 1.25 mm/min. Axial deformations of the cylinders were measured using three LVDTs arranged at 120° separation about the longitudinal axis and operating over an initial gauge length of 100 mm. Cylinders were sulphur capped before testing as per ASTM C617.

The flexure response was determined from 50×50×200 mm prisms under 4-point bending according to ASTM C78 using a universal testing machine with 30 kN capacity. The loading rate was displacement controlled at 0.1 mm/min at mid-span (Figure 3.4(c)). Tests were carried out at the age of 28 days.



(a) Cube test setup



(b) Cylinder test setup



(c) Prism test setup

Figure 3.4- Test setups for compressions and prism test

3.3 Results and Discussions

3.3.1 Result for Magnesium Potassium Phosphate Binder

3.3.1.1 Setting Time

Tests were completed to investigate the viability of controlling the working time by using either Borax or a commercial lignosulphonate as a retarder. Since the difference between the initial and final setting times was very short, only the final setting times are reported. Figure 3.5 compares the final setting times for B5 and B7 binders prepared with Borax (4% mass percent of MgO) or lignosulphonate (6.6 % mass percent of MgO). The final setting times for the B5 binder were approximately 1hr and 2hrs when Borax and lignosulphonate were used, respectively. However, negligible difference in the final setting time was observed for B7 binders prepared with the two admixtures, with a setting time about 2.5 hrs in both cases. Due to the extended working time and simpler mix procedures due

to the liquid format, the lignosulphonate admixture at a dosage of 6.6% mass of MgO was used for all subsequent mixes reported in this Chapter.

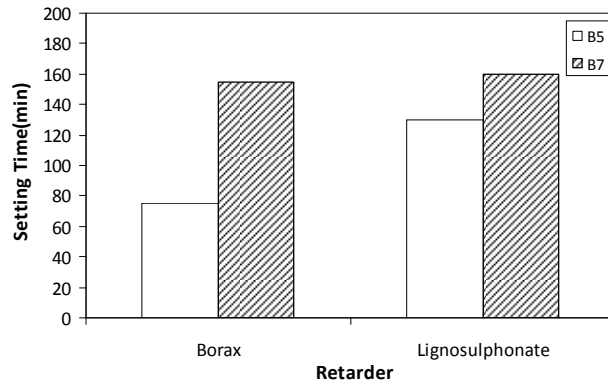


Figure 3.5- Influence of retarder type on the binder setting times

3.3.1.2 Influence of Mixing Time on Compressive Strength

Figure 3.6 shows the influence of mixing time on the average cube compressive strength of type B5 and B7 binders for w/b ratio of 0.20. This figure was plotted to establish trends of compressive strength mixing time and to obtain a trial mixing time for subsequent mixes. The mixing time is measured from the addition of the dry ingredients to the liquid components. As the mixing time increased the average cube compressive strength at 7 days increased for both the B5 and B7 binders. Uniformity of the mix was also visually observed to improve as mixing time increased due to improved dispersion of the constituent elements as mixing proceeded. A mixing time of 7.5 minutes was selected for use in all subsequent mixes reported in this chapter.

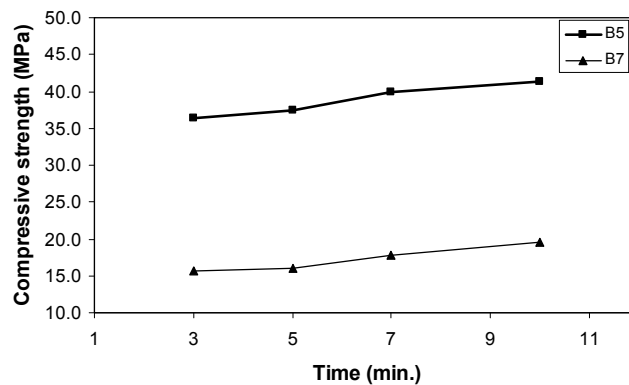


Figure 3.6- Influence of mixing time on 7-day cube compressive strength

3.3.1.3 Influence of Fly Ash Loading on Density

The relationship between the fly ash content and the average density of the hardened MPPC binder is shown in Figure 3.7 for different w/b ratios. However, variations in average density due to the w/b ratio for each fly ash loading were not significant and the variation in average density with fly ash loading can be taken as the solid line in Figure 3.7. This figure was plotted to establish trends of average density with fly ash fraction. It can be observed that the density decreases as the fly ash content is increased. This occurs because the fly ash has a lower unit weight than the $MgO + KH_2PO_4$ reactive components, thereby reducing the overall density of the binder. The average density ranged between 1553 kg/m^3 and 1820 kg/m^3 for fly ash variation between 80% and 40% of the total mass of binder.

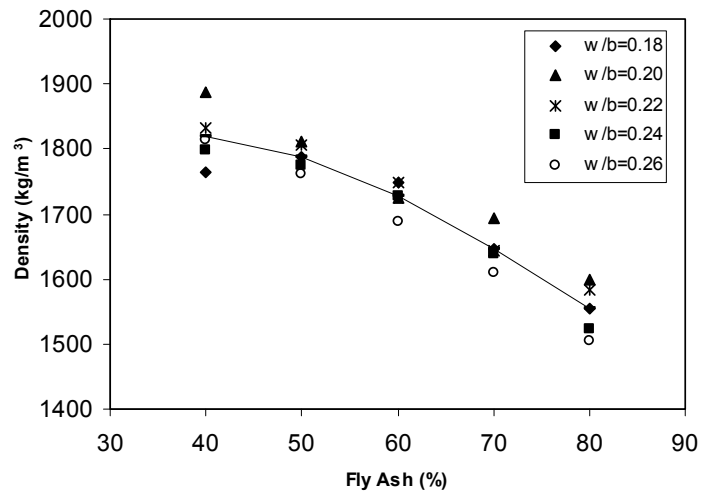


Figure 3.7- Average density vs. fly ash loading by mass of binder

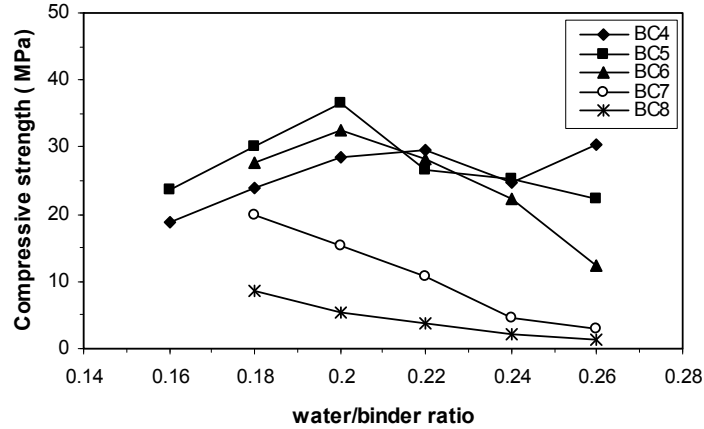
3.3.1.4 Effect of Water to Binder Ratio and Fly Ash Loading on Compressive Cube Strength

The influence of varying w/b ratio on average cube compressive strength at 7 day for ceramic binder with different fly ash content is presented in Figure 3.8(a). This figure was plotted to establish trends of average compressive strengths with fly ash fractions. It can be observed that increases in the w/b ratio reduce the strength when a high fly ash loading (i.e. 70% and 80%) is used. However, when the fly ash loading is in the range 40% to 60%, the compressive strength initially

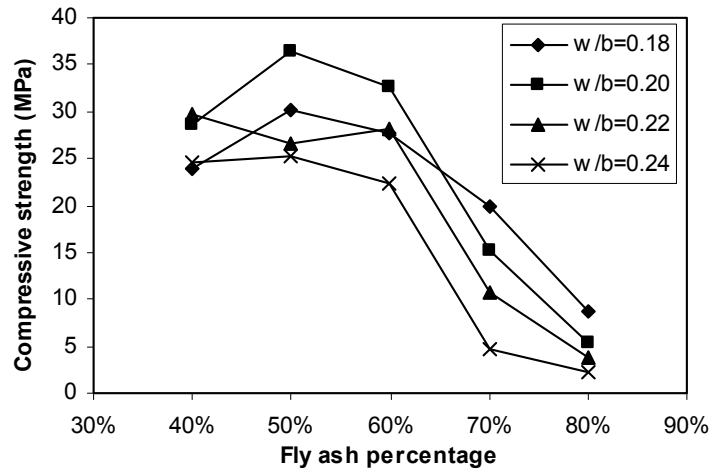
increases as the w/b ratio increases but then begins to decrease as the w/b ratio becomes greater than 0.2.

According to Ding and Li (2005a), including fly ash into the MPPC binder system will improve the binder strength due to two factors. A physical effect may occur in which the fly ash particles fill the voids in the MPPC matrix and densify the overall structure of the MPPC binder. A chemical effect may also occur whereby interaction happens at the interface of the fly ash grains and the phosphate gel. Figure 3.8(b) shows the relationship between the 7-day cube compressive strength and the fly ash content for different w/b ratios. It can be observed that the compression strength was a maximum when the fly ash loading was between 40% and 60% for the $MgO:KH_2PO_4$ and w/b ratios studied, which is similar to the findings of previous research (Wagh, 2003; Ding and Li, 2005a). The binder with 50% fly ash content and a w/b ratio of 0.2 provided the highest compressive strength in this study.

From the results in this initial phase which confirmed the influence of the fly ash loadings on strength, two binders were selected for more detailed evaluation in the second phase: a mix resulting in high compressive strength (using 50% fly ash loading and denoted B5) and a mix resulting in a comparatively low strength (using 70% fly ash loading and denoted B7). Since fly ash has a unit cost substantially lower than the other binder components, the B7 mix will have lower unit cost than B5 binder. A w/b ratio of 0.2 is used in both B5 and B7 binders.



(a) Influence of fly ash loading on average compressive strength



(b) Influence of water/binder ratio on average compressive strength

Figure 3.8- Influence of fly ash loading and water/binder ratio on average compressive strength

3.3.1.5 Relationship Between Compressive Strength and Density

The relationship between the average cube compressive strength at 7 days after casting and the average density is presented in Figure 3.9. This figure was plotted to establish trends of average compressive strength with density. The plot shows that the compressive strength of MPPC binders increase with an increase in density regardless of the fly ash loading or the w/b ratio. This occurs because the fly ash density is smaller than the combined density of the $MgO+KH_2PO_4$ reaction product. Furthermore, a higher proportion of the reactive components $MgO+KH_2PO_4$ due to a smaller fly ash loading lead to an increase in the

compressive strength. Based on a linear regression analysis, the relationship between density and the 7-day compressive strength is given as:

$$f_{cb} = 0.097 \cdot \gamma_b + 147 \quad (3.2)$$

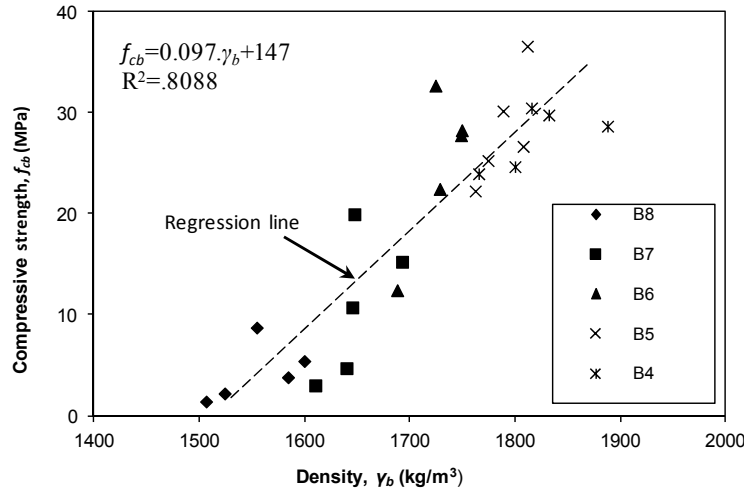
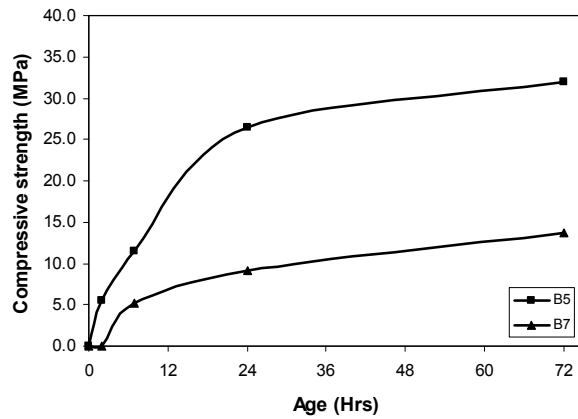


Figure 3.9- Relationship between binder average compressive strength and average density

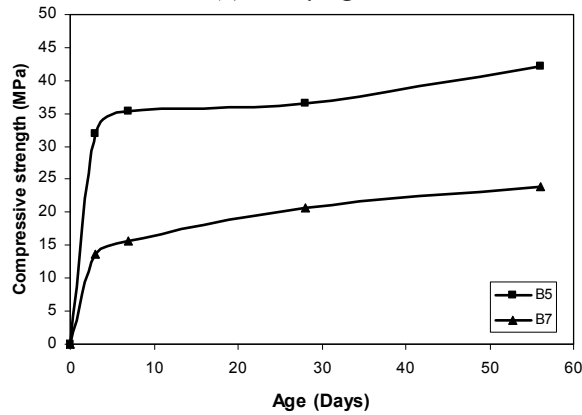
3.3.1.6 Compressive Strength Development

The variation in average compressive cube strength of B5 and B7 binders with time are illustrated in Figure 3.10. This figure was plotted to establish trends of average compressive strength with age. An enlargement of the early age strength development over the first 72 hours is highlighted in Figure 3.10(a). Both binders showed the most rapid strength gains over the initial 24 hours after casting, and a continual gain in strength over the full 56-day study period. Early age strengths gains are considered important in evaluating the viability of using these binders in construction systems that require rapid construction, early formwork removal or introduction of imposed loads. The 28-day compressive strength is a useful benchmark as it corresponds to conventional construction practices using Portland cement binders (Mehta, 1986). The 28-day compressive strength of B5 and B7 binder was measured as 36.6 MPa and 20.6 MPa, respectively. Binder B5 exhibited 15% of its 28 day compressive strength within 2 hrs after casting as shown in Figure 3.10(b), but no strength was observed by B7, as B7 had not yet reached the final setting time at 2 hrs as shown in Figure 3.5. At 7 hours after

casting, binders B5 and B7 reached 31.4% and 25.2% of their 28 days compressive strengths, respectively. Further, B5 and B7 exhibited 72.1% and 44.2% of the 28-day strength within 24 hrs, respectively. The difference is explained by B5 having a higher concentration of the MgO and KH_2PO_4 reactive components than B7 due to the relative fly ash loadings, leading to a faster reaction process. The compressive strengths of B5 at 3, 7 and 56 day were 87.2%, 96.7% and 115% of the 28-day strength, respectively. For B7, the 3, 7 and 56 day compressive strengths were 66.5%, 76.2% and 116% of the 28 strength, respectively. These results indicate that while initial strength development of B5 is faster compared to B7, after 28 days the strength development rate is similar.



(a) Early age results



(b) 56 day study period

Figure 3.10- Compressive strength development with time of B5 and B7

3.3.1.7 Modulus of Elasticity

Figure 3.11 shows typical compressive stress-strain curves for cylinders made from B5 and B7 binder and tested at 28 days according to ASTM C469-02. It can be seen from the figure that the ascending branch of the stress-strain curve for B5 was close to linear up to the peak stress value and a brittle response occurred in the post-peak region. However, B7 showed a more curved stress-strain response to peak with a more gradual failure. The peak stress and the strain at peak stress were both smaller for B7 than B5 (see Table 3.2). The modulus of elasticity of B5 and B7 according to ASTM C469, were 13.6 GPa and 10.8 GPa, respectively, indicating that the modulus of elasticity varies with the compressive strength.

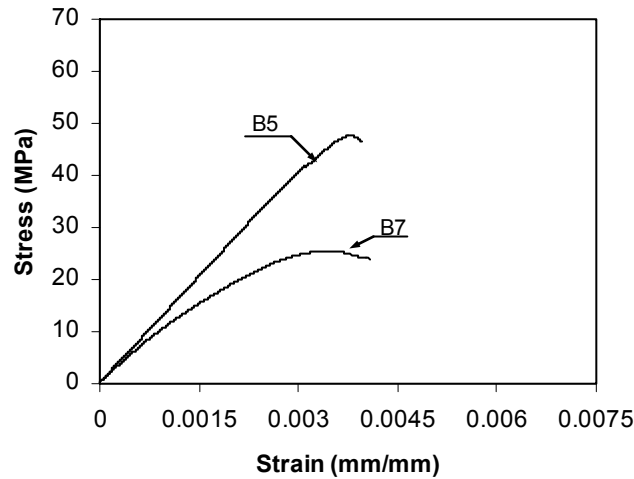


Figure 3.11- Compressive stress-strain response of B5 and B7

3.3.1.8 Flexural Strength

The average modulus of rupture ($f_{r,b}$) for B5 and B7 were determined at 28 days and are given in Table 3.2. The average modulus of rupture for B5 and B7 were 2.4 MPa and 1.6 MPa, respectively, corresponding to 5.0%, and 6.0% of the average compressive strength values.

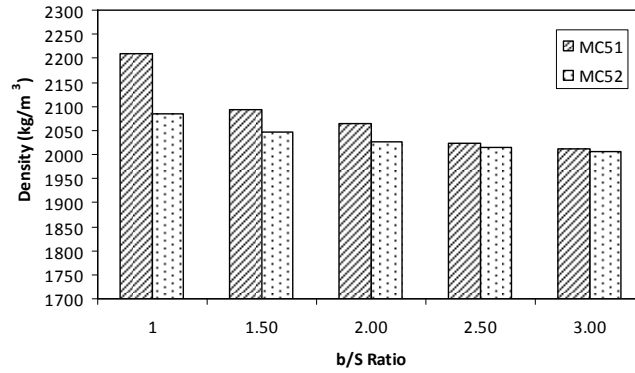
Table 3.2- Average 28 day mechanical properties of the B5 and B7 binders

Binder Type	$f_{c,b}$ (MPa)	ε_b (mm/mm)	E_b (GPa)	$f_{r,b}$ (MPa)
B5	47.6	0.00379	13.6	2.4
B7	25.6	0.00346	10.8	1.6

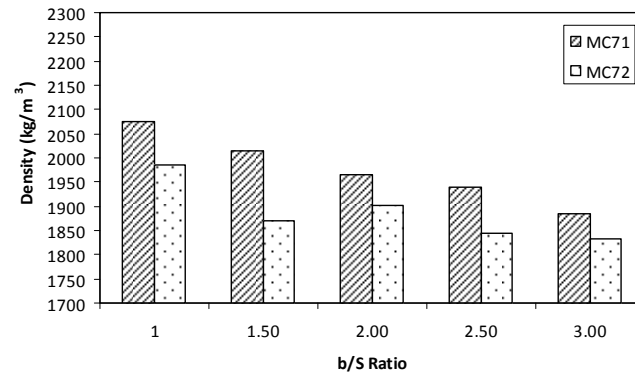
3.3.2 Results for Sand Aggregate Ceramic Mortars

3.3.2.1 Influence of Binder to Sand Ratio on Density

The average densities of sand ceramic mortar (SCM) for the MC5 and MC7 series are given in Figure 3.12. This figure was plotted to establish trends of average density with sand fraction. All data presented are the average values from three specimens tested at 7 days. The figures show that the density of SCM reduces as the binder to sand mass ratio (b/S) increases, regardless of the sand type. This occurs since the density of sand is higher than that of the binder. The figure also shows that mixes with Sand 2 had lower density than Sand 1, but the difference is less pronounced as the b/S ratio increases. This is explained by the different aggregate size grading curves for the two sands (see Figure 3.2), but the grading is less important as the volume fraction of the binder is increased. The average density of MC5 and MC7 series ranged from 2005 to 2210 kg/m³ and 1834 to 2075 kg/m³, respectively.



(a) Sand ceramic mortars MC51 and MC52



(b) Sand ceramic mortars MC71 and MC72

Figure 3.12- Influence of binder to sand ratio on the density of sand ceramic mortars for $w/b = 0.2$

3.3.2.2 Influence of Binder to Sand Ratio on Compressive Strength

The influence of the b/S ratio on the average cube compressive strength at 7 days is presented in Figure 3.13. Only mixes with Sand 1 and Sand 2 were used for this comparison. It can be observed that the compressive strength of both MC51 and MC52 mortars increased by approximately 28.7% as the b/S ratio was increased from 1.0 to 3.0. However, MC71 and MC72 showed no significant variation in compressive strength as the b/S ratio was increased from 1.0 to 3.0. This result occurs due to an overall weaker binder matrix from B7 type binder compared to B5. Since the unit cost of the binder is high compared to the sand, a lower binder to sand ratio will give a lower unit cost for the mortar. For this study, a b/S of 1.5 was selected for detailed investigation since this mix ratio provided relatively good workability and strength for both sand types.

The relationship between the average cube compressive strength at 7 days and the density is shown in Figure 3.14. This figure was plotted to establish trends of average compressive strength with density. The compressive strengths of MC51 and MC52 are observed to decrease for increased densities. As described earlier, mixes with higher b/S ratio will have a lower overall density due to the relative densities of the sand and binder components. Also see Figure 3.13. From Figure 3.14, no definite trends are observed between the average density and average compressive strength of the MC71 and MC72 mortars, which is explained by the relationship between b/S and compressive strength of these mixes given in Figure 3.13.

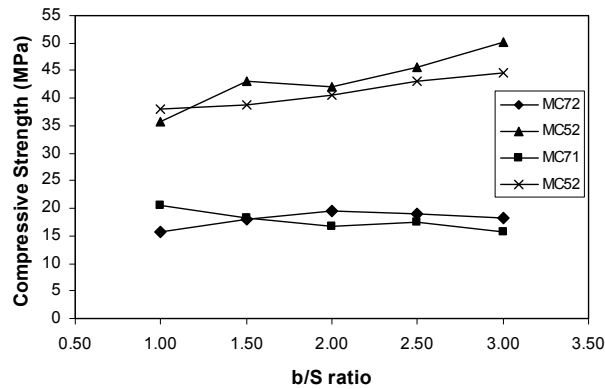


Figure 3.13- Influence of b/S ratio on average compressive strength for 0.20 w/b ratio

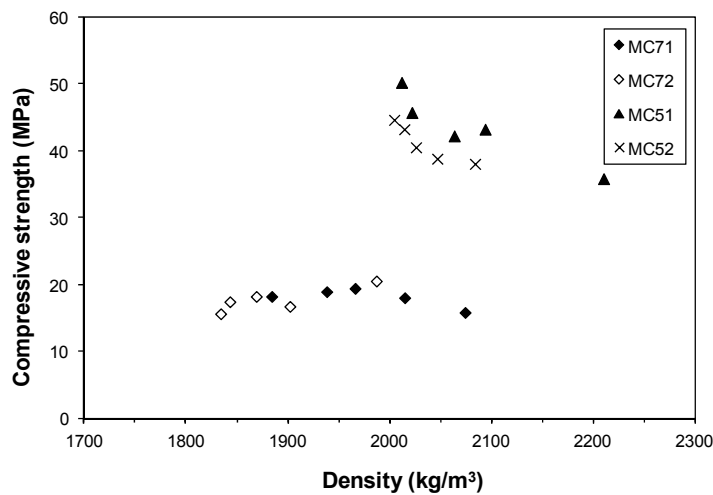
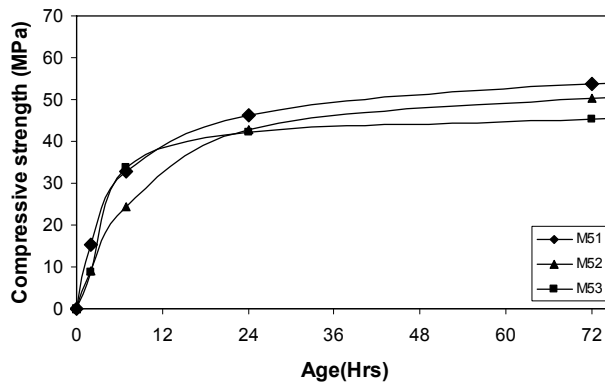


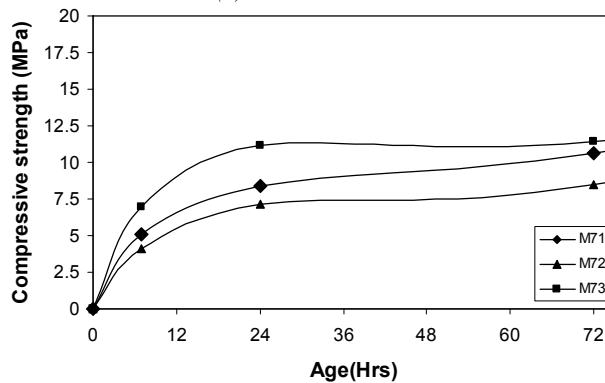
Figure 3.14- Relationship between average compressive strength and average density for 0.20 w/b ratio

3.3.2.3 Compressive Strength Development

The early age strength development of M5 and M7 mortars over the first 72 hrs is presented in Figure 3.15. This figure was plotted to establish trends of average compressive strength with age. M5 mortars had reached 18.3% of 28-day compressive strengths with in 2 hrs. No strength was observed by M7 mortar. After 7 hrs, mortars M5 and M7 had reached about 51.5% and 19.9% of their 28-day compressive strengths, respectively. Further, M5 and M7 had exhibited about 75.9 % and 32.8% of the 28-day strength with in 24 hrs, respectively. The difference in the strength development is similar to the binder’s strength development presented in 3.2.6, due to the influence of the reactive component concentrations of the binders.



(a) For M5 series



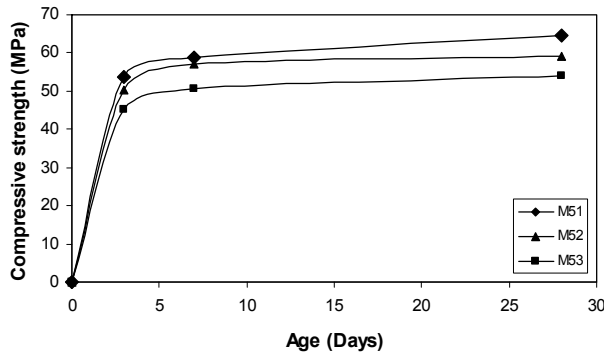
(b) For M7 series

Figure 3.15- Early strength development

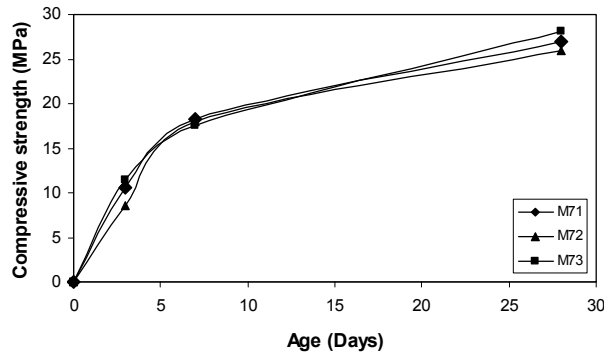
The compressive strength increase of ceramic mortar with age was similar for all types of aggregate as shown in Figure 3.16. It can be seen from both figures that

the strength development of both M5 and M7 showed rapid strength development. However, M5 is very quick as compared to M7, similar to that observed for binders B5 and B7 in Figure 3.8. The M5 series compressive strengths exceeded approximately 84.0% and 93.0% of the 28-day strength at ages of 3 and 7 days, respectively. The M7 series had compression strengths of about 37.5% and 66.5% of the 28-day strength at 3 and 7 days, respectively (Figure 3.16(b)). This lower early age strength gain for M7 mixes is similar to that observed for the corresponding binder B7 tests reported in Figure 3.8(b).

Figure 3.16(a) shows that the type of sand affected the compressive strength for M5 series. However the type of sand has little influence on the strength of M7 series as seen in Figure 3.16(b). The average compressive strength at 28 days for M5 and M7 series ranged from 54.1 to 64.6 MPa and 25.9 to 28.1 MPa, respectively.



(a) For M5 series



(b) For M7 series

Figure 3.16- Compressive strength development with time

3.3.2.4 Modulus of Elasticity

The 28-day uniaxial compressive stress-strain responses for ceramic mortars from the M5 series up to peak stress are presented in Figure 3.17. Note that no modulus of elasticity data collected for M7. It can be observed that the stress-strain response of the SCMs with different sand types all showed similar responses with only minor non-linearity up to the peak stress values. The average modulus of elasticity (E_m) according to ASTM C469-02 is summarized in Table 3.3.

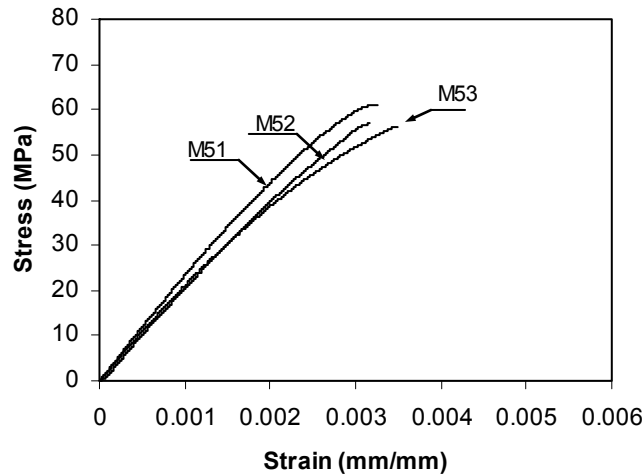


Figure 3.17- Compressive stress-strain response of sand ceramic mortars with B5 binders for b/S ratio of 1.5

3.3.2.5 Flexural Strength

The average modulus of rupture ($f_{r,m}$) obtained at 28 days are shown in Table 3.3. The Modulus of rupture for M51, M52 and M53 were 4.1 MPa, 3.6 and 3.4 MPa, respectively, corresponding to 6.7, 6.3 and 5.8% of the average compressive strength values. It was found that the M51 mortar had the highest compressive strength, modulus of elasticity and modulus of rupture results. Results for M52 and M53 were similar. These results can be explained by the coarser aggregate grading of Sand 1 and the similar grading for Sand 2 and Sand 3 as described in Section 3.2.1.2. This was due to a coarser aggregates grading (Sand 1) resulted in lower aggregates surface area compared to Sand 2 (or Sand 3), as a result, the paste volume in a given mix increased. As the paste volume increased, the bond

between the aggregates and the MPPC paste increased, consequently, the concrete strength and the modulus of rupture increased.

Table 3.3- Average SCM properties

Type	$f_{c,m}$ (MPa)	ε_m (mm/mm)	E_m (GPa)	$f_{r,m}$ (MPa)
M51	61.0	0.00320	24.1	4.1
M52	56.9	0.00317	21.3	3.6
M53	56.3	0.00350	21.7	3.2

3.3.2.6 Effect of Fly Ash Type on Compressive Strength

According to Wagh et al. (2004), MPPC binders made with Class C fly ash give higher compressive strengths than binders made with Class F fly ash. While all other mixes reported in this chapter were formulated using Class C fly ash, a limited study was conducted to directly examine the influence of the fly ash type on the compressive strength of sand ceramic mortars. The mixes studied used Sand 1 and Sand 3 and binder types B5 and B7, where the fly ash types were Class C and Class F. For each mix, the average cube compressive strengths were determined at three different ages and the results are summarized in Figure 3.18. Use of Class C fly ash resulted in higher strengths than use of Class F fly ash regardless of the curing age, sand type or fly ash loading.

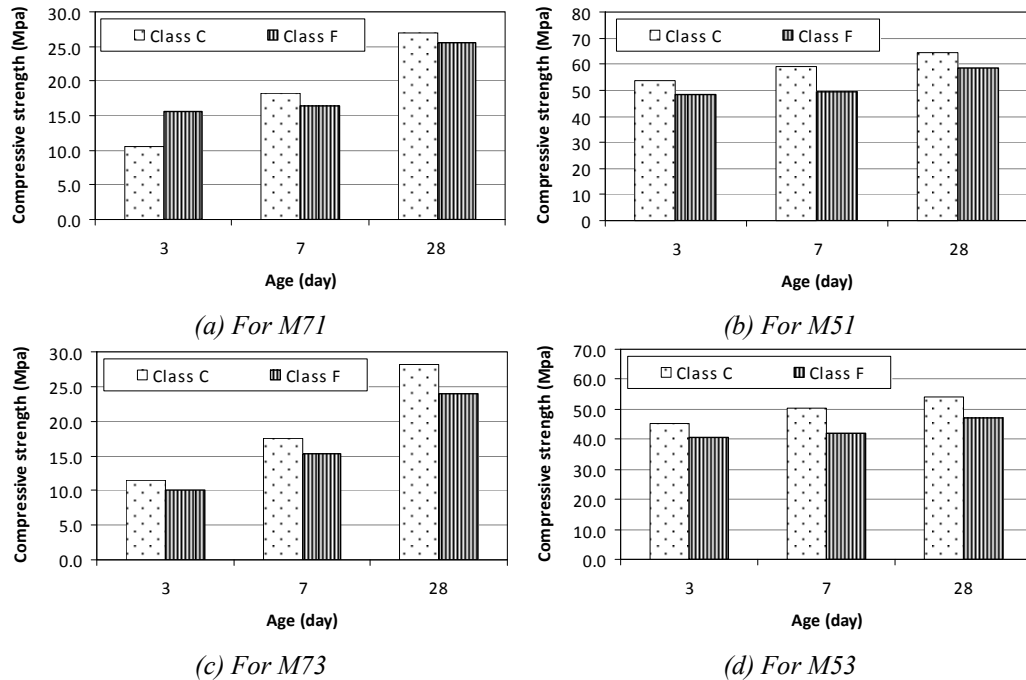


Figure 3.18- Influence of fly ash type on compressive strength

3.4 Conclusions

This study developed MPPC binders and sand ceramic mortar (SCM). The influence of the mix compositions on physical and mechanical properties of the MPPC and SCM were examined. Based on the experimental study of MPPC and SCM, the following conclusions can be drawn:

- The compressive strengths of both MPPC and SCM decreased as the water/binder ratio increased. Use of a w/b ratio of 0.20 resulted in good workability and mechanical properties.
- The compressive strength of MPPC and SCM were both influenced by the fly ash content and was a maximum when the fly ash loading was between 40% and 60%. Use of Class C fly ash resulted in higher compressive strengths of SCM compared to use of Class F fly ash.
- The compressive strength of SCM increased as the binder to sand mass ratio increased, regardless of the fly ash loading. The aggregate gradation

influenced the mechanical properties of SCM, but this influence was less pronounced as the fly ash loading increased.

- B5 binder and M5 mortar were the strongest mixes produced, giving 28 day compressive strength of 36.6 MPa and 60.0 MPa, respectively. Early age strength gain was rapid with above 72% of the 28-day strength with in 24 hrs.

3.5 References

- ASTM C469 (2002). Standard test method for static modulus of elasticity and poisson's ratio of concrete in compression. ASTM International, West Conshohocken, PA.
- ASTM C191 (2008). Standard test method for time of setting of hydraulic cement by vicat needle. ASTM International, West Conshohocken, PA.
- ASTM C39/C39M-09a (2009). Standard Test Method for Compressive Strength of Cylindrical Concrete Specimens, ASTM International, West Conshohocken, PA.
- ASTM C78 (2009). Standard Test Method for Flexural Strength of Concrete (Using Simple Beam with Third-Point Loading). ASTM International, West Conshohocken, PA.
- ASTM C617 (2010). Practice for capping cylindrical concrete specimens. ASTM International, West Conshohocken, PA.
- Ding, Z. and Li, Z. (2005a). High-early-strength magnesium phosphate cement with fly ash. *ACI Material Journal*, 102(6): 357-381.
- Ding, Z. and Li, Z. (2005b). Effect of aggregate and water content on the properties of magnesium phospho-silicate cement. *Cement and Concrete Composites*, 27(1): 11-18.
- Mehta, P. K. (1986). Concrete: Structure, properties and materials. Prentice-Hall, Inc., NJ, 49-51.
- Qiao, F., Chau, C. K. and Li, Z. (2010). Property evaluation of magnesium phosphate cement mortar as patch repair material. *Construction and Building Materials*, 24: 695-700.
- Wagh, A. S. (2004). Chemically bonded phosphate ceramics: Twenty-first century material with diverse application. Elsevier Limited, Amsterdam, 19-25, 37-41, 97-110 and 157-175.

Wagh, A. S., Jeong, S. Y, and Singh, D. (1997). High-strength ceramic (cement) using industrial by-product and slag. *Proceeding of International Conference on High-Strength Concrete*, Kona, HI.

Mechanical Properties of Lightweight Ceramic Concrete²

4.1 Introduction

Structural lightweight concrete is a class of composite material typically composed of a Portland cement binder and lightweight aggregates, having a unit density in the range of 1,680 to 1,920 kg/m³ (ACI 213-09). While Portland cement is the most widely used binder for current commercial applications, Portland cement has very high environmental impacts due to the CO₂ emissions, consumption of resources and energy usage during its manufacture. The production of 1 tonne of Portland cement consumes approximately 1.5 tonnes of raw materials and directly results in 1 tonne of carbon dioxide (CO₂) into the environment during production, with similar CO₂ emissions also attributed to the energy source (Li et al., 2004). It is clear that expanded use of alternative cementitious materials with lower environmental impacts is needed. In recent years, phosphate-based cements have gained attention as an alternative to Portland cements and these can be used to produce so-called chemically bonded phosphate ceramics (CBPC) (Wagh et al., 1997; Wagh et al., 1998; Wagh, 2004). According to Wagh and his colleagues, CBPCs can be formulated to have high

² Contents of this chapter have been published. Reference: Samson T. Tassew and Adam S. Lubell, "Mechanical properties of lightweight ceramic concrete". *Materials and Structures Journal*, vol. 45(4), 2012, 561-574.

early age strength gain, good volume stability, and excellent long-term durability including resistance to chemical attack and deicer scaling. Furthermore, research by Wagh et al. (1997), Wagh (2004), and others have shown that some CBPCs based on a magnesium potassium phosphate binder can be formulated to include very high mass loading of fly ash compared to Portland cement binders, further reducing the equivalent relative environmental impacts from CO₂ emissions and energy usage.

The fresh and hardened properties of magnesium potassium phosphate binders have been reported by several researchers (Qiao et al., 2009; Ding and Li, 2005a & 2005b; Qiao et al., 2010). Qiao et al. (2009) reported that the setting time of CBPC was greatly reduced as the reactivity of the magnesium oxide, measured by its magnesium oxide content, increased. Ding and Li (2005a) found that sand mortars produced with a CBPC binder incorporating fly ash at 30 to 50% of the total binder mass resulted in the highest compressive strengths. Ding and Li (2005b) showed that the compressive strength and modulus of elasticity of CBPC sand mortars decreased with an increase of the water/binder ratio. Ding and Li (2005b) and Qiao et al. (2010) both reported that the compressive strength of CBPC sand mortars decreases as the aggregate content increases.

Synthetic lightweight aggregates are typically produced by a rotary kiln process using natural materials such as clay, shale or slate. The kiln products can be directly sieved to aggregate size fractions or can be crushed prior to screening. The obtained aggregate sizes can also be further blended to achieve a desired size gradation prior to use. The selected raw materials, the kiln process and any subsequent processing prior to use can all impact the surface characteristics of the aggregates. These lightweight aggregate properties influence the quality of the lightweight concretes made with them and Portland cement binders. Due to the large volume fraction of aggregates, typically about 70 to 80% by volume of a concrete mix, their properties exert a major influence on the mechanical properties of the concrete (Chi et al., 2003). The influence of the aggregate characteristics on the characteristics and the mechanical properties of lightweight

concrete have been reported widely including influences on density, compressive strength and modulus of elasticity (e.g., Chi et al., 2003; Lo et al., 2007; and Ke et al., 2009).

However, despite the research on lightweight concrete made using Portland cement binders, there has been no prior research that examined the mechanical properties of lightweight ceramic concrete (LWCC) produced using a CBPC binder and lightweight aggregates.

This chapter reports on a study conducted to develop LWCC using a magnesium potassium phosphate binder system and various lightweight aggregates. The study considered lightweight expanded clay aggregate (LECA), expanded slate, expanded shale and bottom ash. A primary aim of the study was to evaluate the influences of aggregate type, aggregate mass fraction and the water/binder mass ratio on the mechanical properties of LWCC. The influence of aggregate type on the density and on the fresh properties including the slump and the setting time were also examined. LWCC properties were established using standardized test methods from the concrete industry. Correlations between the mechanical properties of compressive strength, flexural strength, direct shear strength, and elastic modulus were also established.

4.2 Experimental Program

4.2.1 Materials

4.2.1.1 Magnesium Potassium Phosphate Binder

Chemically bonded phosphate ceramics (CBPC) are produced through an acid-base reaction in water (Wagh, 2004). For the CBPC used in this study and originally developed by Wagh et al. (1997, 1998), the reactive components are magnesium oxide (MgO) and monopotassium phosphate (KH₂PO₄) given by:



According to Wagh and others, the mechanical properties of this binder system are enhanced by inclusion of fly ash (FA) (Wagh et al., 1997; Ding and Li, 2005a). It has been shown previously that the compressive strength of the binder is optimal when the FA loading is between 50 and 60% of the total mass of the dry binder ingredients (Wagh, 2004). A higher FA loading typically gives a decrease in strength (Wagh, 2004 and Ding and Li, 2005a).

Calcined MgO was utilized in this study. Manufacturer specifications indicated that it was 97% magnesium oxide (MgO) by weight, with a specific surface area of 0.3 m²/g and a minimum of 95% of the particles passing the 200 mesh size. Fertilizer grade KH₂PO₄ was obtained from a local farm supply warehouse. Class C Fly Ash (FA) was also used, with the FA chemical composition given in Table 5.1. Adapted from the molar ratios in Equation 4.1 and using 50% FA loading of the total mass, the dry ingredients of the CBPC binder were prepared at a mass ratio of MgO:KH₂PO₄:FA = 1:3.4:4.4. The product is termed hereafter as magnesium potassium phosphate cement binder with the dry mass designated as parameter *b*. As described later, the typical water to binder mass ratio (*w/b*) was varied for each aggregate type to obtain mixes with acceptable workability and to allow study of the *w/b* influence on the LWCC properties.

Table 4.1- Chemical composition of Fly Ash

Fly Ash Type	Mass fraction of the sample (%)						
	MgO	CaO	SiO ₂	Fe ₂ O ₃	Al ₂ O ₃	SO ₃	Na ₂ O
Class C	1.22	10.97	55.53	3.62	23.24	0.24	2.83

4.2.1.2 Lightweight Aggregate

Six different lightweight aggregates were considered in this study as summarized in Table 4.2. Lightweight expanded clay aggregate (LECA) was examined having two different size gradations: fine (FL) and coarse (CL). One expanded slate aggregate (ST) was considered. Expanded shale aggregate was provided in a so-called coated form (BCO) that was directly sieved from the kiln production line output, and a second so-called uncoated expanded shale (BCR) produced through

a crushing operation was also considered. Finally, a crushed bottom ash (BAA) from a coal-fired thermal generating station was also examined. Physical properties of each aggregate type, including the dry specific gravity and the water absorption were evaluated according to ASTM C127 (2007) and ASTM C128 (2007) and are summarized in Table 4.2. Sieve analysis for each aggregate type was carried out according to ASTM C136 (2006) and the corresponding gradation curves are shown in Figure 4.1.

Table 4.2- Physical properties of lightweight aggregates

Aggregate Type		Specific Gravity (dry)	Water absorption (%)	Max. Size (mm)	Fineness modulus
FL	Fine expanded clay	1.49	10.3	2.5	2.97
CL	Coarse expanded clay	0.995	24.4	10	5.86
BCO	Coated expanded shale	1.58	14.6	2.5	3.74
BCR	Crushed expanded shale	1.69	7.6	2.5	2.80
ST	Expanded slate	1.76	3.2	5	3.26
BAA	Bottom ash	1.65	0.8	5	2.68

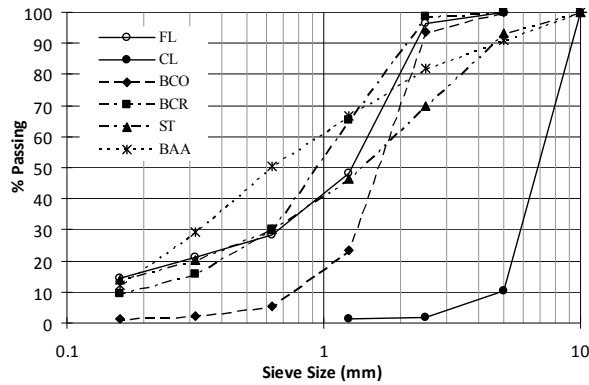


Figure 4.1- Particle size distribution of lightweight aggregates

4.2.2 Specimen Preparation

Five groups of mixes were prepared according to the aggregate type. LWCC made by combining FL and CL aggregates was named as Type LL ceramic concrete. LWCC produced by using FL, ST, BCO, BCR and BAA aggregate were denoted as Types L, S, B, BC and BA ceramic concretes, respectively. Except for

the bottom ash aggregates (i.e. BAA), all lightweight aggregates were immersed in water for 24 hrs and then spread on a paper towel to obtain a saturated surface dry condition prior to use. Due to difficulty in obtaining a saturated surface dry condition for the BAA aggregate, it was used in a dry condition after being stored in the ambient laboratory environment for a minimum of 1 year.

Table 4.3- Mix proportion of lightweight aggregates ceramic composite

LWCC Type	Series	Materials mass ratio					
		b^a	FL ^a	CL ^a	BAA ^a	FL/ST/BCO/BCR ^a	w^a
LL	LL1	1	0.14	0.40	-	-	0.20
	LL2	1	0.14	0.40	-	-	0.22
	LL3	1	0.14	0.40	-	-	0.24
	LL4	1	0.14	0.30	-	-	0.24
	LL5	1	0.14	0.50	-	-	0.24
BA	BA1	1	-	-	0.5	-	0.26
	BA2	1	-	-	0.5	-	0.28
	BA3	1	-	-	0.5	-	0.30
	BA4	1	-	-	0.25	-	0.26
	BA5	1	-	-	0.33	-	0.26
L, S, B, BC	L1/S1/B1/BC1	1	-	-	-	0.67	0.20
	L2/S2/B2/BC2	1	-	-	-	0.67	0.22
	L3/S3/B3/BC3	1	-	-	-	0.67	0.24
	L4/S4/B4/BC4	1	-	-	-	0.5	0.20
	L5/S5/B5/BC5	1	-	-	-	1	0.20
^a b : binder; FL: fine leca; CL: coarse leca; BAA: bottom ash; ST: expanded slate; BCO: coated expanded shale; BCR: crushed expanded shale; w : water							

Three different water to binder (w/b) mass ratios were used for each mix type to study the w/b influence on the compressive strength, modulus of rupture, shear strength and modulus of elasticity. Three aggregate to binder (a/b) mass ratios were used to study the influence of aggregate content on compressive strength. Table 4.3 provides a summary of the mix proportions used in this study normalized to a unit mass of the dry binder, b . Note that for each mix a commercially available lignosulphonate admixture was used at 1.5% by mass of

binder, to control the reaction rate and retard the setting time. The target setting time was between 90 and 120 minutes based on the intended applications for the developed mixes.

Each mixture was prepared by first dry mixing the MgO, KH₂PO₄ and FA components for 5 minutes using a 20 l capacity portable mixer with a mixing bucket speed of 60 revolutions per minute (RPM). The lightweight aggregate, with the moisture state noted above, was gradually added into the running mixer using a scoop and mixed for 60 seconds. The water was combined with the lignosulphonate retarder and then added to the dry ingredients, with further mixing for an additional 4 to 5 minutes. The resulting mix was carefully placed into plastic molds and consolidated using a vibrating table. Specimens were removed from the molds after 2 hrs and stored in the ambient lab environment (i.e. room temperature of 23±2°C and relative humidity of 50±5%) until testing. All results presented in this paper are the average values from three duplicate samples produced from the same batch unless noted otherwise.

4.2.3 Test Set-up

4.2.3.1 Fresh Property Test

To perform slump and flow tests, a flow table as described in ASTM C230 (2008) was used with a mini-slump cone similar to Kantro (1980) with height of 57 mm, top diameter of 19 mm and bottom diameter of 38 mm. The slump cone was placed at the centre of the flow table and filled with the LWCC without tapping, within 1 minute after the mixing was completed. The cone was gently lifted and the average horizontal spread of the concrete was measured, herein termed Initial Spread. The flow table was raised and dropped 20 times over a period of 15 seconds and the new average spread was measured according to ASTM C1437 (2007). The difference between this new spread and the Initial Spread is defined herein as the Slump Flow.

The setting time of LWCC was measured using a Vicat needle apparatus, according to ASTM C191 (2008). Since the difference of initial and final setting

time was negligible, only the final setting time was measured and reported in this paper.

4.2.3.2 Compressive Strength Test

The compressive strength of 50×50×50 mm cubes was determined using a Forney testing machine with capacity of 3100 kN. See Figure 4.2(a). The loading rate corresponded to a compressive stress rate of 0.25 MPa/s as per ASTM C39 (2009). The tests were completed at ages of 3, 7 and 28 days after casting.



(a) Cube specimens



(b) Cylinder specimens

Figure 4.2- *Compressive test configurations*

Compressive strength tests of (100 mm diameter × 200 mm high cylinders) were conducted in accordance with ASTM C469 (2002) using a stiff MTS frame with capacity of 2600 kN. See Figure 4.2(b). The aim of the cylinder tests was to investigate the compressive stress-strain response and modulus of elasticity. Axial deformations were measured using three linear variable displacement transducers (LVDTs) arranged at 120° separation about the longitudinal axis and operating over an initial gauge length of 100 mm. The loading rate was set to a machine stroke of 1.25 mm/min. Cylinders were sulphur capped before testing as per ASTM C617 (2010). Tests on cylinders were carried out at the age of 28 days.

4.2.3.3 Flexure Test

The flexural response of each mix was studied according to ASTM C78 (2009) using prism samples $50 \times 50 \times 200$ mm under 4-point bending with span of 150 mm. However, different from ASTM C78, a 10 mm deep notch was saw cut at mid-span across the bottom face of the sample. The universal test machine had a 30 kN capacity. Loading was applied at a mid-span deflection rate of 0.1 mm/min. A yoke was used to measure the mid-span deflection relative to the supports as the average measurement from two LVDTs as shown in Figure 4.3(a). Flexural tests were conducted at 28 days after casting.

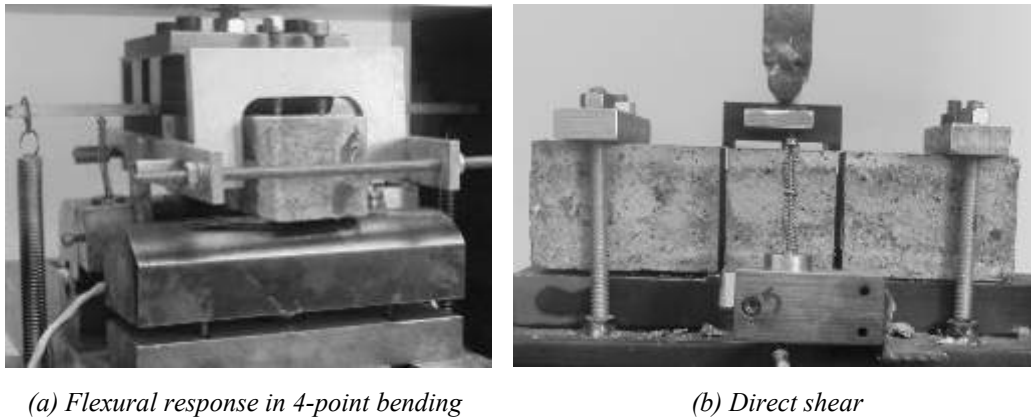


Figure 4.3- Test set-up for prisms

4.2.3.4 Direct Shear Test

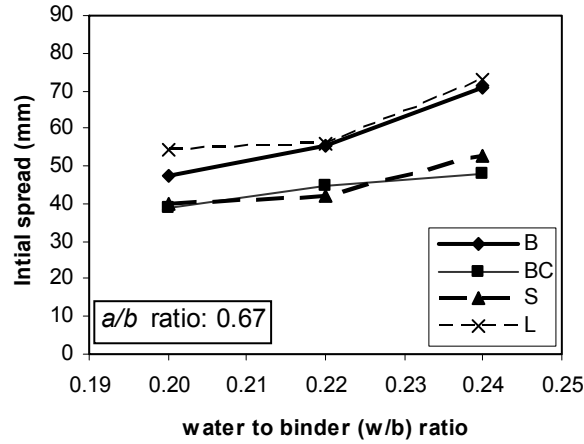
Prism samples $50 \times 50 \times 200$ mm were used to study the direct shear strength using a test method adapted from JSCE-SF6 (1990). The test arrangement is shown in Figure 4.3(b), whereby the upper loading plate causes vertical motion of the central region of the test specimen relative to the clamped end portions. To control the location of the shear planes, 10 mm deep saw cut notches were introduced around the full perimeter of the prism at each shear plane, similar to Mirsayah and Banthia (2002). Tests were conducted in a universal testing machine with capacity of 30 kN at a deformation rate of 0.1 mm/min. Displacement of the loading apparatus was measured using two LVDTs acting against the top loading plate. Direct shear tests were conducted at 28 days after casting.

4.3 Results and Discussion

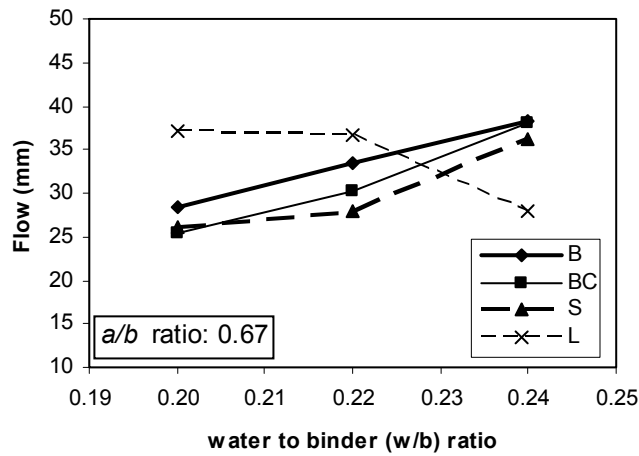
4.3.1 Fresh Ceramic Concrete Properties

4.3.1.1 Slump Flow Test

Figure 4.4(a) illustrates the relationship between the w/b mass ratio and the Initial Spread diameter after the mini-slump cone was removed. Results are shown for different LWCC mixes, all having the same a/b mass ratio of 0.67. As noted earlier, the aggregates were pre-soaked prior to use and added to the mixer in a saturated surface dry condition. The water added during mixing will primarily affect the paste composition of the mix and the resulting workability. Thus, as expected, the Initial Spread increased as the w/b ratio increased. It can also be observed that the Type B and Type L concretes had larger Initial Spread diameters than the Type S and Type BC concretes despite similar w/b and a/b ratios, which may be related to the particle. Figure 4.4(b) plots the relationship between Slump Flow and the w/b ratio for the same mixes. The Slump Flow increases as the w/b ratio increases except for the Type L concrete with $w/b=0.24$. In this latter case, there was complete collapse of the concrete when the cone was initially lifted.



(a) Initial Spread



(b) Slump Flow

Figure 4.4- Results of slump flow tests

4.3.1.2 Setting Time

The final setting times of LWCC with different aggregate types and a constant a/b mass ratio of 0.67 are shown in Table 4.4. All mixes included the same dosage of retarder as a fraction of the binder mass. It was observed that only a small difference in setting time occurred as the w/b ratio changed from 0.20 to 0.22. The final setting times ranged between about 75 and 105 minutes for the LWCC mixes studied. For comparison, the setting time measured for the binder paste alone was measured to be approximately 120 minutes for $w/b = 0.2$. Note that these setting times were near the target values noted earlier and no further study of the retarder dosage or retarder type was completed for the LWCC.

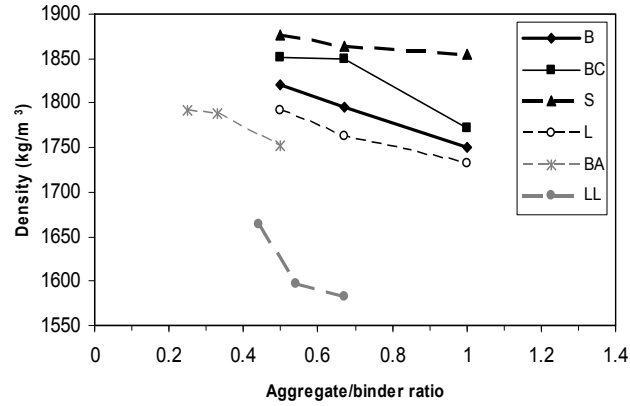
Table 4.4- Setting time of different ceramic concrete

LWCC Type	Setting time (minutes)	
	w/b=0.2	w/b=0.22
B1, B2	80	75
BC1, BC2	95	90
S1, S2	90	95
L1, L2	100	105

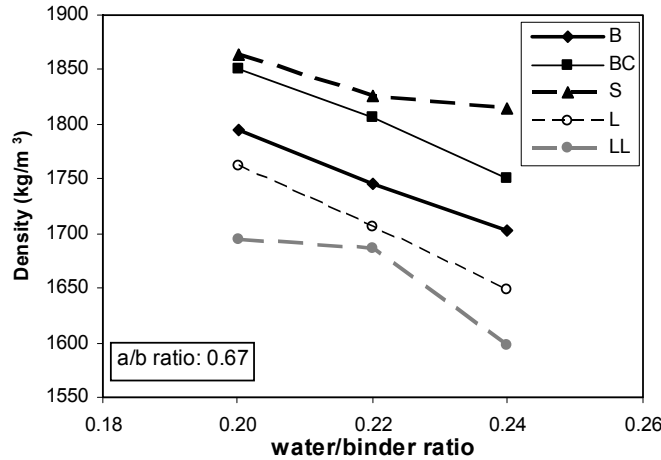
4.3.2 Hardened Ceramic Concrete Properties

4.3.2.1 Density

The density of hardened concrete depends upon a large number of factors including the density of the aggregates, the grading of the aggregates, their initial moisture content, the cement content, and the water/binder ratio (Chandra and Bemtsson, 2002). Densities of LWCC prepared with different a/b and w/b ratios were measured at 28 days after casting and the results are presented in Figure 4.5. It is observed from Figure 4.5(a) that the density of LWCC reduces as the a/b mass ratio increases, regardless of the type of lightweight aggregate. This occurs because the aggregate density is lower than the binder density of 1850 kg/m^3 at $w/b=0.20$. Similarly, it can be seen from Figure 4.5(b) that an increase in the w/b mass ratio resulted in lower density LWCC for a/b mass ratio of 0.67. Further, Figure 4.5 illustrates that the density of LWCC is influenced by the type of lightweight aggregate, similar to the influence identified for Portland cement based lightweight concretes (e.g., Chandra and Bemtsson, 2002; Short and Kinniburgh, 1978). For example, Type S concrete containing ST aggregate had the highest hardened density when other parameters were kept constant, since ST had the highest aggregate density (see Table 4.2). Therefore, the results show that the density of LWCC depends on the aggregate properties and w/b ratio.



(a) aggregate/binder ratio influence with $w/b=0.20$



(b) water/binder ratio influence with $a/b=0.67$

Figure 4.5- Effect of mix proportions on the density of hardened ceramic concrete

4.3.2.2 Compression Strength

The compressive strength of lightweight Portland cement concrete is known to depend on aggregate type, the water/binder ratio, the cement content, and the age of the concrete (e.g., Chandra and Bemtsson 2002; Short and Kinniburgh 1978). The cube compressive strengths of LWCC containing different aggregate types were determined at ages of up to 28 days after casting and the results are summarized in Table 4.5. The compressive strength reduced as the w/b mass ratio increased, similar to lightweight Portland cement concrete. The compressive strength of all specimens increased with specimen age regardless of the w/b ratio or aggregate type. Further, a rapid gain in compressive strength was observed in all cases. At an age of 3 days, approximately 89% of samples exhibited between 65% and 90% of their corresponding 28-day strength. At 7 days, approximately

72% of the samples exhibited between 80 % and 97 % of their corresponding 28-day strengths. This rapid strength gain, much quicker than that typically observed for Portland cement concrete, resulted from the rapid acid-base reaction process of the phosphate binder compared to the slower hydration process of Portland cement binders. The rapid strength gain, combined with adequate working time (Table 4.4) suggests that the developed LWCCs are suitable for applications where short construction duration is required.

Table 4.5- Effect of curing time on cube compressive strength and summary of cylinder compressive, flexure and shear test results

Mix type	w/b	Cube Compressive (MPa)			Cylinder compressive, flexure and shear test results						
		3 (day)	7 (day)	28 (day)	f_c (MPa)	ϵ_c (mm/mm)	f_r (MPa)	δ_r (mm)	f_τ (MPa)	δ_τ (mm)	E (GPa)
B	0.20	26.8	28.7	33.7	35.7	0.0029	2.3	0.0324	1.8	0.232	15.6
	0.22	22.3	27.0	28.5	29.2	0.0026	1.8	0.0449	1.5	0.249	14.3
	0.24	19.9	21.7	25.6	24.3	0.0024	1.4	0.0374	1.2	0.228	12.0
BC	0.20	24.7	26.4	30.8	33.5	0.0029	1.5	0.0424	1.6	0.175	13.8
	0.22	20.7	22.1	25.7	24.2	0.0023	1.5	0.0399	1.5	0.161	13.7
	0.24	15.7	17.7	24.3	23.5	0.0029	1.3	0.0284	1.1	0.204	10.5
S	0.20	25.6	26.5	38.7	33.5	0.0033	2.4	0.0524	2.1	0.273	13.2
	0.22	18.8	20.2	33.6	26.1	0.0028	1.9	0.0499	1.6	0.266	12.1
	0.24	18.6	19.8	30.1	24.2	0.0029	1.7	0.0365	1.3	0.265	11.3
L	0.20	21.8	22.2	32.5	30.5	0.0034	1.8	0.0659	1.9	0.190	11.7
	0.22	17.3	20.9	25.4	26.5	0.0029	1.3	0.0549	1.6	0.172	10.6
	0.24	14.7	18.1	22.3	18.8	0.0023	1.0	0.0399	0.7	0.304	7.1
LL	0.20	23.5	24.2	26.3	23.8	0.0027	1.8	0.0656	1.9	0.221	11.5
	0.22	21.7	21.9	22.2	20.2	0.0024	1.6	0.0449	1.1	0.184	8.9
	0.24	17.2	18.9	21.1	17.4	0.0025	1.3	0.0487	0.7	0.276	8.3
BA	0.26	27.4	28.9	33.2	35.6	0.0035	2.2	0.0524	2.2	0.191	12.4
	0.28	26.7	28.8	29.8	28.9	0.0030	1.7	0.0470	1.8	0.181	12.4
	0.30	23.1	24.6	26.6	24.4	0.0032	1.5	0.0206	1.6	0.205	10.2

The compressive strength of LWCC containing different a/b ratios for a fixed w/b ratio (i.e $w/b=0.26$ for BA, $w/b=0.24$ for LL, and $w/b=0.20$ for other series), are

shown in Figure 4.6 for ages of 7 and 28 days after casting. It can be observed that the cube compressive strength of most mixes decreased as the a/b ratio increased. This phenomenon is similar to Portland cement based lightweight concretes (e.g., Chandra and Bemtsson, 2002; Short and Kinniburgh, 1978). For Type L and Type S LWCC, the highest increase in compressive strength occurred at 28 days for a/b ratios of 0.67. This suggests that there may be an optimum a/b ratio that will achieve a peak long-term strength and that this may be related to the aggregate type. However, this could not be quantified from the results in the current study.

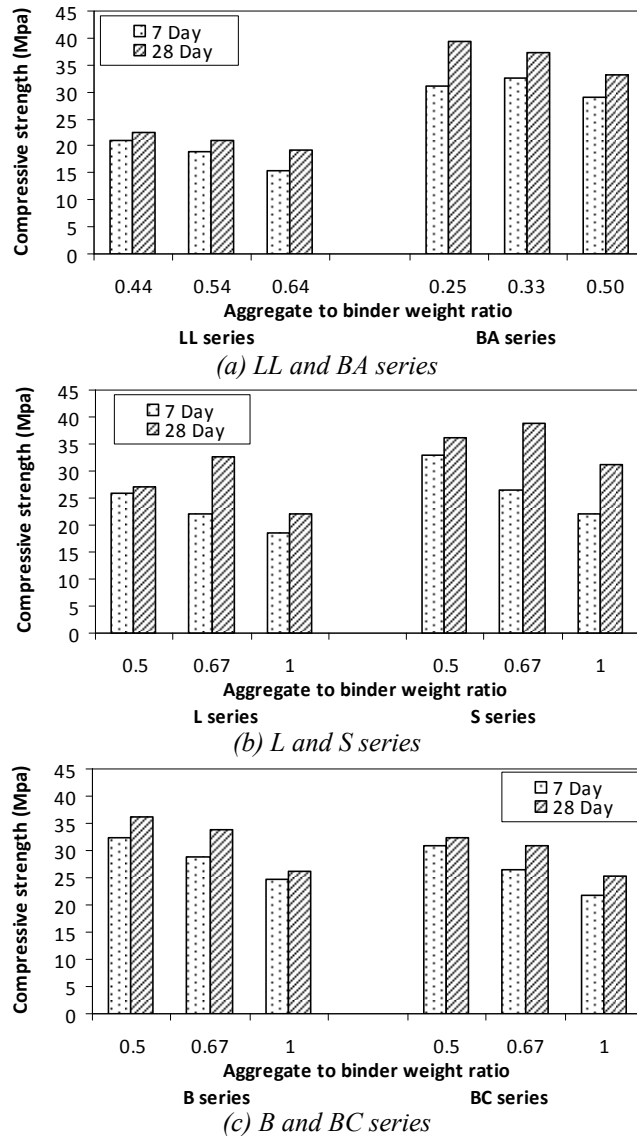


Figure 4.6- Compressive strength of cubes for LWCC at ages of 7 and 28 days

The influence of aggregate type on the 28 day cylinder compressive strength is shown in Figure 4.7 for mixes with $a/b=0.67$. As expected, the compressive strengths of all concretes decreased with an increase in the w/b ratio, similar to lightweight concretes with Portland cement binders (Lo et al., 2007). Type B concrete exhibited the highest compressive strength, while Type LL concrete exhibited the lowest strength. This attributed to physical properties of the aggregates. For a concrete with a given lightweight aggregates has a limiting ceiling strength beyond which there can be no appreciable strength gain despite large increases in cementitious materials (ACI 213-09). The strength ceiling is influenced predominately by the aggregate strength and the maximum coarse aggregate size, which can be increased appreciably by reducing the maximum size of the coarse aggregate (ACI 213-09). The maximum coarse aggregates sizes have an effect on ceiling strength of lightweight concrete due to the amount of pores within the aggregates which limit the concrete strength (e.g., Chandra and Bemtsson, 2002). One reason for decrease in compressive strength for type LL concrete could be that it is a mixture with the largest coarse aggregate size (see Table 4.2). In addition, type CL aggregates is more porous (i.e. higher water absorption, see Table 4.2) which gives lesser density, therefore results in lesser compressive strength of type LL concrete. Further, BCO aggregates are rougher which gives a better aggregate-binder bond and may resulted increase in compressive strength of B concrete, while CL is smooth which might result in weaker aggregate-binder bond and therefore lesser compressive strength. The results therefore clearly indicate that the lightweight aggregate properties influence the compressive strength of LWCC.

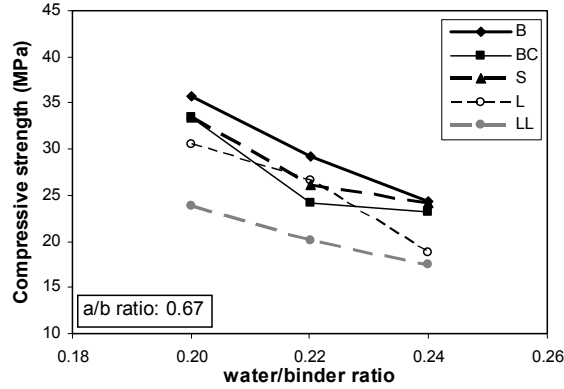


Figure 4.7- Influence of water/binder ratio on compressive strength of LWCC using different aggregate types

The relationship between the hardened density and the cylinder compressive strength of LWCC at 28 days after casting is shown in Figure 4.8. The plot includes all mixes from Table 4.5 and Figure 4.7, and thus includes data representing a variety of w/b ratios and a/b ratios. The overall trend of the data shows that the compressive strength increases with increasing concrete density regardless of the type of aggregates, a similar trend to that identified for Portland cement lightweight concrete (e.g., Chandra and Bemtsson, 2002; Short and Kinniburgh, 1978).

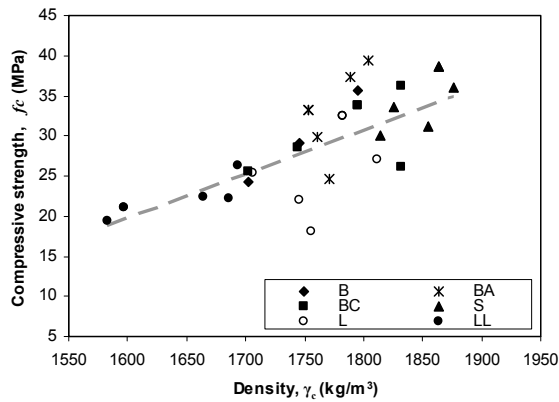


Figure 4.8- Relation between compressive strength and density for different aggregates

It was demonstrated earlier that the compressive strength and density both vary with the w/b ratio. The 28 day density to strength ratio γ_c/f_c was calculated for each mix type and the results are plotted in Figure 4.9. Type B concrete exhibited the smallest density/strength ratio for each w/b ratio considered. This suggests that

using Type BCO aggregate is advantageous compared to the other aggregate types studied.

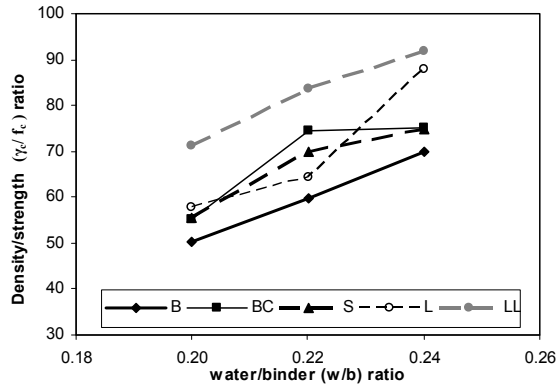


Figure 4.9- Density to strength ratios of lightweight concrete with different aggregate for $a/b=0.67$

4.3.2.3 Stress-strain Relation and Modulus of Elasticity

The compressive stress-strain response of LWCC at 28 days was determined from the uniaxial cylinder tests. Representative stress-strain curves for Type B concrete are provided as Figure 4.10. The stress-strain response of each mix is characterized by a nearly linear ascending branch, similar to the stress-strain curves of lightweight aggregate concretes with Portland cement binders (e.g., Chandra and Bemtsson, 2002; Short and Kinniburgh, 1978). By comparing the 3 curves in Figure 4.10, it can be observed that the stress-strain response is influenced by the w/b mass ratio, whereby the initial stiffness, peak stress and strain at peak stress are all reduced as the w/b ratio increases. Stress-strain relationships for the LWCC containing other lightweight aggregate types had similar characteristics to the Type B curves. Data for the maximum compressive strength and corresponding strains for LWCC with other lightweight aggregate types is presented in Table 4.5.

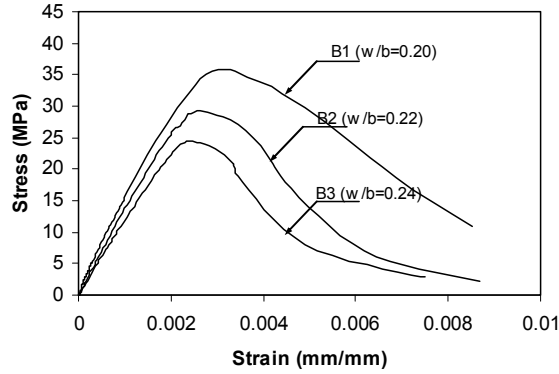


Figure 4.10- Stress-strain relation of B concrete for $a/b=0.67$

It is well known that the modulus of elasticity of lightweight aggregate concrete made with Portland cement binder depends upon the modulus of elasticity of the matrix, the type of aggregate, the water/binder ratio, and the aggregate/binder ratio (Chandra and Bemtsson, 2002). This study found that similar influences also exist for LWCC produced using the magnesium potassium phosphate CBPC binder. The influence of aggregate type on the modulus of elasticity of LWCC is shown in Figure 4.11. The modulus of elasticity of LWCC was found to decrease with increases in the w/b ratio for all aggregate types examined. It can also be observed that the modulus of elasticity varied between different lightweight aggregate types for a given w/b ratio. For example, Type B LWCC had the highest modulus of elasticity for all w/b ratios studied. The modulus of elasticity of LWCC ranged from 7.2 to 15.6 GPa.

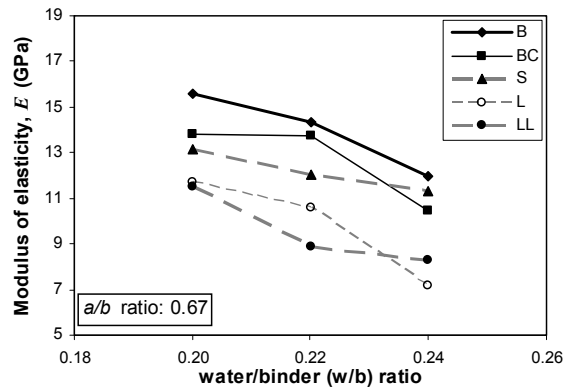


Figure 4.11- Effect of water/binder ratio on modulus of elasticity for LWCC using different types of aggregates

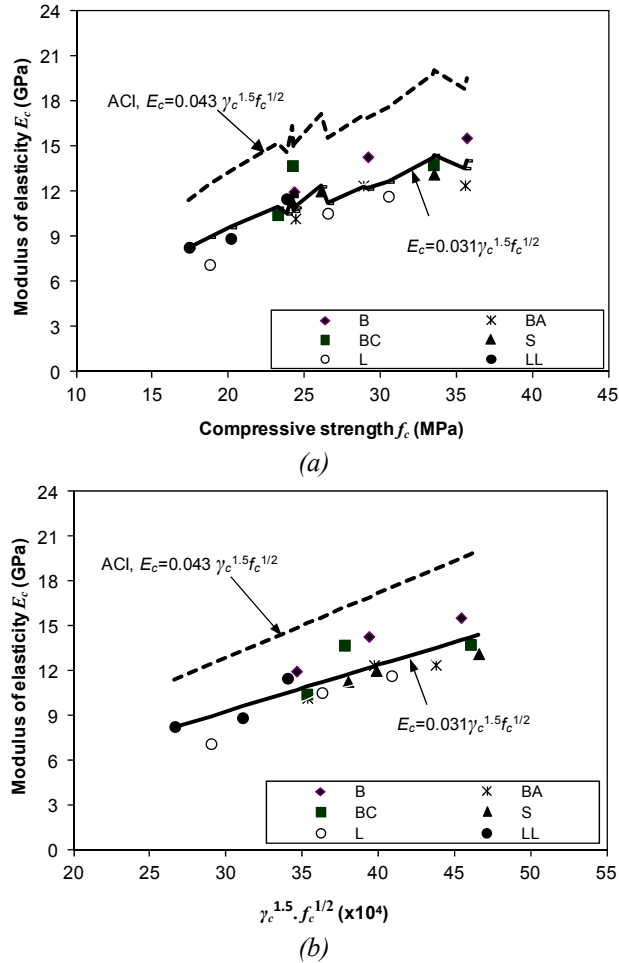


Figure 4.12- Relation between modulus of elasticity and compressive strength

The relationship between modulus of elasticity and compressive strength of LWCC is shown in Figure 4.12. The figure shows that the modulus of elasticity of all LWCCs increased as the compressive strength increased. ACI 213R-03 (2009) suggests that the modulus of elasticity (E_c) of Portland cement based lightweight concrete is related to its density (γ_c) and compressive strength (f_c') according to:

$$E_c = 0.043 \gamma_c^{1.5} \sqrt{f_c'} \quad (4.2)$$

The data in Figure 4.12 shows that the test results of modulus of elasticity were lower than the values estimated using Eqn. 4.2. Based on a least square method to best fit the test data ($R^2= 0.71$), the LWCC results suggest that the relationship be adjusted to:

$$E_c = 0.031\gamma_c^{1.5}\sqrt{f_c'} \quad (4.3)$$

Note that exponents for γ_c and f_c' in Equation 4.3 were not determined but selected to keep same format as ACI expression so regression analysis only looked for the coefficient.

4.3.2.4 Flexural Strength

The flexural stress versus the mid-span displacement of representative Type B concrete prisms is shown in Figure 4.13. The maximum flexural strength f_r (i.e. modulus of rupture) reduced as the w/b was increased. Similar trends between f_r and w/b occurred for the LWCC produced with other lightweight aggregate types and the f_r and corresponding mid-span displacement (δ_r) are summarized in Table 4.5. The relationship between f_r and w/b are illustrated in Figure 4.14. The modulus of rupture varied between 1.0 and 2.4 MPa. It can also be seen from Figure 4.14 that the flexural strength of mixes with different LWCC types varied as the w/b ratio changed. This demonstrates that the modulus of rupture of LWCC is influenced by the properties of the lightweight aggregate type and the mix proportions.

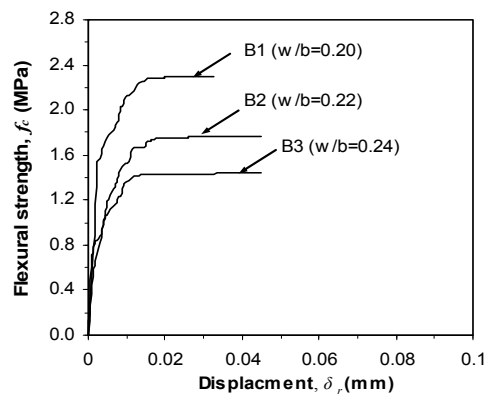


Figure 4.13- Flexural strength of Type B concrete

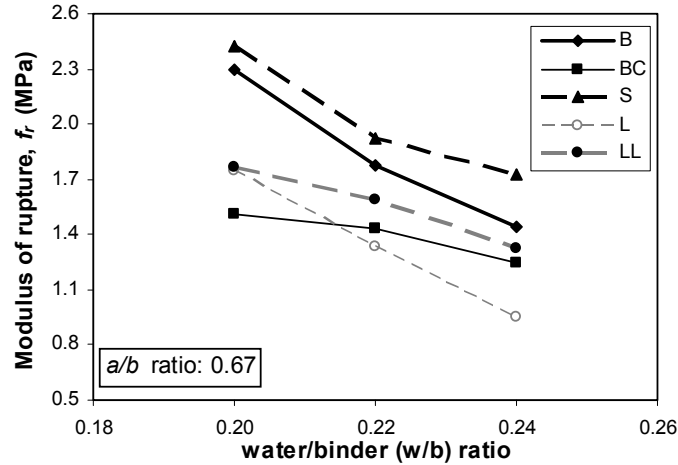


Figure 4.14- Influence of water/binder ratio on modulus of rupture for LWCC using different aggregate types

The relationship between flexural strength and compressive strength is shown in Figure 4.15. For all types of LWCC studied, an increase in the compressive strength corresponded with an increase in the modulus of rupture. The flexural strength ranged between 4.5 % and 7.8 % of the corresponding compressive strength.

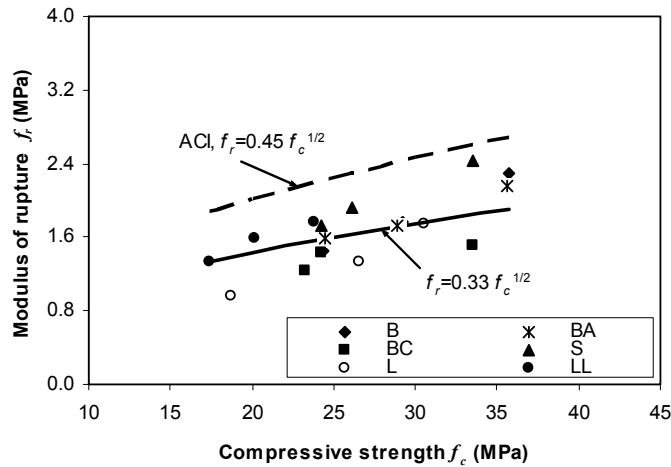


Figure 4.15- Relation between modulus of rupture and compressive strength

ACI 213R-03 (2009) recommended an equation to relate modulus of rupture (f_r) of Portland cement based lightweight concrete with its compressive strength (f_c) as follows:

$$f_r = 0.45\sqrt{f_c'} \quad (4.4)$$

Eqn. 4.4 was found to overestimate the flexural strengths of the LWCC mixes in this test program, as shown in Figure 4.15. Based on a least square method to best fit the test results ($R^2 = 0.48$), the following relationship is proposed for LWCC:

$$f_r = 0.33\sqrt{f_c} \quad (4.5)$$

Note that exponent of f_c in Equation 4.5 was not determined but selected to keep same format as ACI expression so regression analysis only looked for the coefficient.

4.3.2.5 Direct Shear Strength

The relationship between the direct shear stress and the shear displacement is shown in Figure 4.16 for Type B LWCC made with different w/b ratios. It can be observed that the maximum shear strength decreases with increasing w/b ratio. Similar trends were noticed for the other concretes and the maximum shear strength (f_r) and corresponding displacement (δ_r) are summarized in Table 4.5. The shear strength of LWCC varied from 0.7 to 2.1 MPa. Figure 4.17 shows that the shear strength of LWCC produced with different lightweight aggregate types varied at each w/b ratio. However, the difference between aggregate types was not significant except for Type LL concrete. The fracture plane for Type LL concrete samples typically went through the aggregates but went around the aggregates for the other mix types. This was attributed to the aggregate size difference as given in Table 4.2, and the aggregate strengths. This indicates that the shear strength of LWCC is influenced by the properties of the lightweight aggregates and by the strength of the binder.

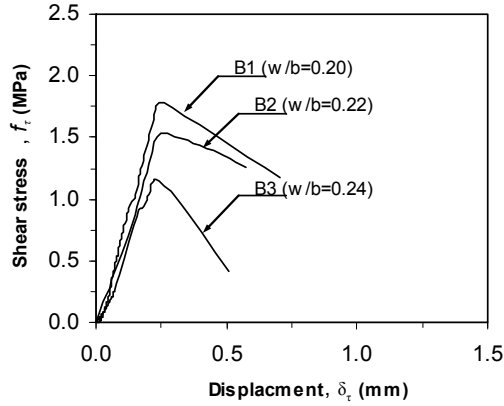


Figure 4.16- Shear strength of B concrete

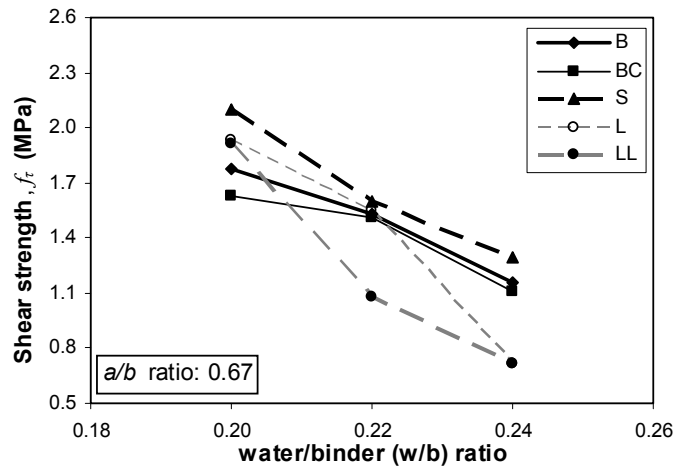


Figure 4.17- Effect of water/binder ratio on shear strength for LWCC using different types of aggregates

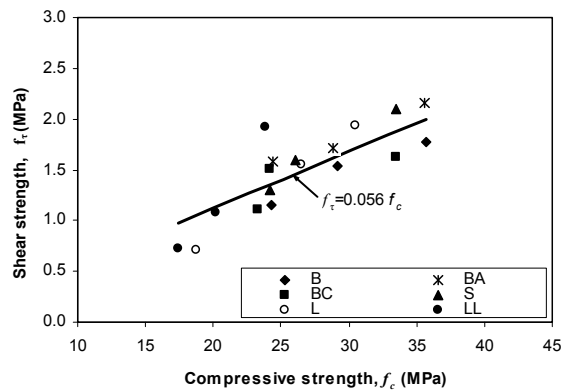


Figure 4.18- Relation between shear strength and compressive strength

Similar to modulus of rupture and modulus of elasticity, all types of LWCC showed an increase in the direct shear strength as the compressive strength increased as shown in Figure 4.18. Based on a least square method to best fit the test results ($R^2= 0.69$) of shear strength and compressive strength, the following relationship is proposed for shear strength of LWCC:

$$f_{\tau} = 0.056 f_c \quad (4.6)$$

4.4 Conclusions

Lightweight ceramic concretes (LWCC) were developed using different lightweight aggregates and a magnesium potassium phosphate binder. The physical and mechanical properties of the LWCC were examined through laboratory testing. The following conclusions can be drawn from this study:

- The fresh properties of LWCC were influenced by the water/binder ratio and type of lightweight aggregate. Higher water/binder ratios resulted in increased slump flow but negligible influence on the setting time.
- Compressive strength of LWCC increased as the density increased. The 28 day compressive strengths and densities ranged from 17 to 36 MPa and 1600 to 1870 kg/m³ respectively, meeting the ACI 213 classification of structural lightweight concrete.
- The rate of compressive strength gain was very rapid with 65 to 90 % of the 28 day strength attained within 3 days for most mixes.
- The compressive strength and density of LWCC both decreased with increases in the aggregate/binder ratio and in the water/binder ratio, regardless of the aggregate type.
- The modulus of elasticity of LWCC decreased as the water/binder ratio increases and increased with increasing compressive strength, regardless of the type of aggregates. The relationship between modulus of elasticity,

compressive strength and density could be captured using a similar format to the ACI 213 model for Portland cement concrete but with a decreased equation constant.

- The modulus of rupture increased with higher compressive strengths and decreased with larger water/binder ratios, regardless of the aggregate type. The relationship between modulus of rupture and compressive strength was developed with similar format but reduced coefficient compared to the equivalent ACI 213 relationship for lightweight Portland cement concrete.
- The direct shear strength of LWCC was found to increase with compressive strength and decrease for larger water/binder ratios, regardless of aggregate type. A linear relationship was proposed between the shear strength and compressive strength.
- The coated expanded shale (i.e. Type B concrete) showed the most favourable properties among the aggregate types studied in terms of workability, compressive strength to density ratio, compressive strength and the modulus of elasticity.

4.5 References

- ACI Committee 213. (2009). Guide for Structural Lightweight-Aggregate Concrete (ACI 213R-03); ACI manual of Concrete Practice (2009 Part 1). American Concrete Institute, Farmington Hills, MI, 1-20.
- ASTM C 230/C 230M. (2008). Standard Specification for Flow Table for use in Tests of Hydraulic Cement. ASTM International, West Conshohocken, PA.
- ASTM C127. (2007). Standard test method for density, relative density (specific gravity), and absorption of coarse aggregate. ASTM International, West Conshohocken, PA.
- ASTM C128. (2007). Standard test method for density, relative density (specific gravity), and absorption of fine aggregate. ASTM International, West Conshohocken, PA.

Chapter 4: Mechanical Properties of Lightweight Ceramic Concrete

- ASTM C136. (2006). Standard test method for sieve analysis of fine and coarse aggregate. ASTM International, West Conshohocken, PA.
- ASTM C1437. (2007). Standard Test Method for Flow of Hydraulic Cement Mortar. ASTM International, West Conshohocken, PA.
- ASTM C191. (2008). Standard Test Method for Time of Setting of Hydraulic Cement by Vicat Needle. ASTM International, West Conshohocken, PA.
- ASTM C39/C39M-09a. (2009). Standard Test Method for Compressive Strength of Cylindrical Concrete Specimens. ASTM International, West Conshohocken, PA.
- ASTM C469-02e1. (2002). Standard Test Method for Static Modulus of Elasticity and Poisson's Ratio of Concrete in Compression. ASTM International, West Conshohocken, PA.
- ASTM C617. (2010). Practice for Capping Cylindrical Concrete Specimens. ASTM International, West Conshohocken, PA.
- ASTM C78. (2009). Standard Test Method for Flexural Strength of Concrete (Using Simple Beam with Third-Point Loading), ASTM International; West Conshohocken, PA.
- Chandra, S. and Berntsson, L. (2002). Lightweight Aggregate Concrete. Noyes Publications, New York, USA, 167-229.
- Chi, J. M., Huang, R., Yang, C. C. and Chang J. J. (2003). Effect of aggregate properties on the strength and stiffness of lightweight concrete. *Cement and Concrete Composites*, 25(2): 197-205.
- Ding, Z. and Li, Z. (2005a) Effect of aggregate and water content on the properties of magnesium phospho-silicate cement. *Cement and Concrete Composites*, 27(1): 11-18.
- Ding, Z. and Li, Z. (2005b). High-early-strength magnesium phosphate cement with fly ash. *ACI Material Journal*, 102(6): 357-381.
- JSCE-SF6. (1990). Method of Test for Shear Strength of Steel Fiber reinforced concrete. Japan Society of Civil Engineering (JSCE), Tokyo, 67-69.
- Kantro, D. L. (1980). Influence of water-reducing admixtures on properties of cement paste-a miniature slump test. *Journal of Cement and Concrete and Aggregates*, 2(2): 95-102.

Chapter 4: Mechanical Properties of Lightweight Ceramic Concrete

- Ke, Y., Beaucour, A. L., Ortola, S., Dumontent, H. and Cabrillac, R. (2009). Influence of volume fraction and characteristics of lightweight aggregates on the mechanical properties of concrete. *Construction and Building Materials*, 23(8): 2821-2828.
- Li, Z., Ding, Z. and Zhang, Y. (2004). Development of sustainable cementitious materials. Proceedings of International Workshop on Sustainable Development and Concrete Technology, Beijing, China: 55–76.
- Lo, T., Tang, W. C. and Cui, H. Z. (2007). The effect of aggregate properties on lightweight concrete. *Building and Environment*, 42(8): 3025-3029.
- Mirsayah, A. A. and Banthia, N. (2002). Shear strength of steel fiber-reinforced concrete. *ACI Materials Journal*, 99(5): 473-479.
- Qiao, F, Chau, C. K. and Li, Z. (2009). Property assessment of magnesium phosphate cement. *Key Engineering Material*, 400-402: 115-120.
- Qiao, F., Chau, C. K. and Li, Z. (2010). Property evaluation of magnesium phosphate cement mortar as patch repair material. *Construction and Building Materials*, 24: 695-700.
- Short, A. and Kinniburgh, W. (1978). Light weight concrete. Applied science publication Ltd. London, 150-171.
- Wagh, A. S. (2004). Chemically bonded phosphate ceramics: Twenty-first century material with diverse applications. Elsevier Limited, Amsterdam, 1-283.
- Wagh, A. S., Jeong, S. Y. and Singh, D. (1997). High-strength ceramic (cement) using industrial by-product Ashes. Proc. of Int. Conf. On High-Strength concrete, Kona, HI: 542-553.
- Wagh, A. S. and Jeong, S. Y. (1998). Method of waste stabilization via chemically bonded phosphate ceramics. U.S. Patent No. 5,830,815.

Proof of Concept Study of Textile Reinforced Ceramic Composite for Structural Infill Slab Applications³

5.1 Introduction

Steel reinforced concrete is typically used for structural infill slab applications. Design and construction of infill structural slabs for civil infrastructure upgrades can be complex due to the interaction of material properties, installation techniques and the overall structural response.

Traditional concrete materials have several disadvantages including high permeability, slow curing and rate of strength gain, undesirable shrinkage and high self-weight. In addition, the Portland cement used for making concrete has high environmental impacts during production. In recent years, phosphate cements have gained attention as an alternative to Portland cements and can be used to produce so-called chemically bonded phosphate ceramics (CBPC) (Wagh, 2004; Ding and Li, 2005a, 2005b). A CBPC is typically formed through chemical reaction of an acid (e.g., phosphoric acid) and a metal oxide base (e.g., magnesium oxide). CBPC can also incorporate Fly Ash (FA) at high loading

³ Contents of this chapter have been published. Reference: Samson Tassew and Adam Lubell, "Textile reinforced ceramic composite for structural infill slab application". Proceedings of 34th IABSE Symposium, Venice, Italy, 2010, A-0317, 1-8.

(Wagh, 2004). FA is a by product from coal-fired thermal power stations and thus a CBPC with FA can result in substantially lower environmental impact and energy consumption during production than Portland cement binders. CBPC with sand aggregates can produce a sand concrete (SC) with high early strength and good durability. Light weight concrete is commonly made using Lightweight Expanded Clay Aggregate (LECA) (Ke et al., 2009; Chi et al., 2003) and it is proposed in this research that CBPC cement combined with LECA will result in a viable light weight concrete (LC).

Reinforcement for flexural tension forces in slab-type elements can be provided by glass fiber textile reinforcement. The use of textile reinforcement has advantages compared to conventional steel reinforcement. Glass fiber textiles can match almost any geometric shape, have excellent resistance to corrosion, are light weight, and offer easier handling and rapid placement to speed the overall construction process. The use of textile reinforcement in Portland cement based concrete has been investigated by prior researchers (Bosche et al., 2008; Bruckner et al., 2008; Bank et al., 2009) but no work has examined use with CBPC concretes.

This chapter reports on a proof-of-concept study to develop an innovative structural infill slab system using textile reinforced ceramic composites. Using candidate ceramic composite made of magnesium phosphate binder and aggregates (sand and lightweight aggregate), and flexible textile reinforcements, a structural panels were produced and tested under three point bending test. The panel configurations represented full depth precast structural system as well as partial-depth precast panels suitable for use in stay-in-place formwork solutions.

Initial Concept Development

The prototype panel concept (Figure 5.1) includes sand concrete (SC) with a strong CBPC binder at the top and bottom layer and central core of lighter weight concrete (LC) containing expanded clay aggregates. Textile fabric reinforcement is placed at the intersection of the two materials. Material production should be

similar to traditional concrete industry practices and curing should be conducted under ambient environmental conditions.



Figure 5.1- Cross-section configuration of prototype panel

To realize this concept, optimized CBPC concretes were developed and characterized and small-scale (plan: 150x600 mm; thickness: 20 – 50 mm) prototype panels were produced for testing under transverse loading.



(a) Prototype panel



(b) Cross-section image of panel

Figure 5.2- Finished prototype and cross-sections

5.2 Materials

5.2.1 Concrete

Wagh et al. (2004) developed a CBPC from the acid-base reaction between calcined magnesium oxide (MgO) and monopotassium phosphate (KH₂PO₄) (MKP) in an aqueous solution. The reaction between these compounds is given by the following equation:



According to Wagh and others, the reaction rate and properties of the resulting material can be altered through variations in the molar ratios of MgO and MKP or through addition of Fly Ash and other compounds. The ceramic composite “concrete” developed in this study is produced using this technology.

Fertilizer grade MKP was obtained from a local farm supply warehouse. MgO products from two suppliers were trialed and the MgO properties were found to significantly affect the ability to produce a viable mix. The calcined MgO selected in this study contained 97% magnesium oxide by weight and had a specific surface area of 0.3 m²/g with minimum 95% of particles passing the 200 mesh size. Class C Fly Ash (FA) was also used, with the FA chemical composition given in Table 5.1. Aggregates consisted of angular quartz sand. Some mixes included lightweight expanded clay aggregate (LECA) in two different gradations: AR 0-2/880 (FL) and AR 4-10/550 (CL). The particle size distribution for the sand and LECA were determined according to ASTM C136-06 and are presented in Figure 5.3. Note that the LECA particle size distribution satisfies ASTM C330-09 requirements. The specific gravity and water absorption were evaluated as 0.995 and 24.4% for the CL LECA and 1.49 and 10.25% for the FL LECA, respectively, according to ASTM C127-07.

Table 5.1- Chemical composition of Fly Ash

Fly Ash Type	Mass fraction of the sample (%)						
	MgO	CaO	SiO ₂	Fe ₂ O ₃	Al ₂ O ₃	SO ₃	Na ₂ O
Class C	1.22	10.97	55.53	3.62	23.24	0.24	2.83

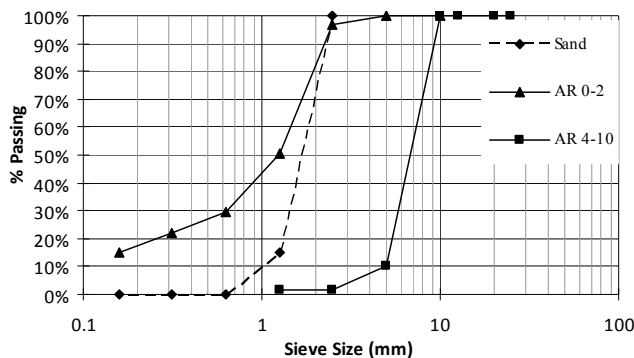


Figure 5.3- Particle size distribution of sand and LECA aggregates

5.2.1.1 Mix Proportions

Mixes were produced using a MgO to KH₂PO₄ weight ratio of 1:3.4, similar to that indicated by the molar ratios in Equation 5.1. The FA content was taken as 50% by weight of the total binder. Prior studies by Wagh et al. (Wagh, 2004; Ding and Li, 2005a) showed that binder containing 30 to 50% fly ash exhibited higher strength than a binder with only MgO and MKP. The required mixing water to achieve a workable mix varied based on the overall mix composition and earlier studies have shown that the water to binder ratio (*w/b*) will also affect the compressive strength of the resulting concrete. To control the reaction rate and retard the setting time, different admixtures were examined and use of a commercially available lignosulphonate admixture at 1.5% by weight of the MgO+KH₂PO₄ was added to the mixing water to achieve the desired rheological properties.

For the sand concrete (SC), sand to binder ratios (*s/b*) from 0.5 to 1.0 were examined. Water/binder ratios (*w/b*) of 0.20 were used for all SC reported in this paper. All lightweight concrete (LC) mixes containing LECA used a Fine LECA (FL) to binder ratio of 0.14 but varying coarse LECA (CL) to binder ratios between 0.3 and 0.5. The *w/b* ratio for all LECA mixes was fixed at 0.24. Note that LECA was soaked in water for 24 hours prior to use and then added to the mixtures in a saturated surface dry condition.

5.2.1.2 Mix Procedures

A 5l Hobart planetary mixer with a mixing speed of 28.5 RPM was used to prepare each mix. For sand concrete, the MgO, KH₂PO₄, FA and sand were dry mixed for 5 minutes. The water was blended with the lignosulphonate retarder then the dry mix was gradually added to the water and mixed for a total duration of 5 minutes. For LECA concrete, the binder ingredients (MgO, KH₂PO₄, FA) were dry mixed for 5 minutes. LECA and 25% of the water were mixed with the retarder and then blended with the dry binder materials for about 2 minutes. The remaining water was added before additional mixing of 5 minutes.

After mixing each batch, the material was carefully placed into plastic molds using a scoop. A vibrating table was used for 45 seconds to consolidate the specimens. All of the specimens were cured and tested in the ambient lab environment. Specimens consisted of 50×50×50 mm cubes for compressive strength testing, 50×50×200 mm prisms for evaluation of modulus of rupture, and 100 diameter × 200 mm cylinders for determining the uniaxial compressive stress-strain response. Three duplicate specimens were typically prepared and the results in this chapter reflect average values.

The setting times were measured for mixes according to ASTM C807-08. The initial and final setting times were typically 120 minutes and 130 minutes respectively, which met the objectives of this study.

5.2.1.3 Test Procedure

The compressive strength of cube specimens was determined using a stiff testing machine with capacity of 3100 kN. The loading rate for these tests was 0.25 MPa/s. Uniaxial stress-strain response in compression was determined through tests on cylinders in an MTS universal testing machine with 2600 kN capacity at a loading rate of 1.25 mm/min. The test arrangement is shown in Figure 5.4(a), and included a collar system with high-precision LVDTs to measure the shortening of the cylinders throughout the loading. The flexural response (Figure 5.4(b)) of small prisms was completed in a testing machine with 30 kN capacity at a loading rate of 0.10 mm/min. All tests were done according to ASTM standards adapted from similar tests for concretes with Portland cement binders.

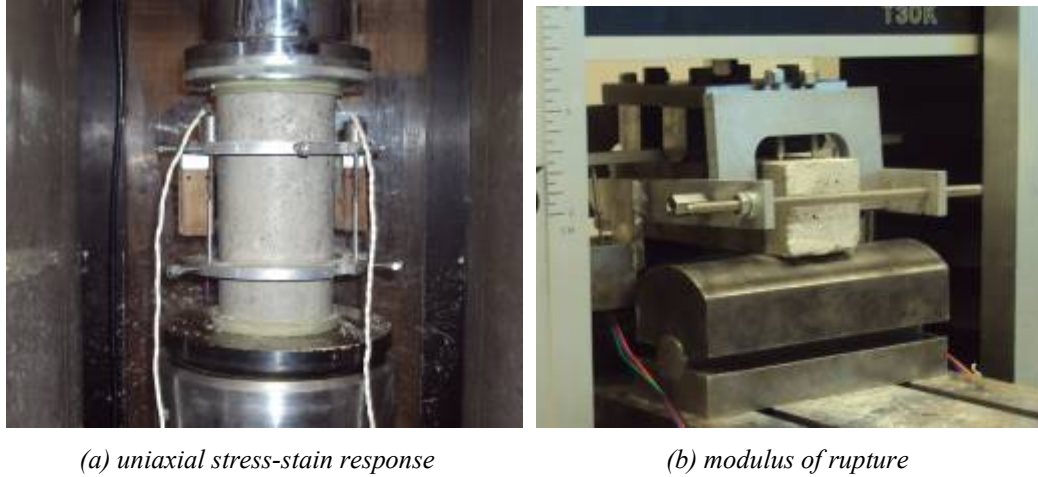


Figure 5.4- Test set-up for material characterization

5.2.1.4 Results

Among parameters affecting the properties of LECA concrete and sand concrete, the influence on strength from the weight percentage of sand and LECA were studied. The compressive strengths of cubes at 7 days are shown in Figure 5.5a for LECA concrete with different binder to LECA weight ratios. It was observed that the strength of LECA concrete reduces as the binder to LECA mass ratio increases. A *b*:FL:CL ratio of 1:0.14:0.40 produced concrete with good strength and workability and was selected for further work in this study under designation LC. The density of LC measured at 7 days was typically 1730 kg/m³.

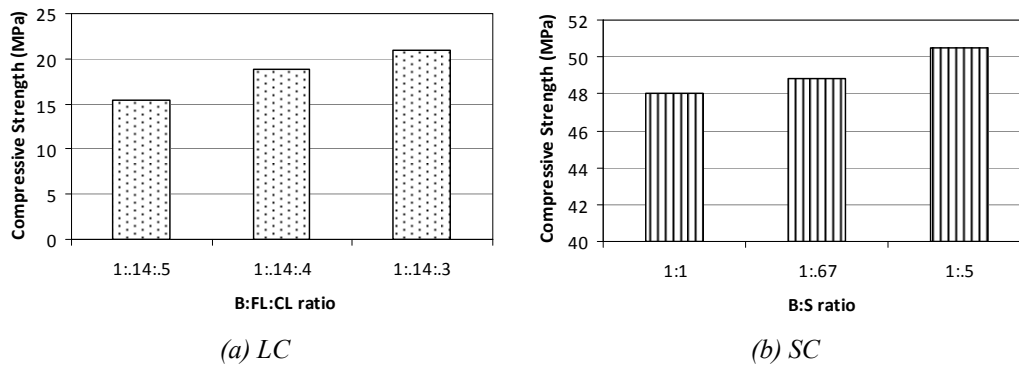


Figure 5.5- 7 days compressive strength

It is observed in Figure 5.5b that the strength of sand concrete reduced as the weight fraction of sand increased. Considering workability for the intended

application, the sand concrete with b/S ratio of 1:0.67 was selected and denoted as SC. The measured density was 2090 kg/m^3 .

The variation of compressive strength was studied for several ages up to 28 days as shown in Figure 5.6. It is observed that both LC and SC have rapid strength gain in the first 3 days, but relatively less strength gain (<15%) between 7 and 28 days. This behaviour is consistent with prior research on $\text{MgO}+\text{KH}_2\text{PO}_4$ binders and is in agreement with the desired properties for the targeted application. In this study, all other testing was completed at 7 days.

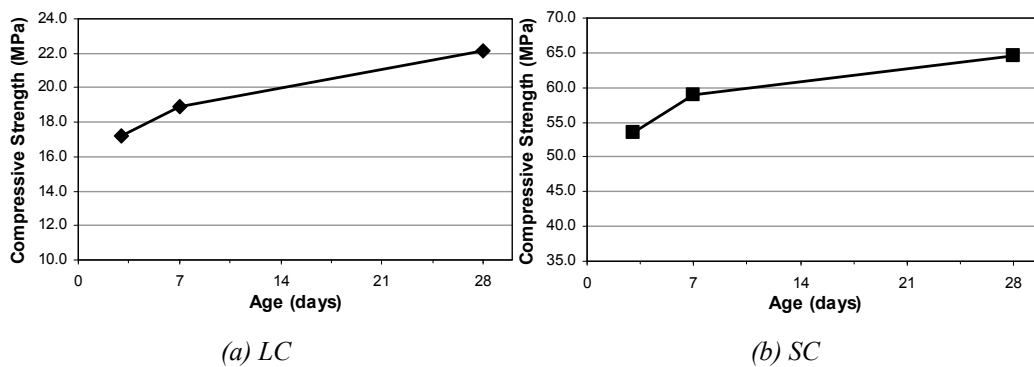


Figure 5.6- Compressive strength development

The typical uniaxial compressive stress-strain response of the LC and SC cylinders at 7 days are presented in Figure 5.7. It can be seen that the stress-strain response of both concretes show only minor non-linearity up to the peak stress. This contrasts with the stress-strain response of concretes containing ordinary Portland cement binders and traditional aggregates where a parabolic stress-strain relationship is typical for similar concrete strengths. The post-peak response of LC and SC showed more brittle behaviour than traditional concretes. The Modulus of Elasticity of LC and SC were obtained according to ASTM C469-02 as 10.63 GPa and 21.49 GPa respectively.

Modulus of Rupture (MOR) was measured on 50x50 mm cross-section prisms at the age of 7 days. The average MOR was 2.2 MPa and 3.2 MPa for LC and SC respectively, corresponding to 12.5 and 6.4% of the corresponding compressive strength values.

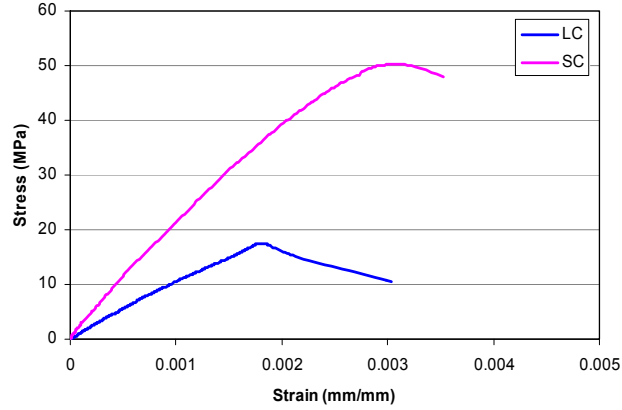
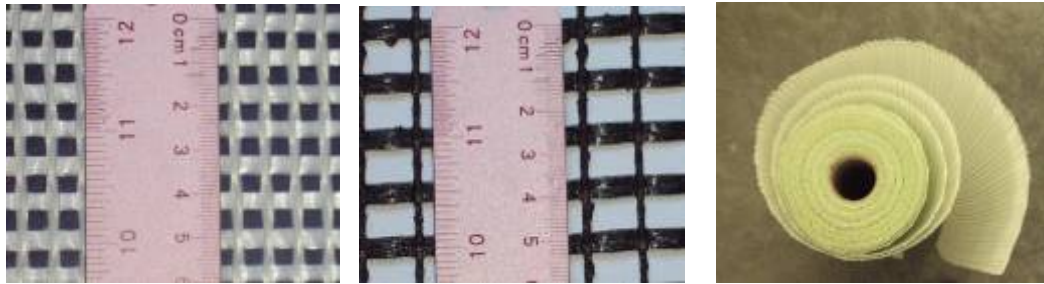


Figure 5.7- Stress-strain responses

5.2.2 Fabric Reinforcement

Two different commercially available fibreglass textile fabric reinforcements were trialled. These textiles differed by fabrication process, mesh spacing and fiber coating as shown in Figure 5.8. Both fabrics are flexible and could be provided in a roll, consistent with the desired installation procedures in the target application. The manufacturer provided the fabric properties summarized in Table 5.2.



(a) Textile type 1

(a) Textile type 2

(c) Textile roll

Figure 5.8- Textile types and orientation

Table 5.2- Textile fabric properties

Textile type	Fiber Spacing (mm)	Breaking strength (kN/m)
1	8.33	200
2	12.5	200

5.3 Panels

5.3.1 Specimen Preparation

Small-scale prototype panel specimens were prepared for testing under the three-point bending set-up depicted in Figure 5.9a. Full depth panels (Figure 5.9b) were constructed from SC and had nominal thickness of 20, 50 and 75 mm. Prototype partial depth precast panels used a 20 mm SC panel with additional LC and SC layers above to a total nominal thickness of 50 mm (Figure 5.9c).

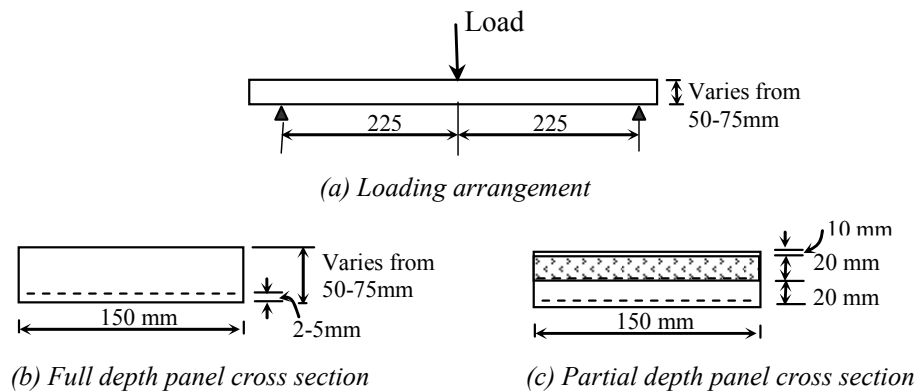


Figure 5.9- Panels cross-sections

Full depth panels

These panels were constructed by placing a thin SC layer in the base of the mold prior to placement of the fabric reinforcement. The fabric reinforcement was gently pressed into the SC and additional SC was used to fill the mold to the required total depths of 20, 50 and 75 mm. Panels with fiber 1 were denoted as FD2_I, FD5_I, FD7_I, and with fiber 2 as FD2_II, FD5_II, FD7_II.

Partial depth precast panels

These panels represent precast stay in place formwork topped with cast-in place concrete. Precast panels of nominal 20 mm depth from SC and containing 1 fabric layer were prepared and put in the molds. Then a 20 mm LC layer was placed followed by a 10 mm SC covering layer. Panels with fiber 1 were denoted as PD1_I and with fiber 2 as PD2_I. For some partial-depth panels, an additional

layer of fabric reinforcement was placed on top of the initial 20 mm SC panel prior to placing the LC layer. Panels in this configuration with fiber 1 were denoted as PD1_II and with fiber 2 as PD2_II.

Table 5.3- Detail of panels

Specimen name	Fabric Type		Width (mm)	Depth (mm)	Span (mm)	Peak Load (kN)	Displacement (mm)
	Type	No of layers					
FD2_I	1	1	150	20	450	0.21	0.79
FD2_II	2	1	150	20	450	0.20	0.86
FD5_I	1	1	150	50	450	1.53	0.27
FD5_II	2	1	150	50	450	1.67	0.28
FD7_I	1	1	150	75	450	4.37	0.39
FD7_II	2	1	150	75	450	4,54	0.33
PD1_I	1	1	150	50	450	1.58	0.21
PD1_II	1	2	150	50	450	1.91	0.33
PD2_I	2	1	150	50	450	1.67	0.21
PD2_II	2	2	150	50	450	2.25	0.24

5.3.2 Test Procedure and Test Set-up

All panel specimens were tested at 7 days using a three-point bending configuration at a loading rate of 0.10 mm/min in a 30 kN capacity universal testing machine. The loading arrangement and test set up are shown in Figures 5.9 and 5.10. During the tests, the vertical deflection of panels at center was measured using two LVDTs, with the average value reported herein.



Figure 5.10- Flexural test setup

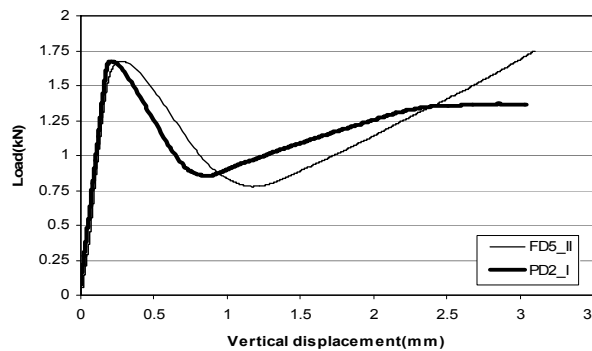


Figure 5.11- Load deflection response

5.3.3 Results and Ongoing Work

The load deflection behaviours of two typical panels are shown in Figure 5.11. All other panels load deflection curves are provided in Appendix A.4. It is observed that a significant drop in load occurs after the first flexural crack forms in the high bending moment region of the specimens. This drop indicates that the fabrics selected in these pilot tests have insufficient stiffness to maintain the desired performance after first cracking. Ongoing work with larger-scale specimens is attempting to better optimize the fabric for this system to improve the post-cracking strength and stiffness. Nevertheless, the results indicate that the structural system provided acceptable post-cracking deformation capacity.

The peak load (at cracking) and the corresponding vertical displacement for each panel are presented in Table 5.3. It can be seen from Table 5.3 that the peak load increases as the thickness of the panels increase, and panels with fiber type 2 carry higher load than similar panels with fiber type 1. The test result also show that the full-depth panels have higher post-peak load carrying capacity than partial depth precast panels of similar thickness. Ongoing work is developing analytical models, which will relate the measured performance of the panels to the measured material properties.

5.4 Conclusions

The following conclusions can be drawn from this study:

- Ceramic composites using magnesium-phosphate binders were produced that exhibit good workability and the desired mechanical properties of rapid strength gain, high compressive strength and high stiffness desired for structural infill slab applications.
- The peak load of the textile reinforced ceramic composite panels was dependent on the depth of concrete, the number of layers of reinforcement and the type of construction.

- Post peak behaviour was depending on the type of fiber, the stiffness of fiber and the type of construction.

5.5 References

- Bank, L. C., Malla, A. P., Oliva, M. G., Russell, J. S., Bentur, A. and Shapira, A. (2009). A model specification for fiber reinforced non-participating permanent formwork panels for concrete bridge deck construction. *Construction and Building Materials*, 23: 2664–2677
- Bosche, A., Jesse, F., Ortlepp, R., Weiland, S. and Curbach, M. (2008). Textile-Reinforced Concrete for Flexural Strength of RC-Structures-Part 1: Structural Behaviour and Design Model. American Concrete Institute, Farmington Hills, MI, ACI SP-251: 19-40.
- Bruckner, A., Ortlepp, R. and Curbach, M. (2006). Textile reinforced concrete for strengthening in bending and shear. *Materials and structures*, 39(8): 741-748.
- Chi, J. M., Huang, R., Yang, C. C. and Chang, J. J. (2003). Effect of aggregate properties on the strength and stiffness of lightweight concrete. *Cement and Concrete Composites*, 25(2): 197-205.
- Ding, Z. and Li, Z. (2005a). High-early-strength magnesium phosphate cement with fly ash. *ACI Material Journal*, 102(6): 357-381.
- Ding, Z. and Li, Z. (2005b). Effect of aggregate and water content on the properties of magnesium phospho-silicate cement. *Cement and Concrete Composites*, 27(1): 11-18.
- Ke, Y., Beaucour, A. L., Ortola, S., Dumontent, H. and Cabrillac, R. (2009). Influence of volume fraction and characteristics of lightweight aggregates on the mechanical properties of concrete. *Construction and Building Materials*, 23(8): 2821-2828.
- Wagh, A. S. (2004). Chemically bonded phosphate ceramics: Twenty-first century material with diverse application. Elsevier Ltd., Amsterdam, 157-165.

Mechanical Properties of Glass Fiber Reinforced Ceramic Concrete⁴

6.1 Introduction

Concretes widely used as general construction materials typically use Portland cement as the binder in combination with well-graded aggregates. However, it is well known that production and use of Portland cement has high environmental impacts from greenhouse gas emissions and overall energy usage. Combined, it has been estimated that Portland cement concrete is responsible for approximately 7% of worldwide greenhouse gas emissions from the calcination process of the raw materials with over 1 tonne of carbon dioxide (CO₂) emitted for each tonne of Portland cement produced (Li and Liang, 2011). While broader use of supplementary cementing materials such as fly ash and slag have allowed partial replacement of Portland cement to reduce the corresponding environmental impacts of some concrete types, there is strong need for an alternative binder to replace Portland cement that will enable cost-effective concretes with superior properties and reduced environmental impacts.

⁴ Contents of this chapter have been published. Reference: S. T. Tassew and A. S. Lubell, "Mechanical properties of glass fiber reinforced ceramic concrete". *Construction and Building Materials Journal*, Vol. 51(31), 2014, 215-224.

Phosphate-based cements have gained attention in recent years as potential alternative binders to Portland cement. The environmental impacts and energy usage to process the raw materials are lower than for Portland cement (Wagh, 2004). As a binder, superior properties result from the type of inter-molecular bonding formed within the hardened phosphate cements. Phosphate cement binders have either ionic or covalent bonds, while the hydration products formed in traditional Portland cement binders have comparatively weaker bonds relying on van der Waals forces (Wagh, 2004). Compared to Portland cement binders, the phosphate cement binders can be formulated to achieve rapid setting times with higher early age strength gains, while at the same time having good dimensional stability and long-term durability in aggressive environments (Wagh, 2004). Further, the properties of some phosphate cement binders, including the binder used in this study, are enhanced at the material-scale by inclusion of a large volume fraction of fly ash (Wagh et al., 1997; Ding and Li, 2005a), itself an industrial waste by-product.

The properties of sand mortars using magnesium potassium phosphate binders have been investigated previously by several research groups (Ding and Li, 2005a; Ding and Li, 2005b; Qiao et al., 2010; Tassew and Lubell, Chapters 3 and 4). The ceramic sand mortars produced in Chapter 3 exhibited a compressive strength of 25.0 to 65.0 MPa at 28 day and modulus of rupture varied between 5.0% and 7.0% of the corresponding compressive strength. Recently, studies by the Tassew and Lubell (Chapter 4) have shown that different lightweight fine or coarse aggregates types can also be used with this binder system, to produce so-called lightweight ceramic concretes (Tassew and Lubell, 2012). The ceramic concretes produced in this prior work exhibited 28-day compressive strengths from 17 to 36 MPa for densities of 1600 to 1870 kg/m³ respectively. The strengths and densities were influenced by the water to binder ratio and the aggregate type. The modulus of rupture for prisms under 4-point bending varied between 4.5% and 8.0% of the corresponding compressive strength, which is lower than typical values obtained for Portland cement concretes. For both sand ceramic mortar and the lightweight ceramic concretes, there is potential concern

that the post-peak tensile response, when applied to concrete structures at the member-scale, may be too brittle with insufficient material ductility for some applications (Tassew and Lubell, 2010).

The addition of discrete fiber reinforcement to a concrete matrix leads to an increased flexural strength, post-cracking capacity, impact resistance and energy absorption capacity (e.g., Bentur and Mindess, 1990; Balaguru and Shah, 1992; Naaman, 2003). Commercially available short fibers are available from different materials, including steel, glass and carbon. The selection of fiber material, its geometry and properties should be appropriate for the intended application and ensure chemical compatibility with the binder. Glass fibers are relatively inexpensive, lightweight and have high tensile strength. Studies have shown that the addition of short glass fibers to concrete can control shrinkage cracking (Barluenga and Hernandez-Olivares, 2007; Mirza and Soroushiann, 2002), improve the flexural and tensile strengths (Mirza and Soroushiann, 2002; Ali et al., 1975) and also increase the post-peak ductility in compression (Fanella and Naaman, 1985). Although several studies have been carried out on the use of glass fibers in Portland cement concrete, little research has been done on the use of glass fibers in concrete made with magnesium potassium phosphate cement binders. It is noted that the matrix-to-fiber bond and the underlying matrix mechanical properties are different between the concretes made with these two binder types. Thus, a laboratory study was initiated to enhance the quantitative understanding of glass-fiber reinforced ceramic concretes (GFRCC).

This study focused on the enhancement of the mechanical properties of ceramic concretes produced with magnesium potassium phosphate binders through incorporation of chopped glass fibers. Mixes were studied that included either lightweight expanded clay aggregates (LECA) or sand aggregates. The main objective of the study was to investigate the influence of fiber content and fiber length on the compression, flexural tension and direct shear properties of GFRCC. Design implications related to differences in the mechanical properties of GFRCC

compared to conventional concretes made with Portland cement binders are discussed.

6.2 Experimental Program

6.2.1 Materials and Mix Design

The ceramic concretes used in this study included a binder based on the magnesium potassium phosphate cement (MPPC) developed by Wagh et al. (Wagh et al., 1997; Wagh and Jeong, 1998). According to Wagh et al., a so-called acid/base reaction occurs between calcined magnesium oxide (MgO) and monopotassium phosphate (KH₂PO₄) in an aqueous solution as:



Fly Ash obtained from coal-fired thermal power stations can be introduced into the binder. It has been shown by Wagh and others that the Fly Ash will enhance the properties of the hardened binder (Ding and Li, 2005*b*; Tassew and Lubell, 2012). The Fly Ash particles are believed to act as gap fillers, but the chemical composition of Fly Ash enables it to also to react chemically with the magnesium phosphate binder components (Ding and Li, 2005*b*). The chemical composition of Fly Ash is given in Table 6.1. It is noted that the chemical composition of Fly Ash will vary based on the source and this will typically be more variable than the relatively pure MgO and KH₂PO₄ compounds. Thus, this study used the same Fly Ash sources and dosages as previous work (Tassew and Lubell, 2012) to allow for more direct comparisons without need to directly evaluate the chemical compositions.

Table 6.1- Chemical composition of Fly Ash

Fly Ash Type	Mass fraction of the sample (%)						
	MgO	CaO	S ₁ O ₂	Fe ₂ O ₃	Al ₂ O ₃	SO ₃	Na ₂ O
Class C	1.22	10.97	55.53	3.62	23.24	0.24	2.83

Calcined magnesium oxide (MgO) was utilized in this study. The manufacturer's specifications indicated that it was 97% MgO by weight, with a specific surface area of 0.3 m²/g and a minimum 95% of particles passing the 200 mesh size. Fertilizer grade monopotassium phosphate (KH₂PO₄) was obtained from a local farm supply warehouse. Based on the controlled manufacturing process of this fertilizer type, it has negligible impurities but no direct chemical analysis was completed. The KH₂PO₄ was combined with the MgO according to the molar ratios in Equation 6.1. Based on the mixes reported in Tassew and Lubell (2012) with desirable characteristics of strength and workability, Class C Fly Ash (FA) was used at a mass dosage of 50% of the total binder mass, *b*. Thus, the dry ingredients of the binder were prepared at the mass ratio of MgO:KH₂PO₄:FA = 1:3.4:4.4.

Two different ceramic concrete types were developed in this study, classified by the aggregate type. Mix Type L contained lightweight expanded clay aggregate (LECA). Mix Type S contained well-graded sand. For Type L concrete, LECA in fine and coarse size gradations were used with maximum particle sizes of 2.5 (i.e. FL) and 10 mm (i.e. CL), respectively. See Figure 6.1. The specific gravity and water absorption were evaluated according to ASTM C128 (2007) and ASTM C127 (2007), as 0.995 and 24.4% for the CL LECA and 1.49 and 10.25% for the FL LECA, respectively, Sand aggregates (SA) having maximum size of 1.25 mm and with a specific gravity of 2.65 was used in Type S mixes (Figure 6.1).

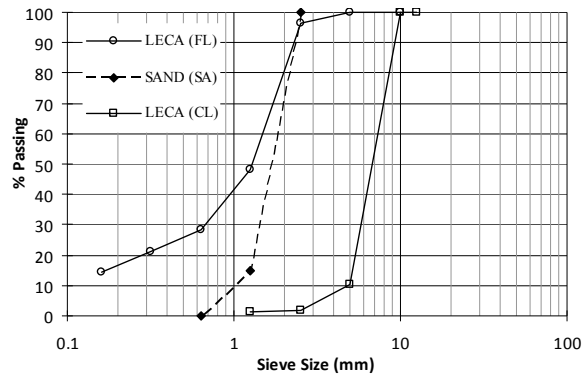


Figure 6.1- Particle size distribution of aggregates

Municipal tap water was used as the mixing water. The water to binder mass ratio (w/b) was fixed at 0.20 based on an earlier phase of the overall study (Tassew and Lubell, 2012). The $w/b=0.20$ ratio provided high compressive strengths for a given mix composition while also resulting in acceptable workability as measured by the ASTM C230 flow test.

To control the setting time to a practical range of about 90 to 120 minutes, a commercially available lignosulphonate admixture was used in all mixes. The dosage used was 1.5% by mass of the binder, established from the earlier investigation (Tassew and Lubell, 2012).

Chopped glass fibers were added to most mixes. The fibers were supplied as chopped strands that were made as of filament bundles designed to resist breaking down to individual filaments during the mixing operation (see Figure 6.2). The manufacturer's specifications indicated that the diameter of the individual glass fibers was $18\mu\text{m}$ and the specific gravity was 2.7. The fibers had tensile strength and modulus of elasticity of 2000 MPa and 76 GPa, respectively. The fiber volume fraction (V_f) was systematically varied between 0 and 2% of the total mix volume to allow direct study of its influence on the ceramic concrete properties. Two different nominal fiber lengths (13 mm and 19 mm) were also examined through use of companion mixes (Figure 6.2).

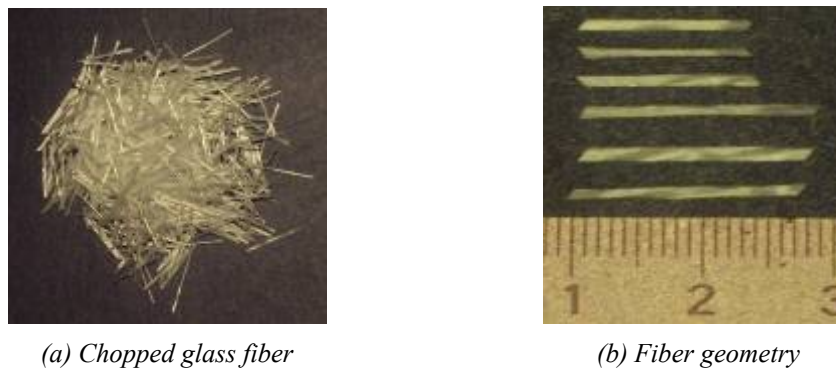


Figure 6.2- Glass fiber and geometry

6.2.2 Mixing Procedures and Specimen Preparation

Two groups of mixes were prepared, classified by the aggregate type: Mix Type L and Mix Type S contained LECA and sand aggregates, respectively. Within each group, mix series were defined based on the mix proportions. See Table 6.2.

Table 6.2- Mix proportion of ceramic concretes

Mix Type	Series	L_f^a (mm)	Materials mass ratio					Volume
			b ^a	FL ^a	CL ^a	SA ^a	w ^a	V_f^a (%)
L	LL0	-	1	0.14	0.40	-	0.20	0
	LL11/LL12/LL13	13	1	0.14	0.40	-	0.20	1.0/1.5/2.0
	LL21/LL22/LL23	19	1	0.14	0.40	-	0.20	1.0/1.5/2.0
S	S0	-	1	-	-	0.67	0.20	0
	S11/S12/S13	13	1	-	-	0.67	0.20	1.0/1.5/2.0
	S21/S22/S23	19	1	-	-	0.67	0.20	1.0/1.5/2.0

^a L_f : Nominal length of fiber; b: binder taken as MgO+KH₂PO₄+FA; FL: fine LECA; CL: coarse LECA; SA: sand aggregate; w: mixing water; V_f : volume fraction of fibers

Each batch was prepared by dry-mixing the MgO, KH₂PO₄ and FA for 5 minutes using a 20 l capacity portable mixer at 60 revolutions per minute. The aggregates were gradually added to the turning mixer and the entire batch was mixed for 60 seconds. The LECA was used in a saturated surface dry condition after soaking for at least for 24 hours while the sand was used in a dry condition. The water was combined with the lignosulphonate retarder and then added to the dry ingredients in the turning mixer, with further mixing of the entire batch for 4 to 5 minutes. Finally, the fibers were added and further mixing for 1 minute was performed. It can be noted that the glass fiber bundles were relatively flexible compared to typical steel fibers. The glass fibers were observed to disperse uniformly in the fresh mix. No fiber balling was observed.

After completing the fresh property test for workability, which took about 2 minutes, the mixes were placed into plastic molds using a scoop and consolidated using a vibrating table. Excess material was carefully screeded from the top. The

100×100×100 mm cube molds used for compression tests were filled as a single layer before they were vibrated. Prism molds 50×50×200 mm used for flexure and direct shear test specimens were also filled as single layers. On the other hand, 100Ø×200 mm long cylinder molds were filled in two layers with vibration after each layer.

Due to the rapid setting characteristics and the high early age strength gain of the ceramic concretes produced, the specimens were removed from the molds after 2 hours. All specimens were stored in the ambient lab environment of 23±2° C and a relative humidity of 50±5% until testing. All results presented in this chapter are the average values from three duplicate samples produced from the same batch and tested at the age of 28 days after casting unless noted otherwise.

6.2.3 Test Procedures

The properties of the fresh and hardened GFRCC mixes were determined using test procedures adapted from those used for traditional Portland cement-based concretes. Test methods were selected to allow simple characterization of the workability of fresh mixes and the mechanical properties of hardened mixes under short-term loading conditions. Shrinkage of the mixes was visually observed to be negligible but was not directly measured in this study. However, prior research has shown that magnesium potassium phosphate mortars exhibited better volume stability than Portland cement-based mortars (e.g., Qiao et al., 2010).

6.2.3.1 Workability

To quantify the workability of the fresh GFRCC mixes, a flow table test according to ASTM C230 (2008) was used. A brass frustum mold was used on a steel surface. The 50 mm high mold had inside dimensions of 70 mm diameter at the top and 100 mm at the bottom. Within 1 minute after the mixing operation was stopped, the mold was filled with a sample of the mix in two layers, each compacted using 20 blows with a tamper with pressure just sufficient to ensure uniform filling of the mold. After lifting the mold the average diameter of the base of the GFRCC sample was quickly obtained using calipers. The flow table

was then dropped 25 times in 15 seconds and the average diameter of the final ceramic concrete sample was measured according to ASTM C1437 (2007). The ratio of the difference in final and initial diameters to the initial diameter, expressed as a percentage, is herein termed the Flow. Higher values of Flow are obtained as the workability of the mix increases.

6.2.3.2 Compressive Strength

The compressive strength of concrete made with Portland cement is commonly determined either by using cylinder specimens (e.g., North America) or using cube specimens in other parts of the world (e.g., Europe) (e.g., Neville, 1996). The compressive strengths of the mixes in this study were determined using both cube and cylindrical specimens. This allowed direct comparison of the influence of specimen shape on the obtained properties, which is influenced in part by end restraint of the specimen from the loading platens (Neville, 1996).

The compressive strengths of 100×100×100 mm cube specimens, f_{cu} , were determined using a stiff MTS test frame with capacity of 2600 kN. The loading rate was set to a machine stroke of 1.25 mm/min. See Figure 6.3(a). The equivalent stress rate on the cube samples ranged from 0.10 to 0.30 MPa/s.



(a) *Cube specimens*



(b) *Cylinder specimens*

Figure 6.3- *Compressive test configurations*

Compressive testing of 100 mm diameter \times 200 mm long cylinders was conducted in accordance with ASTM C469 (2002) using the same MTS frame. See Figure 6.3(b). In addition to the peak strength, f_c' , these tests also allowed direct investigation of the uniaxial stress-strain response and the modulus of elasticity of the GFRCC. Axial deformations were measured using a yoke with three LVDTs arranged at 120° separation about the longitudinal axis and operating over an initial gauge length of 100 mm. The loading rate was set to a machine stroke of 1.25 mm/min. The equivalent stress rate on the cylinder samples ranged from 0.10 to 0.30 MPa/s. Cylinders were sulphur capped before testing as per ASTM C617 (2010).

6.2.3.3 Flexure Test

The flexural response of 50 \times 50 \times 200 mm notched prisms under 4-point bending was determined in accordance with ASTM C1609 (2007). A 10 mm deep notch was sawn at mid-span of the bottom face of each specimen. The measured reduced cross-sectional dimensions were used for all analysis reported in this chapter. Specimens were loaded under a displacement-controlled protocol at a rate of 0.1 mm/min in a universal testing machine with 30 kN capacity. A yoke was used to measure the mid-span deflection relative to the supports as the average measurement from two LVDTs as shown in Figure 6.4(a).

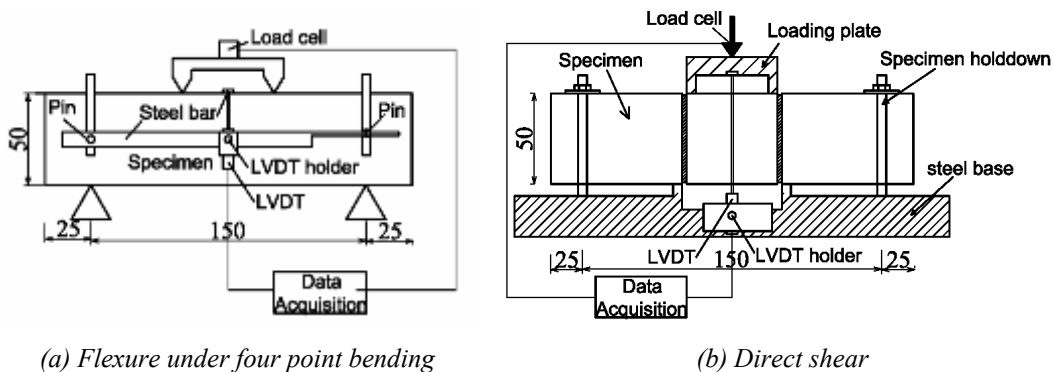


Figure 6.4- Test set-up for prisms

6.2.3.4 Direct Shear Test

Prism samples 50×50×200 mm were used to study the direct shear strength using a test method adapted from JSCE-SF6 (1990). The test arrangement is shown in Figure 6.4(b), whereby the upper loading plate causes vertical motion of the central region of the test specimen relative to the clamped end portions. To control the location of the shear planes, 10 mm deep saw cut notches were introduced around the full perimeter of the prism at each shear plane, similar to Mirsayah and Banthia (2002). The measured reduced cross-section dimensions were used for analysis in this chapter. Tests were conducted in a universal testing machine with capacity of 30 kN at a deformation rate of 0.1 mm/min. Displacement of the loading apparatus was measured using two LVDTs acting against the top loading plate.

6.3 Results and Discussion

6.4.1 Fresh Properties of GFRCC

The results from the flow tests provided a relative measure of workability of the GFRCCs. The average Flow for the ceramic concretes with different fiber-volume fractions is shown in Figure 6.5. It can be observed that the addition of fibers in the ceramic concrete reduced the Flow compared to mixes without fibers regardless of the mix type or fiber lengths. Regression curves to the data shown in Figure 6.5 suggest that the Flow linearly decreased with the V_f content. The flow reduced by more than 75% and 45% for mix Types L and S respectively when the V_f content was raised from 0 to 2%. The greater influence of increasing V_f on the workability of mix Type L compared to mix Type S was attributed to the larger aggregate sizes in mix Type L. On the other hand, negligible difference in Flow was observed between the two different fiber lengths within each mix type. Overall, these results suggest the aggregate size will influence the maximum glass fibre dosage that can be used for a specified workability criterion.

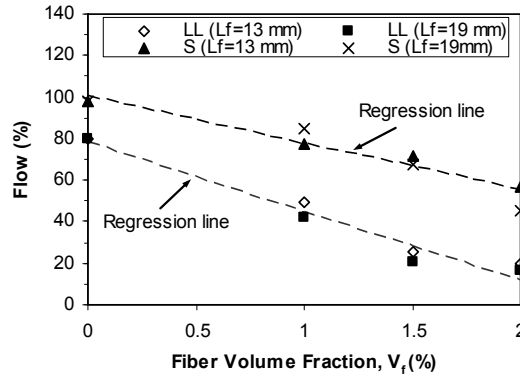


Figure 6.5- Influence of fiber volume fraction on flow

6.4.2 Hardened Properties of GFRCC

6.4.2.1 Density

The density of each specimen at 28 days was determined from the measured air-dry mass of the specimens and the corresponding specimen volume. The relationship between the fiber content and the ceramic concrete density is shown in Figure 6.6. As expected, the glass fiber dosage had a negligible influence on the hardened density of GFRCC. The average density of mix Type L ceramic concrete ranged between 1790 kg/m^3 and 1820 kg/m^3 for V_f fractions between 0% and 2%. Mix Type S had densities between 2150 kg/m^3 and 2200 kg/m^3 .

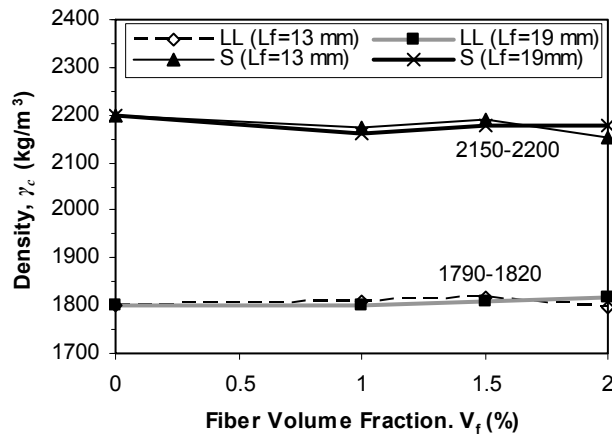


Figure 6.6- Influence of fiber volume fraction on density

6.4.2.2 Compression

6.4.2.2.1 Cube Compression Strength

The stress-displacement characteristics of the GFRCC cubes in compression were similar for all mixes, but variations related to fiber content and aggregate type were observed. Representative stress-displacement curves for ceramic concrete containing 13 mm long fibers are provided as Figure 6.7. Key data recorded for each mix type is summarized in Table 6.3. The stress-displacement response of each mix is characterized by a nearly linear ascending branch, irrespective of the mix type. The fibers had minimal influence on the slope of the ascending branch but influenced the peak stress. An increase in the V_f fraction from 0 to 2% increased the peak stress by 19% and 13% for mix Types L and S, respectively. See Table 6.3. For mix Type L, the peak cube compressive strength (f_{cu}) varied from 21.7 to 26.9 MPa depending on the fiber content whereas f_{cu} for mix Type S ranged from 50.4 to 58.6 MPa. The lower strengths for mix Type L was attributed to the lower aggregate strength and larger maximum aggregate size, both known to influence the strength of concretes made with Portland cement binders (e.g., Mehta, 1986).

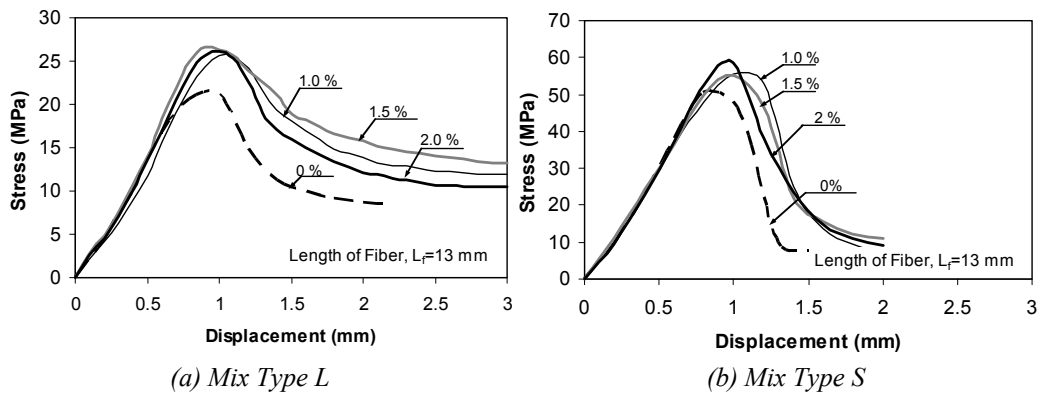


Figure 6.7- Influence of fiber volume fraction on compressive stress to displacement relationship of cube samples

6.4.2.2.2 Cylinder Compression Response

Compressive stress-strain response curves were obtained from uniaxial cylinder tests at 28 days. Representative curves for ceramic concrete with 13 mm fiber length are provided in Figure 6.8. Curves for 19 mm fiber lengths were similar.

The stress-strain response of each mix is characterized by a nearly linear ascending branch. It can be observed from Figure 6.8 that the fibers had negligible influence on the initial stiffness whereas the beneficial effects from the fibers are clearly seen in the post-peak branch, similar to the stress-strain curves of fiber reinforced concretes with Portland cement binders (e.g., Fanella and Naaman, 1985; Ezeldin and Balaguru, 1992).

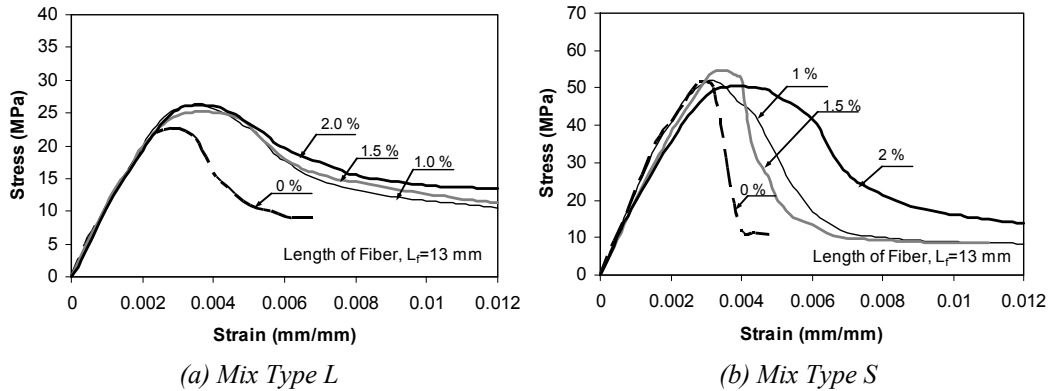


Figure 6.8- Influence of fiber volume fraction on compressive stress-strain relation

The maximum cylinder compressive strengths f_c' and the corresponding strains (ϵ_{co}) are summarized in Table 6.3 for the different GFRCC mixes. It is observed that f_c' increased as the fiber volume fraction increased with an improvement by 14% between V_f fractions of 0 to 2% for mix Type L. However, for the Type S matrix a marginal reduction of the compressive strength by 6% was observed as V_f increased from 0 to 2%. See Figure 6.8(b). For Type L and S ceramic concretes the compressive strengths varied from 22.8 to 26.2 MPa and from 47.3 to 54.8 MPa, respectively, for the various fiber volume fractions.

For plain ceramic concretes a negligible difference in compressive strengths ($\leq 5\%$) was observed between cube and cylinder samples made from the same mix type. However, addition of fibers to the mixes resulted in an increase in the cube-strength to cylinder-strength ratio, f_{cu}/f_c' . One possible reason for this change could be from the use of single layer casting for the cubes but use of two layers for casting of the cylinders. The flexible nature of the glass fibers may have prevented a uniform distribution of fibers near the layer boundary in the cylinders.

The f_{cu}/f_c' ratios for Mix Type L and S ceramic concrete varied from 1.0-1.06 and from 1.0-1.17, respectively. Prior research has shown that the f_{cu}/f_c' ratio for PC concrete can be up to 1.25, but prior research also indicated that there is no simple relationship between the strengths of specimens prepared in two shapes have (Neville, 1996). Nevertheless, the current research in comparing f_{cu} and f_c' for GFRCC can serve as a useful guide.

For the cylinder specimens, a linear increase in the strain ϵ_{co} values at peak-stress was observed as the fiber volume-fraction increased (see Table 6.3). A longer apparent plateau in the stress-strain response at the peak compressive strength level was also observed (Figure 6.8), with the length of the plateau increased as V_f increased. These trends were attributed to the increased quantity of fibers available to arrest cracks as V_f increases. These trends also suggest that, if appropriately designed to exploit the peak strength behaviours, high member ductility could be achieved for higher V_f magnitudes.

Table 6.3- Summary of test results

Mix Type	L_f (mm)	V_f (%)	f_{cu} (MPa)	f_c' (MPa)	ϵ_{co} (mm/mm)	f_r (MPa)	δ_r (mm)	f_t (MPa)	δ_t (mm)	E (GPa)	I_{tc}
L	-	0	21.7	22.8	0.0028	1.1	0.03	1.7	0.23	10.3	-
	13	1.0	25.6	26.2	0.0034	3.8	0.20	3.9	0.31	10.9	5.44
	13	1.5	26.7	25.2	0.0036	4.9	0.30	4.0	0.36	10.8	5.63
	13	2.0	26.2	26.2	0.0036	7.6	0.25	4.2	0.55	10.7	6.07
	19	1.0	26.9	25.4	0.0032	3.0	0.15	3.6	0.70	10.4	5.24
	19	1.5	26.1	24.9	0.0034	5.0	0.25	4.9	0.40	10.8	5.14
	19	2.0	25.6	25.7	0.0036	7.3	0.30	5.1	0.39	10.9	5.78
S	-	0	50.4	51.9	0.0030	2.1	0.03	2.8	0.30	22.3	-
	13	1.0	55.6	52.0	0.0032	5.4	0.20	6.0	0.30	21.9	3.01
	13	1.5	55.2	54.8	0.0036	9.0	0.23	6.5	0.34	19.7	2.79
	13	2.0	58.6	50.4	0.0040	10.1	0.38	7.1	0.50	19.4	4.04
	19	1.0	53.0	50.7	0.0030	7.6	0.35	4.1	0.29	21.5	2.95
	19	1.5	50.4	51.7	0.0040	9.7	0.30	6.9	0.30	19.9	3.30
	19	2.0	55.7	47.3	0.0034	10.8	0.33	7.1	0.20	19.2	3.50

The modulus of elasticity E_c of GFRCC cylinders were determined as per ASTM C469 (2002) and the results are summarized in Table 6.3. Mix Types L and S exhibited modulus of elasticity values between 10.3 and 10.9 GPa and between 19.2 and 22.3 GPa, respectively. Thus, E_c was strongly influenced by the aggregate type as seen previously in a study of magnesium potassium phosphate mixes with different lightweight aggregate types (Tassew and Lubell, 2012). However, the fiber length L_f and volume fraction V_f both had negligible influence on E_c .

ACI 318 (2008) presented a formula $E_c=3525\sqrt{f_c'}$ to relate modulus of elasticity of lightweight concrete to its compressive strength. This model results in prediction of E_c that are significantly higher than the test data obtained in the current study. Therefore, modifications of this equation are proposed to better represent the test data for the two mix types as follows:

$$E_c = 2100\sqrt{f_c'} \quad \text{Mix Type L} \quad (6.2)$$

$$E_c = 2800\sqrt{f_c'} \quad \text{Mix Type S} \quad (6.3)$$

The mean value for the coefficient of $\sqrt{f_c'}$ in Equation 6.2 and Equation 6.3 is 2130 (CV=2.0%) and 2830 (CV=6.2%), respectively.

Compression Toughness Index (I_{tc})

Toughness is a measure of the ability of a material to absorb energy prior to failure. Toughness can be determined from the area under the cylinder stress-strain curve (Balaguru and Shah, 1992). The relative ductility of fiber reinforced cementitious composites can be established by a toughness index, I_{tc} , which other researchers (e.g., Fanella and Naaman, 1985) have defined as the ratio between the compression toughness of the fiber reinforced matrix to that of the plain matrix up to a certain defined strain limit. In this study, the I_{tc} is determined as the ratio of toughness of GFRCC to a strain of 0.015 mm/mm to the toughness of a similar mix with $V_f=0\%$ up to a strain of ϵ_{co} . The I_{tc} results are given in Table 6.3

and the relationship between V_f and I_{tc} is summarized in Figure 6.9 for different values of L_f . The I_{tc} was observed to increase as V_f increased, regardless of the aggregates type or L_f . The I_{tc} of mix Types L and S ranged between 5.1 and 6.1, and between 2.9 and 4.1, respectively. For both mix types, L_f had minimal influence on I_{tc} suggesting that fiber fracture probably controlled the capacity mechanism rather than fiber pullout, a similar controlling mechanism that has been reported for glass fiber reinforced Portland cement mortars (Fanella and Naaman, 1985). Considering the average values of compression toughness index for the two fiber lengths and regression analysis ($R^2= 0.81$ for both equations) the following equations were obtained to relate I_{tc} with V_f :

$$I_{tc} = 59.0V_f + 4.67 \quad \text{Mix Type L} \quad (6.4)$$

$$I_{tc} = 79.0V_f + 2.10 \quad \text{Mix Type S} \quad (6.5)$$

Note that Equations 6.4 and 6.5 are valid only for mix types with fibers.

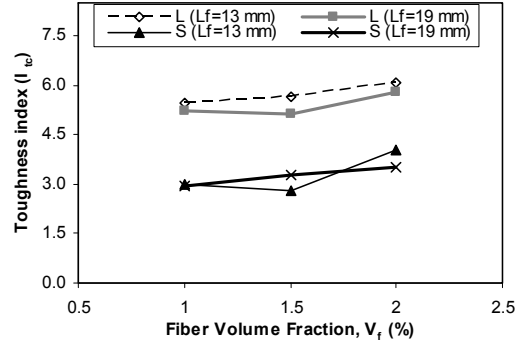


Figure 6.9- Relationship between compression toughness index and fiber volume fraction

6.4.2.3 Flexure

The average load-deflection response under four-point bending up to a mid-span deflection of span/150 is shown in Figure 6.10 for $L_f=13$ mm. The addition of fibers had negligible influence on the initial stiffness of the response, but resulted in significantly higher peak loads as the fiber dosage increased, irrespective of the aggregates type. The deflections at the peak load for mix Types L and S with

fibers ranged from 0.20 to 0.30 mm and from 0.20 to 0.40 mm, respectively, with larger deflections occurring as V_f increased. Further, the post-peak response region of the load-displacement curve (Figure 6.10) exhibited similar slopes, irrespective of the mix type. This behavior was attributed to failure modes dominated by fiber fracture. Observation of the fractured surface of samples indicated many fractured fibers but few fiber pullouts. Similar results were observed for mixes with $L_f=19$ mm.

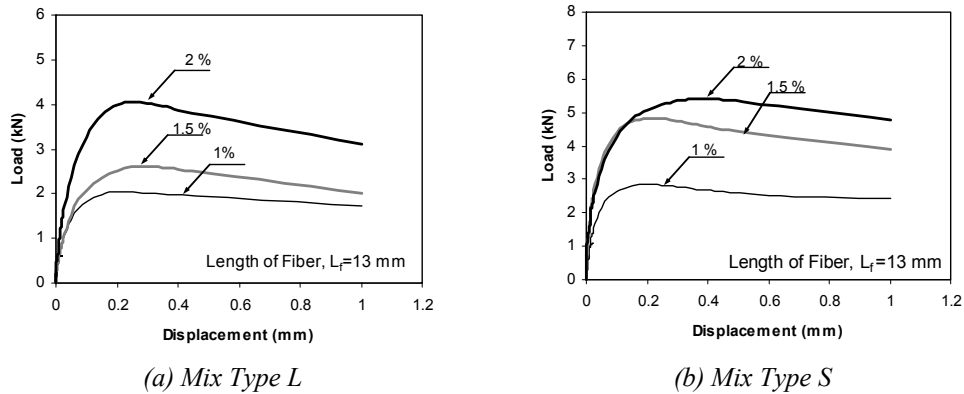


Figure 6.10- Influence of fiber volume fraction on load-displacement under flexure

The peak flexural strength (f_r) of each sample was calculated by using the peak load and modulus of rupture formula according to ASTM 1609 (2007) recommendation. A summary of the average results from replicate specimens is presented in Table 6.3. The flexural strength of Type L and Type S ceramic concrete varied from 1.1 to 7.6 MPa and from 2.1 to 10.8 MPa, respectively, with the flexural strength increasing significantly for higher fiber dosages. In comparison, Wagh (2004) demonstrated that the flexural strength of MPPC binder samples increased significantly when glass fibers were added into the mix. For example, Wagh reported that the flexural strength of MPPC with 60% Fly Ash increased by 89% when 13 mm long glass fibers were added at 3% by weight of the total mix. As these enhancements were lower than in the current study which used concretes containing aggregate rather than just MPPC paste, the results suggest that the influence of the glass fibers on flexural strength cannot be examined independently from the co-existing influence of the aggregates.

For GFRCC, the matrix will crack when the flexural tensile stress reaches the tensile strength of the matrix. After cracking, a so-called deflection hardening behaviour was observed for mixes with fibers (see Figure 6.10), which bridged the cracks. This occurred since the high fiber volume across the crack was sufficient to allow a higher total resistance as the increasing deformation led to increased crack opening (Balaguru and Shah, 1992). However, the fibers bridging capacity will be limited by the pullout or fracture strength of each fiber, causing a reduction in flexural resistance once the deformation and corresponding crack width increase past a certain value. Irrespective of the mix type, the test results (Table 6.3) show that L_f had minimal influence on the peak flexural strength, suggesting that the fiber failure modes were dominated by fracture rather than pullout for both fiber lengths studied.

The peak flexural strength to compressive strength (f_r/f_c') ratio ranged from 4% to 5% for matrices without fibers. These ratios were relatively low, at less than half of the values for a typical Portland cement concretes (e.g., Mehta, 1986). However, when glass fibers were added in to the matrix, the f_r/f_c' ratio increased significantly. The f_r/f_c' ratio for $V_f = 1\%$ was approximately 13% for both mix types. When V_f was increased from 1 to 2%, an increase in the f_r/f_c' ratio was observed from 13 to 29% and from 13 to 21% for mix Type L and S, respectively.

To illustrate the influence of the fiber contribution to the flexural strength, the f_r results were plotted against the product $V_f L_f$ in Figure 6.11. Use of a product $V_f L_f$ was selected to be similar to analysis by other researchers for fiber-reinforced concretes (e.g., Gao et al., 1997). It is observed from Figure 6.11 that f_r increased with increases in $V_f L_f$ irrespective of the mix type, a similar observation as Portland cement based fiber composites (e.g., Gao et al., 1997).

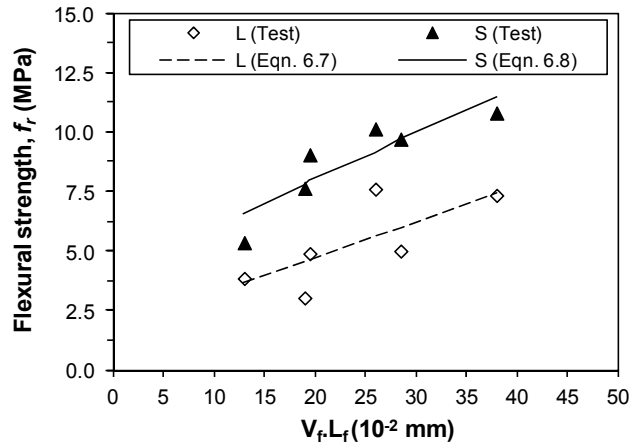


Figure 6.11- Effect of fibers on flexural strength

The rule of mixtures for flexural strength has been applied to fiber reinforced composites in prior studies (e.g., Bentur and Mindess, 1990; Swamy and Mangat 1974). The law states that the composite flexural strength σ_r should account for both the flexural strength of the plain matrix σ_m and a contribution from the fibers (length L_f , diameter d and fiber volume fraction V_f) through the expression:

$$\sigma_r = A\sigma_m(1 - V_f) + BV_f L_f / d \quad (6.6)$$

In Equation 6.6, parameters A and B are constants that are calibrated to the composite type. Using a similar format to Equation 6.6 and by employing regression analysis of the flexural strength test data in this study, the following equations are proposed:

$$f_r = 0.33\sqrt{f'_c}(1 - V_f) + 15.24V_f L_f \quad \text{Mix Type L} \quad (6.7)$$

$$f_r = 0.54\sqrt{f'_c}(1 - V_f) + 20.62V_f L_f \quad \text{Mix Type S} \quad (6.8)$$

Note that $0.33\sqrt{f'_c}$ in Equation 6.7 is the flexural strength of plain lightweight ceramic concrete proposed by the authors in a previous study (Tassew and Lubell,

2012). Equations 6.7 ($R^2= 0.57$) and 6.8 ($R^2= 0.80$) are in good agreement with the flexural strength test data as shown in Figure 6.11 for different $V_f L_f$ values.

Flexural Toughness

ASTM C1609 (2007) defines different flexural toughness parameters that can be calculated using the flexural load-deflection curves. The toughness parameters depend on the maximum deflection considered with parameters defined for deflections corresponding to the peak-stress, or deflections of span/600 or span/150. In this study, the flexural toughness was determined using the area under the load-deflection curve up to a deflection corresponding to the peak-stress f_r and denoted by the parameter $T_{\delta r}$. The influence on $T_{\delta r}$ from the ceramic matrix type, V_f and L_f are all presented in Figure 6.12. Parameter $T_{\delta r}$ increased with the increase in the fiber volume fraction, irrespective of L_f or aggregate type. For example, the flexural toughness $T_{\delta r}$ exhibited 45-fold and 47-fold increases when V_f was raised from 0 to 2% for mix Types L and S, respectively. The increase in $T_{\delta r}$ with V_f was attributed to the greater number of fibers bridging the crack. However, no significant difference in $T_{\delta r}$ was observed among similar mixes differing by L_f . This is explained by fiber failure modes governed by fiber fracture rather than fiber pullout. It can also be seen from Figure 6.12 that mix Type L had lower $T_{\delta r}$ magnitudes compared to Type S, due to a greater proportion of cracks occurring through the lightweight aggregates rather than mainly through the binder.

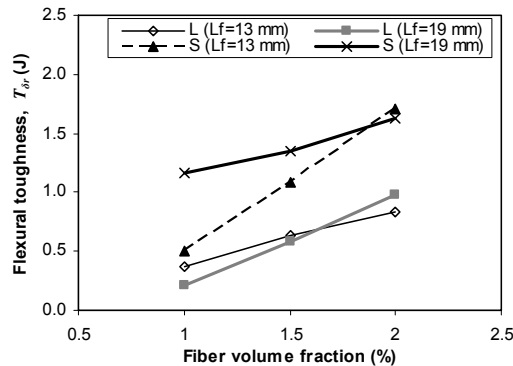


Figure 6.12- Relationship between flexural toughness and fiber volume fraction

6.4.2.4 Direct Shear

Figure 6.13 provides the direct shear load versus displacement curves for mixes with $L_f = 13$ mm. The trends for mixes with $L_f = 19$ mm were similar. A nearly linear pre-peak shear load to displacement relationship with positive slope was observed for all mixes, followed by a nearly linear post-peak relationship of negative slope. There was a small increase in the pre-peak stiffness as the fiber volume fraction increased, but the post-peak stiffness was largely unaffected.

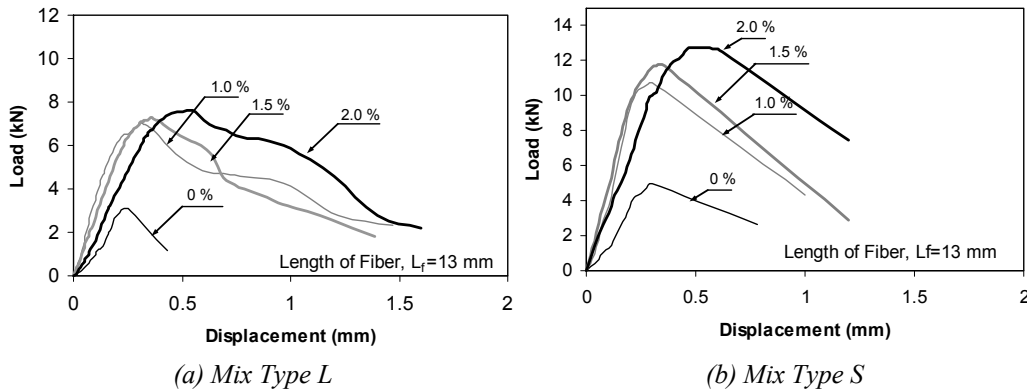


Figure 6.13- Influence of fiber volume fraction on load-displacement under shear

The direct shear strength f_τ was calculated as the total peak force divided by the reduced cross-sectional area of both shear planes in the specimens. The results are summarized in Table 6.3 for mix Types L and S. For both mix types, f_τ increased with the fiber volume fraction. A significant increase occurred as V_f increased from 0% to 1%, but the relative influence of the fibers decreased as V_f was increased further to 1.5% and to 2.0%. For example, the direct shear strength of Mix Type L with $L_f = 13$ mm increased by 40% as V_f increased from 0 to 1% whereas a further increase of only 8% occurred as V_f increased from 1 to 2%. The results in Table 6.3 show that the fiber length had minimal influence on the shear strength, regardless of the mix type, similar finding to the flexural test results. Observation of the failure surfaces of samples revealed fiber fractures rather than fiber pullout.

To illustrate the influence of the fiber contribution on f_τ , the test results for f_τ were plotted against $V_f L_f$ values in Figure 6.14, similar to prior works (e.g., Majdzadh

et al., 2006). It can be seen from Figure 6.14 that f_τ increased with increasing $V_f L_f$, similar to the observations by others for Portland cement fiber reinforced concrete (e.g., Majdzadh et al., 2006). This trend occurred irrespective of the aggregate type.

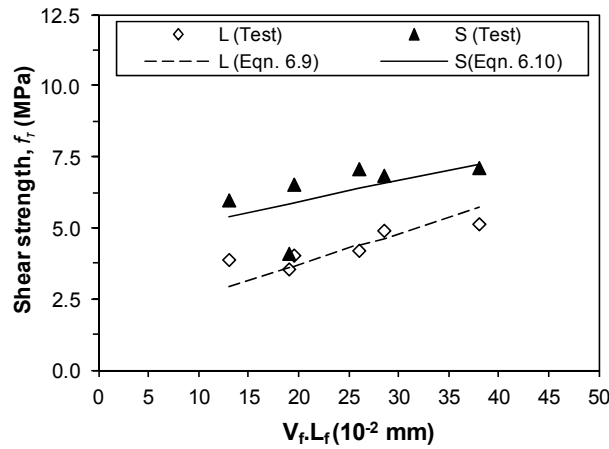


Figure 6.14- Effect of fibers on shear strength

Adopting a similar format to the rule of mixtures expressed in Equation 6.6 and by employing regression analysis of the shear strength data, the following equations are proposed:

$$f_\tau = 0.056f_c'(1 - V_f) + 11.4V_f L_f \quad \text{Mix Type L} \quad (6.9)$$

$$f_\tau = 0.082f_c'(1 - V_f) + 9.0V_f L_f \quad \text{Mix Type S} \quad (6.10)$$

Note that the term $0.056 f_c'$ in Equation 6.9 is the shear strength of lightweight ceramic concrete without fibers determined in an earlier study (Tassew and Lubell, 2012). Equation 6.9 and 10 are in good agreement with the shear strength test data shown in Figure 6.14 for different $V_f L_f$ values.

Shear Toughness

The shear toughness (T_τ) was calculated using the area under the shear load versus displacement curves up to the peak-load to provide a relative measure of the

energy absorption characteristics for each mix in direct shear. The results are summarized in Figure 6.15 where a significant increase in shear toughness occurred as V_f increased, regardless of the mix type or fiber length. Again, like flexural toughness, L_f had no significant influence on T_r (see Figure 6.15), which can be explained by fiber failure modes governed by fiber fracture rather than fiber pullout.

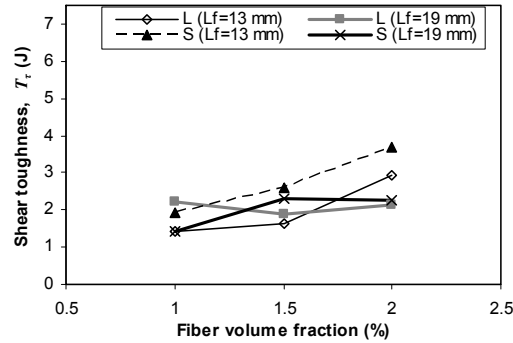


Figure 6.15- Relationship between shear toughness and fiber volume fraction

6.4.3 Outlook and Implications Towards Member design

The test results presented in this study indicate that it is viable to produce structural lightweight ceramic concretes with or without short glass fibers that have acceptable rheological and mechanical properties. Thus, these ceramic concretes can be used as substitutes for Portland cement based concretes for various structural elements such as slabs or cladding panels. These applications could potentially exploit the durability or rapid strength gain characteristics of the ceramic concrete, while offsetting the higher unit costs of the binder compared to Portland cement binders (Tassew and Lubell, 2012). Two candidate mixes are presented in this chapter, including a lightweight mix with lower strength and a somewhat denser mix with higher strength. Both mixes have dry densities lower than typical Portland cement concretes of comparable compressive strength. Further optimization of mix designs could be completed to target further enhancements to specific mechanical properties.

It is noted that the modulus of elasticity of the produced lightweight ceramic concretes was considerably lower than that of similar lightweight Portland cement concretes. As the modulus of elasticity has a bearing on the overall member stiffness under flexure and/or axial effects, a low modulus of elasticity may necessitate larger member cross-sections, thereby negating some of the weight savings that could otherwise be achieved by using a lightweight material. For a flexure dominated reinforced concrete member, the post-cracking residual tensile strength will also influence the overall member stiffness. The considerable enhancement in flexural strength and toughness through use of up to 2% short glass fibers in the current study suggests that this may offset some of the influence of the low modulus of elasticity. The current study has also shown that adding glass fibers can enhance the shear capacity, thereby eliminating the need for shear reinforcement, which is impractical in thin members.

6.4 Conclusions

This study developed a quantitative understanding of behavior of glass fiber reinforced ceramic concretes, which can be used for fabrication of new structural elements or for strengthening of existing concrete structures. The following conclusions can be drawn from this study:

- Addition of glass fibers to a ceramic concrete matrix reduced the flow of the concrete. However the fibers had negligible effect on the densities of the hardened ceramic concrete, which were approximately 1800 kg/m^3 and 2200 kg/m^3 for mixes with LECA and sand aggregates respectively.
- For mixes with LECA aggregate, the compressive strength increased with increases in the glass fiber volume fraction, but the fibers had negligible effect on the modulus of elasticity. For ceramic concrete with sand aggregates, a marginal decrease in both the compressive strength and modulus of elasticity occurred for higher fiber dosages.

- The flexural strength of ceramic concrete increased with increases in the glass fiber volume fraction irrespective of the mix composition or fiber length. The flexural strengths of glass fiber reinforced ceramic concrete were 13-30% of the corresponding compressive strength. Based on the rule of mixture, a relation was proposed between flexural strength and the fiber parameters.
- The direct shear strength of ceramic concrete increased with increase in the glass fiber volume dosage irrespective of the mix composition or fiber length. The rule of mixture was successfully used to relate the shear strength with fiber volume and length.
- The compression toughness index, flexural toughness and shear toughness of ceramic concrete showed a considerable increase with an increase in the fiber content. This was true regardless of the type of matrix or fiber length.
- The compression, flexure and shear strength results all indicated that the fiber failure mode was predominantly by fracture rather than pullout, even for the shortest fibers in use in this study.

6.5 References

- ACI Committee 318. (2011). Building Code Requirements for Structural Concrete (ACI 318-08) and Commentary. American Concrete Institute, Farmington Hills, MI, 107-108.
- Ali, M. A., Majumdar, A. J. and Singh, B. (1975). Properties of glass fiber reinforced cement-the effect of fiber length and content. *Journal of Material Science*, 10: 1732-40.
- ASTM C 230/C 230M. (2008). Standard specification for flow table for use in tests of hydraulic cement. ASTM International, West Conshohocken, PA.
- ASTM C127. (2007). Standard test method for density, relative density (specific gravity), and absorption of coarse aggregate. ASTM International, West Conshohocken, PA.
- ASTM C128. (2007). Standard test method for density, relative density (specific gravity), and absorption of fine aggregate. ASTM International, West Conshohocken, PA.

Chapter 6: Mechanical Properties of Glass Fiber Reinforced Ceramic Concrete

- ASTM C1437. (2007). Standard test method for flow of hydraulic cement mortar. ASTM International, West Conshohocken, PA.
- ASTM C1609/C1609M. (2007). Standard test method for flexural performance of fiber-reinforced concrete (using beam with third-point loading). ASTM International, West Conshohocken, PA.
- ASTM C469/C469M. (2002). Standard test method for static modulus of elasticity and poisson's ratio of concrete in compression. ASTM International, West Conshohocken, PA.
- ASTM C617. (2010). Practice for capping cylindrical concrete specimens. ASTM International, West Conshohocken, PA.
- Balaguru, P. N. and Shah S. P. (1992). Fiber reinforced cement composites McGraw Hill Inc. Publishers, New York, 70-80.
- Barluenga, G. and Hernández-Olivares, F. (2007). Cracking control of concretes modified with short AR-glass fibers at early age. Experimental results on standard concrete and SCC. *Cement Concrete Research*, 37(12): 1624–38.
- Bentur, A. and Mindess, S. (1990). Fibre reinforced cementitious composites, Elsevier Applied Science, London, 1-10, 31-41, 105-125, 189-204 & 390-393.
- Ding, Z. and Li, Z. (2005a). Effect of aggregate and water content on the properties of magnesium phospho-silicate cement. *Cement and Concrete Composites*, 27(1): 11-8.
- Ding, Z. and Li, Z. (2005b). High-early-strength magnesium phosphate cement with fly ash. *ACI Material Journal*, 102(6): 357-381.
- Ezeldin, A. S. and Balaguru, P. N. (1992). Normal and high strength fiber-reinforced concrete under compression. *Journal of Material Civil Engineering*, 4(4): 415-29.
- Fanella, D. A. and Naaman, A. E. (1985). Stress-strain properties of fiber reinforced mortar in compression. *ACI Journal*, 82(4): 475-583.
- Gao, J., Sun, W. and Morino, K. (1997). Mechanical properties of steel fiber-reinforced, high-strength, lightweight concrete. *Cement Concrete Composite*, 19(4): 307–313.
- JSCE-SF6. (1990). Method of test for shear strength of steel fiber reinforced concrete. Japan Society of Civil Engineering (JSCE), Tokyo, 67-69.

Chapter 6: Mechanical Properties of Glass Fiber Reinforced Ceramic Concrete

- Li, Z. and Liang, W. (2011). Advanced concrete technology. Hoboken, NJ: John Wiley & Sons, 33-34 & 476-477.
- Majdzadeh, F. Soleimani, M. S. and Banthia, N. (2006). Shear strength of reinforced concrete beams with a fiber concrete matrix. *Canadian Journal of Civil Engineering*, 33(6): 726-734.
- Mehta, P. K. (1986). Concrete structure, properties and materials: Prentice-hill, NJ, 42-68 & 238-242.
- Mirsayah, A. A. and Banthia, N. (2002). Shear strength of steel fiber-reinforced concrete. *ACI Material Journal*, 99(5): 473-479.
- Mirza, F. A. and Soroushiand, P. (2002). Effects of alkali-resistant glass fiber reinforcement on crack and temperature resistance of lightweight concrete. *Cement and Concrete Composite*, 24(2): 223-227.
- Naaman, A. E. (2003). Engineered steel fibers with optimal properties for reinforcement of cement composites. *Journal of Advanced Concrete Technology*, 1(3): 241-52.
- Neville, A. M. (1996). Properties of concrete. John Wiley & Sons Ltd., New York. 529-545.
- Qiao, F., Chau, C. K. and Li, Z. (2010). Property evaluation of magnesium phosphate cement mortar as patch repair material. *Construction Building Material*, 24: 695-700.
- Swamy, R. N. and Mangat, P. S. (1974). A theory for the flexural strength of steel fiber reinforced concrete. *Cement and Concrete Research*, 42: 113-25.
- Tassew, S. T. and Lubell, A. S. (2010). Textile reinforced ceramic composite for structural infill slab application. Proceedings of 34th IABSE Symposium, Venice, Italy, A-0317, 1-8.
- Tassew, S. T. and Lubell, A. S. (2012). Mechanical properties of lightweight ceramic concrete, *Materials and Structures Journal*, 45(4): 561-574.
- Wagh, A. S. (2004). Chemically bonded phosphate ceramics: Twenty-first century material with diverse applications. Elsevier Limited, Amsterdam, 1-5, 15-25, 97-111 & 157-175.
- Wagh, A. S. and Jeong, S. Y. (1998). Method of waste stabilization via chemically bonded phosphate ceramics U.S. Patent No. 5,830,815, 1-14.

Chapter 6: Mechanical Properties of Glass Fiber Reinforced Ceramic Concrete

Wagh, A. S., Jeong, S. Y. and Singh, D. (1997). High-strength ceramic (cement) using industrial by-product Ashes. Proceeding of International Conference on High-Strength concrete, Kona HI: 542-53.

Uniaxial Tensile Behaviour of Textile Reinforced Ceramic Concrete

7.1 Introduction

Textile reinforced concrete (TRC) is a composite material consisting of one or more layers of a textile fabric mesh embedded within a finely grained cement-based matrix. Textile fabrics are continuous rovings that are prepared from a bundle of a large number of filaments (e.g., Lepenies et al., 2007). Commonly used textile materials contain alkali-resistant (AR) glass, carbon, or aramid fibers (e.g., Hegger et al., 2006). These reinforcement materials do not corrode (e.g., Bruckner, 2006; Hegger et al., 2006) and thus can be used in some applications with significantly thinner concrete covers than are normally required for steel reinforcement in structural concrete members. Furthermore, due to the very small diameter of the individual fibers within the fabric mesh, the reinforcement layer remains flexible during construction, allowing the textile to conform to the geometric shape of the formwork. These characteristics make it possible to produce very thin, lightweight concrete elements with complex shapes (e.g., Bruckner et al., 2006).

The tensile behaviour of well-proportioned TRC elements is normally characterized by a high peak strength and large deformation capacity resulting from distributed, multiple cracking in the concrete matrix (Butler et al., 2009;

Barhum and Mechtcherine, 2012). These characteristics are desirable element properties with regard to their influence on structural safety and energy dissipation capacity, especially for structures under extreme loading (Barhum and Mechtcherine, 2012).

Because of its high load-bearing capacity, TRC can be used for the production of thin structural members. Specifically, it can be used as lightweight structural elements for applications such as structural wall panels and stay-in-place formworks (Hegger and Voss, 2008; Hegger et al., 2012). TRC is also applicable for the rehabilitation of existing concrete structural elements, including slabs, beams, columns, and masonry walls (Bruckner et al., 2006; Bosche et al., 2008).

The properties of textile reinforced concrete demands a special mix type of concrete (Hegger et al., 2008). In order for the matrix to fully penetrate into the fabric and create a better bond between these elements, the maximum aggregate size of concrete is usually limited to 2 mm or less, depending on the mesh size (Lepenes et al., 2007; Hartig et al., 2008; Hegger et al., 2008).

The tensile behaviour of TRC is considerably influenced by the bond behaviour between the textile and the matrix, which depends on the matrix behaviour (e.g., Lepenes et al., 2007). The bond behavior of textile and concrete differs from that of reinforcing steel bar and concrete, since textile reinforcements are a bundle of multiple filaments. In textile reinforcement, overall bond behavior is dependent on the filaments and concrete as well as on the bond between the filaments (e.g., Hartig et al., 2008), such that multiple numbers of filaments can lead to inhomogeneous penetration of the matrix into the yarn. Outer filaments usually have direct contact with the cement matrix, whereas central filaments may not have an immediate connection to the matrix or may be partially connected to it (Hartig et al., 2008; Hegger et al., 2006). Thus, outer filaments exhibit a better bond to the matrix compared to the inner filaments. This results in a non-uniform stress distribution over the cross-section of the roving. Outer filaments are subjected to higher stress and strain than inner filaments (Hegger et al., 2006).

Due to this non-uniform stress distribution, the tensile strength of all filaments cannot be fully achieved and some individual filaments are expected to fracture during loading before the entire roving fails (Lepeniec et al., 2007).

The beneficial influences on the mechanical properties of TRC from adding distributed short fibers in combination with the textile mesh have been reported in previous research (e.g., Hinzen and Brameshuber, 2009; Barhum and Mechtcherine, 2012). Tensile load-bearing behaviours, such as the first crack stress and the uniaxial tensile strength of TRC, are enhanced in comparison to TRC without short fibers (Hinzen and Brameshuber, 2009; Barhum and Mechtcherine, 2012). A strain-hardening behaviour of TRC after first cracking in the concrete matrix was reported by Hinzen and Brameshuber (2009) due to the addition of short glass fibers at 1.5% by volume combined with 1% by volume of short aramid fibers. The addition of short glass fibers has been reported to result in finer cracks as well as improved bond between the textile and the surrounding cement matrix (e.g., Barhum and Mechtcherine 2012).

As reported in Chapters 3, 4 and 6, different types of ceramic concrete have been developed using magnesium potassium phosphate binders and various aggregates (i.e., sand and lightweight aggregates). The mixes contained or omitted short glass fibers, depending on the mix composition. These ceramic concretes had 28-day compressive strengths between 17 and 55 MPa for densities between 1600 and 2200 kg/m³, respectively. In order to increase the tensile load-carrying capacity and the ductility of these ceramic concretes so that they can be used for thin structural elements, the use of glass textile reinforcements was also examined. The resulting composite materials are herein termed textile-reinforced ceramic concrete (TRCC).

The flexural behaviour of thin, prototype TRCC panels was evaluated using 3-point bending tests in an earlier study (Tassew and Lubell, 2010). The influence on the bending behaviour from the cross-section configuration, including the number of layers of textile reinforcement and the type of construction, were of

primary interest. Results from the tested panels showed that large deformation capacity was available before failure, but a significant loss of flexural stiffness occurred after the formation of the first flexural crack in the concrete matrix (which did not include chopped fibers). However, as the tensile behaviour of TRCC was not examined in the prior study, it was not possible to directly link the properties of TRCC components to the structural behaviour of the panels.

This chapter examines the load-bearing behaviour of TRCC through uniaxial tensile testing. TRCCs with and without short glass fibers were considered. The main aim of this investigation was to establish a relationship between axial load and axial deformation of TRCC. As an equivalent stress-strain model, the relationship could then be used for modeling the structural behaviour of structural elements made from TRCC.

The axial tensile behaviour of TRCC was determined using dog-bone shaped specimens containing up to two layers of glass textile reinforcement and short glass fibers at 0 or 1.5% by volume. The mechanical properties of the matrices used for the dog-bone shaped specimens were also examined using tests for compression, direct tension, splitting tension, and the flexural tension response. The influence of the test method on evaluating the tensile strength was also investigated.

7.2 Materials

7.2.1 Ceramic Concrete

The ceramic concrete matrix used in this study consists of a magnesium potassium phosphate binder (MPPC) and various aggregates. The MPPC binder contained magnesium oxide (MgO), monopotassium phosphate (KH₂PO₄) and Class C fly ash (FA). The dry ingredients of the MPPC binder (*b*) were prepared at a mass ratio of MgO:KH₂PO₄:FA = 1:3.4:4.4, established in Chapter 4. The physical properties of the binder ingredients are described in Chapter 4.

Three different groups of mixes were used, namely mix types LL, B and S, which contained the aggregate types of lightweight expanded clay (LECA), expanded shale (Buildex) and well-graded sand, respectively. The mix details are given in Table 7.1. The physical properties of the aggregates are described in Chapter 3. The lightweight aggregates (i.e., LECA and Buildex) were used in a saturated surface dry condition after soaking for at least for 24 hours, while the sand was used in a dry condition. Note that, due to differences in aggregates unit weight, the aggregate-to-binder mass ratios were not constant for all mixes (see Table 7.1). These mix ratios were adopted from Chapter 6.

Table 7.1- Mix proportion of ceramic composite

Group	Series	Materials mass ratio			Volume (%) V_f	N_L^a
		b^a	LL/SA/BC ^a	w^a		
LL	LL00.0	1	0.54	0.20	0	0
	LL01.5	1	0.54	0.20	1.5	0
	LL10.0	1	0.54	0.20	0	1
	LL11.5	1	0.54	0.20	1.5	1
	LL21.5	1	0.54	0.20	1.5	2
S	S00.0	1	0.67	0.20	0	0
	S01.5	1	0.67	0.20	1.5	0
	S10.0	1	0.67	0.20	0	1
	S11.5	1	0.67	0.20	1.5	1
	S21.5	1	0.67	0.20	1.5	2
B	B00.0	1	0.67	0.20	0	0
	B01.5	1	0.67	0.20	1.5	0
	B10.0	1	0.67	0.20	0	1
	B11.5	1	0.67	0.20	1.5	1
	B21.5	1	0.67	0.20	1.5	2

^a b : binder; LL: coarse and fine LECA aggregates; BC: Buildex expanded shale aggregates; SA: sand aggregates; w : water; V_f : volume fraction of chopped glass fibers; N_L : number of textile layers


The water-to-binder ratio (w/b) was fixed at 0.20, taken from Chapter 4 (see Table 7.1). This ratio provided a high compressive strength and adequate workability. To control the setting time, a commercially available lignosulphonate admixture

was used in all mixes with a dosage of 1.5% by mass of the binder, established from Chapter 4.

Chopped glass fibers with a nominal length of $L_f=13$ mm were used in some mixes. The volume fraction of fibers was $V_f=1.5\%$ of the total mix adopted from Chapter 6. This ratio was selected because it provides a ceramic concrete with an acceptable workability. The glass fiber used in this study has the characteristics shown in Table 7.2 as obtained from the manufacturer.

Table 7.2- Characteristics of chopped glass fiber

Fiber Properties	Quantity
Length, mm	13
Diameter, μm	18
Tensile strength, MPa	2000
Young's Modulus, GPa	76
Breaking elongation, %	2
Specific gravity	2.7



The ceramic concrete used for the dog-bone shaped specimens was prepared using the mixing procedure described in section 6.2.2. Another series of mixes with the same mix proportions were prepared using mixing procedures described in section 8.4.2 to determine the effect of curing age on the mechanical properties of glass fiber reinforced ceramic concrete cylinder and prism samples. Two different mix procedures were used due to differences in the type of mixing equipment used (i.e., 20 l and 70 l capacity).

7.2.2 Textile Reinforcement

Woven textile fabric made from glass fibers was used for the dog-bone shaped uniaxial tension test specimens. The fabric had spacing between yarns of approximately 7 mm in both directions (see Figure 7.1). The warp and weft directions of the textile are shown schematically in Figure 7.1(b). Note that the warp yarns are aligned in the longitudinal axis direction of the dog-bone

specimen. A similar arrangement of textiles was also used for slab specimens in Chapter 8.

The tensile strength of the textile fabric in the warp direction was determined using a direct tensile test. The test was completed using bare fabric specimens with dimensions according to ASTM D6637 (2010). The textile strip specimen had a width of 200 mm, and total length of 400 mm, which includes a gauge length of 300 mm and a 50 mm length at each end to clamp the specimen. Three specimens were tested. The loading rate was taken as a machine cross-head speed of 10 mm/min. The strain values were calculated by dividing the machine extension by the original textile length between grips. The stress values per meter were evaluated by dividing the machine load by the specimen width (200 mm).

The average tensile stress-strain curve for the bare textile fabric is shown in Figure 7.2. Detailed information for each test is given in Appendix A-6. The ascending branch of the stress-strain curve was linear up to the peak stress. After the peak stress, the stress-strain response was nonlinear with a negative slope. The test was stopped due to fiber fracture in the warp direction. The test results indicated that the average tensile strength of the textile fabric was 32 kN/m (CV=8.96%) at a strain of 1.4% (CV=15.30%). The average modulus of elasticity of the textile fabric, which was taken as the slope of the linear ascending region of the stress-strain plot, was 33700 kN/m (CV=8.70%).

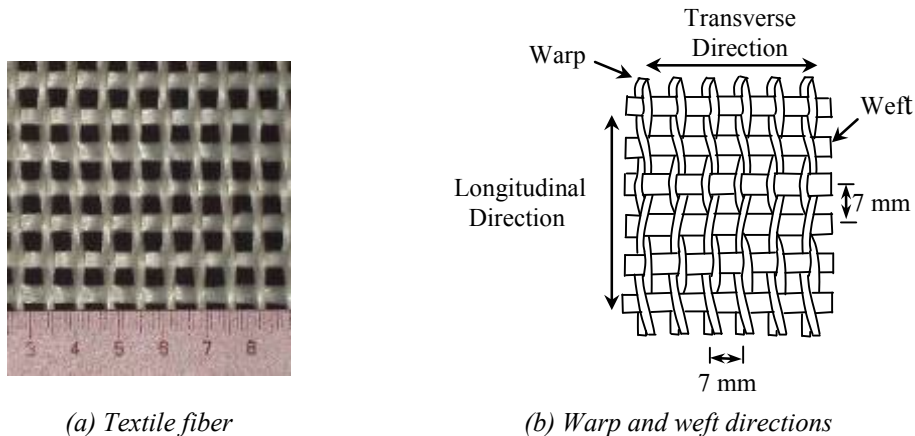


Figure 7.1- Textile fiber and geometry

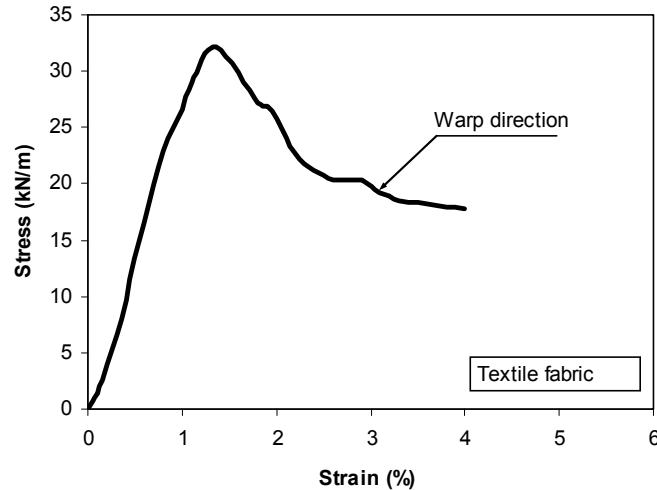


Figure 7.2- Average tensile stress-strain curve for textile fabric

7.3 Specimen Preparation

7.3.1 Cube, Cylinder and Prism Specimens

The compressive strength of each batch of ceramic concrete used for the dog-bone shaped specimens was evaluated using three cubes measuring $50 \times 50 \times 50$ mm. These tests were completed at the same age as the uniaxial tensile tests (28 days).

Cylinder and prism specimens were prepared for each GFRCC mix type to determine the effect of curing age on mechanical properties, including the compressive strength and the flexural and splitting strength. These samples were tested at age 28 and 60 days. Two batches of concrete were used due to limited mold availability. These mix compositions are the same as mixtures used for slab specimen preparation in Chapter 8. From the first batch, six 100×200 mm cylinder samples were prepared for compressive test and splitting tensile test. From the same batch of ceramic concrete, three $100 \times 100 \times 400$ mm prism samples were also prepared for 4-point bending tests. The second batch of concrete was used to prepare similar numbers and sizes of samples for testing at 60 days.

All specimens were prepared using plastic molds. The casting was done by filling each mold with fresh ceramic concrete in two layers. Cubes were filled in a single

layer. The fresh concrete was consolidated on a vibrating table. All specimens were demolded at the age of 3 hrs after casting. The specimens were then stored in the ambient laboratory environment of $23\pm 2^{\circ}\text{C}$ and a relative humidity of $50\pm 5\%$ until testing at ages of 28 and 60 days.

7.3.2 Dog-bone Shaped Specimens

Dog-bone shaped specimens were used for the uniaxial tension tests. The geometry of the specimens is shown in Figure 7.3. Three specimens were cast for each configuration using specially machined plexi-glass molds shown in Figure 7.4(a). The molds had an overall length of 500 mm and a test region 20 mm thick and 60 mm wide. The end regions had a width of 80 mm. The base and topping elements of the molds were connected by 10 mm socket head allen bolts (see Figure 7.4(a)). These bolts allowed for easy demolding of the specimens.

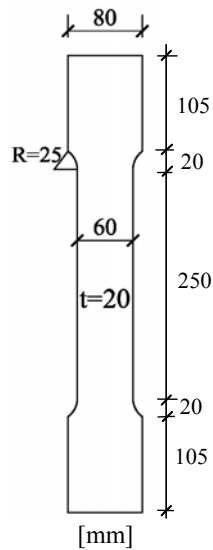


Figure 7.3- Dog-bone specimen geometry



(a) Plexi-glass mold



(b) Placing ceramic concrete



(c) Textile fabric

Figure 7.4-Dog-bone specimen preparation stage

As illustrated in Table 7.1, various configurations of the dog-bone shaped specimens were examined: (a) plain ceramic concrete samples; (b) samples reinforced with short glass fibers but no textile reinforcement; (c) samples reinforced with one layer of textile but no short glass fibers; (d) samples reinforced with one layer of textile reinforcement and short glass fibers; and (e) samples reinforced with two layers of textiles and short glass fibers.

The following procedures were carried out to prepare each specimen configuration containing one layer of textile. After mixing the ceramic concrete, the mixes were placed in molds to a depth of about 10 mm, using a scoop, after which they were consolidated on a vibrating table (Figure 7.4(b)). Next, a textile fabric layer cut to match the dog-bone shape (Figure 7.4(c)) was pressed manually into the ceramic concrete. The fabric was oriented with the warp direction parallel to the dog-bone longitudinal axis, with the textile being located near the mid-thickness location. Finally, the remaining depth of the mold was filled with

additional concrete. The concrete was consolidated through vibration and the surface was screeded flat with a trowel.

For samples with two layers of textile, a layer of textile fabric reinforcement was placed in an empty mold, followed by ceramic concrete about 17 mm deep. After placing the second layer of textile on top of the concrete, the remaining depth was filled with more ceramic concrete. This procedure resulted in the textile fabric near the two surfaces arranged at approximately symmetric locations. The mold was then vibrated to consolidate the concrete and the surface was smoothed with a trowel.

For samples without textiles, the molds were filled in a single layer and consolidated using the vibrating table.

All specimens were demolded at the age of 3 hrs after casting and were then stored in the ambient laboratory environment of $23\pm 2^{\circ}\text{C}$ and a relative humidity of $50\pm 5\%$ until testing at age 28 days.

7.4 Test Methods

7.4.1 Hardened GFRCC Properties

7.4.1.1 Compression Tests

The compressive strength of the $50 \times 50 \times 50$ mm cube specimens were determined using a Forney testing machine with a capacity of 3100 kN, as shown in Figure 7.5(a). The loading rate was set to 0.25 MPa/sec according to ASTM C39 (2009).



(a) Cube



(b) Cylinder

Figure 7.5- Compression test set-up

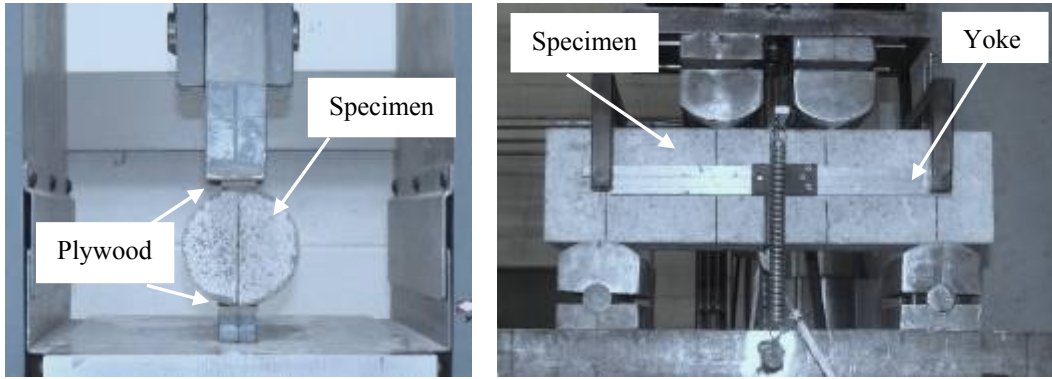
Compressive testing of the 100 mm diameter \times 200 mm long cylinders was conducted in accordance with ASTM C469 (2002) using a stiff MTS frame with a 2600 kN capacity (see Figure 7.5(b)). Axial deformations were measured using a collar and three LVDTs arranged at 120° separations about the longitudinal axis and operating over an initial gauge length of 100 mm. The loading rate was set to a machine stroke of 1 mm/min. All cylinder samples were end-ground prior to testing, as per ASTM C39 (2009).

7.4.1.2 Splitting Tensile Test

The splitting tensile strength of 100 \times 200 mm cylinders was determined using a Forney testing machine with a capacity of 3100 kN. Before commencing loading, the specimen was placed between two 3 mm thick plywood strips at the top and the bottom, aligned so that the loaded diameter of the cylinder was between the plywood strips, as shown in Figure 7.6(a). The loading rate was set to 1 MPa/min splitting tensile stress, according to ASTM C496 (2011). The splitting tensile strength, $f_{ct,st}$ (MPa), was calculated from:

$$f_{ct,st} = \frac{2P}{\pi l_c D} \quad (7.1)$$

where P is the peak load (N), l_c is the length of the specimen (mm), and D is the diameter (mm) of the cylinder specimen.



(a) Splitting cylinder test

(b) Four-point bending test

Figure 7.6- Splitting cylinder and bending test set-up

7.4.1.3 Third-point Loading Bending Test

Third-point loading bending tests to determine the flexural response of $100 \times 100 \times 400$ mm notched prisms with a span of 300 mm were carried out according to ASTM C1609 (2007). A 10 mm deep notch was sawn at the mid-span of the bottom face of each specimen using a diamond saw with a thickness of 3.6 mm. Specimens were loaded at a displacement controlled rate of 0.1 mm/min using a stiff MTS frame with a 1000 kN capacity. A yoke was attached to the specimen, as shown in Figure 7.6(b), to measure the mid-span deflection relative to the supports as the average measurement from two LVDTs. The flexural strength, $f_{ct,r}$ (MPa) was calculated as follows:

$$f_{ct,r} = \frac{PL_{pr}}{b(d_p - a)^2} \quad (7.2)$$

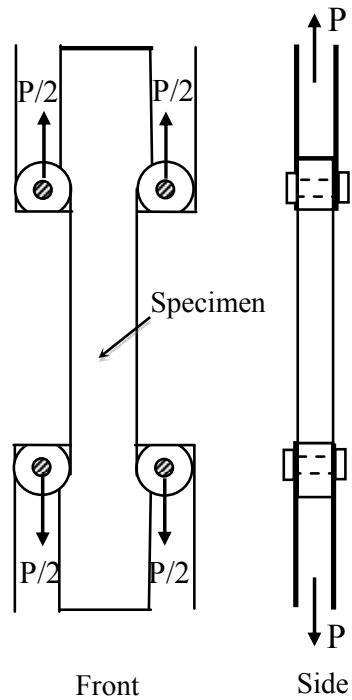
where P is the peak load (N), L_{pr} is the total span length (mm), b is the width of the specimen (mm), d_p is the overall depth of the specimen (mm), and a is the depth of notch (mm).

In Equation 7.2, a linear distribution of axial stresses over the cross-section height is assumed up to the peak load (P).

7.4.2 Uniaxial Tensile Test of Textile Reinforced Ceramic Concrete

The test set-up for the dog-bone shaped specimens was similar to the test set-up in prior studies for fiber-reinforced Portland cement concretes (e.g., Orlosky and Raupach, 2006; Heggar et al., 2011; Kim et al., 2011) (see Figure 7.7). The specimen was clamped between two rectangular steel plates that contained round steel collars, which were welded to the plates. These collars fit against the rounded edges of the specimen and transmitted the load from the plate to the specimen, as illustrated in Figure 7.7(a). The two steel plates at each end were connected to a stiff testing machine of 30 kN capacity through bolts in circular holes aligned with the central axes of the specimen. The specimens were loaded using a displacement-controlled protocol with a machine stroke rate of 1 mm/min. The average displacement was determined from measurements by two LVDTs attached to the sides of the specimen, as shown in Figure 7.7(b). The initial gauge length of the LVDTs was 195 mm.

The axial tensile stress was calculated by dividing the applied load by the measured cross-sectional area of the specimen. Average strains were evaluated by using the average displacement measurement from the two LVDTs and the initial gauge length.



(a) Schematic view of load transfer

(b) Test set-up

Figure 7.7- Uniaxial tensile test set-up

7.5 Experimental Results

7.5.1 Hardened GFRCC Properties

7.5.1.1 Air-dried Density

The densities of the GFRCC mixes were determined at 28 days after casting the prism and cylinder specimens. The average densities were 1775 kg/m^3 , 1940 kg/m^3 , and 2180 kg/m^3 for mix types LL, B and S, respectively. The average densities of GFRCC measured at age 60 days were within $\pm 2\%$ of the corresponding 28-day densities.

7.5.1.2 Compressive Strength

The average 28-day cube compressive strength (f_{cu}) of the GFRCC batches used for the dog-bone specimens are shown in Table 7.2. The average f_{cu} of the GFRCC was 28.4 MPa for mix type LL, 44.2 MPa for mix type B, and 49.8 MPa

for mix type S. The corresponding results for ceramic concrete mixes without fibers were 27.3 MPa, 40.7 MPa and 46.3 MPa for mix types LL, B and S, respectively. As expected, these results showed that the addition of glass fibers to ceramic concrete had no significant effect on the compressive strength, similar to the results presented in Chapter 6.

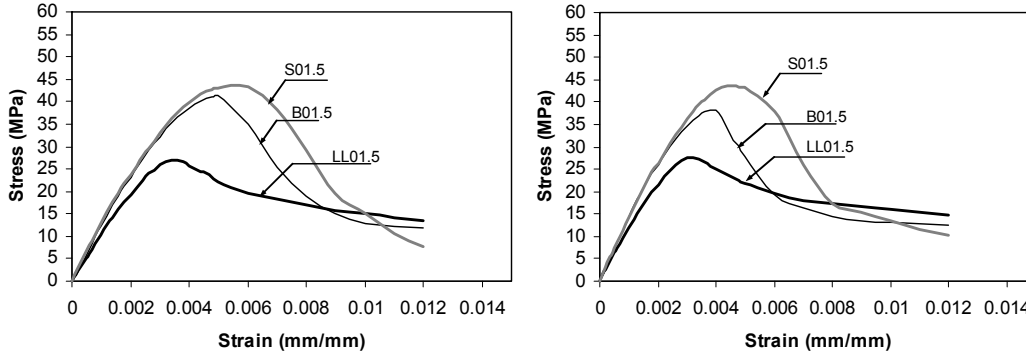
Table 7.3- Cube compressive strength (f_{cu}) of ceramic concrete at 28 days

Group	Series	V_f (%)	f_{cu} MPa (CV*)
LL	LL00.0	0	27.8 (7.86)
	LL01.5	1.5	29.0 (5.81)
	LL10.0	0	26.8 (5.96)
	LL11.5	1.5	27.8 (2.64)
	LL21.5	1.5	28.3 (6.29)
B	B00.0	0	46.9 (1.27)
	B01.5	1.5	38.0 (6.73)
	B10.0	0	44.6 (4.90)
	B11.5	1.5	42.9 (4.76)
	B21.5	1.5	45.0 (1.89)
S	S00.0	0	43.7 (0.19)
	S01.5	1.5	52.4 (10.31)
	S10.0	0	52.2 (4.15)
	S11.5	1.5	51.1 (5.98)
	S21.5	1.5	46.1 (1.54)

* CV: Coefficient of variation, V_f : volume fraction of chopped fibers

The stress-strain response in uniaxial compression was determined from 100 mm diameter x 200 mm long cylinders tested at age 28 and 60 days. The average stress-strain relationships are shown in Figure 7.8. This figure illustrates that the ascending branches of the stress-strain curves were initially nearly linear for all mix types at both test ages. Nonlinear behaviour was observed beginning at about 70% of the peak stress. After the peak stress, the slopes of the descending region of the stress-strain curves were nonlinear. The descending slope for mix type LL was flatter compared to mix type B or S, indicating that the mix type affected the

slope. Mix type LL showed the lowest compressive strength compared to mix types B or S (see Figure 7.8(a)). This can be attributed to the lower aggregate strength and largest maximum aggregates size in mix type LL.



(a) At age of 28 days

(b) At age of 60 days

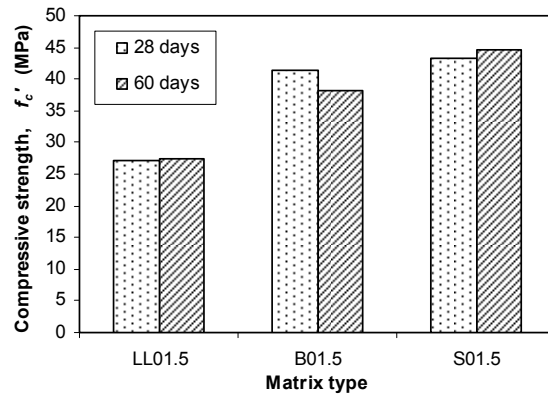
Figure 7.8- Average stress-strain curves in uniaxial compression

The average compressive strengths of each mix type at age 28 and 60 days are given in Table 7.4. The compressive strengths of each mix type are shown in Figure 7.9(a), which reveals that the difference between the compressive strength at 28 and 60 days is not significant. The cylinder compressive strengths at 60 days were found to be within 7% of the corresponding 28-day values. It was also established in Chapter 3 that the typical strength gain of these ceramic concrete matrices after 28 days was negligible.

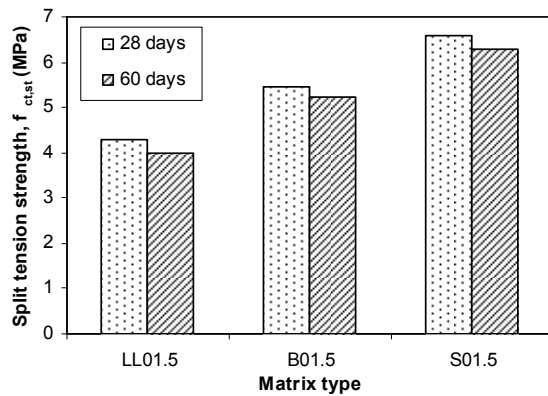
Table 7.4- Compressive strength ($f_{c,t}$), flexural strength ($f_{c,r}$) and splitting tensile strength ($f_{c,st}$) of glass fiber reinforced ceramic concrete ($V_f=1.5\%$)

Age	LL01.5 MPa (CV *)			B01.5 MPa (CV *)			S01.5 MPa (CV *)		
	f_c'	$f_{c,r}$	$f_{c,st}$	f_c'	$f_{c,r}$	$f_{c,st}$	f_c'	$f_{c,r}$	$f_{c,st}$
28 day	27.2 (3.47)	5.2 (4.06)	4.3 (8.03)	41.2 (1.28)	6.5 (3.09)	5.5 (4.46)	44.3 (2.90)	7.8 (7.52)	6.6 (4.46)
60 day	28.0 (1.62)	5.4 (8.57)	4.0 (4.78)	38.3 (6.84)	7.8 (1.30)	5.2 (6.34)	44.9 (5.42)	7.9 (8.61)	6.3 (10.07)

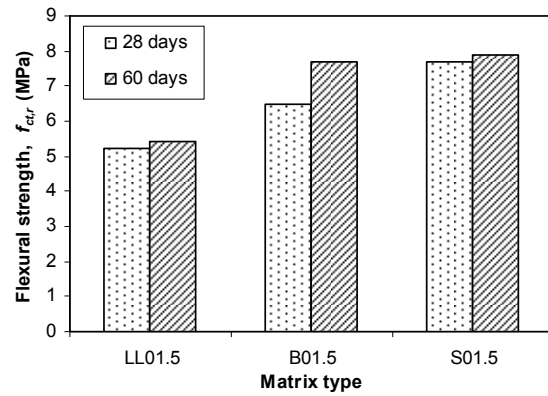
* CV: Coefficient of variation (%)



(a) Cylinder compressive strength



(b) Splitting tensile strength



(c) Flexural strength

Figure 7.9- Compressive, flexural and splitting strengths of GFRCC

7.5.1.3 Splitting Tensile Strength

The average splitting tensile strengths of GFRCC at age 28 and 60 days are presented in Table 7.4 and Figure 7.9(b). Differences between the splitting tensile strength at 28 and 60 days were not significant, with the splitting tensile strengths at 60 days found to be within 7% of the corresponding 28-day values. Some slight reduction of splitting tensile strength from 28-day compared to 60-day was caused due to the differences in mix batches (see section 7.3.1).

The splitting tensile strength of GFRCC was different for each mix type (see Figure 7.9b), a finding which suggests that the splitting tensile strength was influenced by the aggregate type and maximum aggregate size. However, it was not possible to differentiate each contribution from this study. Mix types with lightweight aggregates having the largest maximum aggregate sizes (type LL) resulted in lower splitting strength. This was likely due to failure that occurred through the lightweight aggregates rather than only through the binder. The test results also showed that the splitting tensile strength increased as the ceramic concrete strength increased (see Figures 7.9(a) and (b)). The splitting tensile strength of GFRCC ranged from 13% to 16% of its compressive strength at 28 and 60 days. This range is slightly higher than the range of 12% to 13% reported by Choia and Yuan (2005) for glass fiber reinforced Portland cement-based concrete with similar fiber content.

7.5.1.4 Flexure Tensile Strength

The average flexural stress versus mid-span deflection relationships for prism specimens under four-point bending are presented in Figure 7.10. Detailed information about these test results are presented in Appendix A-6. Figure 7.10 shows that all flexural stress mid-span deflection curves revealed similar patterns, but the mix type influenced the peak stress values. This suggests that aggregate type and maximum aggregate size can influence flexural strength. A general trend of the flexural stress to mid-span displacement response was characterized by a steep linear slope to approximately $0.4f_{ct,r}$, followed by more gradual non-linear relationships up to peak stress. All specimens exhibited deflection-hardening

behaviour in this region due to the glass fiber contributions. Figures 7.10(a) and (b) show that LL01.5 specimen produced the lowest peak stress ($f_{ct,r}$) compared to B01.5 and S01.5. Negligible differences in the deflection at peak stress were observed for the different mix types (see Figure 7.10). The deflections at peak stress for all curves ranged between 0.27 and 0.35 mm. After the peak stress, shallower and parallel decaying slopes were observed due to the crack-bridging effect of the glass fibers. These had lower stress magnitudes for mix containing lightweight aggregates with the largest maximum aggregate size (i.e., mix type LL).

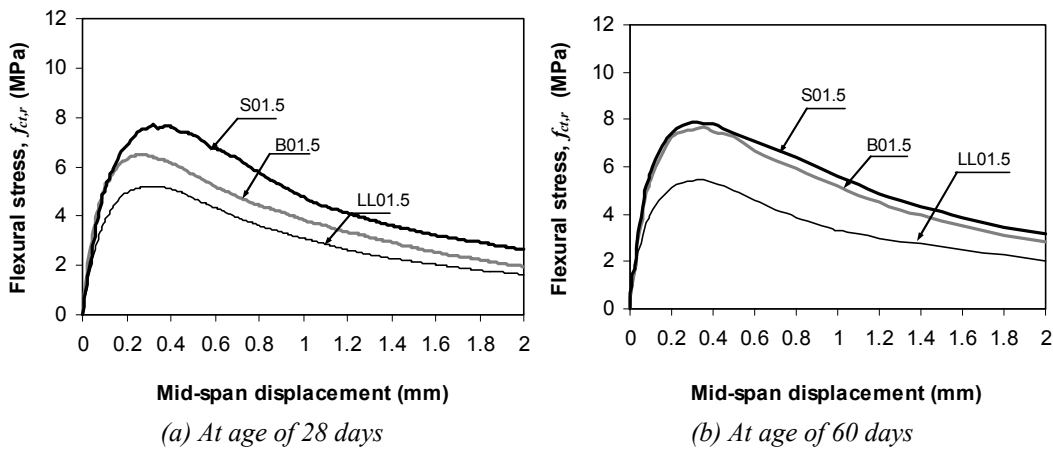


Figure 7.10- Average flexural stress versus mid-span displacement curves of GFRCC

The flexural strengths ($f_{ct,r}$) of GFRCC are presented in Figure 7.9(c). From this figure, it is observed that the mix types of lightweight aggregates had the lowest flexural strength, similar to a previous study (Tassew and Lubell, 2012). The flexural strength increased as the compressive strength increased (see Figures 7.9(a) and (c)). The average flexural tensile strength of GFRCC at 28 or 60 days ranged between 15% and 20% of the corresponding compressive strength (f_c').

The flexural tensile strengths were higher than the splitting tensile strengths, irrespective of the mix type (see Figures 7.9(b) and (c)). The ratio of splitting tensile strength to flexural strength ranged from 0.68 to 0.90. This could be due to two reasons. First, it could be related to the failure surface. The flexure test failure

is controlled by the strength at the tension surface of the sample where the notch was located. Splitting tension failure can be initiated anywhere in the portion of diameter plane that is in tension, which is larger than the controlling region of flexure test. The second potential explanation is that the overall size of the failure region in a splitting tensile test was larger than the flexure tensile test which can be explained by Weibull weakest link theory (Weibull, 1939). Weibull (1939) explained that as a concrete specimen sizes increases, the probability of containing of weak element within the specimen increases and thus the strength decreases.

7.5.2 Uniaxial Tensile Test of Textile Reinforced Ceramic Concrete

The influence of reinforcement configuration on the response of dog-bone shaped specimens under axial tensile load was examined. The number of textile reinforcement layers and the volume fraction of short fibers were the two main parameters considered. The axial responses reported in this section are average results and the details of individual tests are documented in Appendix A-6. The axial response of all of the tests were analysed and grouped in five cases in accordance with the fiber volume fraction and the textile reinforcement amount. The results are discussed as follows.

Case (a): Plain ceramic concrete matrices.

The axial stress-strain curves of plain ceramic concrete matrices obtained from the uniaxial tensile tests are presented in Figure 7.11. The average axial tensile strengths from the dog-bone tests are presented in Table 7.5. The axial tensile strengths ($f_{ct,t}$) of specimens LL00.0, B00.0, and S00.0 were 0.6 MPa, 1.0 MPa and 1.2 MPa, respectively. LL00.0 exhibited the lowest tensile strength compared to B00.0 and S00.0, which was attributed to the presence of coarse lightweight aggregates in the mix, with failure occurring through the lightweight aggregate. The fractured samples for all mix types revealed that failure occurred only by a

single macro crack that propagated across the entire cross-section in each sample (see Figure 7.13(a)).

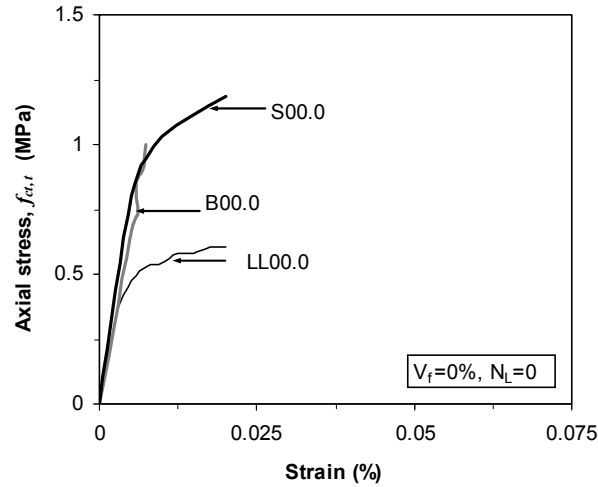


Figure 7.11- Average axial stress-strain of ceramic concrete

Table 7.5- Axial tensile strength, $f_{ct,t}$ (MPa) from dog-bone specimens

Reinforcement type	Mix Type LL	Mix Type B	Mix Type S
	$f_{ct,t}$ MPa (CV *)	$f_{ct,t}$ MPa (CV *)	$f_{ct,t}$ MPa (CV *)
Textile ($N_L=0$) and short fiber ($V_f=0.0\%$)	0.6 (26.02)	1.0 (5.89)	1.2 (1.86)
Textile ($N_L=0$) and short fiber ($V_f=1.5\%$)	1.3 (18.95)	2.7 (0.73)	1.8 (9.72)
Textile ($N_L=1$) and short fiber ($V_f=0.0\%$)	1.6 (24.63)	3.0 (9.09)	2.7 (11.70)
Textile ($N_L=1$) and short fiber ($V_f=1.5\%$)	3.4 (5.53)	3.3(10.35)	3.5 (4.33)
Textile ($N_L=2$) and short fiber ($V_f=1.5\%$)	4.1 (6.3)	3.6 (11.49)	4.6 (4.82)
* CV: Coefficient of variation (%)			

Case (b): Ceramic concrete with 1.5 Vol-% short fibers and without textile reinforcement.

Similar trends were observed for the tensile stress-strain response of all dog-bone shaped specimens with different matrices containing only 1.5 Vol-% short glass fibers (see Figure 7.12). The axial stress-strain curves revealed that the pre-peak stress-strain response was nearly linear up to the peak stress, and that gradual softening behaviour was observed after the peak load, due to the short fibers. The addition of short fibers into a matrix increased the axial tensile strength ($f_{ct,t}$),

irrespective of the matrix type (see Table 7.5). The $f_{ct,t}$ increased by a factor of 2.1, 2.7, and 1.5 for mix Type LL, B and S, respectively, compared to plain ceramic concrete. At the same time, the fractured samples revealed only a single macro crack that propagated across the entire cross-section in each sample, similar to plain samples (see Figure 7.13(b)). The failure surface of samples after testing showed that the majority of the fibers failed by fracture rather than pullout.

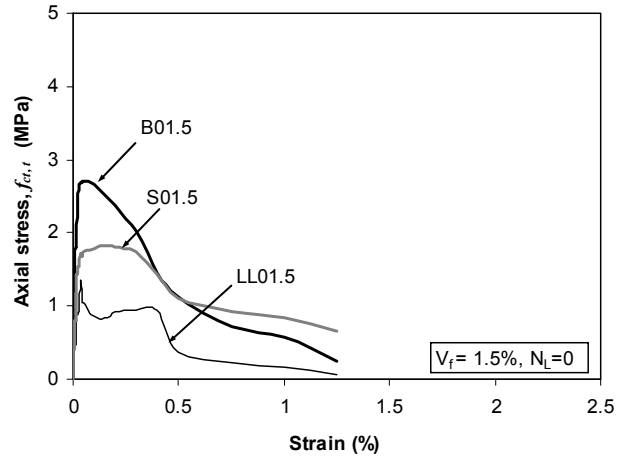


Figure 7.12- Average axial stress-strain of ceramic concrete reinforced with 1.5% short fibers and without textile fabric



(a) $V_f=0$ and $N_L=0$ (e.g., Mix type LL)



(b) $V_f=1.5$ and $N_L=0$ (e.g., Mix type LL)



(c) $V_f=0$ and $N_L=1$ (e.g., Mix type B)



(d) $V_f=1.5$ and $N_L=1$ (e.g., Mix type S)



(e) $V_f=1.5$ and $N_L=2$ (e.g., Mix type B)

Figure 7.13- Typical cracking pattern of tensile test specimens

Case (c): Ceramic concrete with one layer of textile reinforcement and without short fibers.

Specimens in cases (a) and (b) above contained no textile reinforcements, whereas specimens in cases (c) to (e) were reinforced with either one or two layers of textile reinforcements combined with or without short fibers. The cracking behaviour of these specimens during uniaxial tensile tests was typically similar. At relatively lower loads, depending on the reinforcement configuration, one or more matrix cracks formed perpendicular to the longitudinal axis of the specimen (see Figure 7.14(a)). After these cracks formed, the textile reinforcement dominated the composite behaviour and a debonding of textile reinforcement from the surrounding ceramic concrete followed. The debonding crack that formed was parallel to the longitudinal axis of the specimen (see Figure 7.14(b)). The crack likely occurred due to poor bonding between the matrix and the textile that is dependent on the matrix mix type and textile properties such as mesh spacing (Lepenies et al., 2007; Hartig et al., 2008; Hegger et al., 2008).

The actual influence of the mix type on the bond behaviour of textile reinforced specimens cannot be identified from the limited number of matrix types and textile types in the current study. It is well-known in textile reinforced concrete that the overall behaviour of textile reinforced concrete is highly influenced by the bond behaviour between the roving and the surrounding matrix (e.g., Lepenies et al., 2007). In all cases with textile in the current study (i.e., (c) to (e)), the tests were stopped when the failure of the TRCC composite occurred due to significant debonding cracks between the textile reinforcement and the ceramic concrete matrix; however, complete rupture of textile reinforcement was not observed.

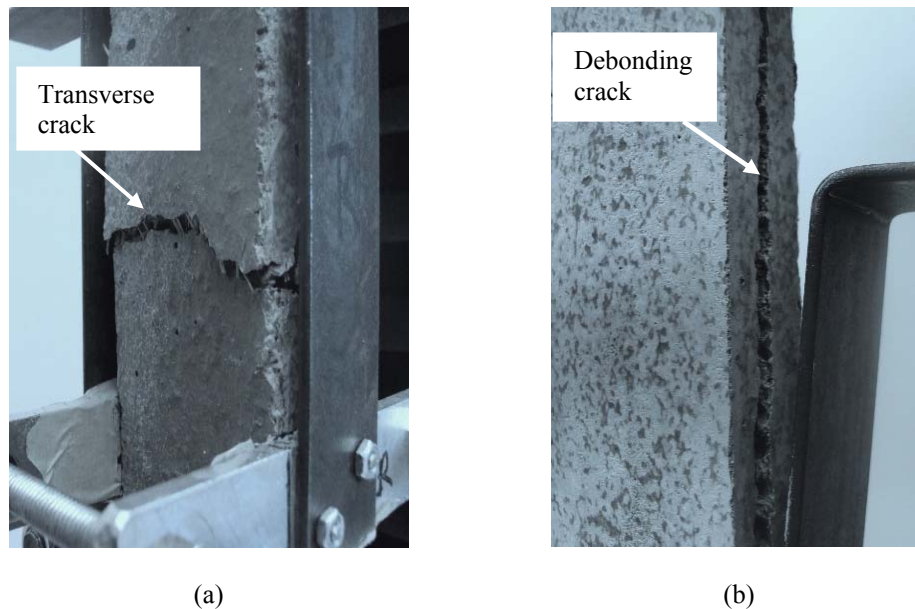


Figure 7.14- Typical observed crack pattern at failure of textile reinforced concrete: (a) transverse crack; (b) Longitudinal or splitting cracks

Figure 7.15 shows the average axial tensile stress-strain response of dog-bone shaped specimens containing different matrices and reinforced with one layer of textile fabric. The stiffness of bare textile reinforcement normalized to the dog-bone shaped concrete specimen thickness is also included in this figure. The addition of one layer of textile fabric resulted in three distinct parts in the stress-strain curves, similar to the behaviour of textile reinforced concrete made with Portland cement (e.g., Barhum and Mechtcherine, 2012). In the first part, before cracking of concrete, the stress-strain response is nearly linear, up to the formation of the first crack. After the initial cracking of the ceramic concrete, nearly horizontal stress-strain responses were observed, followed eventually by an increase in stiffness. This plateau is the region in which multiple cracks were formed (e.g., Barhum and Mechtcherine, 2012). The difference in length in the horizontal region was attributed to the number of cracks, which was affected by the mix type. Examination of samples after testing revealed that multiple cracks were formed in the specimen (see Figure 7.13(c)). More cracks were observed in mixes with small maximum aggregate sizes, giving a nearly flat plateau. This is due to lower aggregate size in mixes potentially improving the bond between the

textiles and the surrounding matrix and enabling a transfer of stress from the textile back to the uncracked concrete.

As noted earlier, an increase in stiffness was observed up to the peak stress point, which shows the contribution of the textile fabric. The slopes in this region of Fig 7.15 were nearly parallel to the bare textile. The peak stress of all specimens with $N_L=1.0$ was higher than the bare textile peak stress due to the concrete contribution in the TRCC. The strain capacity of LL10.0, B10.0, and S10.0 were similar but higher than the bare textile strain capacity. Larger strains in the TRCC specimens compared to bare textile resulted from larger deformations when the matrix cracked, which occurred due to the initial waviness in the fabric warp direction during the textile production process (Hegger et al., 2008; Hartig et al., 2009).

The addition of one layer of textile reinforcement into a plain matrix increased the axial tensile strength ($f_{ct,t}$), irrespective of the matrix type (see Table 7.5). The $f_{ct,t}$ of samples with one layer of textile reinforcement were 2.7, 3.0, and 2.3 times greater than plain samples for mix type LL, B and S, respectively. Moreover, large deformations were observed before peak load due to the textile reinforced concrete tolerance of multiple cracking and higher textile strain capacity. The specimens after testing revealed that multiple cracks formed followed by debonding of the textile reinforcement from the surrounding matrix (see Figures 7.13(c) and 7.14(b)), unlike specimens without textile reinforcement which had only a single failure plane (see Figure 7.13(a)).

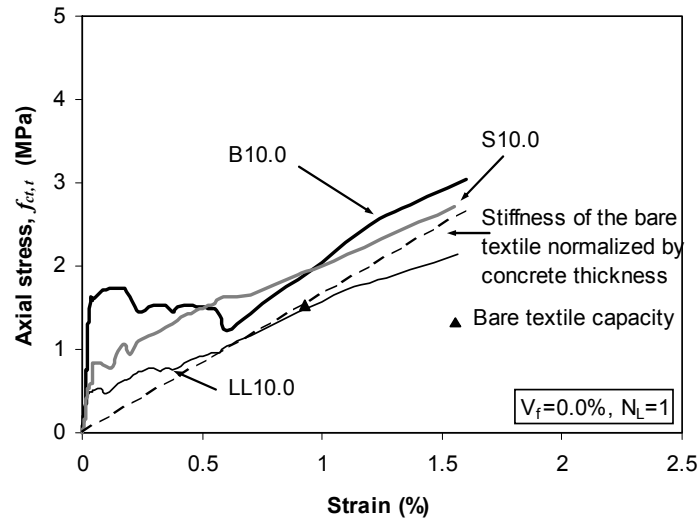


Figure 7.15- Average axial stress-strain of ceramic concrete reinforced with one layer of textile only

Case (d): Ceramic concrete containing 1.5 Vol-% short fibers and one layer of textile reinforcement.

Figure 7.16 shows that the axial tensile stress-strain response of dog-bone samples reinforced with one layer of textile and 1.5 Vol-% short glass fibers were similar, irrespective of the type of matrix. After the first cracking, a strain-hardening behaviour was observed, similar to Portland cement-based textile reinforced concrete with short fibers (e.g., Hinzen and Brameshuber, 2009). The slope of all TRCC curves at the final stage were nearly parallel, indicating that textile reinforcement dominated the behaviour but the stiffness were lower than the bare fabric stiffness due to the debonding crack that occurred (see Figure 7.14). As can be seen from Figure 7.16, the peak stress of LL11.5, B11.5 and S11.5 was similar, indicating the mix type had minimal influence on the stress level. These peak stress values were higher than the bare fabric peak stress value due to the combined contribution of the uncracked concrete section and the short glass fibers which also bridge the cracks. The strain capacity of LL11.5, B11.5 and S11.5 were all higher than the bare textile strain capacity, similar to TRCC specimens without short fibers described in case (c).

It was observed that the presence of short fibers in ceramic concrete reinforced with one layer of textile increased the peak strength ($f_{ct,t}$) of TRCC when compared to similar samples without short fibers (see Table 7.5). This occurred irrespective of matrix type and was caused by short fibers bridging the cracks. The addition of short glass fibers in specimens with one layer of textile increased the first-cracking stress by 2.7, 1.6 and 2.2 times and $f_{ct,t}$ by 1.6, 1.1 and 1.3 times for mix Types LL, B and S, respectively, compared to samples with only one layer of textile reinforcement (see Table 7.5). The differences in ratios for different mix types were attributed to aggregate type and size, which can affect the first-cracking stress as well as the bond between the textile and the matrix. At the same time, large deformations at peak load were observed due to the textile fabric, similar to TRCC samples without short fibers.

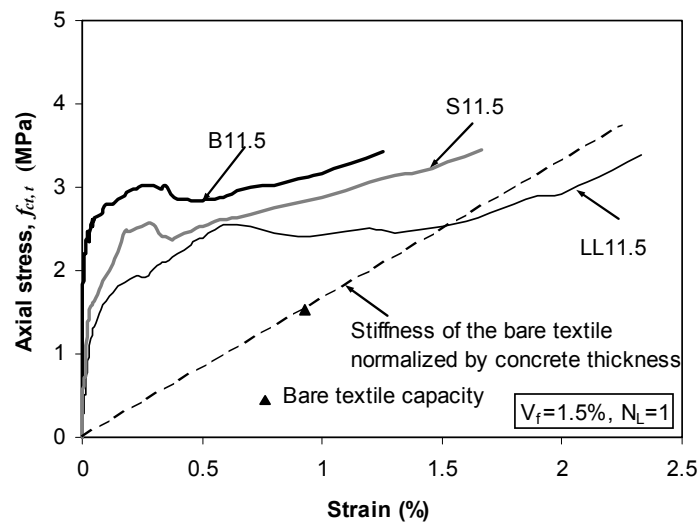


Figure 7.16- Average axial stress-strain of ceramic concrete reinforced with one layer of textile and 1.5% short fibers

The inspection of specimens after testing indicated that the addition of short fibers showed a single macro crack formation along the cross-section, unlike specimens containing only textile reinforcement, which showed multiple cracks (see Figure 7.13(d)). This phenomenon is due to the fibers-bridging effect of the cracking, which inhibits crack growth (e.g., Barhum and Mechtcherine, 2012). It was indicated in part (c) that specimens reinforced with only textile reinforcement tolerated multiple cracks. Additional cracks propagating along the specimen

length were also observed due to the debonding of textile reinforcement from the surrounding concrete matrix, similar to specimens containing only textile reinforcement (see Figure 7.14).

Case (e): Ceramic concrete with two layers of textile and 1.5 Vol-% short fibers.

Figure 7.17 illustrates the average axial tensile stress-strain of dog-bone shaped samples containing 1.5 Vol-% short glass fibers reinforced with two layers of textile reinforcements. The figure shows that the stress-strain responses were similar, irrespective of the type of matrix, and indicating a strain-hardening response after first-cracking in the matrix due to the contribution of the textile fabrics and the short fibers. After cracking, the textile reinforced ceramic composite was stiffer compared to bare textile reinforcement due to the ceramic concrete cross-sectional area between the cracks and the effect of the short fibers bridging the cracks. These stiffnesses were also higher compared to samples reinforced with one layer of textile (compare Figure 7.16 to Figure 7.17), due to higher N_L at cracks. The peak stresses of LL21.5, B21.5 and S21.5 were comparable (3.8-4.5 MPa), indicating the mix type had minimal influence on peak stress when the number of textile layers increased. The peak stresses of LL21.5, B21.5 and S21.5 were higher compared to bare textile peak stress due to short fibers bridging the cracks. At the same time, the strain capacities of these specimens were lower than the bare textile strain capacity due to the textiles and short fiber bridging-effect of the cracking, which slowed down the crack growth.

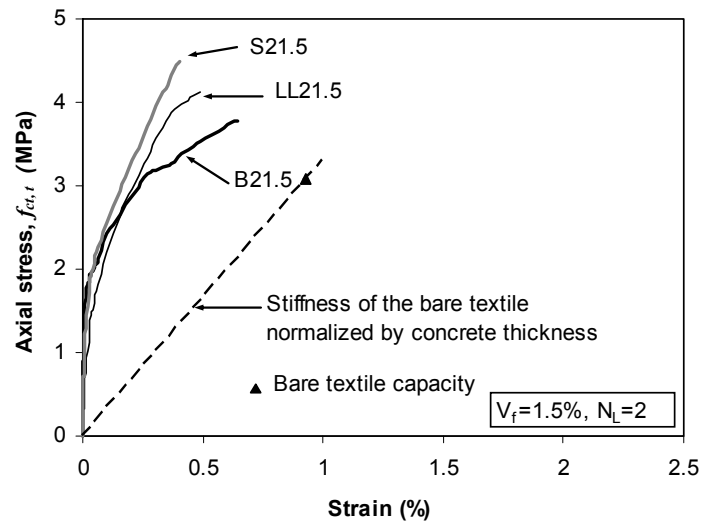


Figure 7.17- Average axial stress-strain of ceramic concrete reinforced with two layers of textile and 1.5% short fibers

The specimens with two layers of textile reinforcements revealed a higher stiffness and load-bearing capacity than specimens with only one layer of textiles (see Figures 7.16 and 7.17). The stiffness values were higher due to the contribution of higher textile reinforcement area when the number of textile layers increased. Compared to one layer of textile reinforcement, two layers of textile reinforcement increased the $f_{ct,t}$ by 1.2, 1.1, and 1.3 times for mix Types LL, B and S, respectively. It was also observed that the strain at peak stress reduced as the number of textile layers increased. The strain corresponding to the peak stress decreased by 0.2, 0.5, and 0.2 times for mix types LL, B and S, respectively, when the number of textile layers increased from one to two. However, the cracking behaviours were similar, in that a single macro crack formation was observed, followed by debonding of the textile reinforcements from the matrix (see Figures 7.13(e) and 7.14(b)).

7.5.3 Comparison of Test Method Influence on Tensile Strength

As described in section 7.4.1, the tensile strengths of various ceramic concretes were determined via three different test methods: direct tension test using dog-bones, four-point flexure test, and splitting tension test. Average values of each

test result are used for this comparison. The tensile strength versus the cylinder compressive strength for different GFRCC mix types at 28 days is illustrated in Figure 7.18. It can be observed from this figure that the $f_{ct,t}$, $f_{ct,r}$ or $f_{ct,st}$ of GFRCC increased as the compressive strength increased. It can also be seen that, regardless of compressive strength, the $f_{ct,t} < f_{ct,st} < f_{ct,r}$, which is a similar result as Portland cement-based concrete and is attributed to the methods in which loads are applied and the area over which the failure occurred (e.g., Neville, 1996). The ratios of $f_{ct,t}/f_{ct,r}$, $f_{ct,t}/f_{ct,st}$ varied by mix type. The ratio of $f_{ct,t}/f_{ct,r}$ was 0.25, 0.42, and 0.15 for LL01.5, B01.5 and S01.5, respectively, while the ratio of $f_{ct,t}/f_{ct,st}$ was 0.30, 0.49, and 0.27 for LL01.5, B01.5 and S01.5, respectively.

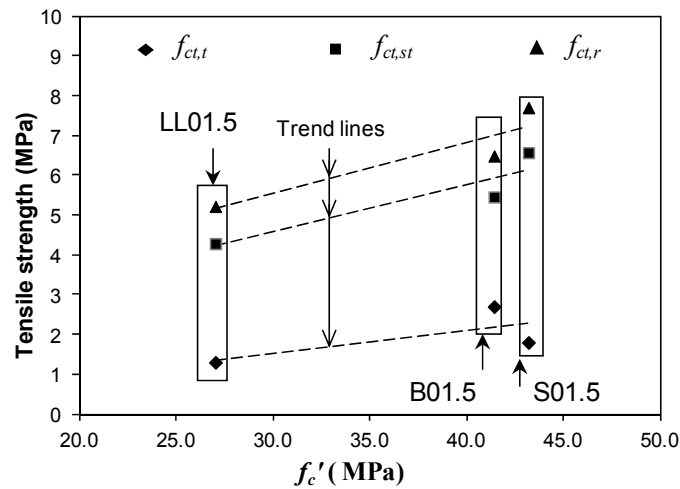


Figure 7.18- Relation of compressive strength and tensile strengths of GFRCC ($V_f=1.5\%$)

7.6 Conclusions

This chapter examined the tensile load-bearing behaviour of TRCC dog-bone shaped specimens. The TRCC specimens contained or omitted chopped glass fibers. The tensile test results presented in this study demonstrated that textile-reinforced ceramic concrete has promising potential for use as a structural material. An example of a potential application of these TRCCs is in the construction of thin lightweight wall panels and stay-in-place formwork for supporting bridges decks or building slab constructions. However, further

research is needed in order to optimize the amount and type of textile reinforcements and fibers.

Based on the experimental investigations presented in this chapter, the following conclusions can be drawn:

- After 28 days, no significant changes were observed for the compressive strength, split tensile strength or flexural tensile strength of GFRCC.
- The direct tensile strength, flexural and splitting tensile strength of GFRCC all increased as the compressive strength increased.
- The direct tensile strength, splitting tensile strength and the flexural strength of GFRCC ranged from 4% to 7%, 13% to 16% and 15% to 20% of the corresponding cylinder compressive strength, respectively.
- For GFRCC, the ratios of the axial tensile strength to flexural tensile strength and to splitting tensile strength were found to be 0.15 to 0.40 and 0.25 to 0.50, respectively.
- Compared to plain samples, the addition of one layer of textile reinforcement to plain ceramic concrete samples resulted in the formation of multiple cracking, improved the post-cracking performance, and increased the axial tensile strength by a factor of 2 to 3 times.
- The addition of 1.5% by volume of short glass fibers increased the first-crack stress and the axial tensile strength value by a factor of 1.5 to 3 and 1.2 to 2, respectively for specimens with one layer of textile.
- Compared to samples with one layer textile reinforcement, the axial tensile strength value of TRCC specimens increased by 1.1 to 1.3 times, while the corresponding strain reduced by 0.2 to 0.5 times when two layers of textiles were used.

7.7 References

- ASTM C469/C469M. (2002). Standard test method for static modulus of elasticity and poisson's ratio of concrete in compression. ASTM International, West Conshohocken, PA.
- ASTM C1609/C1609M. (2010). Standard test method for flexural performance of fiber-reinforced concrete (using beam with third-point loading). ASTM International, West Conshohocken, PA.
- ASTM C39/C39M–09a. (2009). Standard Test Method for Compressive Strength of Cylindrical Concrete Specimens. ASTM International, West Conshohocken, PA.
- ASTM C496. (2011). Standard Test Method for Splitting Tensile Strength of Cylindrical Concrete Specimens. ASTM International, West Conshohocken, PA.
- ASTM D6637. (2010). Standard test method for determining tensile properties of geogrids by the single or multi-rib tensile method. ASTM International, West Conshohocken, PA.
- Barhum, R. and Mechtcherine, V. (2012). Effect of short, dispersed glass and carbon fibres on the behaviour of textile-reinforced concrete under tensile loading. *Journal of Engineering Fracture Mechanics*, 92: 56-71.
- Bosche, A., Jesse, F., Ortlepp, R., Weiland, S. and Curbach, M. (2008). Textile-Reinforced Concrete for flexural strength of RC-structures-Part 1: structural behaviour and design Model. American Concrete Institute, Farmington Hills, MI, ACI SP-251: 19-40.
- Brameshuber, W., Koster, M., Hegger, J., Voss, S., Gries, T., Barle, M., Reinhardt, H. W. and Kruger, M. (2004). Integrated Formwork Elements Made of Textile Reinforced Concrete. American Concrete Institute, MI, ACI SP-224: 45-54.
- Bruckner, A., Ortlepp, R. and Curbach, M. (2006). Textile Reinforced Concrete for Strengthening in Bending and Shear. *Material and Structure Journal*, 39(8): 741-748.
- Butler, M., Mechtcherine, V. and Hempel, S. (2009). Experimental investigations on the durability of fibre-matrix interfaces in textile-reinforced concrete. *Cement and Concrete Composites*, 31: 221-231.

- Choi, Y. and Yuan, R. L. (2005). Experimental relationship between splitting tensile strength and compressive strength of GFRC and PFRC. *Cement and Concrete Research*, 35 (8): 1587-1591.
- Hartig, J., Haußler-Combe, U. and Schicktanz, K. (2008). Influence of bond properties on the tensile behaviour of Textile Reinforced Concrete. *Cement & Concrete Composites*, 30(10): 898–906.
- Hegger, J., Will, N., Bruckermann, S. and Voss, S. (2006). Loading-bearing behaviour and simulation of textile-reinforced concrete. *Materials and Structures Journal*, 39(8): 765-776.
- Hegger, J. and Voss, S. (2008). Investigations on the bearing behaviour and application potential of textile reinforced concrete. *Engineering Structures Journal*, 30(7): 2050-2056.
- Hegger, J., Schneider H., Voss, S., and Bergmann, I. (2008). Dimensioning and application of textile-reinforced concrete. American Concrete Institute, MI, ACI SP-250: 69-84.
- Heggar, J., Kulas, C. and Hortsmann, M. (2011). Realization of TRC facades with impregnated AR-glass textiles. *Key Engineering Materials*, 466: 121-130.
- Hinzen, M. and Brameshuber, W. (2009). Improvement of serviceability and strength of Textile Reinforced Concrete by using short fibres. *Proceeding*, 4th colloquium on textile reinforced structures (CTRS4), Dresden, 261–272.
- Kim, D. J., Wille, K., Naaman, A. E. and El-Tawil, S. (2011). Strength dependent tensile behavior of strain hardening fiber reinforced concrete. *In Proceedings: High Performance Fiber Reinforced Cement Composites (HPFRCC-6)*, Ann Arbor, MI: 20-22.
- Lepenies, I., Meyer, C., Schorn, H. and Zastrau, B. (2007). Modeling of the Load Transfer Behavior of AR-Glass-Rovings in Textile Reinforced Concrete. American Concrete Institute, MI, ACI SP-244: 109-124.
- Neville, A. M. (1996). Properties of concrete. John Wiley & Sons Ltd., New York. 580-600.
- Orlowsky, J. and Raupach, M. (2006). Modelling the loss in strength of AR-glass fibres in textile-reinforced concrete. *Materials and Structures Journal*, 39(6): 635–643.
- Tassew, S. T. and Lubell, A. S. (2010). Textile reinforced ceramic composite for structural infill slab application. *Proceeding of 34th IABSE Symposium*, Venice, Italy, A-0317, 1-8.

Chapter 7: Uniaxial Tensile Behaviour of Textile Reinforced Ceramic Concrete

Tassew, S. T. and Lubell, A. S. (2012). Mechanical properties of lightweight ceramic concrete. *Materials and Structures Journal*, 45(4): 561-574.

Weibull, W. (1939). The phenomenon of rupture in solids. *Proceedings of Royal Swedish Institute of Engineering Research*, Stockholm, 151:1–45.

Experimental Study on Reinforced Ceramic Concrete Slabs

8.1 Introduction

Lightweight concrete (LWC) has many applications including, but not limited to, bridge decks and building floor slabs. The use of LWC for structural members has several advantages compared to normal weight concretes by providing lower self weight, reducing substructure cost, allowing longer spans, reducing steel reinforcement requirements due to lower self weight, and improving the seismic structural response of the structure due to lower mass and density (Chandra and Berstsson, 2002).

The use of LWC for flexure critical structural members was investigated previously (e.g., Lim et al., 2006, 2011; Wu et al., 2011; Ahmad and Barker, 1991; Ahimad and Batts, 1991; Swamy and Lambert, 1984). The amount of longitudinal reinforcing steel and the concrete compressive strength are two important parameters that are well known to affect the flexural behaviour of reinforced LWC members. As the amount of tensile reinforcement is increased, the post-cracking stiffness as well as the ultimate strength of the flexural member increases, but the flexural ductility and the maximum crack widths for a given loading reduce (e.g., Lim et al., 2006, 2011; Wu et al., 2011; Ahimad and Batts, 1991). Similarly, as the concrete compressive strengths of LWC flexural members

increase, the first cracking load, the post-cracking stiffness, ultimate strength and flexural ductility all increase (e.g., Lim et al., 2006).

Recently, several researchers have studied the performance of textile reinforced concrete (e.g., Hegger et al., 2006; Bruckner et al., 2006, 2008; Bosche et al., 2008; Hegger and Voss, 2008). Textile reinforced concrete (TRC) is an innovative composite material consisting of multi-layers of textile fabric reinforcing mesh and a fine-grained concrete. Use of TRC has several advantages compared to conventional steel reinforcement, such as resistance to corrosion when non-metallic textile is used (Hegger et al., 2006; Bosche et al., 2008). Due to the very small diameter of fibers making up the textile reinforcement, it is possible to produce very thin and lightweight concrete elements that conform to complex shapes (Bruckner et al., 2006).

TRC can be used for both new structures as well as for strengthening of existing structures. Application of TRC for new structures includes construction of bridge components (e.g., Hegger et al., 2011), and as wall panels in buildings (e.g., Hegger and Voss, 2008; Hegger et al., 2012). On the other hand, applications of TRC for strengthening of structural elements include slabs, beams and columns (e.g., Bruckner et al., 2006; Bosche et al., 2008). Reinforced concrete flexural elements strengthened by TRC can noticeably improve both the load-bearing behaviour as well as the serviceability performance (e.g., Bruckner et al., 2006). However, the strengthening effect of TRC greatly depends on the material properties of the textiles used (Bosche et al., 2008), the amount of the textile reinforcements and the properties of the fine concrete matrix (Hegger et al., 2006).

The performance enhancement to the mechanical properties of ceramic concrete made using magnesium potassium phosphate binder and different aggregates by adding textile reinforcement or short discontinuous glass fibers were demonstrated in Chapters 6, 7 and Tassew et al. (2011). The mechanical properties of glass fiber reinforced ceramic concretes (GFRCC) were studied in

Chapter 6. These concretes showed mechanical properties comparable to those of Portland cement based LWC. The compressive strength and density of GFRCC containing lightweight aggregates ranged between 22.8 and 26.2 MPa and 1790 and 1820 kg/m³, respectively, depending on the fiber volume fraction. Even though these ceramic concretes exhibited acceptable compressive strengths and densities, they lack the required tensile strength to be used for structural application for flexure critical members.

In Chapter 5 it was shown that the tensile strength of ceramic concrete panels was increased when textile reinforcement was used, but large deformations were observed. These large deformations may affect the ability to satisfy serviceability requirements when used in some flexure critical members. Therefore, when using textile reinforced ceramic composite for flexure critical structural members and to overcome the potentially brittle post-peak response and large deformations, it is proposed to additionally use deformed steel reinforcing bars that have a significantly higher axial stiffness than the textile fabrics. This chapter examines the behaviour of this composite system for flexure critical structural elements.

An experimental investigation of the flexural behaviour of 6 full-scale composite slab strips made using GFRCC concrete and reinforced with both conventional deformed steel reinforcing bars and textile fabrics was completed. The overall dimensions of all slab specimens were kept constant but other parameters including the number of textile layers, the longitudinal steel reinforcement ratio and the composition of concrete mix were varied. The slab strips were tested under four-point bending. The primary objective was to investigate the flexural behaviour of the slabs including the load carrying capacity, failure modes, deformation and ductility as well as the crack development during loading.

8.2 Slab Configurations

A total of six slab strip specimens were constructed and tested to failure under four-point bending (see Figure 8.1). All the slab specimens had a nominal depth (h) of 150 mm, width (b) of 200 mm and overall length of 2200 mm. The cross-

section configuration of each specimen was different, as illustrated in Figure 8.2, to investigate the influence of configuration on the structural response.

Among the specimens, different design parameters were varied:

- number of textile layers ($N_L = 0$ or 2 layers)
- longitudinal steel reinforcement ratio ($\rho = 1.15\%$ or 1.92%), determined as $\rho = A_s / (b d)$, where A_s is the total bar area, b is the slab cross-section width and d is the effective depth of the reinforcing bars measured from the compression face
- type of GFRCC matrix (FLL, FB or FS)

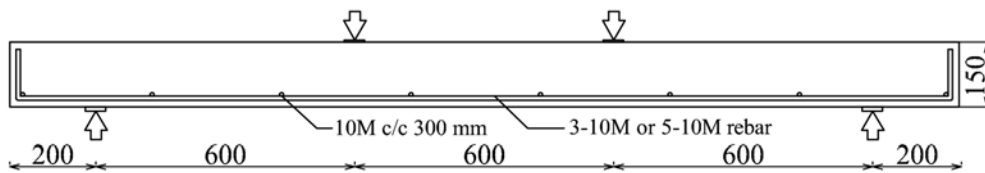


Figure 8.1- Dimensions of reinforcement details for test specimens

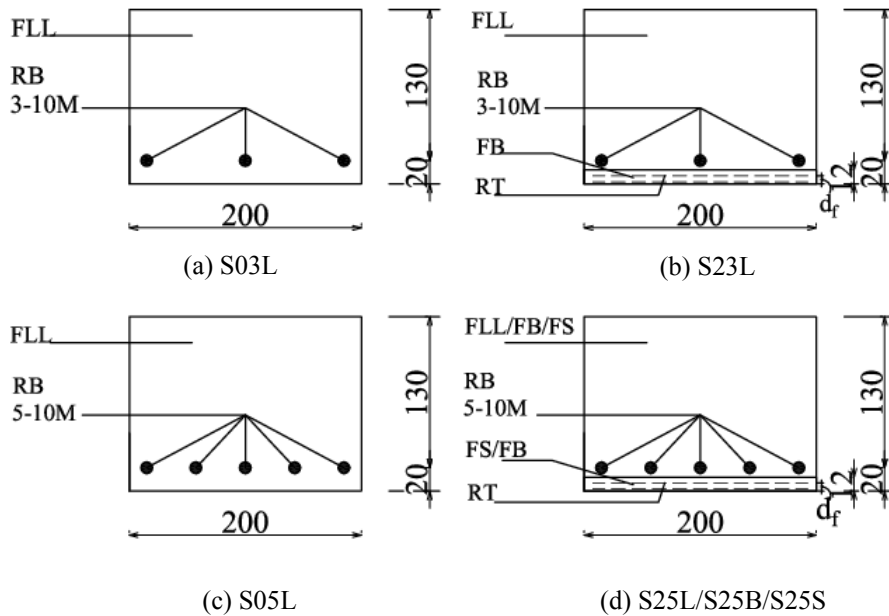


Figure 8.2- Cross-sections for the test slab

The nomenclature to identify the slab specimens is illustrated in Figure 8.3. The naming convention has four components: the first letter indicates the type of member (a letter “S” to represent slabs), the first number indicates the number of textile layers (N_L , 0 or 2 layers), the second number indicates the number of 10M steel reinforcing bars (3 or 5), and the last letter indicates the type of GFRCC matrix used (L for mix type FLL, B for mix type FB and S for mix type FS).

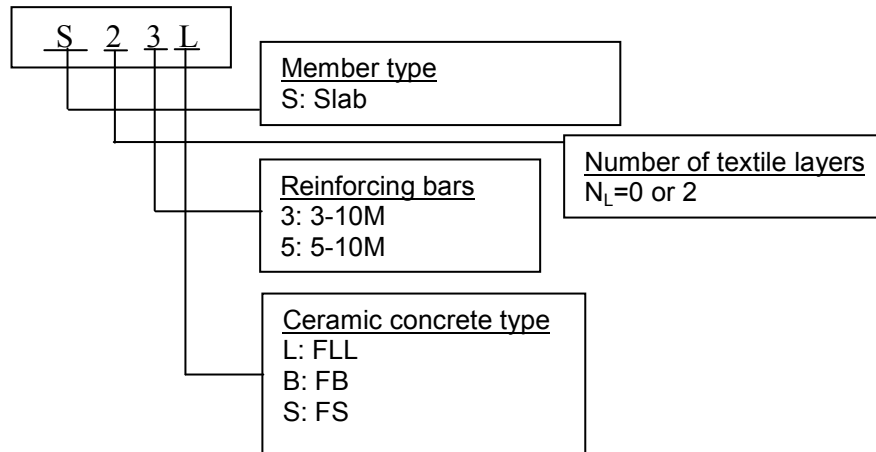


Figure 8.3- Detail of test specimens identification

The summary of geometry and material properties of the six tested slab specimens are presented in Table 8.1.

Table 8.1- Slab geometry and ceramic concrete material properties

Specimen ID	Cross-section (mm)		d (mm)	Reinforcement				Concrete		
	b	h		Textile		Steel		f'_c (MPa)	ϵ_{co}	E_c (GPa)
				N_L	d_f (mm)	A_s (mm ²)	ρ (%)			
S03L	201	155	130	0	0	300	1.15	26.1	0.0030	13.1
S23L	201	155	120	2	8	300	1.24	23.2	0.0030	11.1
S05L	202	154	130	0	0	500	1.90	24.5	0.0030	11.0
S25L	203	155	120	2	8	500	2.05	22.8	0.0028	10.4
S25B	201	153	120	2	8	500	2.07	35.7	0.0038	13.1
S25S	204	153	120	2	8	500	2.04	42.7	0.0042	12.1

As illustrated in Figure 8.2, the cross-section configuration of each specimen was different. Four slab samples were produced using FLL concrete. Specimen S03L was reinforced with 3-10M longitudinal bars and contained no textile reinforcement (Figure 8.2(a)). Specimen S23L was similar to S03L, but the bottom 12 mm depth of the slab was replaced by a textile reinforced ceramic concrete (TRCC) layer made from FB concrete and two textiles fabric sheets (RT) (Figure 8.2(b)). FB was used in the TRCC layer instead of FLL as the maximum aggregate size in FLL was larger than the textile fabric openings. The other slabs made from mix type FLL (i.e., S05L and S25L) were produced similar to S03L and S23L, but 5-10M steel bars replaced the 3-10M longitudinal reinforcing steel bars as shown in Figure 8.2 (c) and (d). No transverse reinforcement was used in any of the specimens, but short 10M bars across the width of the specimens were used as shown in Figure 8.1 for spacing and tying the longitudinal reinforcements at a specific position.

An additional two slabs were also produced using FB concrete (S25B) or FS concrete (S25S). Similar to S25L, these slabs were reinforced with 5-10M bars and two layers of textile reinforcement at the bottom of the slab (see Figure 8.2 (d)).

The textile reinforcement used had a total effective depth measured from the tension face (d_f) of 8 mm (see Figure 8.2) that includes the total depth of two textile fabric sheets and the ceramic concrete between them. The total width of textile reinforcement was 185 mm and had a clear cover of approximately 7.5 mm at each side of the mold.

8.3 Materials

The materials used to produce the slab specimens were glass fiber reinforced ceramic concrete (GFRCC), textile fabric and steel reinforcement. The mechanical properties of these materials are discussed in this section.

8.3.1 Ceramic Concretes

Adopting ceramic concrete mixes from Chapters 6 and 7, three GFRCC matrices were produced with a magnesium potassium phosphate (MPPC) binder, different aggregate types and short glass fibers. The mix compositions are given in Table 8.2.

Table 8.2- Mix proportion of GFRCC

Mix type	Materials mass ratio			Volume fraction
	b^a	LL/SA/BC ^a	w^a	$V_f(\%)$
FLL	1	0.54	0.20	1.5
FB	1	0.67	0.20	1.5
FS	1	0.67	0.20	1.5

^a b : binder; LL: LECA aggregates; SA: sand aggregates; BC: Buildex expanded shale aggregates; w : water; V_f : volume of fiber

The MPPC binder (b) was composed of magnesium oxide (MgO), monopotassium phosphate (KH₂PO₄) and fly ash (FA). The properties of these materials were given in section 4.2. The dry ingredients of the MPPC binder (b) were prepared at a mass ratio of MgO: KH₂PO₄:FA = 1:3.4:4.4.

Mix type FLL contained lightweight expanded clay aggregate (LECA) in two different gradations: fine and coarse. The maximum particle size of the fine LECA (i.e. FL) was 2.5 mm and the maximum particle size of coarse LECA (i.e. CL) was 10 mm. The specific gravity and water absorption were 0.995 and 24.4% for the CL and 1.49 and 10.25% for the FL, respectively. In mix type FB, Buildex coated expanded shale aggregate was used with maximum aggregate size of 2.5 mm and specific gravity of 1.58. The aggregate used in mix FS was sand having maximum aggregate size of 1.25 mm and with specific gravity of 2.65. The aggregate gradation curves were given in section 6.2.1.

All GFRCC mixes contained 13 mm chopped glass fibers at a volume fraction of 1.5% of the total mix. The dosage was established from section 6.2 considering

the workability of the mix. The glass fibers had a diameter and a specific gravity of 18 μm and 2.7, respectively.

The water to binder ratio (w/b) was fixed at 0.20 based on Chapter 4 selected to satisfy the desired strength and workability. To control the setting time a commercially available lignosulphonate admixture was used in all mixes at a dosage of 1.5% by mass of the binder, established from Chapter 4.

The mixing process used to prepare all GFRCC mixes was similar and is described in section 8.4.2.

The workability of some batches of the GFRCC used in the slab specimens was measured by a slump test that was conducted in conformance with ASTM C143 (2010). This test was completed within 2 minutes after mixing was stopped. A standard frustum mold with base diameter of 200 mm, top diameter of 100 mm and height of 300 mm was used. The mold was firmly held in place and filled with the GFRCC in three layers, compacting by rod each layer 25 times. After lifting the mold, the average diameter of spread was recorded. The slump flow of ceramic GFRCC is expressed here as the percentage increase in diameter of the spread over the base diameter of the cone. The measured slump flow varied from 65-85%, 115-120% and 135-155% for mix types FLL, FB and FS, respectively. This suggested that the mixes had a good consistency. All the GFRCC mixes exhibited a good workability during placing and compacting.

The cylinder compression test of GFRCC used in each mix batch was evaluated using 100 mm diameter and 200 mm high cylinders. These tests were completed according to ASTM 469 (2002) on the same date when the slabs were tested. Note that two batches of each mix were required to prepare each slab due to the capacity of the mixer. Three cylinders were tested for each of the two batches of each mix type. The average of all 6 six cylinders per mix type is reported here. No significant difference was observed between the two mix batch results (maximum 9%). Further, the average stress-strain curves of GFRCC from the two batches were developed and the results are summarized in Figure 8.4 and Table 8.3. From

Table 8.3, the f_c' of mix types FLL, FB and FS were 22.8-26.1 MPa (CV=1.10-6.21%), 35.7 MPa (CV=4.39%) and 42.7 MPa (CV=3.56%), respectively at the day of test of the corresponding slabs. Note that prior study showed that the mechanical properties of GFRCC varied only slightly with ages beyond 28 days (Chapter 7). The strain values at peak stresses of Portland cement lightweight concrete typically range between 0.003 and 0.0035 (e.g., Nilson et al., 2004). In this study, the ϵ_{co} values of the GFRCC ranged between 0.0028-0.0042 mm/mm.

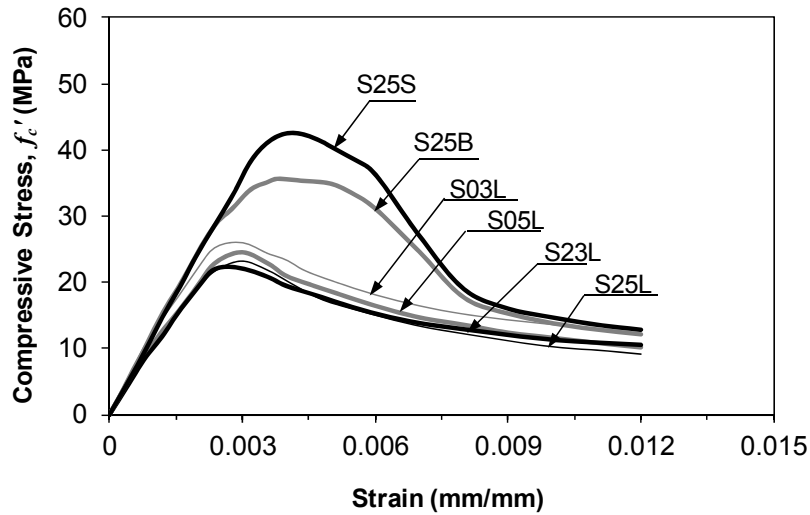


Figure 8.4- Average compressive stress-strain curves for all the slab samples

Table 8.3- GFRCC properties (Average)

Slab ID	Concrete type	Age of test (Days)	f_c' (MPa)	ϵ_{co} (mm/mm)	E_c (GPa)
S03L	FLL	70	26.1	0.0030	13.1
S23L	FLL	65	23.2	0.0030	11.1
S05L	FLL	68	24.5	0.0030	11.0
S25L	FLL	63	22.8	0.0028	10.4
S25B	FB	59	35.7	0.0038	13.1
S25S	FS	57	42.7	0.0042	12.1

The secant modulus of elasticity of GFRCC was determined from the slope of a straight line that connects the stress corresponding to a strain value of 50×10^{-6} to a stress corresponding to $0.4f_c'$ (ASTM 469, 2000) and summarized in Table 8.3.

The modulus of elasticity of structural lightweight Portland cement concrete is generally lower than for normal weight concrete of similar compressive strength (Short and Kinniburgh, 1978). Values of E_c for lightweight Portland cement concrete typically range between 10 to 24 GPa (FIP Manual, 1983) and flexure critical members made using lightweight concrete are more flexible because bending stiffness is related to the product of modulus of elasticity and moment of inertia (ACI Committee 213, 2009). In this study, the E_c -values for the GFRCC ranged between 10.4-13.1 GPa, within the range for PC based lightweight concrete.

In Chapter 7, the modulus of rupture of 100 x 100 x 400 mm³ notched prisms under four-point bending were evaluated at 60 days age, which was close to the average test age of specimens in this study. The mix compositions used for preparing prisms in Chapter 7 were similar to the mix compositions used for preparing slab specimens. Thus, the Chapter 7 results are considered representative since these specimens were prepared from different mix batches as for the slabs. For mix types FLL, FB and FS, the average modulus of rupture of three samples was 5.4 MPa, 7.7 MPa and 7.9 MPa, with CV of 8.57%, 1.34% and 8.61%, respectively (Chapter 7). The load versus deflection results for prisms are discussed in Chapter 7.

8.3.2 Textile Fabric

A bi-directional glass woven textile fabric with a yarn spacing of 7 mm in the longitudinal as well as transverse direction was used (see Figure 8.5(a)). The warp yarns were aligned in the longitudinal direction of the slab specimens. The mechanical properties of the textile fabric determined using tensile tests are given in section 7.2.2. The average tensile strength of the textile fabric was 32 kN/m (CV=8.96%) at a strain of 1.4% (CV=15.30%) and modulus of elasticity of 33700 kN/m (CV=8.70%).



(a) Woven glass textile fabric



(b) Deformed steel reinforcing bars

Figure 8.5- Slab reinforcement materials

8.3.3 Steel Reinforcement

Deformed steel reinforcing bars (see Figure 8.5 (b)) in the Canadian customary size of No. 10M were used as longitudinal reinforcing bars. Each bar has a cross-sectional area of 100 mm^2 (CSA A23.3-04). The bars were Grade 400.

The mechanical properties of the steel were evaluated using tension coupon tests. Three test coupons were cut from randomly selected bars from the steel used. All steel bars were from the same heat of steel. The total length of each coupon was approximately 600 mm, which included a gauge length of 200 mm and a minimum length of 125 mm at each end used within the machine grips.

After the coupons had been cut to the required length, marks spaced at 50 mm were punched along the gauge length, according to ASTM A370 (2011). The steel coupons were tested in a 1000 kN capacity MTS testing machine. First, the bottom 125 mm length was placed into the hydraulic grip, followed by lifting the lower crosshead of the machine. The steel coupon was aligned and the top hydraulic grip was applied to the specimen. A 50 mm gauge length extensometer was attached to the central part of the reinforcing steel coupon as shown in Figure 8.6. After setting the load and extensometer reading in the data acquisition system to zero, the load was applied using a machine crosshead speed of 5 mm/min according to ASTM A370 (2011). When the extensometer reading reached a strain of 0.03 mm/mm, loading was paused and the extensometer was removed to prevent damage. Loading was resumed at the same rate until fracture of the steel coupon occurred.

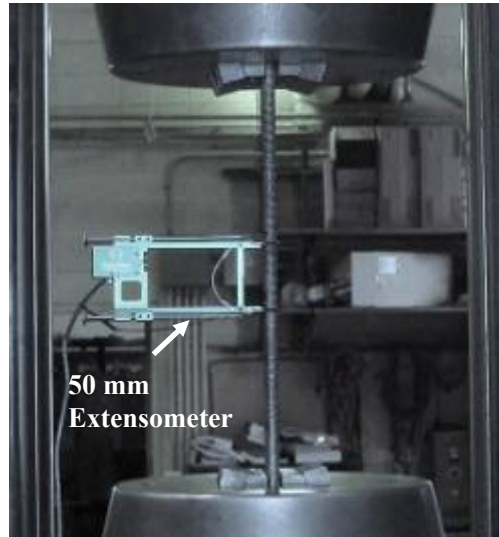


Figure 8.6- Reinforcement tensile test set-up

An average stress-strain diagram obtained from the coupon tests of reinforcing steel is given in Figure 8.7. The stress values shown were calculated by dividing the recorded load by the nominal cross-sectional area (100 mm^2). The strain values indicated were directly measured by the extensometer. Since the stress-strain curve showed no well-defined yield plateau, the yield stress (f_y) was obtained by using the 0.2% offset method specified in ASTM A370 (2011).

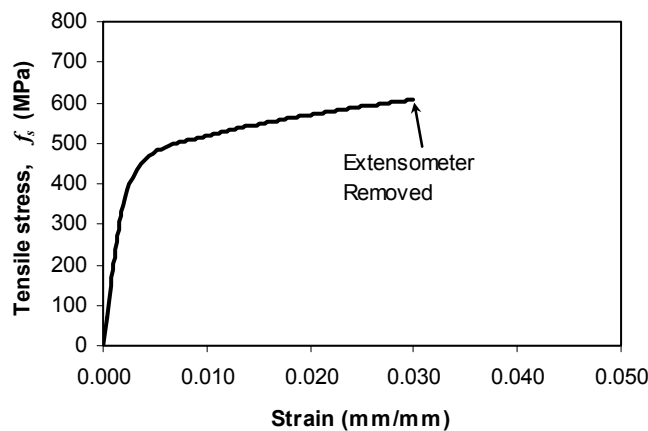


Figure 8.7- Average tensile stress-strain curve of reinforcing steel

The average properties of reinforcing steel in the test slabs are summarized in Table 8.4. The modulus of elasticity (E_s) was determined from the slope of the

linear part of stress-strain curve. The yield strain (ϵ_{ys}) was calculated by dividing f_y by E_s . The ultimate stress (f_{us}) shown in Table 8.4 was found by using the recorded peak-load and rebar nominal area, and the corresponding strain (ϵ_{us}) was calculated from the elongation of the final gauge length and original gauge length (200 mm). The final gauge length was found manually by fitting the two fractured coupon pieces together after tensile test and measuring between previously marked gauge points.

Table 8.4- Reinforcing steel properties

Bar designation	Area (mm ²)	f_y (MPa)	ϵ_{ys} (mm/mm)	E_s (GPa)	f_{us} (MPa)	ϵ_{us} (mm/mm)
10 M	100	470	0.0024	198	669	0.17

8.4 Slab Specimen Fabrication

8.4.1 Formwork and Reinforcing Material Preparation

Formwork was fabricated at the University of Alberta structural engineering laboratory by assembling different sizes of timber and plywood. Timbers with a size of 38 x 89 mm (1.5" x 3.5") cross-section and length of 3500 mm (12'), and plywood with size of 1220 x 2400 mm (4 x 8') and thickness of 18.5 mm (3/4") were used. After production of the molds, two coats of epoxy paint were applied on the forms to minimize sticking of the ceramic concrete to the form. The completed form is shown in Figure 8.8(a).

The steel reinforcement cages were tied together using steel wires according to the arrangements described in Figures 8.1 and 8.2. All longitudinal reinforcement bars had 90° hooks at each end with a hook length of 120 mm to enhance the anchorage. The reinforcement bars were evenly spaced across the cross-section width as shown in Figure 8.2. Spacer bars having similar diameter as longitudinal reinforcement were also provided across the specimen width at centre-to-centre spacing of 300 mm as illustrated in Figure 8.1. The locations of the steel reinforcement in the molds were achieved using small chairs cut from similar

ceramic concrete as the specimen and produced earlier. Two 10M steel lifting hooks were placed at the two ends of the slab located outside of the test regions. The typical formwork and reinforcement configuration prior to casting of concrete is shown in Figure 8.8(b). Note that the formwork was reused multiple times to construct all specimens. It was cleaned and oiled prior to placement of the reinforcements for each use.



(a) Form work

(b) Reinforcement cage

Figure 8.8- *Form work and reinforcement layout*

8.4.2 Mixing Concrete, Casting and Curing of Slab Specimens

8.4.2.1 Mix Procedure

The mixing of ceramic concrete was done at the University of Alberta concrete laboratory. All mixes were prepared using a 70l capacity rotary drum mixer. The mixing sequence used for all specimens was similar and contained two phases: dry mix and wet mix. The dry binder was composed of magnesium oxide, monopotassium phosphate and fly ash. For mix type FS, sand was also included into the dry mix. After weighing and preparing the dry binder materials, the dry binder was placed into empty pails and hand mixed using a scoop to obtain uniform distribution of the binder materials. Hand mixing was preferred over use of the drum mixer for the dry mix ingredients to prevent spillage out of the mixer.

For the wet mix, about 2/3 of the mixing water combined with 2/3 of the lignosulphonate retarder, 2/3 of the dry binder mix and 2/3 of the aggregates were added into a standing mixer. Note that the lightweight aggregates were used in a saturated surface dry condition after soaking for at least 24 hours. The mixer was started and the batch was mixed for approximately 3 minutes until a uniform mix consistency was achieved. The mixer was then stopped and the sides were scraped. The mixer was restarted and the remaining batch materials (dry binder mix, water and aggregates) were gradually added to the mixer in the same order as stated and mixed until a uniform colour and consistency was observed in the mixer. This mixing period took a total of about 3 minutes. While the mixing drum was still rotating the glass fibers were gradually added by hand over a period of 2 minutes to disperse them into the mix. The mixing drum was rotated for an additional 2 minutes before it was stopped to scrape the sides. Finally, the material was mixed for an additional 2 minutes until a visually uniform mix was achieved. No fiber balling effect was observed. The entire wet mixing process time was 12-15 minutes.

8.4.2.2 Casting Slab Specimens

The fresh concrete was poured from the mixer directly into the mold using a plywood chute (see Figure 8.9(a)). The mix was spread in the mold to a uniform height using a scoop and compacted using an electrical immersion vibrator. The top surface was then screeded as shown in Figure 8.9(b).

Two batches of concrete were needed to fill each slab mold due to the mixer capacity. About half height of the molds were filled by each batch. As noted in Section 8.3.1, three cylinders of size 100 mm diameter and 200 mm high were prepared for each batch, to determine the complete stress-strain response, the compressive strength and modulus of elasticity at the same age as the slabs.

After casting, all slab specimens and cylinders were covered with plastic sheets. All slabs and cylinders were demolded after 24 hours and air cured in the laboratory until tested.

A total of six specimens were prepared. As shown in Figure 8.2 the slab specimen cross-section configurations were different. Four specimens contained two layers of textile reinforcement in addition to the steel reinforcing bars while two specimens were prepared without textile reinforcement. The construction steps used to prepare each slab configuration are described below:

(a) Slabs with textile fabric (S23L, S25L, S25B, S25S)

First, a layer of textile fabric reinforcement was placed in the formwork followed by approximately 6 mm depth of ceramic concrete (mix type FS or FB), which was vibrated. Then another layer of textile reinforcement was placed (Figure 8.10(a)) and gently pressed manually into the wet concrete. Another thin layer of ceramic concrete (mix type FS or FB) about 6 mm thick was placed on top of the upper textile reinforcement and vibrated. After some minutes the top concrete surfaces were hand scraped parallel to the length of the form using a 10 mm steel rod to obtain a rougher surface for bonding of subsequent layers of concrete (see Figure 8.10(b)).

After the TRCC layer had set, the steel reinforcement cage was placed in position (see Figure 8.2) using thin concrete chairs. The upper ceramic concrete (FLL, FS or FB) was placed to a total specimen nominal depth of 150 mm. Note that the upper ceramic concrete depth was filled using two batches of GFRCC due to the capacity of the mixer. However, when the second layer was placed, the first layer was still wet and the vibrator was inserted to reach the top of the TRCC. Thus, both batches were vibrated together to obtain continuity between the two layers. A so-called cold joint could be present to the lower TRCC.

(b) Slabs without textile fabric (S03L and S05L)

The steel cages were placed into the wooden molds at planned position using concrete chairs. The molds were then filled using two batches of mix type FLL concrete using similar procedures as the slabs with textile fabric described in (a).



(a) Pouring and spreading of concrete



(b) After screeding

Figure 8.9- Slab specimen preparation process



(a) Placing textile



(b) Scraping

Figure 8.10- Textile reinforced layer preparation and surface scraping

8.5 Test Set-up, Instrumentation and Procedure

8.5.1 Test Set-up

All specimens were tested under four point bending. A schematic of the test set-up is shown in Figure 8.11. The general view of the test set-up is presented in Figure 8.12.

The slab specimen was supported by two support assemblies, each containing a roller, a knife-edge, a 100 kN capacity load cell and a bearing plate (see Figure 8.13(b)). The distance between the support centrelines for all specimens was 1800 mm. The two support assemblies were situated on a stiff steel beam, which was fixed to the laboratory strong floor. Loading was applied using a hydraulic actuator with a capacity of 529 kN mounted in a steel reaction frame. The load was transferred from the actuator to the specimen as two equal concentrated loads using a stiff spreader beam and two loading assemblies each containing a roller, a knife edge and a bearing plate (see Figure 8.13(a)). The distance between the centres of loads was 600 mm for all specimens. The bearing plates at the loading points and at the supports were the full width of the specimens and had dimensions of 200 x 100 x 10 mm and 200 x 100 x 50 mm, respectively. A thin layer of plaster was used between all bearing plates and the specimens to ensure uniform contact.

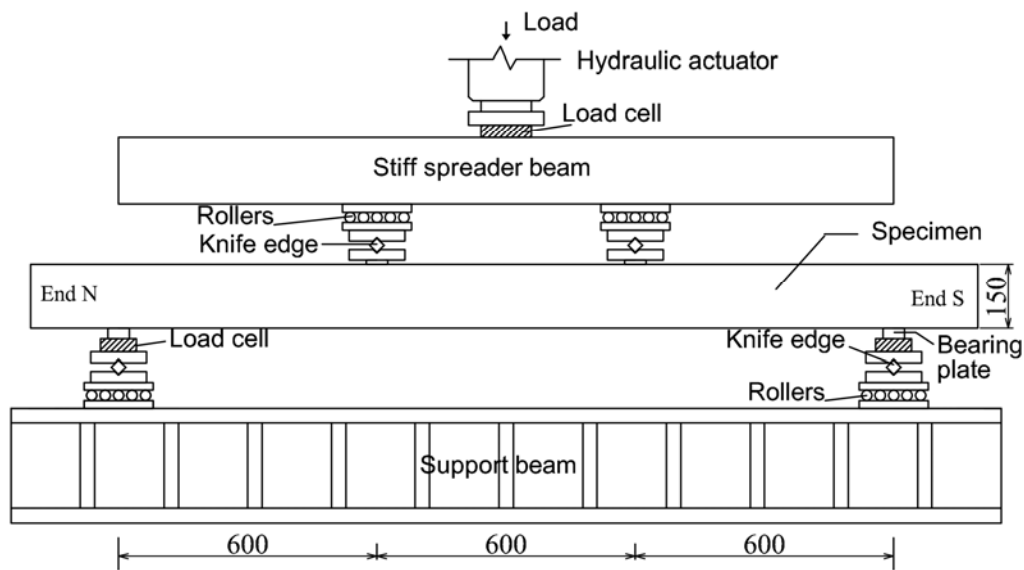


Figure 8.11- Schematic of the test set-up for slab specimens



a) East side view



b) West side view

Figure 8.12- General views of the test set-up and instrumentations

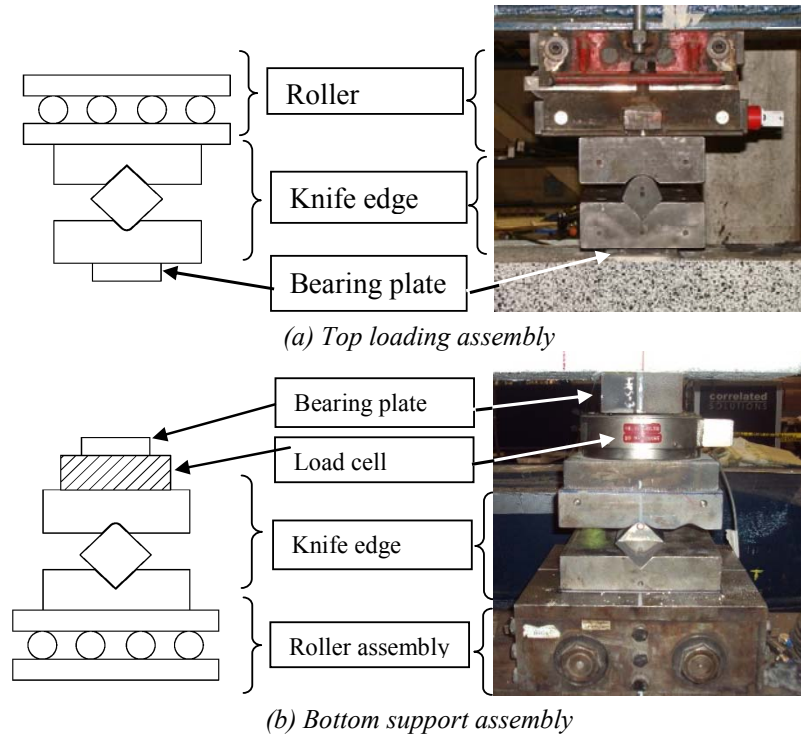


Figure 8.13- Detail of support systems

8.5.2 Instrumentation

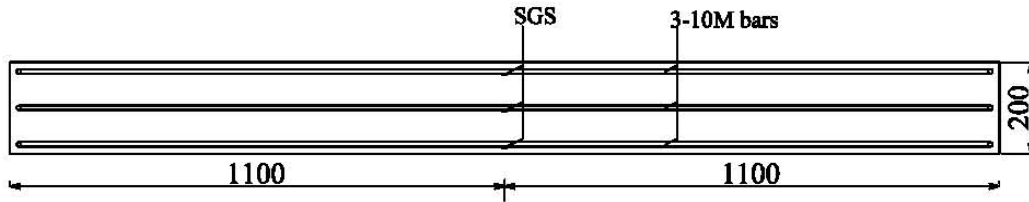
The instrumentation for all specimens was similar. During the tests the flexural responses including the applied load and reaction force, strains at mid-span on the flexural compression and tension sides, the vertical deflection, the inclination at constant moment region and crack development were recorded. All data except the crack behaviour was continuously recorded by the main data acquisition system at a sampling rate of 0.1 Hz. The crack behaviour was investigated using a digital image correlation (DIC) system and this data was recorded by a second data acquisition system. The load data was recorded by both data acquisition systems to allow synchronization. The summary of instruments used during the tests and the corresponding designations are presented in Table 8.5 and described below.

Table 8.5- List of instrumentation for each specimen

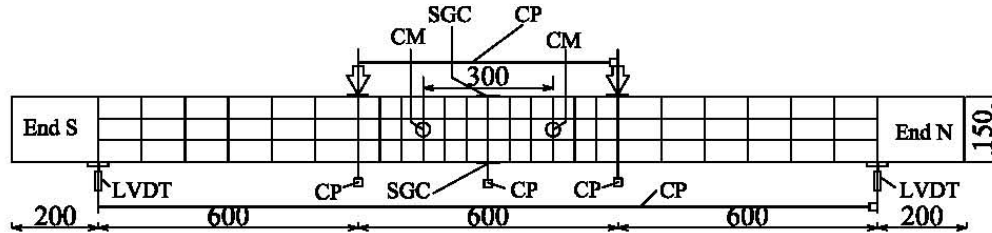
No.	Type of instrumentation*		Measurement direction	Designation	Total number
1	Strain gauge on reinforcement		Axial	SGS	3
2	Strain gauge on concrete		Axial	SGC	2
3	Linear variable differential transducer		Vertical	LVDT	2
4	Cable potentiometer		Vertical/ Horizontal	CP	6
5	Inclinometer		Rotational	CM	2
6	Camera system (Vic-2009)	At North side	-		1
		At South side	-		1
7	Load cells at supports		Vertical	LC	2
8	Hydraulic actuator (Load cell)		-	LD	1
* See Figure 8.14 for locations					

Strain gauge on reinforcement (SGS). Electrical resistance strain gauges of type KFG-5-120-C1-11 with gauge length of 5 mm were installed on three different reinforcing bars at the mid-span as shown in Figure 8.14(a).

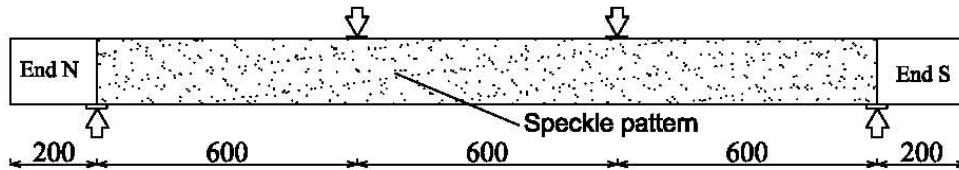
The strain gauge installation procedure was similar in all cases. First, a small portion of the rebar at the strain gauge location was levelled using a small hand grinder. The surface of the bars was degreased and the surface was made smooth using sand paper. After scrubbing the area thoroughly with Neutralizer 5A, the strain gauge was attached to the rebar using M-Bond adhesive. The strain gauge was connected to a wire using a soldering iron. Finally, to protect the strain gauge from damage the area was covered using a thin layer of silicon gel. All strain gauges were installed prior to assembling the reinforcement cages.



(a) Typical steel strain gauge location (Plan view)



(b) LVDTs, CP, CM, LVDT and concrete strain gauge locations (East side view)



(c) DIC speckle pattern paint (West side view)

Figure 8.14- Schematic view of instrumentation for slab specimen

Strain gauge on concrete (SGC). Two strain gauges of type N2A-06-20CBW-350 with gauge length of 50.8 mm (2.0 inches) were installed on each specimen at mid-span to measure the longitudinal concrete strains during loading. One gauge was placed on the top surface and the other gauge on the bottom concrete surface as shown in Figure 8.14(b).

The strain gauge installation procedure was similar for all specimens. First, a small portion of the concrete surface at the strain gauge location was made smooth using sand paper. After cleaning the area, a thin layer of 5-minute epoxy was applied and the surface was levelled. The strain gauge was attached to the prepared surface using M-Bond adhesive. The strain gauge was connected to a wire using a soldering iron. M-coat A was applied over the strain gauge to protect it from damage.

Linear variable differential transducer (LVDT). Two LVDTs with working range of 50 mm were used to measure vertical settlement between the specimen and each support as shown in Figure 8.14(b). Also see Fig. 8.12(b).

Cable potentiometer (CP). Four cable potentiometers were used to measure the deflection profile. Two of the CP's were placed at mid-span: one at the West (Nominal range: 250 mm) and the other at the East edge (Nominal range: 508 mm) (Figure 8.14(b)). The average of these two measurements was taken as the mid-span deflection. The other two CP's (Nominal range: 250 mm) were placed below the specimen at the location of each applied load, as shown in Figure 8.14(b). In all cases, the end of the CP cable was attached to the specimen using a small aluminum plate glued to the specimen surface using 5 min epoxy adhesive. Additionally, one CP (Nominal range: 508 mm) was used to measure the horizontal movement between the two supports and another one (Nominal range: 508 mm) to measure the horizontal movement between the two loading points (see Figure 8.14(b)). These were used to examine the horizontal deformation of the shear spans to confirm that the rollers were not restrained from motion.

Inclinometer (CM). Two inclinometers with working range of $\pm 60^\circ$ were used to measure the rotation of the specimens at two locations in the constant moment region separated by 300 mm as shown in Figure 8.14(b). The measurements were subsequently used to obtain the average curvature of the specimen in the constant moment region. The CM's were fixed to the specimen surface using 6 mm (1/4") threaded rods securely fixed to rod anchors embedded approximately 10 mm deep into the specimen surface.

Camera system (CN and CS). An optical instrumentation system based on the digital image correlation (DIC) technique was used to monitor the West face of each specimen (See Figure 8.15). This allowed studying the cracking behaviour throughout the load history using the software Vic-Snap 2009 and Vic-3D 2009 (Correlation Solutions, 2009). Similar specimen preparation was used for all specimens. A thin coat of white latex paint was first applied to the specimen

surface. A speckle pattern using black paint was applied following the recommendations in the Vic-3D Testing guide (Correlated Solutions Inc., 2007). Typical speckle sizes between 3 and 4 pixels were used (see Figure 8.14(c)).

Two pairs of cameras were positioned as shown in Figure 8.15. One camera pair was placed at North end (CN) and the other at South end (CS) of the specimen mid-span. Each image covered one half of the specimen elevation with minimal overlapping area at the mid-span. All cameras had 12.5 mm focal length lenses (FUJION 1:1.4/12.5 mm HF12.5SA-1). The set up, focusing and calibration of the cameras were done according to the procedure outlined in Vic-3D Testing Guide (Correlated Solutions Inc., 2007). Each camera pair was connected to a data acquisition system that allowed viewing of the camera images in real time. The load channel from the main data acquisition system was also connected to allow synchronizing of the test data sets. The image acquisition interval was 10 seconds per image pair.

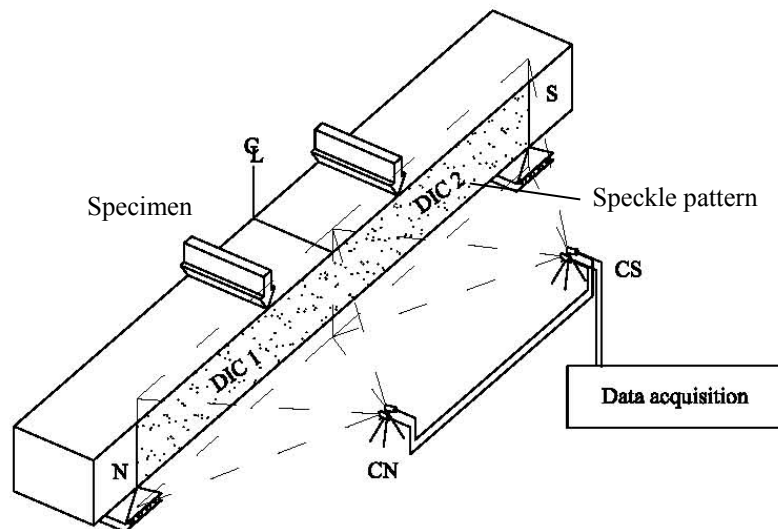


Figure 8.15- West side view and digital camera system set-up

Load cell (LC). Two load cells with a capacity of 100 kN each were placed below the specimens at the support assemblies. See Figure 8.11.

Loading device (LD). The force from the hydraulic actuator was measured by a load cell mounted between the actuator and the top spreader beam. This load cell results were used for all load values reported in this chapter. The stroke of the actuator was measured by an LVDT directly mounted on the actuator that was also used to control the loading rate.

8.5.3 Test Procedures

All specimens were tested using similar procedures described below:

1. A bearing plate was placed on the support assembly system. The specimen was then placed on the bearing plate after placing a thin layer of plaster. The loading spreader beam was not in contact with the specimen.
2. All instruments were connected and were checked to ensure they functioned correctly.
3. The readings of the load cells at the supports were set to zero.
4. Initial reference images were taken by the DIC system.
5. Continuous readings by the main data acquisition system were started.
6. A bearing plate was placed on the specimen at the loading location after placing a thin layer of plaster.
7. The spreader beam and loading assemblies were initially supported above the specimen using a chain pulley system. These were slowly lowered until they were in contact with the bearing plates (see Figure 8.12) and the load cells measured the full weight of this loading apparatus. Note that the spreader beam together with the loading assembly was approximately 10.2 kN.
8. The hydraulic actuator was slowly moved until it touched the spreader beam.

9. Photographs were taken.
10. Continuous reading by the DIC system was started.
11. The hydraulic actuator was started at a loading rate of 0.5 mm/min.
12. When the applied loading reached 20 kN, the loading was paused. The DIC system was also paused, but the recording of all other data continued.
13. All visible cracks were traced. Photographs were taken.
14. Steps 9 to 12 were repeated for 30 and 50 kN load stages.
15. After the 50 kN loading stage the test was continued without stopping until a significant drop in load was observed and the test was halted.

The total time taken for testing each specimen ranged between 3 to 5 hours.

8.6 Test Results and Discussion

A total of six slab specimens were constructed and tested to determine their flexural behaviour. The cross-section configuration of each specimen was different, as described in Section 8.3.1. The influences of configuration on flexural behaviour including the concrete type, tensile reinforcement ratios (ρ) and textile configurations are discussed here.

8.6.1 Load-Deflection Behaviour

The effect of ceramic concrete type and strength (f_c') on the load-deflection response of tested slab specimens is shown in Figure 8.16 for specimens S25L, S25B and S25S. These slabs were reinforced with similar ρ and a similar number of textile layers, but they had different f_c' and aggregate type. From the load-deflection curves, three distinct regions are observed (Figure 8.16). The curves are nearly linear up to $P=14$ kN, 21 kN and 21 kN for S25L, S25B and S25S, respectively. These loads correspond to the cracking of GFRCC (point I in Figure 8.16), a phenomenon that is similar to Portland cement-based LWC (e.g., Lim et

al., 2006; Wu et al., 2011). After cracking, a non-linear response with a gradually decreasing slope was observed until yielding of the reinforcement occurred for specimen S25S (point II in Figure 8.16) and the peak load was reached for S25L and S25B. After yielding of the steel reinforcement, a nearly horizontal response was observed up to failure for S25S, but no yielding point was observed for S25L and S25B due to different failure modes (see section 8.6.2). Note that, to protect instruments from damage, all tests were stopped when the load dropped by 12 to 26% of the peak load.

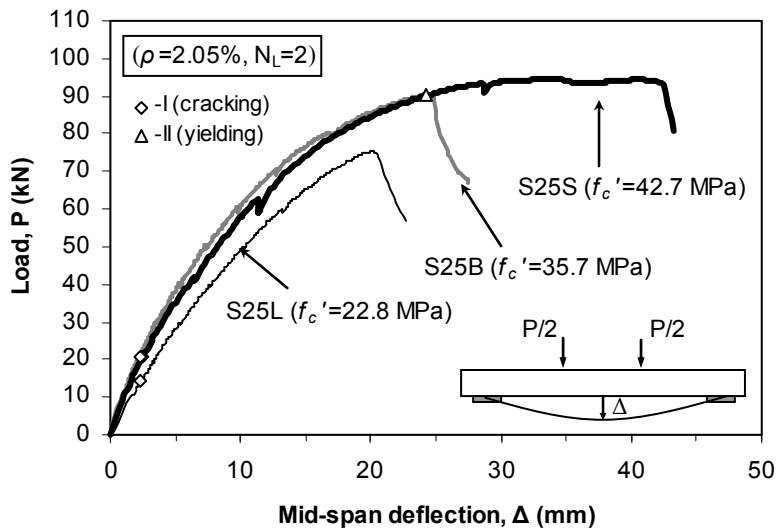


Figure 8.16- Effect of concrete type and f_c' on load-deflection behaviour

Figure 8.16 clearly shows a notable increase in stiffness when the mix type was changed, with f_c' increasing from 22.8 MPa (FLL) to 35.7 MPa (FB). This phenomenon is similar to that of Portland cement-based LWC (e.g., Lim et al., 2006). This occurred due to the higher modulus of elasticity E_c of mix type FB compared to FLL (see Table 8.1). However, no significant change in stiffness was observed when the f_c' was increased from 35.7 to 42.7 MPa, as the FB and FS mixes had similar modulus of elasticity values (see Table 8.1).

In prior studies for flexure-critical reinforced concrete members, the equivalent service loads were derived from the experimental peak loads by assuming a factor ranging between 50 and 70% (e.g., Rashid and Mansur, 2005; Lim et al., 2006;

Bosche et al., 2008). In this study, the equivalent service load (P_s) was assumed as 60% of the peak load (P_u).

Table 8.6 presents the measured mid-span deflections of the specimens at the equivalent service and peak loads. It shows that the peak load deflection as well as the peak load increased as f_c' increased (S25L and S25S), due to different failure modes. However, these mix changes had a smaller effect on the equivalent service load deflection (Δ_s).

Table 8.6- Test results at different loading stages

Slab ID	f_c' (MPa)	ρ (%)	N_L	At service		At yielding		At peak		Failure Mode
				P_s^* (kN)	Δ_s (mm)	P_y (kN)	Δ_y (mm)	P_u (kN)	Δ_u (mm)	
S03L	26.1	1.15	0	37.0	6.2	57.8	15.7	61.6	25.3	I and II
S23L	23.2	1.24	2	37.4	8.0	61.9	25.3	62.3	26.9	I and II
S05L	24.5	1.90	0	47.7	7.3	-	-	79.5	19.3	I
S25L	22.8	2.05	2	45.2	9.0	-	-	75.3	20.1	I and III
S25B	35.7	2.07	2	54.2	8.4	-	-	90.3	24.6	I and III
S25S	42.7	2.04	2	56.8	9.8	90.0	24.1	94.7	34.2	I, II and III
* Equivalent service load (P_s) was taken as 60% of peak load (P_u)										

Failure modes	
I	Compression failure of concrete
II	Yielding of reinforcement
III	Splitting fracture between layers (TRCC layer and main slab)

The effect of the tensile reinforcement configuration on the load versus mid-span deflection behaviour for specimens S03L, S23L, S05L and S25L are illustrated in Figure 8.17. The tensile reinforcement ratio ρ was varied. In addition, textile fabric with 0 or 2 number of layers (N_L) was considered. However, all specimens were made of similar ceramic concrete with f_c' ranging between 22.8 and 26.1 MPa.

From the load-deflection curves of Figure 8.17, at least two distinct regions can be observed. First, the curves are nearly linear and similar up to a load of approximately $P_u=14$ kN, corresponding to the initial cracking of the GFRCC (point I in Figure 8.17). Beyond this point, gradually decreasing slopes occurred until failure for the heavily reinforced specimens (S05L and S25L) and until reinforcement yielding for lightly reinforced S03L and S23L (point II in Figure 8.17). Finally, a nearly horizontal response was observed up to failure for the lightly reinforced specimens S03L and S23L.

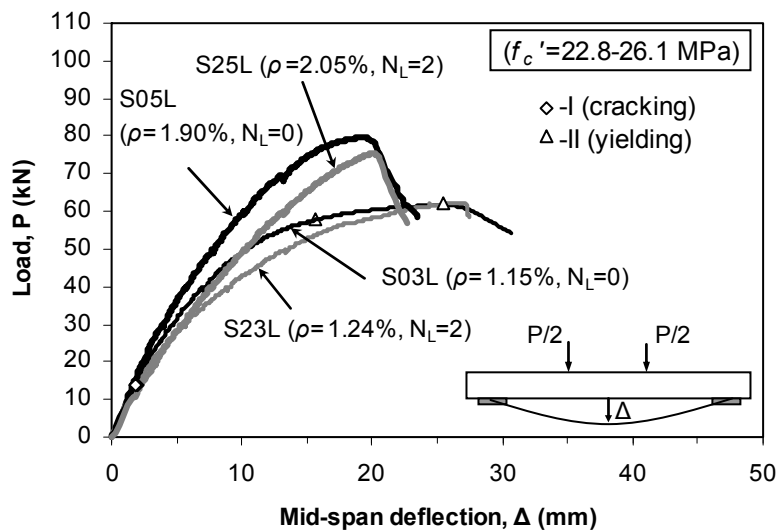


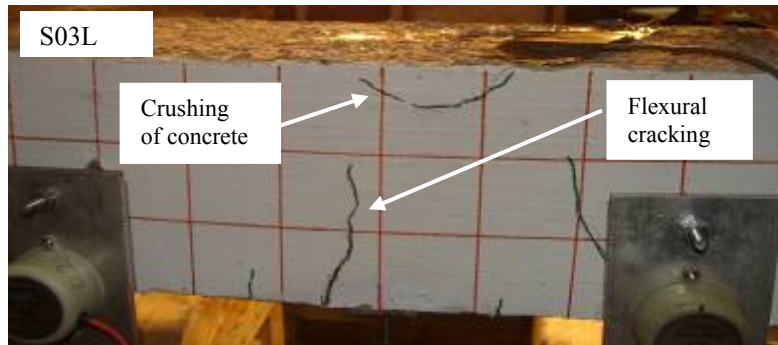
Figure 8.17- Effect of reinforcement configuration on load-deflection behaviour

When comparing specimens with similar number of textile layers, the ultimate load capacity increased as ρ increased (compare S03L and S05L, S23L and S25L) (see Figure 8.17), which is similar in behaviours to PC-based LWC (e.g., Lim et al., 2006). This is attributed to the high total tensile force that was part of internal couple. However, when comparing specimens with similar ρ , no significant change in ultimate load was observed when the number of textile fabric reinforcement layers was increased (S03L and S23L, S05L and S25L). This is attributed to the weaker tensile strength and lower stiffness of the textile fabric compared to steel. Hence, its contribution to the total tensile force was low as compared to the reinforcing steel. As can be seen in sections 8.3.2 and 8.3.3, the tensile strength of the textile fabric is only 6% of the steel.

Figure 8.17 shows that, irrespective of the number of textile layers, the stiffness of a slab specimen increases as ρ increases, due to the increased effective moment of inertia of the flexurally cracked specimens. This scenario is similar to the behaviour of Portland cement-based LWC (e.g., Lim et al., 2006). The same figure also indicates that for specimens with similar ρ the stiffness decreased as the number of textile layers increased (compare S03L and S23L, S05L and S25L). This was caused by a reduction of the effective moment of inertia for specimens S23L and S25L as a result of splitting cracking gradually forming along the intersection of the TRCC layer and the main slab. Note that a layered construction was used for specimen S23L and S25L, but for specimen S03L and S05L a full depth construction type was used. Thus, for specimens S03L and S05L, the effective moment of inertia was higher compared to S23L and S25L. This is due to the contribution of the concrete beneath the steel reinforcement for S03L and S05L as a result of short fibers' role in arresting the cracks.

8.6.2 Failure Modes

The static conditions of the slabs were simply supported and subjected to two equal loads at the third points. Hence, the middle third of each slab was subjected to relatively constant bending moment, while the remaining sections were under relatively constant shear force and varying moment. The typical failure modes for the tested specimens are given in Figure 8.18. Three different failure modes were observed: crushing of concrete (Mode I), yielding of reinforcing steel (Mode II), and splitting failure (Mode III) (see Table 8.6). Depending on the GFRCC type, tensile reinforcement ratio (ρ), and slab cross-section configuration, either one or a combination of failure modes occurred in each slab. For all tested slabs, however, no horizontal cracks at the steel reinforcement location were observed, which indicates that bond failure had not occurred between the concrete and reinforcing steel. The observed failure modes in each slab are discussed below.



(a) Slab without textile reinforcement (S03L)



(b) Slab with textile reinforcement (S25S)

Figure 8.18- Typical observed failure modes for slabs

The mode of failure for specimens S03L and S23L was steel yielding (Mode II), followed by crushing of concrete at mid-span (Mode I) due to the relatively small ρ (see Figure 8.18(a)). This was confirmed by strain gauge results, as discussed in sections 8.6.4.2 and 8.6.4.3.

Specimen S05L failed by crushing of concrete at mid-span (Mode I) before the reinforcing steel yielded due to relatively large ρ . This was confirmed by strain gauge results as discussed in sections 8.6.4.2 and 8.6.4.3.

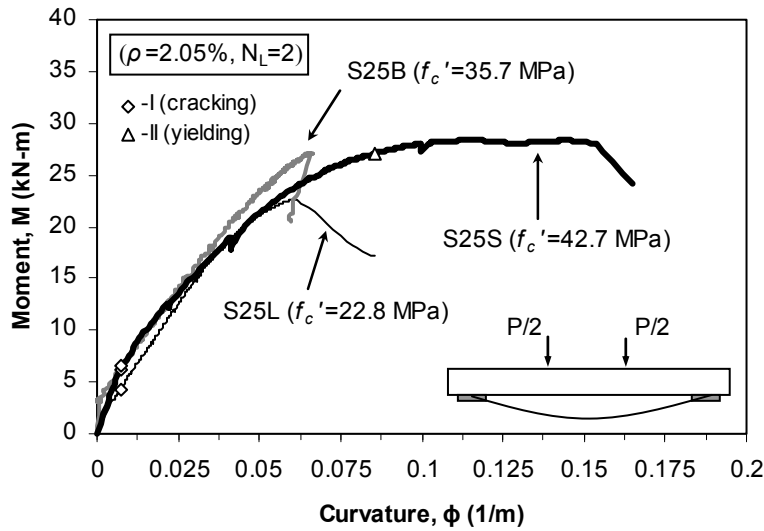
The mode of failure for specimens S25L, S25B and S25S were all similar, namely by splitting fractures between the TRCC layer and the main slab and crushing of concrete (Modes III and I, respectively) (see Figure 8.18(b)). Splitting cracks occurred due to discontinuity between layers, since layered construction was used. However, no yielding of reinforcement was observed for S25L and S25B, while

yielding occurred for S25S (see Figure 8.21(a)). This was because all of these slabs contained relatively large ρ , but slab S25S had relatively large f_c' .

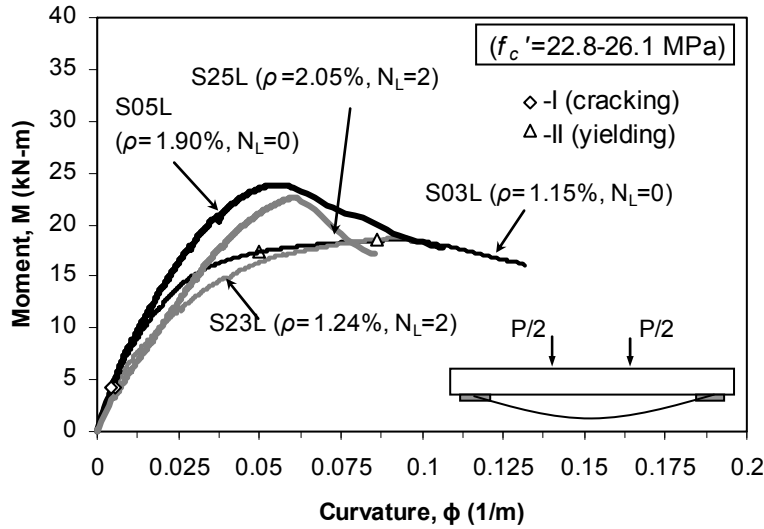
8.6.3 Moment-Curvature Responses

The moment-curvature responses of the slab specimens are discussed in this section. The moment was calculated using the applied loads and the initial slab geometry. The curvature of a slab specimen was determined from the rotations measured by the inclinometers described in section 8.5.2. The curvature was calculated by dividing the inclinometer results by the distance between the slab mid-span and the inclinometer location (i.e., 150 mm). The results reported here are the average values of curvature calculated using the two inclinometers. Note that for specimens S25L, S25B and S25S the curvature determined from the inclinometers represented the curvature of the portion above the TRCC layer due to the mounting location of the inclinometers.

Specimens S25L, S25B and S25S had the same reinforcement configuration but differed by concrete type. The effects of the ceramic concrete type and corresponding strength (f_c') on the moment-curvature relationships for these specimens are shown in Figure 8.19(a). Inclinometers for S25B malfunctioned up to a moment of $M=6.0$ kN-m. The curves are nearly linear up to moments of approximately $M=4.5$ kN-m and 6.5 kN-m for S25L and S25S, respectively, corresponding to flexural cracking (point I in Figure 8.17(a)). After this point, a gradually decreasing slope was observed until failure occurred on S25L and yielding of reinforcement occurred in S25S. Finally, for the S25S specimen, a nearly horizontal moment-curvature response was observed up to failure due to yielding of reinforcement (point II in Figure 8.19(a)), as confirmed by reinforcement strain gauges (see Section 8.6.4.2).



(a) Effect of concrete type and f_c' on moment-curvature response



(b) Effect of reinforcement configuration on moment-curvature response

Figure 8.19- Moment-curvature response

Specimens S03L, S23L, S05L and S25L had similar concrete types but differed in their reinforcement configuration. The effect of the tensile reinforcement configuration on the moment-curvature response of these specimens is illustrated in Figure 8.19(b). All of the curves were nearly linear and similar up to a bending moment of approximately $M=4.5$ kN-m, when flexural cracking occurred (point I in Figure 8.19(b)). Beyond this point, gradually decreasing slopes were observed until the peak load was reached by the two heavily reinforced sections (S05L and

S25L), and reinforcement yielding occurred in S03L and S23L (point II in Figure 8.19(b)). A nearly horizontal response was observed up to failure for S03L and S23L.

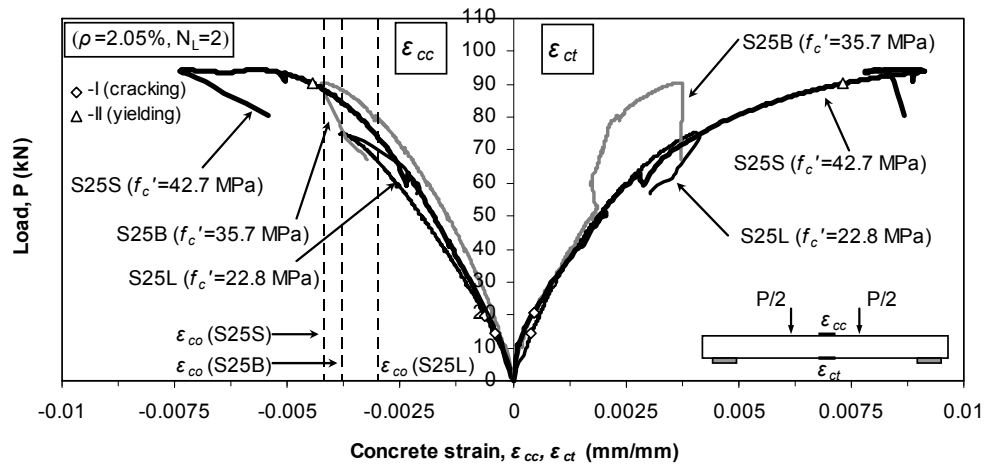
8.6.4 Strain Response

The reinforcing steel strain (ϵ_s) and the extreme fiber concrete compressive strain (ϵ_{cc}) and concrete tensile strain (ϵ_{ct}) were measured using strain gauges installed at the mid-span of each specimen. The effects of concrete mix type and reinforcement configurations on these strains are discussed below.

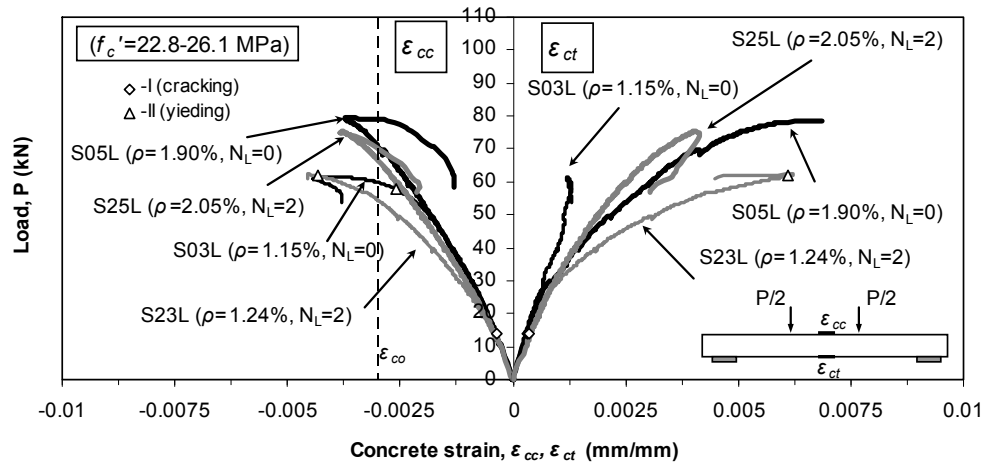
8.6.4.1 Concrete Strain

The effects of mix type on the load versus extreme fiber compressive and tensile concrete strain (ϵ_{cc} and ϵ_{ct}) response are shown in Figure 8.20(a). It can be seen from the figure that all of the ϵ_{cc} or ϵ_{ct} curves are of similar shape. The load- ϵ_{cc} or load- ϵ_{ct} curves are similar in shape and nearly linear up to 21 kN for S25L and S25B (point I in Figure 8.20(a)). No significant difference in ϵ_{cc} or ϵ_{ct} was observed beyond this point until yielding of reinforcement occurred (point II in Figure 8.20(a)). The discrepancy of ϵ_{ct} in specimen S25B after approximately $P=50$ kN was attributed to a malfunctioning response of the strain gauge located at the bottom of the specimen. Figure 8.20(a) indicates that slab S25S showed the highest ϵ_{cc} value at peak load, indicating that the ϵ_{cu} was influenced by mix type. The larger value of ϵ_{cu} in S25S was due to higher concrete strength compared to S25B or S25L.

Previous studies have shown that the concrete compression failure in Portland cement based flexure critical rectangular cross-sections occurs when extreme fiber compressive concrete strains reach value of about $\epsilon_{cu} = 0.003$ to 0.004 mm/mm (e.g., Nilson et al., 2004). The ϵ_{cu} values for the slab specimens in the current study with ceramic concrete were in the range of 0.0037 to 0.0058 mm/mm (Table 8.7). Compared to the corresponding cylinder compression test results of each slab, these values were between 10 and 50% higher than the cylinder compression strain at peak stress (ϵ_{co} , see Table 8.4 and Figure 8.20).



(a) Effect of mix type on concrete strain



(b) Effect of reinforcement configuration on concrete strain

Figure 8.20- Load versus extreme fiber compressive concrete strain at mid-span

The effect of reinforcement configuration on the load- ϵ_{cc} and load- ϵ_{ct} response is shown in Figure 8.20(b). The strain gauge at the tension side of the specimen S03L malfunctioned after 25.0 kN. The ϵ_{cc} was similar and nearly linear up to $P_u=14$ kN for specimens S03L, S23L, S05L and S25L (Figure 8.20(b)). No significant difference in ϵ_{cc} was observed beyond this point until yielding of reinforcement occurred (point II in Figure 8.20(b)) for slabs having smaller ρ (S03L and S23L).

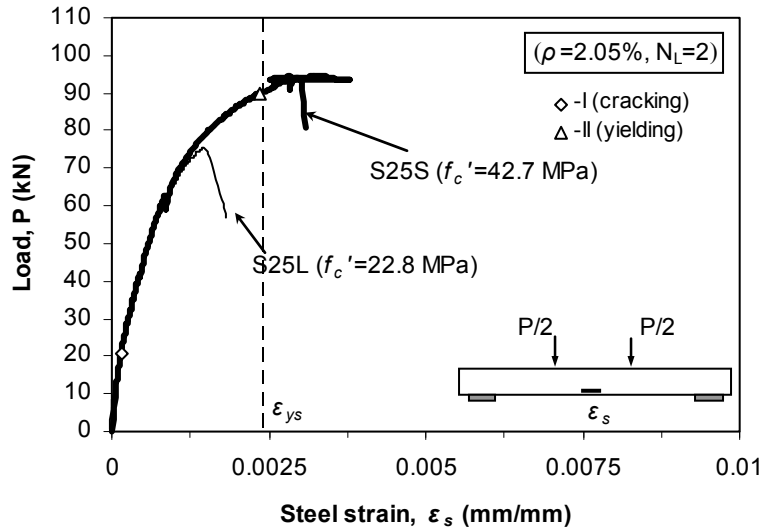
Figure 8.20(b) indicates that slabs S03L and S23L showed higher ε_{cc} values at peak load compared to S05L and S25L, indicating that ε_{cu} increased as ρ decreased. This is due to large deformations (see Figure 8.24) occurring rapidly after the yielding of reinforcement prior to peak load, when ρ decreased. As a result, higher ε_{cu} is expected (e.g., Swamy and Lambert, 1984).

8.6.4.2 Reinforcing Steel Strain

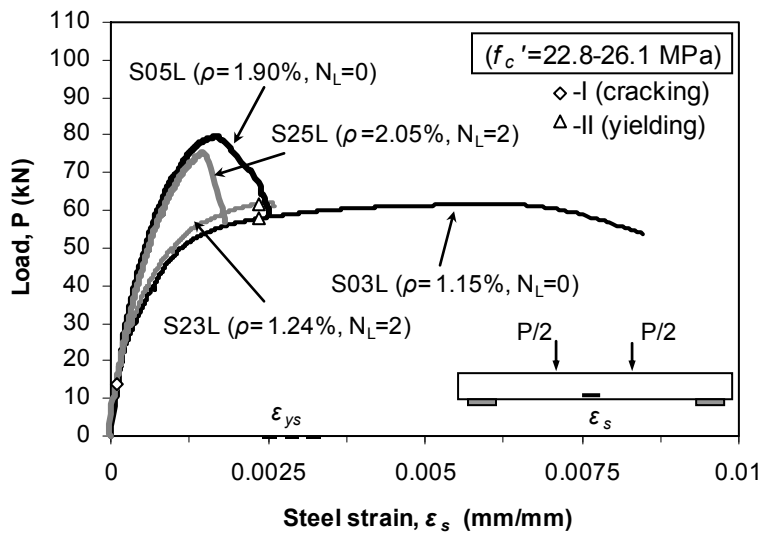
The load versus the reinforcing steel strain (ε_s) at the mid-span of the slab specimens is shown in Figure 8.21. Unfortunately, the strain gauges in S25B malfunctioned.

The effect of mix type and f_c' on the load- ε_s response is shown in Figure 8.21(a). The figure shows that the ε_s values were similar for specimens S25L and S25S until failure of the former specimen, indicating that mix type and f_c' had a negligible effect on the load- ε_s response up to this stage. At the ultimate stage, however, S25S had the highest ε_s exceeding the yield strain, indicating that ε_s values at peak load were influenced by failure modes. This is due to higher load in S25S as a result of higher f_c' . As f_c' increased, the neutral axis depth at peak load decreased, as a result, the steel strain increased (e.g., Park and Paulay, 1975).

The effect of reinforcement configuration on the load- ε_s response for slab specimens S03L, S23L, S05L and S25L is illustrated in Figure 8.21(b). The figure shows that the curves were of a similar shape and nearly linear up to 14 kN. Furthermore, the load- ε_s response was similar for samples S03L and S23L until yielding (point II in Figure 8.21(b)). Beyond the yielding point, the S23L specimen failed after exhibiting a minimal increase in ε_s . However, S03L showed a long yield plateau due to relatively lower ρ (Figure 8.21(b)). The ε_s values at peak load for S03L and S23L were 0.0061 mm/mm and 0.0025 mm/mm, respectively.



(a) Effect of concrete type on steel strain



(b) Effect of reinforcement configuration on steel strain

Figure 8.21- Load versus reinforcing steel strain at mid-span

Since ρ was similar, the load versus steel strain response was similar for S05L and S25L up to peak load, as expected (Figure 8.21(b)). No yielding of reinforcement occurred in S05L and S25L due to relatively higher ρ compared to S03L and S23L, respectively. These specimens also showed that the load- ϵ_s response was not significantly influenced by N_L .

8.6.4.3 Strain Distribution Through the Slab Depth

The mid-span strain distribution through the depth of the slab section for specimens S23L, S05L, S25L and S25S are illustrated in Figure 8.22. No plot was provided for specimens S03L and S25B, since the concrete strain gauge at the bottom of S03L and steel strain gauge for S25B malfunctioned. The vertical axis in Figure 8.22 represents the measurement location above the bottom surface of the specimen. The horizontal axis represents the strains of extreme concrete compressive strain, extreme concrete tensile strain, and reinforcing steel strain. These strains were determined at loads corresponding to 20%, 40%, 60% and 80% of the peak load (P_u). Figure 8.22 shows that the strain distributions were nearly proportional to the distance from the neutral axis (i.e., zero strain point) until 60% P_u lines but shows larger variation for the 80% P_u lines. These nearly linear distributions of strains along the cross-sectional depth indicate that the assumption of a plane cross-section before and after bending is valid for the slab specimens. Figure 8.22 also indicates that the linear distribution of strain altered as P_u increased. This was expected, due to the cracks on the concrete tension side widening as P_u increased leading to higher strains. This is confirmed by the cracks pattern at concrete tension side of each specimen as discussed in section 8.6.

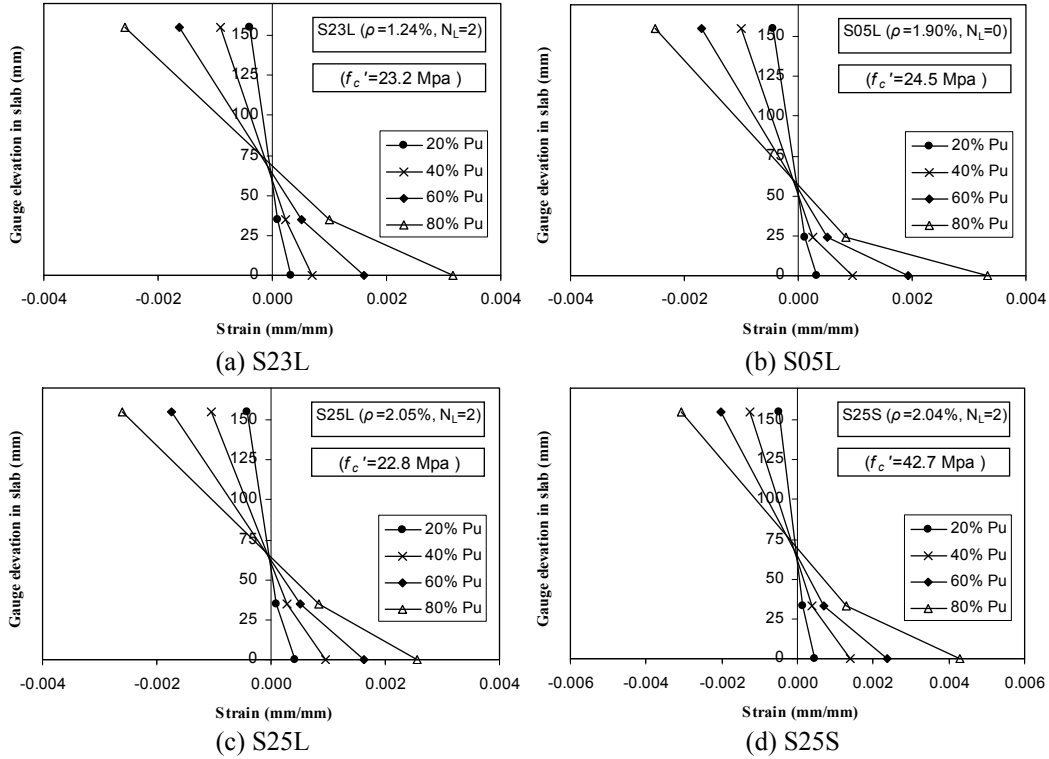


Figure 8.22- Strain distribution through depth of slab at mid-span

8.6.5 Ductility

Ductility is a desirable property of structures, since it allows stress redistribution and large deformation capacity to give sufficient warning before failure (e.g., Park and Paulay, 1975). Two common ways of evaluating ductility of reinforced concrete members are by establishing either a curvature-ductility index (μ_c) or a displacement-ductility index (μ_d). Both methods were considered in this study.

The ductility of singly reinforced sections is influenced by factors including f'_c , ρ , and yield strength of reinforcement (e.g., Park and Paulay, 1975). The effects of mix type and reinforcement configuration on the ductility of the tested slabs are discussed here.

The curvature-ductility index (μ_c) is expressed as a ratio of the curvature at peak load (ϕ_u) to the curvature when the tension steel first yields, ϕ_y (e.g., Park and Paulay, 1975; Rashid and Mansur, 2005), which is taken at the load when the steel strain gauge reaches ϵ_y . The μ_c values from the test results are listed in Table

8.7. No values were provided in the table for S25L or S25B, as both specimens failed before yielding of the steel reinforcement occurred. In comparison to S25L or S25B, the μ_c value of S25S is 1.4, due to different failure modes as a result of f_c' . This indicates that increasing the f_c' increased the ductility, similar to reinforced PC-based sections (e.g., Park and Paulay, 1975; Lim et al., 2006). As f_c' increased, the neutral axis depth at peak load decreased, and consequently ϕ_u and thus the ductility, increased (e.g., Park and Paulay, 1975).

The μ_c value of S03L is 1.9 while no value was provided for S05L since the latter specimen failed before yielding of steel (see Table 8.7). This suggests that the μ_c of the slab specimens decreased as ρ increased, similar to reinforced PC-based sections (e.g., Park and Paulay, 1975; Lim et al., 2006; Wu et al., 2011). This is because as ρ increased, the neutral axis depth at failure increased. As a result, ϕ_u and thus the ductility decreased (e.g., Park and Paulay). The μ_c values of S03L and S23L from Table 8.7 showed that the μ_c of the slab specimens also decreased as the N_L increased.

Table 8.7- Curvature-ductility of tested slabs

Slab ID	f_c' (MPa)	ρ (%)	N_L	At yielding		At ultimate		Curvature-ductility Index	ϵ_{cu}
				M_y (kN-m)	ϕ_y (1/m)	M_u (kN-m)	ϕ_u (1/m)	$\mu_c = \phi_u/\phi_y$	
S03L	26.1	1.15	0	17.3	0.0498	18.5	0.0925	1.9	0.00405
S23L	23.2	1.24	2	18.6	0.0858	18.7	0.0938	1.1	0.00453
S05L	24.5	1.90	0	-	-	23.9	0.0563	-	0.00372
S25L	22.8	2.05	2	-	-	22.6	0.0604	-	0.00378
S25B	35.7	2.07	2	-	-	27.1	0.0814	-	0.00420
S25S	42.7	2.04	2	27.0	0.0856	28.4	0.1178	1.4	0.00581

The deflection-ductility index (μ_d) is expressed as a ratio of the deflection at peak load (Δ_u) to the deflection at yielding of tension steel, Δ_y (e.g., Ahmad and Barker, 1991). The values Δ_y is taken for the load when the steel strain gauge reaches ϵ_y .

The μ_d values for the tested slabs are given in Table 8.8. As can be seen in Figure 8.21(a), S25L and S25B failed before yielding of reinforcement, and therefore no μ_d values were provided. S25S showed a μ_d value of 1.4, indicating that as the f_c' increased, the μ_d increased, similar to μ_c . This is due to different failure mode.

The μ_d value of 1.6 was provided for specimen S03L in Table 8.8 while no value was given for S05L. This indicates that the μ_d of the specimens decreased as the ρ increased, similar to μ_c . This is due to difference in failure mode.

Table 8.8- Displacement-ductility index

Slab ID	f_c' (MPa)	ρ (%)	N_L	At yielding		At ultimate		Displacement-ductility Index	ϵ_{cu}
				P_y (kN-m)	Δ_y (1/m)	P_u (kN-m)	Δ_u (1/m)	$\mu_d = \Delta_u/\Delta_y$	
S03L	26.1	1.15	0	57.8	15.7	61.6	25.3	1.6	0.00405
S23L	23.2	1.24	2	61.9	25.3	62.3	26.9	1.1	0.00453
S05L	24.5	1.90	0	-	-	79.5	19.3	-	0.00372
S25L	22.8	2.05	2	-	-	75.3	20.1	-	0.00378
S25B	35.7	2.07	2	-	-	90.3	24.6	-	0.00420
S25S	42.7	2.04	2	90.0	24.1	94.7	34.2	1.4	0.00581

8.6.6 Cracking Pattern and Crack Widths

As explained in Section 8.4.2, the DIC system was used to monitor the crack development on the western face of each specimen. The crack widths were extracted from DIC images using Vic-3D image analysis software (Correlated Solutions Inc., 2009).

First, the last DIC image was inspected to locate the flexural crack with probable maximum width. A virtual extensometer perpendicular to each crack was defined at extreme surface of concrete. The data was then extracted and used to determine the crack width (w) for each location. The crack with maximum width is reported here. Plots were developed to identify the applied load versus maximum crack width relationship.

The effect of mix type and f_c' on load-crack width behaviour is shown in Figure 8.23. The location of the crack width in the constant moment region is indicated in Figure 8.23 (point A or B on Figure 8.23). Figure 8.23 shows that the load crack-width relationships were nearly zero up to cracking approximately at total loads P of 14 kN, 21 kN and 21 kN for S25L, S25B and S25S, respectively (point I in Figure 8.21). From these loads up to approximately P=40 kN, the slopes of the load-crack width curves were reduced but were similar and relatively linear.

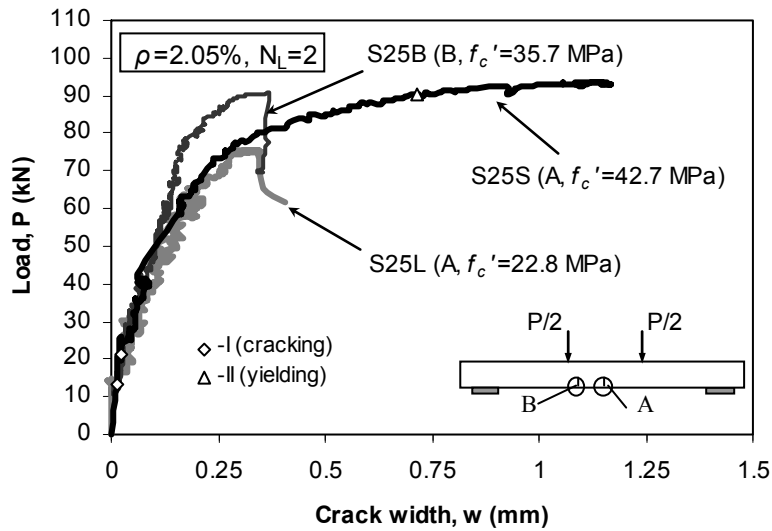


Figure 8.23- Effect of concrete type and f_c' on load-crack width behaviour

The load-crack width curves diverged after approximately P=40 kN, as shown in Figure 8.23. However, from this figure, it is observed that increasing the f_c' had minimal effect on the crack width up to P=65 kN. However, a different crack width was observed at peak load, due to different failure modes.

The influence of reinforcement configuration on load-crack width behaviour is shown in Figure 8.24. The location of the crack widths in the constant moment region is indicated in Figure 8.24 (points A, B and C in Figure 8.24). Figure 8.24 shows that the load crack-width relationships were nearly zero up to cracking load P of approximately 14 kN (point I in Figure 8.24). From these loads up to approximately P=40 kN the slope of the load-crack width curves were reduced, but were similar and linear.

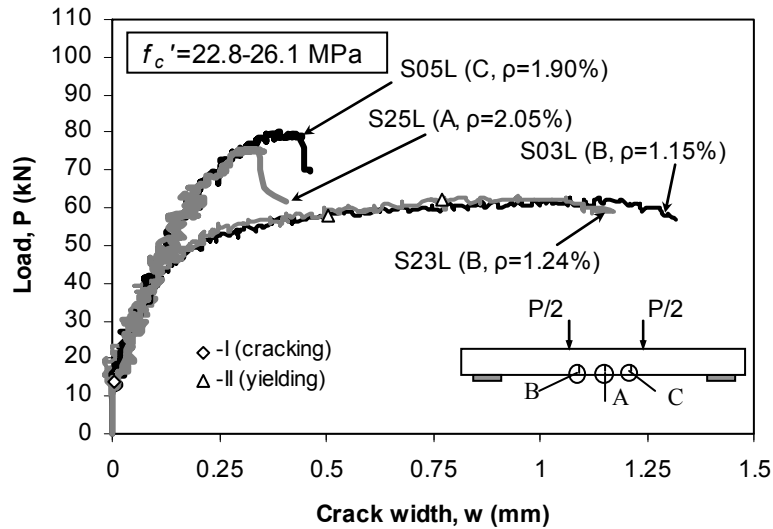


Figure 8.24- Effect of reinforcement configuration on load-crack width behaviour

Figure 8.24 clearly shows that after approximately $P=40$ kN, the load-crack width curves diverge. After this load, S05L and S25L showed smaller crack widths when compared to crack widths of S03L and S23L at comparable loads. The crack width was reduced due to increasing ρ , similar to PC-based LW concrete (e.g., Lim et al., 2011). This is due to ρ and crack width are inversely related. Basic theoretical equations for flexural cracking in reinforced concrete indicate that the crack width is related to the elongation of the steel between two cracks (e.g., Park and Paulay, 1975). The crack width is related to $f_s S_c / E_s$, where f_s is the stress in the steel which is equal to the tensile load in the steel over the total cross-sectional area of the steel which is a function of ρ , S_c is cracking spacing and E_s is modulus of elasticity of steel. This suggests that as the ρ increase, the stress in the reinforcing steel decreases and hence the crack width reduces.

Inspection of the service load crack widths taken at 60% of peak load (see Table 8.9) revealed that changing either mix type or reinforcement configuration had no significant effect on service load crack width for the tested specimens in this study. The service load crack widths varied between 0.08 and 0.14 mm, within the typical limits specified in codes for humid and moist moderate environment (ACI Committee 224, 2008).

Table 8.9- Load and maximum flexural crack width at service and peak load conditions

Slab ID	f'_c (MPa)	ρ (%)	N_L	At service		At peak		Failure Mode
				P_s^* (kN)	w_s (mm)	P_u (kN)	w_u (mm)	
S03L	26.1	1.15	0	37.6	0.08	62.7	1.14	I and II
S23L	23.2	1.24	2	38.0	0.10	63.3	0.95	I and II
S05L	24.5	1.90	0	48.3	0.13	80.40	0.39	I
S25L	22.8	2.05	2	45.1	0.09	75.2	0.35	I and III
S25B	35.7	2.07	2	54.2	0.11	90.3	0.35	I and III
S25S	42.7	2.04	2	56.3	0.14	93.8	1.14	I, II and III

* Equivalent service load (P_s) was taken as 60% of peak load (P_u)

Failure modes	
I	Compression failure of concrete
II	Yielding of reinforcement
III	Splitting fracture between layers

The load-crack width curves were similar in shape for specimens with and without textile reinforcement (see Figure 8.24). Table 8.9 shows that the peak load crack widths reduced by 17% and 12% for $\rho = 1.15\%$ (S03L, S23L) and $\rho = 2.05\%$ (S05L, S25L), respectively, when textile fabric was used in the specimens. Results also showed that for relatively lightly reinforced slabs (S03L and S23L) the average crack spacing was reduced when textile fabric was used (see Table 8.10).

A photograph was taken of the eastern face of each slab specimen immediately after removal from the loading frame. The cracking patterns after failure for this face are shown in Figure 8.25. To allow comparisons of eastern- and western-face crack patterns, the schematic view of both for each tested specimen are presented in Figure 8.26.

Inspection of Figure 8.26 indicates that flexural cracks on most slab specimens were comparable. A typical flexural cracking pattern showed vertically oriented cracks in the constant moment region. No diagonal shear cracks were observed.

The number of flexural cracks and average crack spacing for slab specimens between the loads points are shown in Table 8.10. Comparing slab specimens S03L and S05L, it can be concluded that the number of flexural cracks increased as ρ increased (see Figure 8.24). For relatively lightly reinforced slabs (S03L and S23L), the number of cracks increased as N_L increased.

Table 8.10- Number of flexural cracks and average crack spacing

Slab ID	f_c' (MPa)	ρ (%)	N_L	Number of cracks	Average crack spacing (mm)
S03L	26.1	1.15	0	4	130
S23L	23.2	1.24	2	8	86
S05L	24.5	1.90	0	8	91
S25L	22.8	2.05	2	4	135
S25B	35.7	2.07	2	7	88
S25S	42.7	2.04	2	4	107

The number of cracks and average crack spacing for S25L, S25B and S25S shown in Table 8.10 indicated that mix type has no discernable effect on the amount of cracking or crack spacing.

Figure 8.26 shows that, in addition to the flexural cracks, slabs with textile reinforcement also exhibited a horizontal splitting crack at the interface between the main slab and the TRCC layer (S25L, S25B and S25S). This crack was observed in both the constant moment region and in some remaining regions of the slab. It was formed due to layered construction and having no fibers along the interface of the TRCC layer and main slab. The splitting crack was occurred at a load of 65-90% of the peak load.

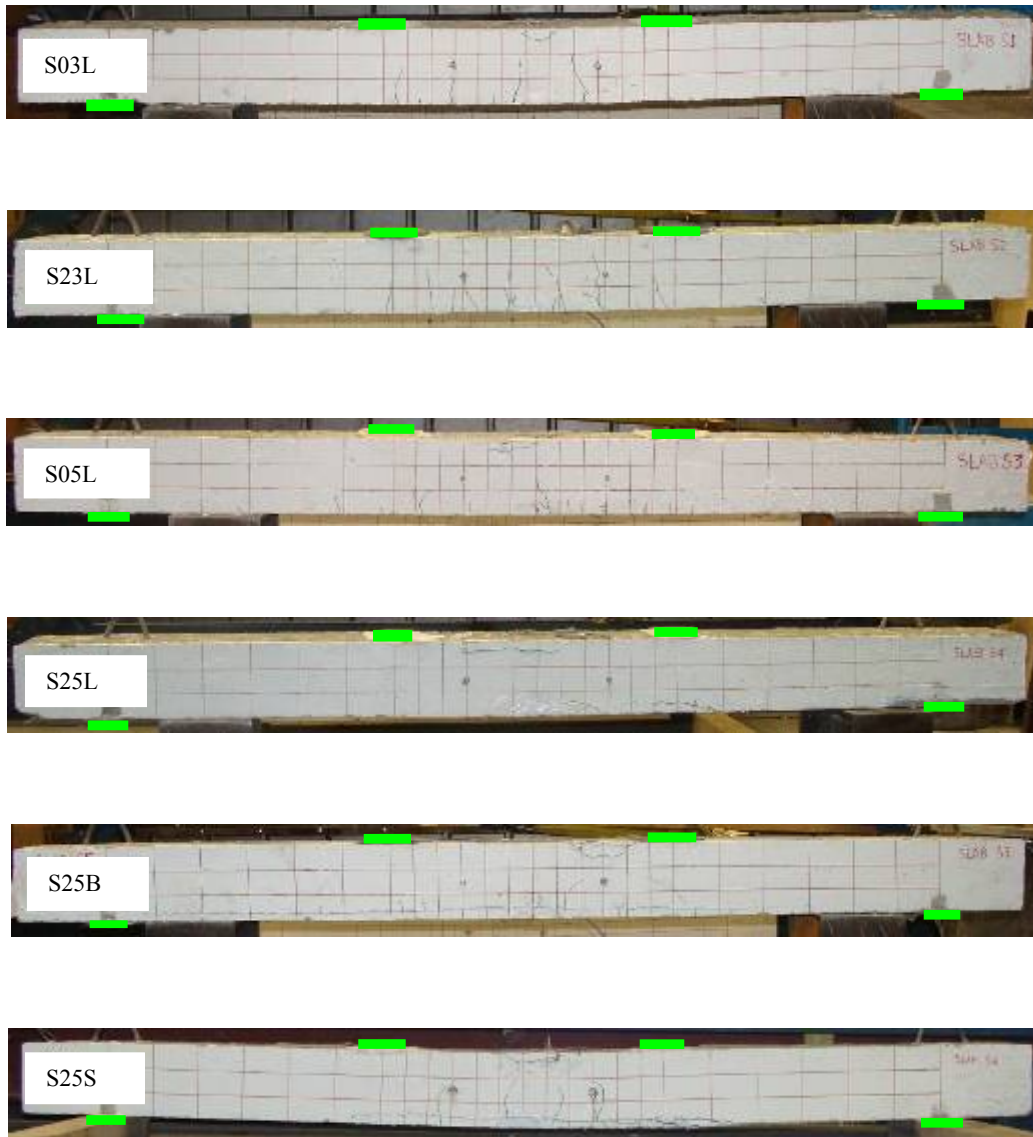


Figure 8.25- Test specimen crack patterns after failure

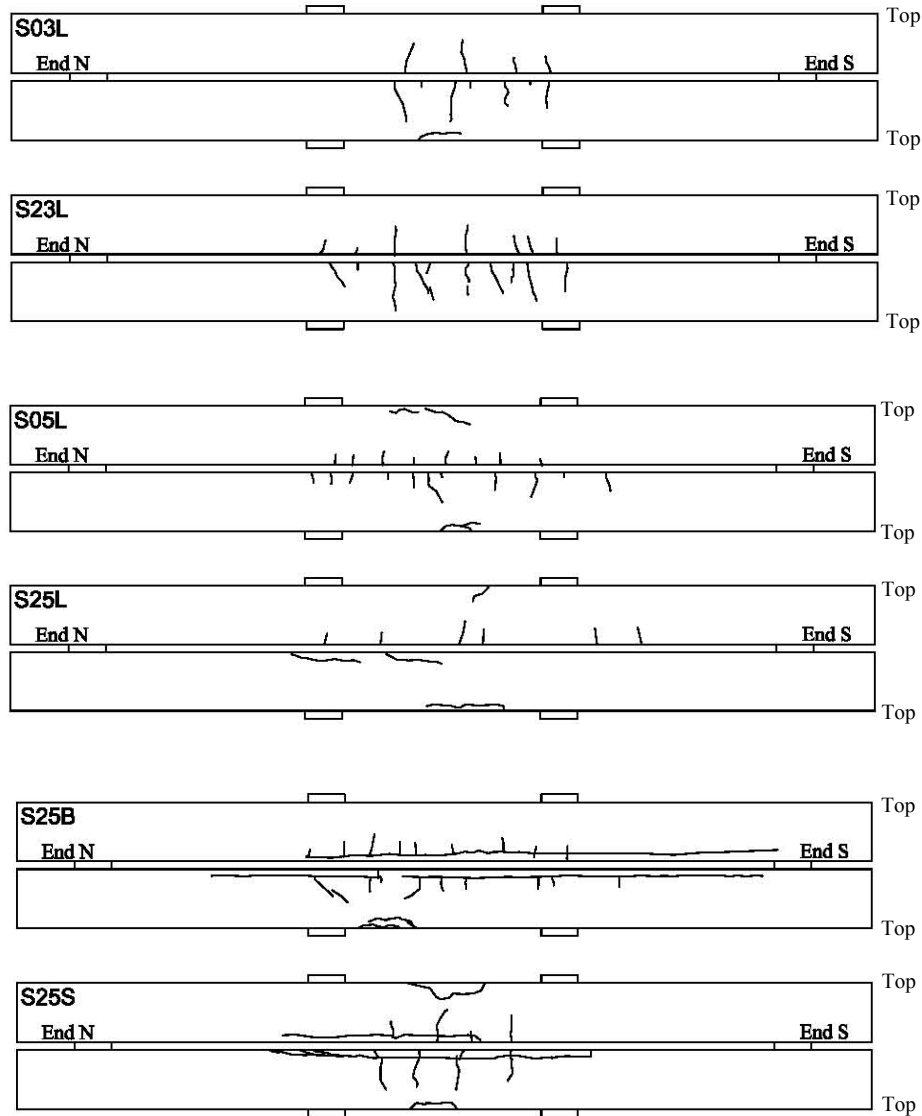


Figure 8.26- Schematic of crack patterns after failure

8.7 Implication of Test Results

The test results in this study provided useful information on the flexural response of composite slabs composed of glass fiber reinforced ceramic concrete (GFRCC), reinforcing steel, and textile reinforcement. These composite slabs were made using unique concrete mix compositions and employed two types of construction (i.e. layered type and full depth type). The test results provide insight into flexural performance and allow for the future refinement of the composite system to be used for bridge decking or building slab applications.

Both the layered construction type and full depth construction type showed good flexural performance. The TRCC layer used in the layered construction type was advantageous compared to the full depth type, as it allows for the removal of formwork to support fresh concrete for cast-in-place concrete applications. However, the test results for this type of construction did not show an increase in the load-carrying capacity of the slabs, due to the splitting between layers and the type of textile fabric used. Better flexural performance of such composite systems would be expected if new improved types of textiles (e.g. Hegger et al., 2011; 2012) were to be used. Further tests are required to optimize the composite materials and fully understand the composite flexural performance before using these on site.

8.8 Conclusions

This chapter presented a laboratory based study to develop a novel composite slab composed of glass fiber reinforced ceramic concrete (GFRCC), reinforcing steel and textile reinforcement. The flexural behaviour of these slabs was evaluated experimentally using four point bending tests. The overall dimensions of the slabs were constant but the cross-section configurations were varied. Parameters including the longitudinal steel reinforcement ratio, the number of textile reinforcement layers, and the concrete mix were varied. The load carrying capacity, deformation, failure mode, ductility, crack widths and cracking pattern were of primary interest. Two slab construction cases were investigated: layered construction type and full depth construction type. Both types of construction of the slab specimens showed a good flexural performance. The following conclusions can be drawn:

- The overall load-deflection response of reinforced GFRCC slabs was similar to typical Portland cement based reinforced concrete slabs. The load-deflection behaviours were nearly linear up to concrete flexural cracking, followed by gradually decreasing slope up to yielding of

reinforcement and then nearly horizontal response until failure depending on the amount of steel reinforcement.

- An increase in the ceramic concrete compressive strength or the amount of steel reinforcement increased the post-cracking stiffness and the peak load of GFRCC slabs.
- Increasing the ceramic concrete compressive strength or the amount of steel reinforcement had no trend with the service load deflection.
- For specimens whose steel bars yielded, the displacement and curvature ductility both increased when the ceramic concrete strength increased, and both decreased when the tension steel content increased.
- For the type and the number of textile layers considered in this study, addition of textile fabric had negligible effect on the ultimate load. However, it reduced the ultimate load deflection.
- The results indicated the crack type, crack pattern and flexural crack widths of reinforced ceramic concrete slab depend on the amount of tensile reinforcement, the concrete strength, and the type of cross-section used. In general, as the amount of steel bars increased, the crack width and crack spacing reduced. The service load crack widths of tested slabs were varied between 0.08 and 0.14 mm and this is within the maximum allowable limit specified in ACI 224R-01.
- The number of flexural cracks increased when textile fabric was used.
- Results also showed that splitting cracking occurred irrespective of the ceramic concrete mix type when layered constructions were used.

8.9 References

- ACI Committee 213. (2009). Guide for Structural Lightweight-Aggregate Concrete (ACI 213R-03), ACI manual of Concrete Practice (2009 Part 1). American Concrete Institute, Farmington Hills, MI, 24-25.
- ACI Committee 224. (2008). Control of Cracking in Concrete Structures (ACI 224R-01). American Concrete Institute, Farmington Hills, MI, 19-20.
- ASTM C143/C143M-10a. (2008). Standard test method for slump of hydraulic-cement concrete. ASTM International, West Conshohocken, PA.
- ASTM C469. (2002). Standard test method for static modulus of elasticity and poisson's ratio of concrete in compression. ASTM International, West Conshohocken, PA.
- ASTM A370-11. (2011). Standard test methods and definitions for mechanical testing of steel products. ASTM International, West Conshohocken, PA.
- Ahmad, S. H. and Barker, R. (1991). Flexural Behavior of Reinforced High-Strength Lightweight Concrete Beams. *ACI Structural Journal*, 88(1): 69-77.
- Ahmad, S. H. and Batts, J. (1991). Flexural behavior of double reinforced high-strength lightweight concrete beams with web reinforcement. *ACI Structural Journal*, 88(3), 351-358.
- Bosche, A., Jesse, F., Ortlepp, R., Weiland, S. and Curbach, M. (2008). Textile-Reinforced Concrete for flexural strength of RC-structures-Part 1: structural behaviour and design Model. American Concrete Institute, Farmington Hills, MI, ACI SP-251: 19-40.
- Bruckner, A., Ortlepp, R. and Curbach, M. (2006). Textile Reinforced Concrete for Strengthening in Bending and Shear. *Material and Structure Journal*, 39(8): 741-748.
- Bruckner, A., Ortlepp, R. and Curbach, M. (2008). Anchoring of shear strengthening for T-beams made of textile reinforced concrete (TRC). *Material and Structure Journal*, 41(4): 407-418.
- Canadian Standards Association. (2004). CSA A23.3-04: Design of Concrete Structures, Canadian Standards Association, Mississauga, Ontario, Canada, 52.
- Chandra, S. and Berntsson, L. (2002). Lightweight aggregates concrete- Science, Technology and Application. Noyes Publications, New York, USA, 369-400.

Chapter 8: Experimental Study on Reinforced Ceramic Concrete Slabs

Correlated Solutions Inc. (2009). Vic-Snap 2009 and Vic-3D 2009. www.correlatedsolutions.com.

Last accessed April, 2013

Correlated Solutions Inc. (2007). Vic-3D 2007 Testing Guide. www.correlatedsolutions.com. Last

accessed April, 2013

FIP Manual. (1983). FIP Manual of Lightweight Aggregate Concrete. Surrey University Press, London, 104-107.

Hegger, J., Will, N., Bruckermann, S. and Voss, S. (2006). Loading-bearing behaviour and simulation of textile-reinforced concrete. *Materials and Structures Journal*, 39(8): 765-776.

Hegger, J. and Voss, S. (2008). Investigations on the bearing behaviour and application potential of textile reinforced concrete. *Engineering Structures*, 30: 2050-2056.

Hegger, J., Kulas, C., Raupach, M. and Buttner, T. (2011). Tragverhalten und Dauerhaftigkeit einer schlanken Textilbetonbrücke. *Beton- und Stahlbetonbau* 106, Heft 2, S. 72- 80.

Hegger, J., Kulas, C. and Horstmann, M. (2012). Spatial textile reinforcement structures for ventilated and sandwich facade elements. *Advances in Structural Engineering*, 15 (4): 665-675.

Lim, H. S., Wee, T. H., Mansur, M. A. and Kong, K. H. (2006). Flexural behaviour of reinforced lightweight aggregates concrete beam. *Proceeding of the 6th APSEC*. Kuala Lumpur, Malaysia, A68-82.

Lim, H. S., Wee, T. H., Islam, M. R. and Mansur, M. A. (2011). Reinforced lightweight concrete beams in flexure. *ACI Structural Journal*, 108(1): 3-12.

Nilson, H., Darwin, D. and Dolan, C. W. (2004). Design of concrete structures. The McGraw-Hill companies, 38-39&68-69.

Park, P. and Paulay, T. (1975). Reinforced concrete structures. John Wiley & Sons Inc, Canada, 37-41, 195-211 & 479-483.

Rashed, M. A and Mansur, M. A. (2005). Reinforced high-strength concrete beams in flexure. *ACI Structural Journal*, 102(3): 462-471.

Short, A. and Kinniburgh, W. (1978). Lightweight concrete. Applied science publication Ltd. London, 150-171.

- Swamy, R. N. and Lambert, G. H. (1984). Flexural behaviour of reinforced concrete beams made with fly ash coarse aggregates. *The International Journal of Cement Composites and Lightweight Concrete*, 6(3): 189-200.
- Tassew, S. T., Mutsuddy, R., Bindiganavile, V. S. and Lubell, A. S. (2011). Drop Weight Impact Response of Glass Fiber Reinforced Ceramic Composites. *In Proceedings: High Performance Fiber Reinforced Cement Composites (HPFRCC-6)*, Ann Arbor, MI: 289-296.
- Tassew, S. T. and Lubell, A. S. (2012). Mechanical properties of lightweight ceramic concrete. *Materials and Structures Journal*, 45(4): 561-574.
- Tassew, S. T. and Lubell, A. S. (2010). Textile reinforced ceramic composite for structural infill slab application. *Proceeding of 34th IABSE Symposium*, Venice, Italy, A-0317, 1-8.
- Wu, C. H., Kan, Y. C., Huang, C. H., Yen, T. and Chen, L. H. (2011). Flexural behaviour and size effect of full scale reinforced lightweight concrete beam. *Journal of Marine Science and Technology*, 19(2): 132-140.

Modeling the Flexural Behaviour of Reinforced Ceramic Concrete Slabs

9.1 Introduction

Chapter 8 presented an experimental study focussed on the flexural behaviour of glass fiber reinforced ceramic concrete (GFRCC) slabs that were additionally reinforced with steel bars and textile reinforcement. The current chapter focuses on the numerical modelling of the flexural behaviour of these slabs.

Numerical models can be used to predict flexural behaviour of reinforced concrete members. The development of a numerical model has several advantages, such as characterizing non-linear material behaviour and offering a chance to study the influence of different geometry. Such models can also delineate the material parameters of the structural response and can be useful for predicting the flexural behaviour of similar members.

This chapter has three main objectives. The first is to develop the constitutive equations of the different components comprising the composite slabs. The second objective is to use these equations to develop a numerical model to analyse the flexural behaviour of glass fiber reinforced composite slabs subjected to two concentrated loads that is validated with the experimental results from Chapter 8, and the third objective is to use the model to complete parameter studies.

The three main constituent elements in the slabs are glass fiber reinforced ceramic concrete, reinforcing steel, and glass textile reinforcement. Constitutive equations of these materials were developed using the laboratory results presented in the preceding chapters. The strain-softening behaviour of GFRCC in tension has been accounted for in the proposed model.

A non-linear analysis model to investigate the flexural behaviour was proposed using Bernoulli's hypothesis (i.e., that plane sections before bending remain plane after bending). The applicability of this assumption to the slabs in this study was verified in section 8.6.4. The reinforcing steel or textile reinforcement is assumed perfectly bonded in the GFRCC. A cross-section model is used to apply the materials' constitutive equations and compatibility conditions along with static equilibrium conditions. The model was developed for simply supported slabs with prismatic, rectangular cross-sections under four-point bending.

The moment-curvature response of the slabs was determined based on the tensile and compressive stress-strain response of glass fiber reinforced concrete and the tensile stress-strain of reinforcing steel and textile fabric reinforcement. A full composite action in the cross-section is assumed, and a layer-by-layer evaluation approach at cross-sections adopted from previous work (e.g., Collins and Mitchell, 1997), was used to develop the moment-curvature response.

The member response model was developed by considering multiple cross-sections along the member length. By adopting similar approaches as previous works (e.g., Collins and Mitchell, 1997), the deflection at any point along the length of the slab is determined by applying the numerical integration of the moment-curvature response along the length of the slab.

The developed model required iterative procedures and employed numerical integration. To simplify its application, the model was implemented using MATLAB® software. The program systematically generates moment-curvature relationships for the cross-sections and then derives the corresponding load-deflection curves of the slab at each load stage. The program also directly

generates the applied load versus axial strain diagrams of the constituent materials at mid-span.

To validate the model, simply supported GFRCC slabs with geometry and material properties for the test specimens in Chapter 8 were considered. The accuracy of the proposed model was evaluated by comparing the load-deflection and moment-curvature responses predicted by the model with the experimental results from Chapter 8. Comparisons between the experimental results and model predictions for the concrete strains and reinforcement strains at different load levels were also performed.

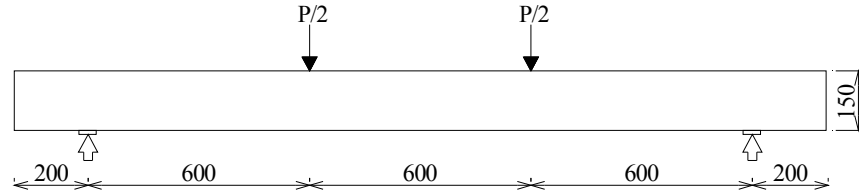
A parametric study was carried out using the developed model to study the effect of variations in ceramic concrete compressive strengths and steel reinforcement ratios on the moment-curvature response and curvature ductility.

9.2 Slab Configurations

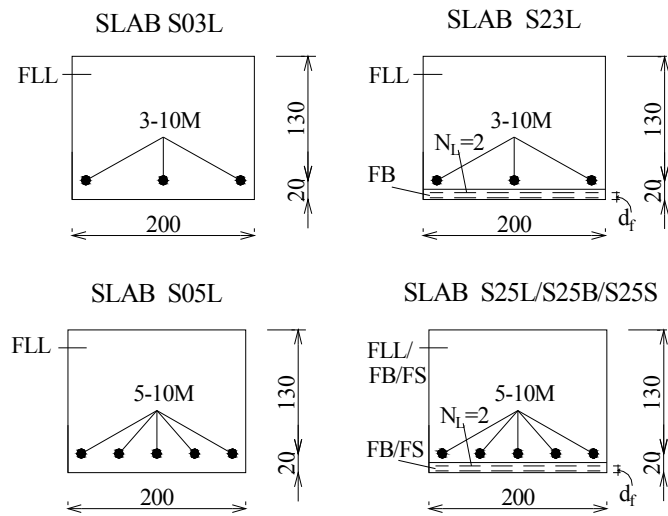
The experimental results of six-slab specimens were presented in Chapter 8. All specimens were 200 x 150 x 2200 mm³ and tested under four-point bending with a span of 1800 mm as shown in Figure 9.1(a). The slab configurations are summarized in Table 9.1. The slab cross-section configurations varied by the type of glass fiber reinforced concrete (FLL, FB or FS), the number of textile layers, and the longitudinal steel reinforcement ratios. Specimen designations consist of a four part slab ID. An initial letter “S” is used to represent the member as a slab. The second digit indicates the number of textile layers (0 or 2), and the third digit represents the number of 10M steel bars (3 or 5). The last part of the slab ID contains a letter to represent the type of ceramic concrete (FLL, FB or FS).

The reinforcement details used in the tested slabs are given in Figure 9.1(b) and Table 9.1. Four slabs (S03L, S23L, S05L and S25L) were prepared using mix type FLL that differed by steel reinforcement ratio (3 or 5-10M bars) and the number of textile layers (0 or 2) used, as illustrated in Figure 9.1(b). Two additional slabs (S25B and S25S) were produced using 5-10M bars and two layers

of textile reinforcements placed in the tension side, with one slab containing mix type of FB and the other mix type FS, as shown in Figure 9.1(b).



(a) Slab test setup



(b) Description of slab cross section

Figure 9.1- Dimensions and reinforcement details for test specimens

Table 9.1- Slab geometry and concrete material properties

Slab ID	Cross-section		d (mm)	Reinforcement				Concrete		
	b (mm)	h (mm)		Textile		Steel		f'_c (MPa)	ϵ_{co}	E_c (GPa)
				N_L	A_f (mm ²)	A_s (mm ²)	ρ (%)			
S03L	201	155	130	0	0	300	1.15	26.1	0.0030	13.1
S23L	201	155	120	2	1480	300	1.24	23.2	0.0030	11.1
S05L	202	154	130	0	0	500	1.90	24.5	0.0030	11.0
S25L	203	155	120	2	1480	500	2.05	22.8	0.0028	10.4
S25B	201	153	120	2	1480	500	2.07	35.7	0.0038	13.1
S25S	204	153	120	2	1480	500	2.04	42.7	0.0042	12.1

9.3 Material Models

As described in Chapter 8, the GFRCC composite slabs contained three main constituent materials: GFRCC concrete, deformed steel reinforcing bars, and glass textile reinforcement. In order to model the flexural behaviour of the GFRCC slabs, the uniaxial constitutive relations of these materials were developed. The constitutive equation for GFRCC both in compression and tension were considered. A tensile constitutive equation was developed for reinforcing bars and textile reinforcement. The following sections discuss how these relations were developed from the corresponding material test results presented in Chapters 7 and 8.

9.3.1 Glass Fiber Reinforced Ceramic Concrete (GFRCC)

The GFRCC matrices contained a magnesium potassium phosphate binder, glass fibers, and different aggregates. Three types of GFRCC were used for the slabs that differed by aggregates types: mix type FLL contained lightweight expanded clay aggregate (LECA); mix type FB contained Buildex-coated aggregate; and mix type FS contained sand. The details of the mix compositions are described in section 8.2.1.

Compression Modeling

Experimental results from compression tests of GFRCC cylinders presented in Chapter 8 were used to develop a model for the compression stress-strain response. These cylinders were cast along with the slabs and tested on the same day as the corresponding slab. The average measured compression properties of six cylinders for each tested slab are presented in Table 9.1.

A number of analytical models have been proposed to represent the uniaxial compression stress-strain curves of Portland cement-based fiber reinforced concrete (e.g., Fanella and Naaman, 1985; Ezeldin and Balaguru, 1992; Nataraja et al., 1999; Mansur et al., 1999; Barros and Figueiras, 1999). The general expression proposed by Mansur et al. (1999) for steel fiber reinforced concrete,

based on the expression given by Carreira and Chu (1985), has been adopted in this study, as it was in good agreement with the test results. The equation has the following form:

$$f_c = f_c' \frac{\beta_a \left(\frac{\varepsilon}{\varepsilon_{co}} \right)}{\beta_a - 1 + \left(\frac{\varepsilon}{\varepsilon_{co}} \right)^{\beta_b}} \quad (9.1)$$

To obtain a σ - ε curve for known values of f_c' , ε_{co} and E_c , only the material parameters β_a and β_b are needed. The stress and strain in this case are both considered as positive (i.e., compression).

Previous researchers have used a parameter $\beta_a = \beta_b$ to generate the pre-peak stress-strain curve of steel fiber reinforced concrete (e.g., Mansur et al., 1999), given as:

$$\beta_a = \beta_b = \frac{1}{(1 - f_c' / (\varepsilon_{co} \cdot E_c))} \quad (9.2)$$

When Equations 9.1 and 9.2 were adopted for the test results of the current study, it was observed that the model could describe the ascending branch of the compression σ - ε curves (see Figure 9.2). However, for the descending branch, the model was not in good agreement with the test result.

Therefore, another expression was needed for the descending branch of the σ - ε curve. The expressions proposed by others could not be directly used here, since the descending branch is influenced by fiber type, fiber content, fiber length, and diameter, as well as the concrete matrix. Hence, the experimental result was best fitted to Equation 9.1 to obtain different values of β_a and β_b for the descending branch of each type of GFRCC. The β_a and β_b values for different mix types are given in Table 9.2.

Figure 9.2 illustrates that, for each GFRCC type, a good agreement between curves generated using the proposed model (from Table 9.2, $R^2 = 0.99$ - 0.998) and

the experimental results are observed up to strain values of 0.008 mm/mm. Because of limited mixes available in this study, the proposed model cannot be generalized; hence the fitted parameters were adopted.

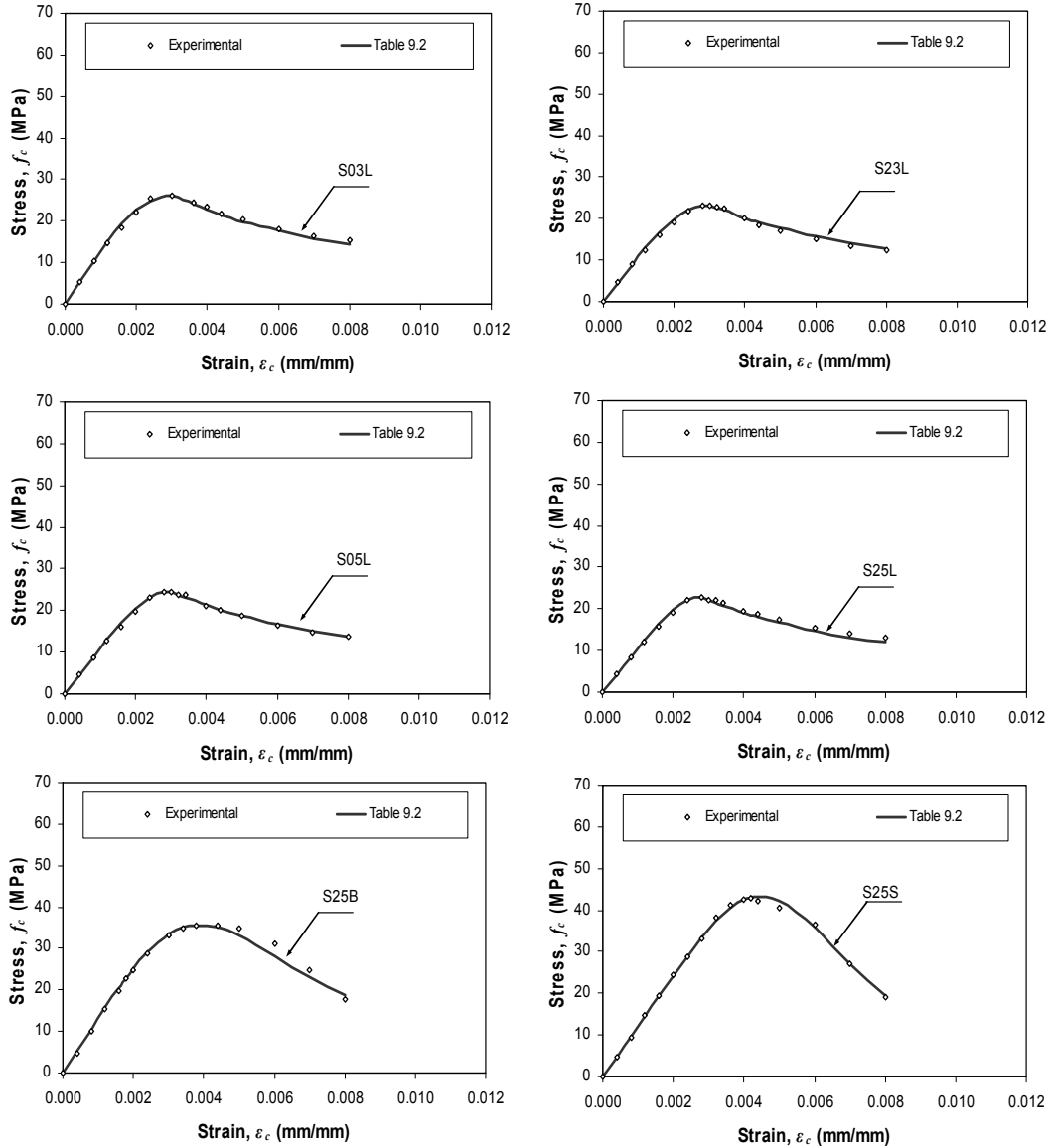


Figure 9.2- Comparison of predicted with experimental compressive stress-strain curves for GFRCC

Table 9.2- Summary of GFRCC compression stress-strain curve parameters

Type	Compressive			Tensile			
	Ascending	Descending		f_{ct}	f_{ctl}	ϵ_{ct1}	ϵ_{ctu}
	$\beta_a = \beta_b$	β_a	β_b	(MPa)	(MPa)	(mm/mm)	(mm/mm)
FLL	$1/(1 - (f_c' / \epsilon_{co} E_c))$	1.30	1.82	-1.4	-0.9	-0.0008	-0.012
FB		4.72	3.30	-2.8	-1.0	-0.0054	-0.015
FS		6.26	4.72	-2.0	-1.0	-0.0060	-0.020

Simplified Tensile Modelling

GFRCC dog-bone shaped specimens were tested under uniaxial tension and the results were presented in Chapter 7. These experimental results were used to establish a model for the uniaxial tensile stress-strain response of GFRCC.

Simplified σ - ϵ models have been previously proposed to represent the tensile stress-strain response of steel fiber reinforced concrete containing Portland cement (e.g., Barros and Figueiras, 1999; RILEM TC 162TDF, 2003). Both Barros and Figueiras (1999) and RILEM TC 162TDF (2003) proposed similar tensile models, shaped as shown in Figure 9.3(a). In the first stage up to the cracking strain ϵ_{ct} , the tensile response is assumed to behave linearly elastic. After cracking, a bi-linear strain softening response is used to represent the contribution of the fibers.

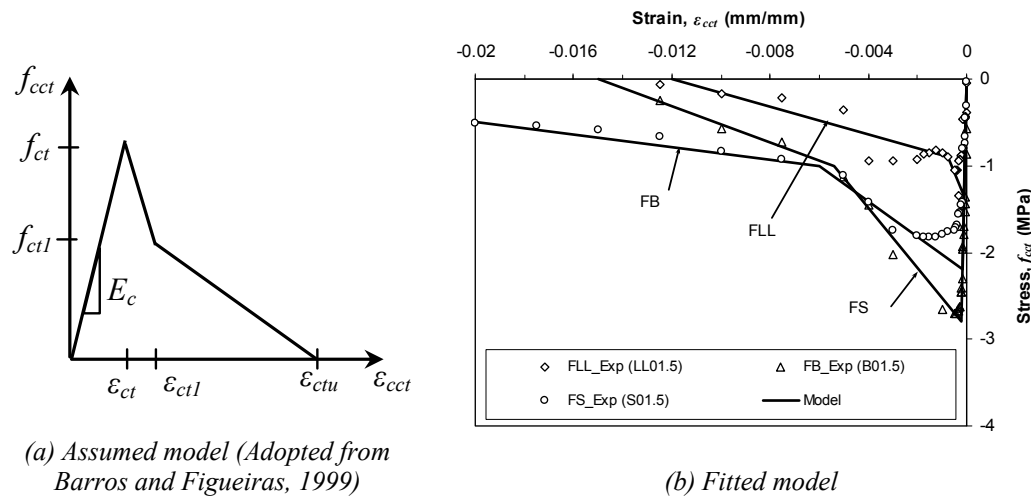


Figure 9.3- Idealized tensile stress-strain curves for GFRCC

Generally, the tensile stress-strain model parameters (f_{ct} , f_{ct1} , ε_{ct} , ε_{ct1} , ε_{ctu}) are obtained by the so-called inverse analysis (back calculation) method when the uniaxial tensile test data are not available or by fitting the tension model to the tensile experimental data when the uniaxial tension test data are available (e.g., Mobasher, 2011). In this study, the uniaxial tensile response of GFRCC dog-bone specimen with 1.5% short fibers but without textiles recorded in Chapter 7 was used to determine the best-fit GFRCC tensile model parameters for each mix Type.

Referring to Figure 9.3, the following equation describes the tensile stress-strain response of GFRCC.

$$\begin{cases} f_{cct} = E_c \varepsilon & \varepsilon_{ct} \leq \varepsilon \leq 0 \\ f_{cct} = f_{ct} + (f_{ct1} - f_{ct}) / (\varepsilon_{ct1} - \varepsilon_{ct}) \cdot (\varepsilon - \varepsilon_{ct}) & \varepsilon_{ct1} < \varepsilon \leq \varepsilon_{ct} \\ f_{cct} = f_{ct1} + (f_{ctu} - f_{ct1}) / (\varepsilon_{ctu} - \varepsilon_{ct1}) \cdot (\varepsilon - \varepsilon_{ct1}) & \varepsilon_{ctu} < \varepsilon \leq \varepsilon_{ct1} \\ f_{cct} = 0 & \varepsilon_{ctu} > \varepsilon \end{cases} \quad (9.3)$$

The tensile model parameters are given in Table 9.2. The negative sign in this table indicates that the stress and strain in concrete are both in tension. Figure 9.3(b) shows the stress-strain of the fitted models and the experimental results from the direct tension tests. The model curves were in good agreement with the experimental data. The tensile response is assumed to behave in a linearly elastic fashion up to the cracking strain ε_{ct} , after which, the response continued reducing on the post-cracking region until the strain reached ε_{ctu} . As shown in Figure 9.3(b), the cracking stress for FS obtained by the model is slightly higher than the experimental results. This increase created only marginal change in the non-linear analysis model results discussed in section 9.6. A further refinement of the model parameters in Table 9.2 is possible as additional test data becomes available. A limited number of tests were completed in the current study. A generalization of the parameters by mix type is possible when further test data are available.

9.3.2 Textile Reinforcement

Two layers of glass textile fabric were used at the tension face of specimens S23L, S25L, S25B and S25S. Both the warp and weft spacing between yarns was approximately 7 mm. The warp yarns were aligned in the longitudinal direction of the slabs with a textile fabric width of 185 mm (Chapter 8).

Experimental results from textile reinforced GFRCC dog-bone specimens tested under direct tension (presented in Chapter 7) were used to establish the textile reinforcement stress-strain model. The dog-bone specimens each contained two layers of textile similar to the number of layers and thickness of layers used in the slabs. The average experimental results of the dog-bone specimens are shown in Figure 9.4.

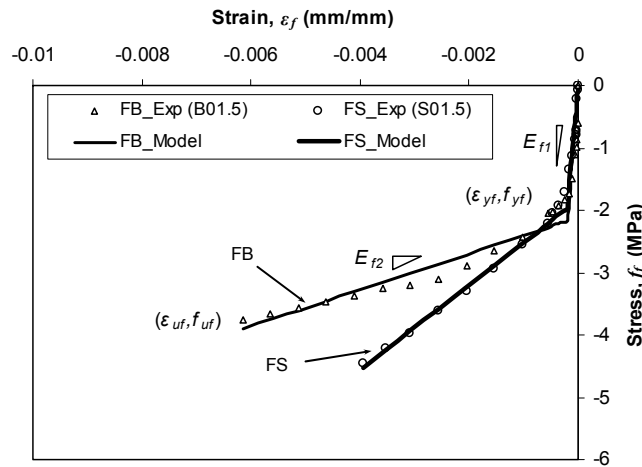


Figure 9.4- Idealized tensile stress-strain curves for textile reinforced ceramic concrete

Adopting similar equations as Bosche et al. (2008), the stress-stain relationship was approximate with a bi-linear model defined by:

$$\begin{cases} f_f = E_{f1}\varepsilon_f & \varepsilon_{yf} \leq \varepsilon_f \leq 0 \\ f_f = f_{yf} + E_{f2}(\varepsilon_f - \varepsilon_{yf}) & \varepsilon_{uf} < \varepsilon_f \leq \varepsilon_{yf} \\ f_f = 0 & \varepsilon_{uf} > \varepsilon_f \end{cases} \quad (9.4)$$

The results presented in Figure 9.4 shows that the results found from Equation 9.4 fitted well to experimental data ($R^2=0.93$ for FB and $R^2=0.97$ for FS). The textile reinforced GFRCC parameters that defined the model obtained by regression analysis are given in Table 9.3. The negative sign in this table indicates that the stress and strain are both in tension.

Table 9.3- Textile tensile stress-strain parameters

	ϵ_{yf}	E_{f1} (MPa)	ϵ_{uf}	E_{f2} (MPa)
FB	-0.0002	-10865	-0.0062	-291
FS	-0.0002	-9850	-0.0039	-684

Note that Equation 9.4 considers the properties of both textile fabric and surrounding concrete and thus Equation 9.3 is not used for TRCC element.

9.3.3 Reinforcing Steel

Deformed longitudinal 10M steel bars with a cross-sectional area of 100 mm² were used (CSA A23.3-04). No shear reinforcement was used. The steel coupon test results presented in Chapter 8 were applied to establish the model for the tensile stress-strain response of steel.

The tensile stress-strain of reinforcing steel may be idealized for analysis and design using: a) a bi-linear elastic-perfectly plastic model; b) a tri-linear approximation; or c) use of actual complete stress-strain curve (e.g., Park and Paulay, 1975). Since the stress-strain curves from the coupon test results showed strain hardening behaviour (Figure 9.5), a simple bi-linear elastic-plastic with a hardening stress–strain model was considered. This model was best fitted to the reinforcement test result. The stress-strain response of the bi-linear model and the test result is shown in Figure 9.5(a). The model was defined by two slopes: The first slope was represented by E_s and the second slope by $Q.E_s$. The parameter Q is a constant that relates the two slopes. The reinforcement parameter E_s obtained from the coupon test is given in Table 9.4. The negative sign in this table indicates that both the stress and strain are in tension. When the bi-linear model

was used, some discrepancy between the assumed model and the test stress-strain response was observed around the intersection of the two slopes (see Figure 9.5(a)). Hence, another model is used.

Table 9.4- Reinforcing steel stress-strain parameters

ε_{ys}	f_y (MPa)	ε_{us}^*	E_s (GPa)
-0.0024	-470	-0.03	-198.4
* Maximum steel strain value recorded by extensometer			

A better representation of the reinforcement stress-strain relationship was obtained by applying the modified Ramberg-Osgood function (Mattock, 1979), given as:

$$\begin{cases} f_s = E_s \varepsilon_s \left[Q + \frac{1-Q}{(1+(K \varepsilon_s)^R)^{1/R}} \right] & \varepsilon_{us} \leq \varepsilon_s \leq 0 \\ f_s = 0 & \varepsilon_{us} > \varepsilon_s \end{cases} \quad (9.5)$$

where K , Q , and R are curve-fitting parameters.

The parameters of Equation 9.5 were obtained using a procedure given by Collins and Mitchell (1997). The parameter Q was obtained from the ratio of the slope of the two lines (see Figure 9.5(b)). The value of the intersection of the second slope ($Q.E_s$) to f_s axis was defined as $E_s(1-Q)/K$, thus K was determined from this relation once Q was determined. The value of R was obtained by trial and error to best fit the experimental results. The values of K , Q , and R that were in good agreement with the reinforcement test result were 412.4, 0.024 and 3.0, respectively.

It can be seen from Figure 9.5(b) that good agreement between the stress-strain response of the proposed model and the experimental results was achieved up to a steel strain of 0.03 mm/mm which was the maximum value recorded by extensometer (see section 8.2.3, $R^2=0.999$).

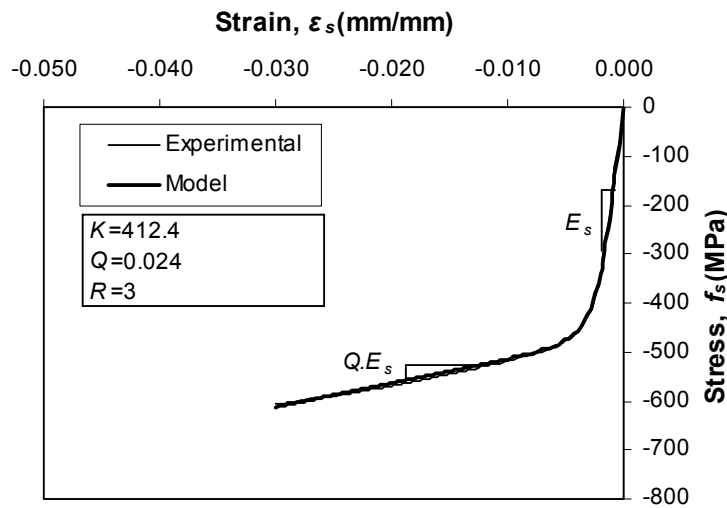
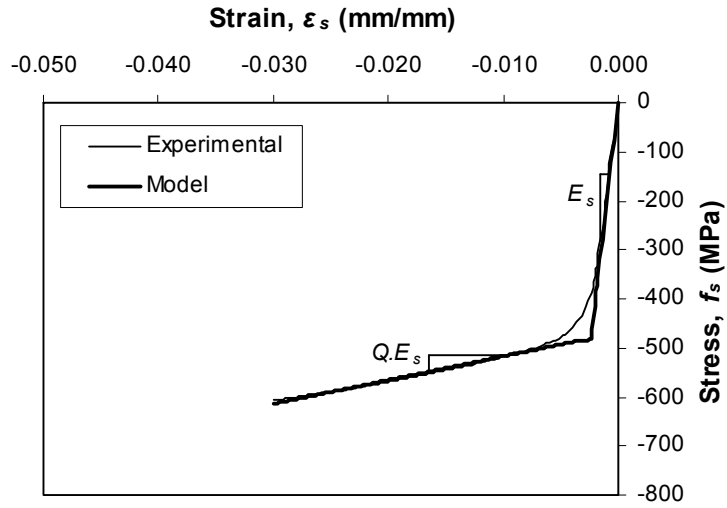


Figure 9.5- Tensile stress-strain behaviour of steel reinforcement

9.4 Non-linear Analysis Model for Flexural Behaviour

As described in section 8.6.4, the axial strain was observed to vary linearly over the depth of the member, up to failure. Hence, plane sections that remain plane and normal to the axis of the slab before and after bending at all stages of loading was considered as a valid assumption for the slab specimens. This observation was used as the bases for developing a non-linear analysis model to represent the

flexural behaviour at each cross-section along the length of the member. Additional assumptions made in this modeling approach included: a) the steel or textile is perfectly bonded to the GFRCC, and hence the strain is continuous with depth and; (b) shear deformation is neglected.

A non-linear analysis model developed in this study was based on material constitutive equations established in section 9.3 and by applying the force equilibrium and strain compatibility conditions. The moment curvature relation is first determined using a layer-by-layer evaluation approach at each cross-section, which is adopted from previous work (e.g., Collins and Mitchell, 1997). See Figure 9.6. To obtain the full member load-deflection response the slab is first divided into small individual elements along the length. The load-deflection response at any load level is then obtained by integrating the curvature at cross-sections along the slab's length. See Figure 9.7.

As discussed in Chapter 8, the slab specimens exhibited a variable spacing of cracks at the constant moment region between the concentrated loads (see Figure 8.25). Between these cracks, the concrete was un-cracked and the tension carried by the un-cracked concrete contributed towards an increased stiffness of the slab. In addition, the tensile force in the reinforcement located at the un-cracked concrete portion is lower than at the cracked location due to sharing of the tension force by the un-cracked concrete. This phenomenon is also known in Portland cement reinforced concrete and termed as tension stiffening (e.g., Vecchio and Collins, 1986; Bischoff and Paixao, 2004; Stramandinoli and Rovere, 2008). The proposed model did not consider the effect of tension stiffening from the rebar since no data on tension stiffening of GFRCC were available to incorporate into the proposed model. Tension stiffening of the textile is implicitly considered in the TRCC model in section 9.3.2. Hence, the stiffness of the slab and reinforcing steel strain predicted by the model is expected to differ from experimental results.

9.4.1 Moment Curvature Response

In the numerical model, the moment-curvature response of individual cross-sections subjected to a bending moment was predicted.

A prismatic cross-section reinforced with steel bars and textile reinforcements was considered, as illustrated in Figure 9.6. The figure shows the cross-section of the composite slab, the axial strain distribution, the axial stress distribution, and the internal forces. The dashed line indicates the neutral axis (NA) located a distance of y_o from the top concrete compression fiber. For convenience in the analysis, the strains and stresses in compression are all considered positive and in tension negative. This sign convention matched with the material sign convention shown in section 9.3.

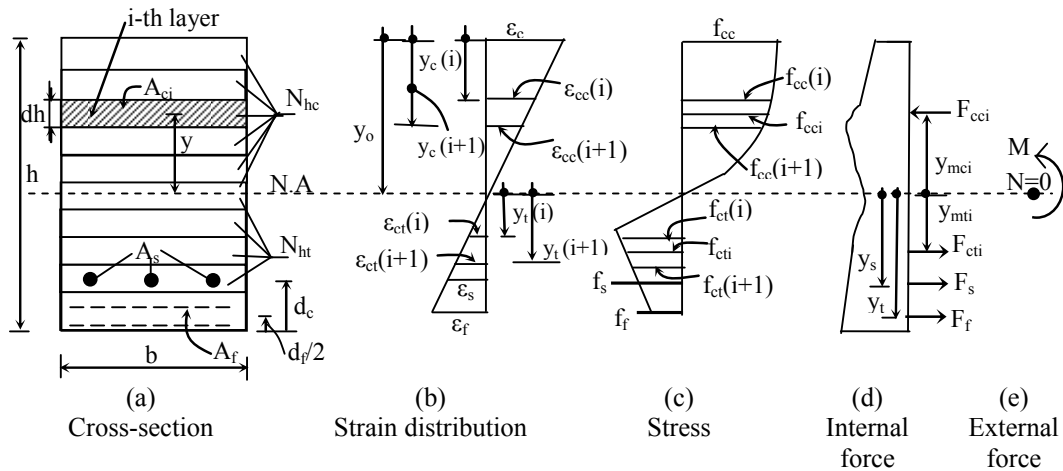


Figure 9.6- Strain, stress and force distribution considered for moment-curvature analysis

The slab cross-section is assumed to be subjected to bending moment M and axial force $N=0$, as shown in Figure 9.6. To satisfy the equilibrium of internal and external forces at the cross-section, the following equation is used (e.g., Popov, 1978):

$$\begin{aligned}
 N &= \int_h f \cdot b \, dh = 0 & (a) \\
 M &= -\int_h f \cdot y \cdot b \, dh & (b)
 \end{aligned}
 \tag{9.6}$$

In Equation 9.6, b is the slab width and dh is a small strip depth, f is the stress at the middle of the strip which is located at y distance from the neutral axis.

Due to the non-linear material behaviour and inhomogeneous cross-section, Equation 9.6 was solved using numerical integration techniques by applying a layer-by-layer analysis technique obtained in literature (e.g., Collins and Mitchell, 1997).

The numerical integration was done by sub-dividing the cross-section height into m layers, each with a height of dh , as shown in Figure 9.6(a). For slabs with TRCC, only the upper part of the cross-section (above the TRCC) was subdivided into m layers. This total number of layers m was shared by the compression zone number of layers N_{hc} and the tension zone number of layers N_{ht} with both having the same layer depth dh . However, one layer of N_{hc} or N_{ht} may have a depth of less than dh , depending on the location of the neutral axis (see Figure 9.6(a)).

The moment curvature response was determined by using the following procedures:

- (a) The concrete strain at the extreme compression fiber (ϵ_c) was assumed.
- (b) The neutral axis (NA) depth y_o was assumed, with y_o measured from the flexure concrete compression fiber, as shown in Figure 9.6(b).
- (c) The number of concrete compression layers (N_{hc}) was calculated using the following formula, and the result was rounded to the next larger integer (see Figure 9.6(a)).

$$N_{hc} = \frac{y_o}{dh} \quad (9.7)$$

The number of concrete tension layers (N_{ht}) was calculated using Equation 9.7, but y_o was replaced by $h-d_f-y_o$ and the result was then rounded to the next larger integer.

- (d) The compression zone layers' top and bottom locations ($i=1, 2, \dots, N_{hc}$) measured from the flexure concrete compression were calculated using the following equation. Note that the last strip bottom location $y_c(N_{hc}+1)$ is equal to y_o and that this strip depth is usually less than or equal to dh .

$$y_c(i) = (i-1)dh \quad (9.8)$$

The tension zone layers' top and bottom locations $y_t(i)$ measured from the NA were also determined using a similar procedure.

- (e) Using the strain distribution shown in Figure 9.6(b), the strain at the top or bottom of each strip ($i=1, 2 \dots, N_{hc}+1$) in the compression zone (above NA) was calculated using the following equation:

$$\varepsilon_{cc}(i) = \frac{\varepsilon_c(y_o - y_c(i))}{y_o} \quad (9.9)$$

Equation 9.9 was also used to calculate strains in the tension zone of the cross-section (below NA), but $\varepsilon_{cc}(i)$ and $y_c(i)$ was replaced by $\varepsilon_{ct}(i)$ and $y_t(i)$, respectively (see Figure 9.6(b)).

- (f) The steel strain was calculated assuming no slip by using:

$$\varepsilon_s = \frac{\varepsilon_c(y_o - h + d_c)}{y_o} \quad (9.10)$$

- (g) The strain at the center of the textile reinforcements was obtained from :

$$\varepsilon_f = \frac{\varepsilon_c(y_o - h + d_f / 2)}{y_o} \quad (9.11)$$

- (h) The corresponding stresses for each strain (Equations 9.9-9.11) were evaluated using the stress-strain models given in Equations 9.1 to 9.5. For each strip of concrete, the average values of the stresses were used. The i -th

strip average concrete stress ($f_{cc1}, f_{cc2} \dots N_{hc}$), for example (see Figure 9.6(c)), was evaluated using the following formula:

$$f_{cci} = \frac{f_{cc}(i) + f_{cc}(i+1)}{2} \quad (9.12)$$

- (i) Using evaluated stress from step (h) and considering the corresponding area (Figure 9.6(a)), the equilibrium of horizontal forces was checked from 9.6(a) using:

$$N = \sum_{i=1}^{m_1} f_{cci} A_{ci} + \sum_{i=1}^{m_2} f_{cti} A_{ci} + f_s A_s + f_f A_f = 0 \quad (9.13)$$

- (j) If force equilibrium was not satisfied (i.e., Equation 9.13) to an accuracy taken here as ± 0.01 kN, the same process was repeated starting from (b) by assuming another NA depth y_o . To simplify the iteration process that is needed to solve non-linear Equation 9.13, the bisection method was adopted (e.g., Chapra, 2012). According to Chapra (2012), the bisection method is a variation of the incremental search method used for solving a function. If a function changes sign over an interval, the bisection method evaluates the function at the midpoint of these intervals. The new interval will then be the midpoint and a point with a different sign than the midpoint. The process is repeated until the required precision is obtained.

- (k) If force equilibrium was satisfied (i.e. Equation 9.13), the moment was calculated using the moment equilibrium equation given by:

$$M = \sum_{i=1}^{m_1} f_{cci} A_{ci} y_{mci} + \sum_{i=1}^{m_2} f_{cti} A_{ci} y_{mti} + f_s A_s y_s + f_f A_f y_f \quad (9.14)$$

where y_{mti} , y_s and y_f are the distance from the corresponding element to the neutral axis and all are taken as negative, but y_{mci} is positive.

- (1) For the concrete strain at the top fiber (ϵ_c) selected at step (a) and NA depth (y_o) at step (b), the curvature of a section was obtained from:

$$\phi = \frac{\epsilon_c}{y_o} \quad (9.15)$$

This procedure was repeated by increasing the concrete strain at the top compression fiber (ϵ_c) at step (a) with a strain increment value of 0.0001. The complete moment-curvature relationship was determined up to the point at which either the concrete at the top extreme compression fiber or the tension reinforcing steel reached their corresponding assumed ultimate strain values, or when the textile reinforcement reached its assumed ultimate strain value. (See section 9.3).

The analysis model in this study assumed the cross-section remains intact and thus it is acknowledged that this cross-section analysis approach will not predict the formation of the splitting cracks between the TRCC and upper concrete that was observed in specimens S25L, S25B and S25S near the peak loads.

9.4.2 Deflection and Slope Computation

The slabs tested in this study (Chapter 8) were simply supported and subjected to two concentrated loads, as shown in Figure 9.7(a). The bending moment diagram obtained by using static equilibrium along the axis of the slab at any load stage k is shown in Figure 9.7(b). The curvature values for each moment along the axis of the slab (at any distance x from left support $M(x)$) were obtained by using the moment-curvature relations generated with the techniques described in section 9.4.1. The slopes and deflections were obtained from the curvature by applying the two well-known moment area theorems (e.g., Ghali and Neville, 1989). The slope and the deflection along the axis of the slab at any load stage k are shown in Figures 9.7(c) and (d), respectively. Due to geometric and loading symmetry, only half of the slab was analyzed. Half of the span result is then mirror-reflected at mid-span to obtain a complete span response.

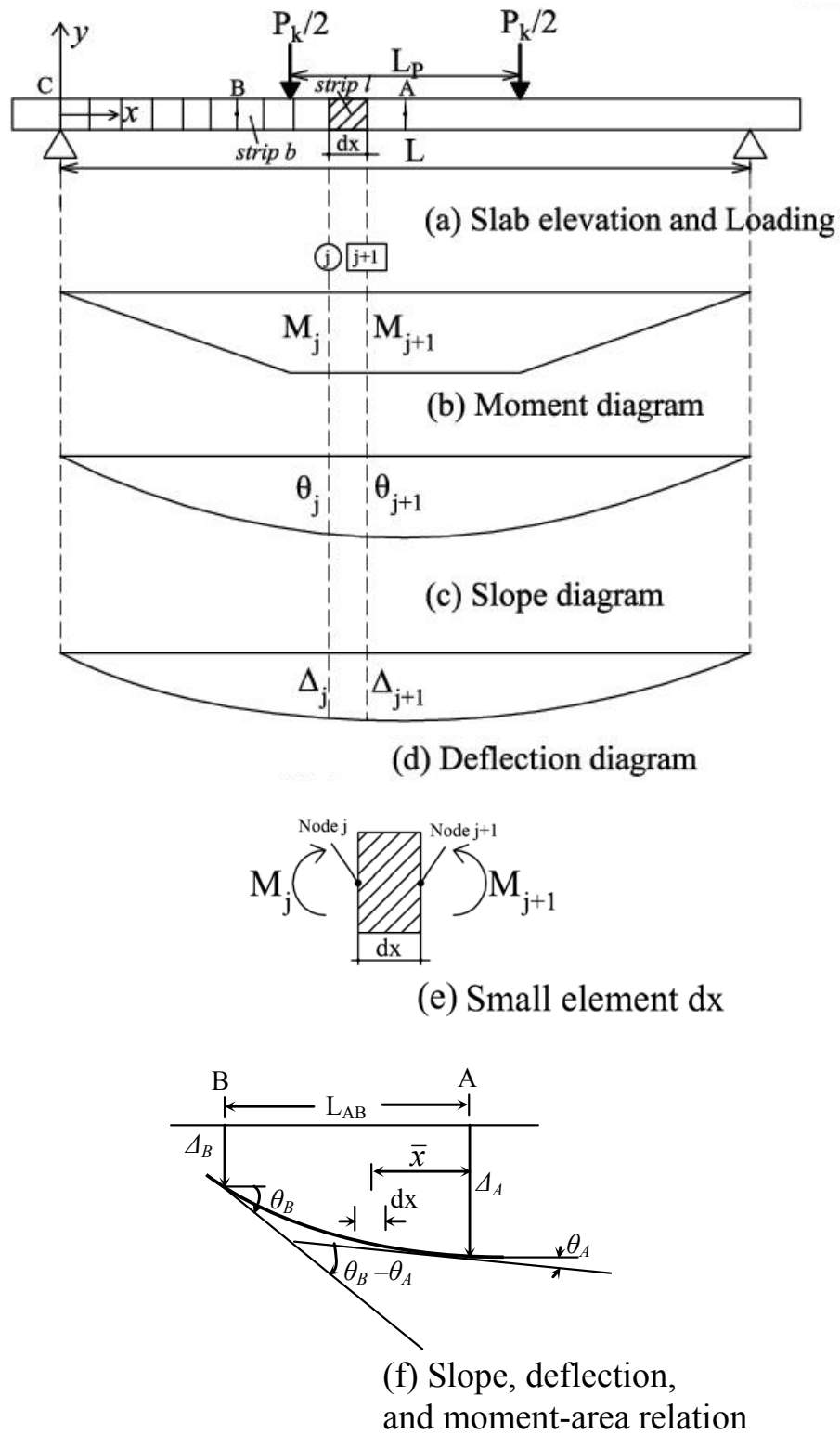


Figure 9.7- Slope and deflection diagrams of slab

Using the first moment-area theorem (e.g., Park and Paulay, 1975; Ghali and Neville, 1989), the change in rotation between any two points (e.g., A and B Figure 9.7(a)) is determined by integration of the curvature between these two points, using Equation 9.16.

$$\theta_B - \theta_A = -\int_A^B \phi_{AB} dx \quad (9.16)$$

Applying the second moment-area theorem (e.g., Park, and Paulay, 1975; Ghali and Neville, 1989), the difference in deflection between two points (e.g., A and B Figure 9.7(a)) along the axis of the slab is obtained using Equation 9.17. The first part of Equation 9.17 indicates the product of the slope (θ_B) at point B and the distance between the two points A and B (L_{AB}). The second part indicates the integration of the first moment of the curvature taken from reference point B.

$$\Delta_B - \Delta_A = \theta_B L_{AB} - \int_A^B x \phi_{AB} dx \quad (9.17)$$

Since the evaluation of these integrals cannot be easily determined due to variation in the moment-curvature response and variations of curvature along the slab's length, numerical integration techniques were applied. The slab half-span length was divided into n sections, with length dx and each element named, l , as shown in Figure 9.7(a). Thus, the total number of nodes along the half-length of the slab is $n+1$. A small segment of the slab dx is shown in Figure 9.7(e). The left and right ends of this segment are considered as node j and $j+1$, respectively. The internal moments (M_j and M_{j+1}) needed to keep the segment l in static equilibrium are shown in Figure 9.7(e). The slope and the deflection at each node along the slabs' length are obtained as follows:

(a) Since the slope at the centre of the slab was zero ($\theta_A=0$) where the deflection was maximum due to symmetry, the computation was started from the slab centre. Slopes at subsequent nodes were calculated starting from the mid-span node using

Equation 9.18. Thus, the slope at the end of the b -th segment (e.g., point B, Figure 9.7(a)) was determined from:

$$\theta_B = \theta_A - \sum_{j=1}^b \theta_j = -\frac{L/2}{n} \sum_{j=1}^b \frac{\phi_j + \phi_{j+1}}{2} \quad (9.18)$$

In Equation 9.18, the counter-clockwise slope (θ) from the positive x -axis was assumed as positive.

(b) Similarly, Equation 9.17 was approximated by Equation 9.19. Since the deflection at the left support was zero, the computation started at the left-end support of the slab. Thus, the deflection at the end of the b -th segment (e.g., point B) was obtained using the following equation:

$$\begin{aligned} \Delta_B &= \Delta_C - \sum_{j=1}^b \theta_j \frac{L/2}{n} + \frac{1}{2} \left(\frac{L/2}{n} \right)^2 \sum_{j=1}^b \frac{\phi_j + \phi_{j+1}}{2} \\ &= -\frac{L/2}{n} \sum_{j=1}^b \theta_j + \frac{1}{2} \left(\frac{L/2}{n} \right)^2 \sum_{j=1}^b \frac{\phi_j + \phi_{j+1}}{2} \end{aligned} \quad (9.19)$$

When the slope and deflection points for all $n+1$ nodes were obtained using the above procedures, the slope and deflection curves were plotted along the length of the slab. The half-span results are mirror-copied at mid-span to obtain the complete length.

9.5 Model Implementation

The proposed numerical model for performing an analysis of GFRCC slabs required iterative analysis and numerical integration at each stage of loading. To simplify the application of the model described in section 9.4, MATLAB® software was used. A flow chart to describe the programming logic for the evaluation of the moment-curvature response and the load-deflection relationship is shown in Figure 9.8. After obtaining the input data, the program analyses the slab and generates the load-deflection response, the moment-curvature response,

the load versus strain response for the reinforcing steel and the load versus strain response for the concrete.

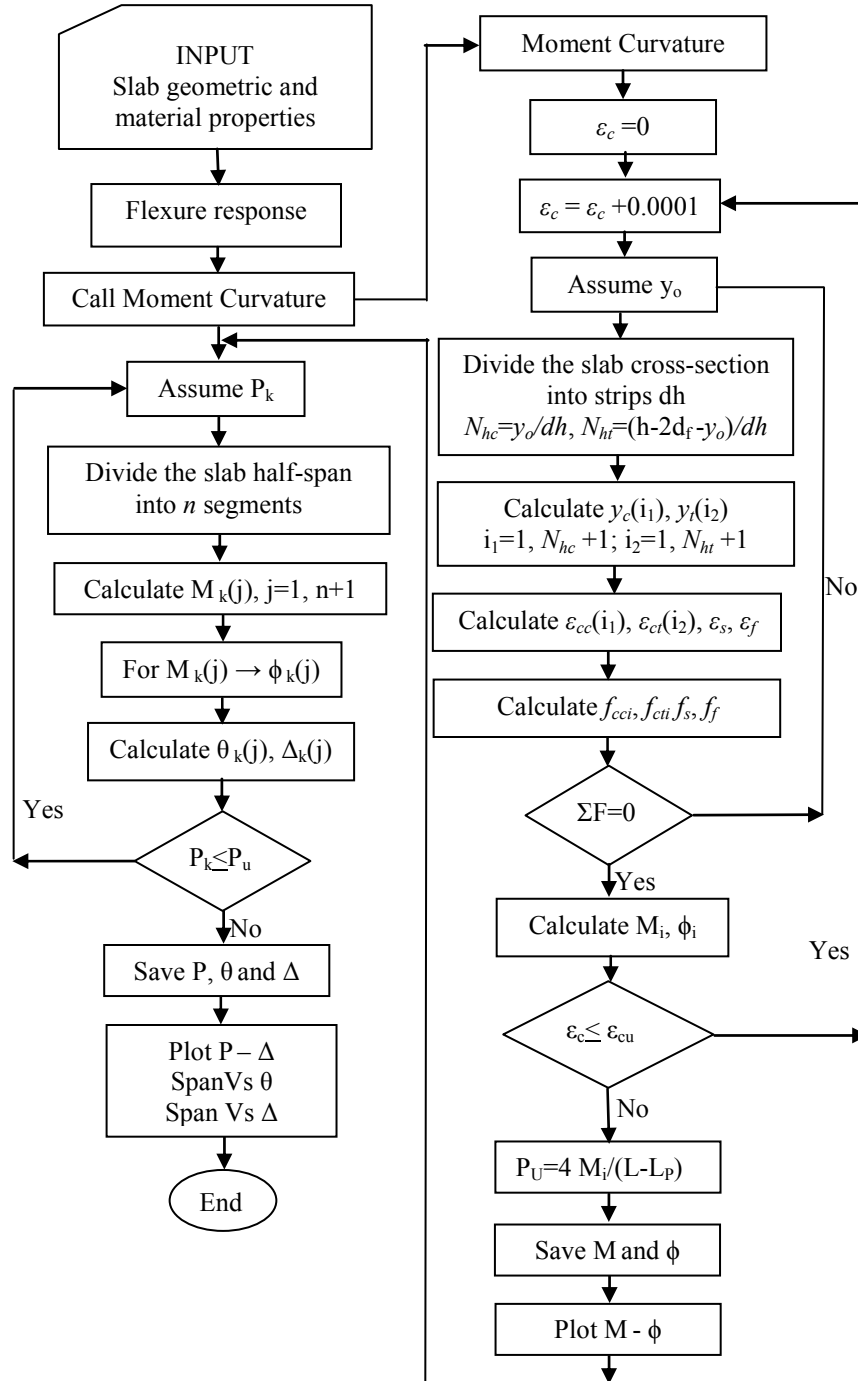


Figure 9.8- Program flow chart

9.5.1 Analysis Using Computer Program

The analysis process of the developed computer program for GFRCC composite slabs is illustrated using Figure 9.9. The input data required are:

- Geometry: slab cross-section and lengths, amount and location of steel reinforcement, and amount and location of textile reinforcement (see Figure 9.9).
- Material properties: GFRCC, reinforcing steel and TRCC (see Figure 9.9).

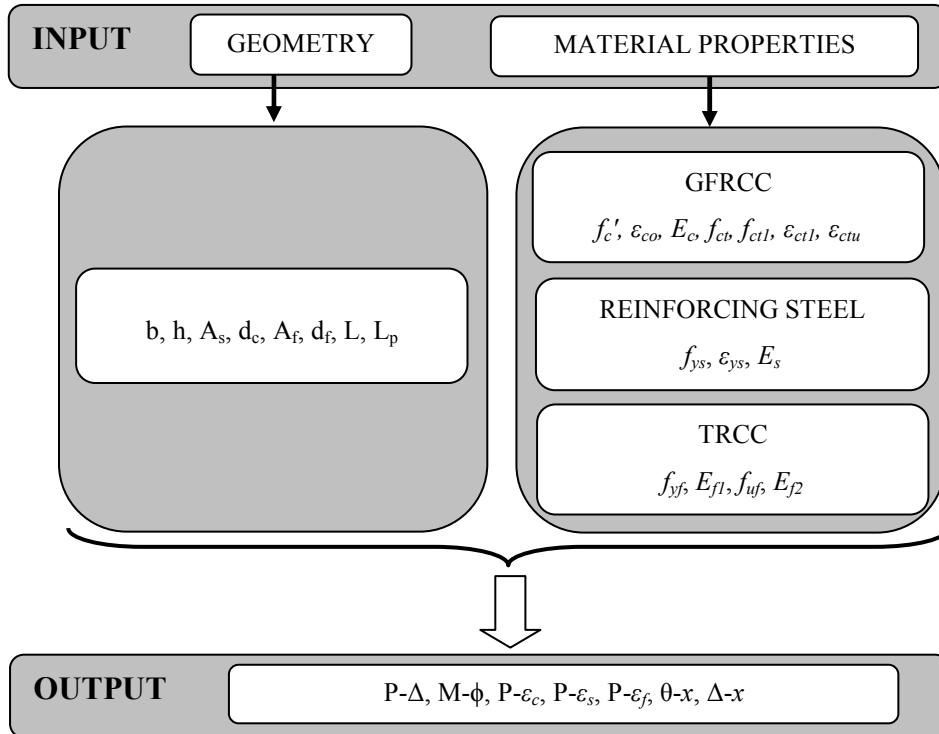


Figure 9.9- Analysis program process

Output from the program is provided in two forms:

(a) Direct graphical creation:

The analysis program directly plots the results. These direct graphical prints were useful for a quick check of the results. Examples of directly generated printout by the program for specimen S03L are shown in Figure 9.10. These results included the material properties for GFRCC, reinforcing steel and the slope diagram along the length of the slab, the deflection profile along the length of the slab, the moment-curvature response and the load versus mid-span deflection response (see Figures 9.10(a) to (e)).

(b) Saving the output as text files:

The analysis program also saves the output as text files. These outputs included the stress versus strain diagram in each material, the load-deflection response and the moment-curvature response. The text files can be used for plotting the results in the user desired format. The model results plots shown in the next section were generated from the text files obtained from each slab modeling results.

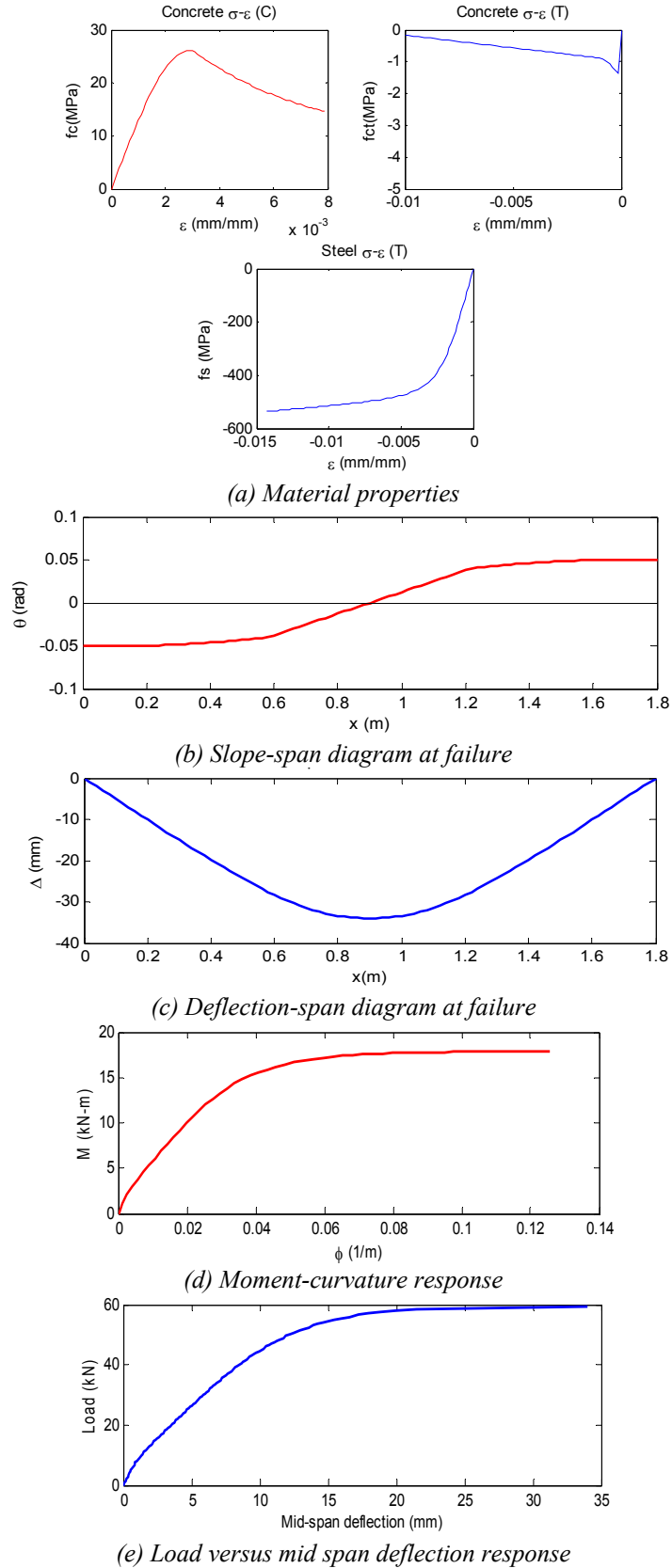


Figure 9.10- Illustrative output figures from the analysis program (S03L)

9.5.2 Convergence Study

The analysis model in section 9.4 was based on dividing the slab cross-section into m layers in the y -direction of height dh (Figure 9.6). The half slab was also divided into n segments along the length (i.e. x -direction), with a segment length of dx (Figure 9.7). A convergence study was performed to select appropriate values of dh and dx . These values (i.e. dh and dx) were assumed as independent values and the selection of one will not affect the convergence result of the other.

A convergence study was carried out first for dh . Six different values of dh were used and the corresponding peak load was evaluated using the developed model. Three different slabs were considered.

The slab cross-section strip height dh selection is expected to depend on the overall slab thickness. The dh versus calculated peak load convergence study was done only for the slab thicknesses considered in this study. For other slab thicknesses different from this study, different dh values may be needed. Figure 9.11(a) shows a dh versus calculated peak load convergence study plot for three different slabs (S03L, S05L and S25B). Figure 9.11(a) indicated negligible change (0.6%) in loads when dh was reduced beyond 15 mm. Therefore, for this study, a value of $dh=10$ mm was chosen.

By using a dh value of 10 mm, the dx values were varied and the peak load deflection was computed using the model. The convergence studies of strip length dx versus the calculated peak load deflection for three different slabs were shown in Figure 9.11(b). The figure showed negligible difference (0.6%) in mid-span deflection when dx was below 30 mm. A value of $dx=20$ mm was chosen for this study.

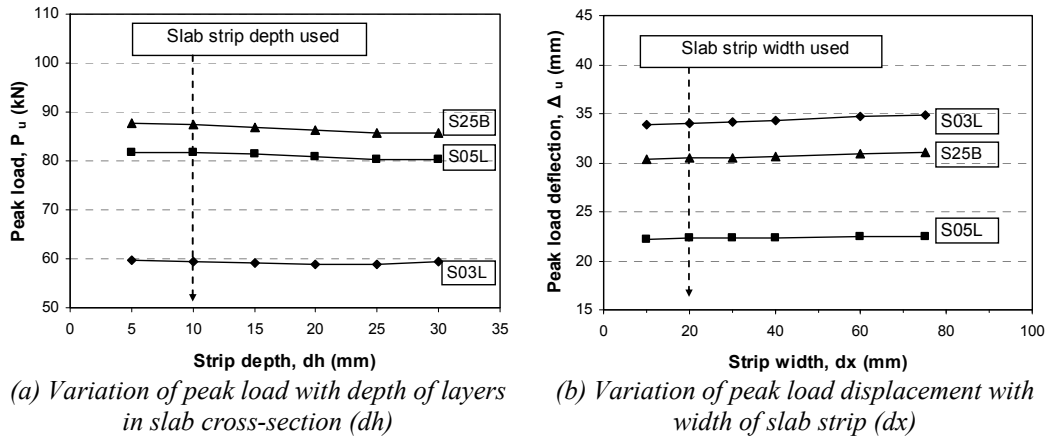


Figure 9.11- Convergence study of the computer program

9.6 Comparison Between Experimental and Model Results

In order to verify the proposed analytical model, the load versus mid-span deflection response, the moment-curvature response, the load versus steel strain response and load versus concrete strain response predicted using the model are compared with the corresponding experimental results from Chapter 8. The comparison is carried out for all six tested slabs.

9.6.1 Comparison of Moment-Curvature Response

A comparison between the experimental and the analytical results of the moment-curvature responses of all specimens are shown in Figure 9.12. The experimental moment-curvature responses were taken from section 8.6.3. The analytical results from the model at each loading stage showed a good correlation with those from the experimental data. However, a discrepancy was observed between the model and the test results at the ultimate stage for some specimen. For S23L, the discrepancy was attributed to the predicted failure of the textile fabric in the model, whereas a discrepancy between the model and test results for specimen S25B at the peak moment stage resulted from malfunctioning of the inclinometer used to measure the curvature (see section 8.6.2).

A summary of experimental and model results at peak load are given in Table 9.5. The numerical model predicted the ultimate curvatures reasonably well for most slabs with mean and CV of experimental-to-predicted ultimate curvature of 0.80 and 8.3%, respectively. Ultimate curvature indicates the curvature at peak load. The experimental ultimate curvatures were 13% to 26% lower than the values predicted by the model (see Table 9.5). However, the value for S23L was 45% higher than the predicted value. This occurred due to the predicted failure of the textiles in the model, which lowered the predicted ultimate curvature. The maximum tension strain used for the textile model makes the strain of the dog-bones failing in part by splitting cracks. This suggests that there may be opportunity to refine the textile model as more data becomes available.

Table 9.5- Summary of experimental and model results

Slab	Experimental					P_u	Δ_u	ϕ_u	ϵ_{cu}	ϵ_{su}
	P_u (kN-m)	Δ_u (mm)	ϕ_u (1/m)	ϵ_{cu}	ϵ_{su}	$P_{u,ana}^*$	$\Delta_{u,ana}$	$\phi_{u,ana}$	$\epsilon_{cu,ana}$	$\epsilon_{su,ana}$
S03L	61.6	25.30	0.0925	0.0040	0.0059	1.04	0.75	0.74	0.72	0.54
S23L	62.3	26.94	0.0938	0.0045	0.0025	1.18	1.43	1.45	1.30	0.52
S05L	79.5	19.30	0.0563	0.0037	0.0017	0.97	0.86	0.76	0.72	0.37
S25L	75.3	20.07	0.0604	0.0038	0.0015	1.07	0.95	0.87	0.76	0.44
S25B	90.3	24.58	0.0814	0.0042	0.0020	1.03	0.81	0.75	0.73	-
S25S	94.7	34.20	0.1178	0.0058	0.0034	1.03	0.91	0.87	0.91	0.34

* ana= analytical results

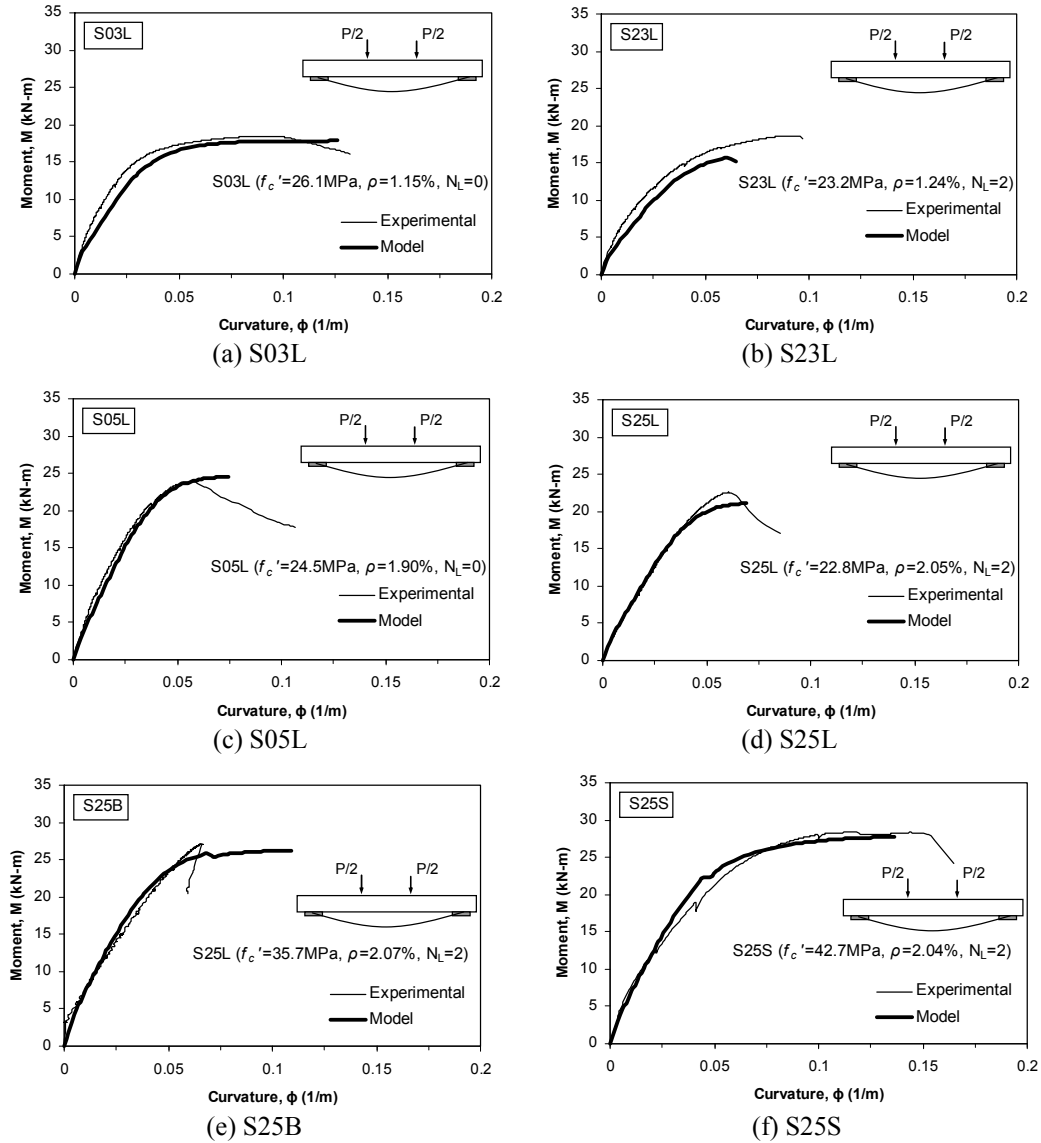


Figure 9.12- Measured and predicted moment-curvature comparison

9.6.2 Comparisons of Concrete Strain

A comparison between experimental and analytical load versus extreme fiber concrete compression strain at mid-span is shown in Figure 9.13. The predicted concrete strains at each load stage were in good agreement with the experimental results. The measured concrete strains at peak load were 9% to 28% lower than the predicted results (mean of experimental-to-predicted peak load concrete strain = 0.77 and CV = 10.6%). However, for specimen S23L, this value was 30% higher than the predicted results due to premature failure of the textile in the

model (see Table 9.5). This predicted failure of textile also showed similar effect on moment-curvature of specimen S23L (see section 9.6.1).

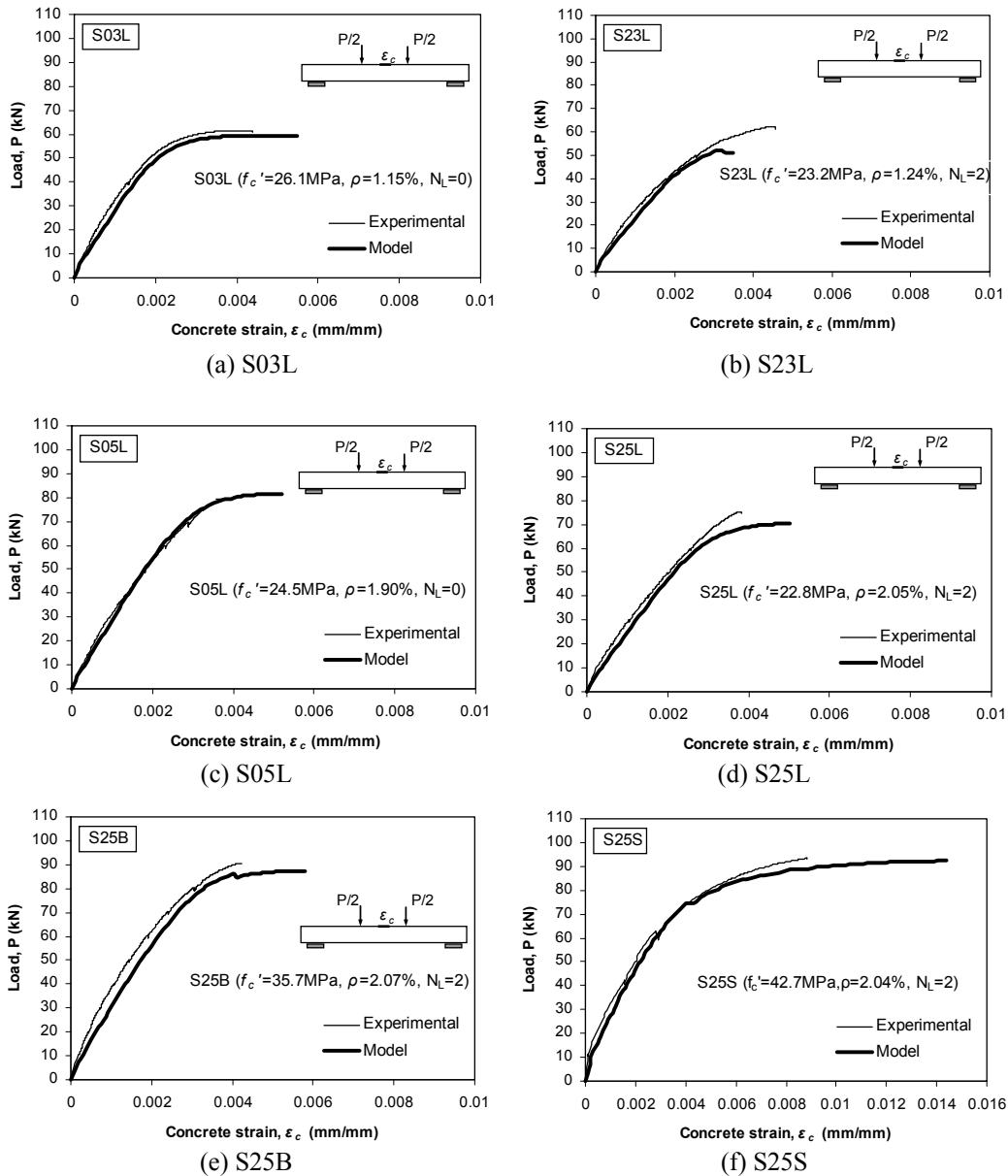


Figure 9.13- Measured and predicted load versus extreme fiber compressive concrete strain comparison at mid-span

9.6.3 Comparison of Reinforcement Strain

Predicted and measured strains in the steel reinforcement are compared in Figure 9.14. The predicted steel strains at each load stage were higher compared to the experimental results. The strain gauges may not be located at a crack location

(referring to Figure 8.25), and steel strains between cracks are typically lower than those at crack locations due to the tension stiffening effect (e.g., Bischoff and Paixao, 2004; Stramandinoli and Rovere, 2008). The numerical model did not consider the tension stiffening effect and predicted the steel strains at a crack. As a result, the measured strains showed lower values than the predicted strains. The experimental ultimate steel strain results were 46% to 66% lower than the predicted values (see Table 9.5). The result of S25B was not included in this range, since the strain gauges installed in this specimen malfunctioned.

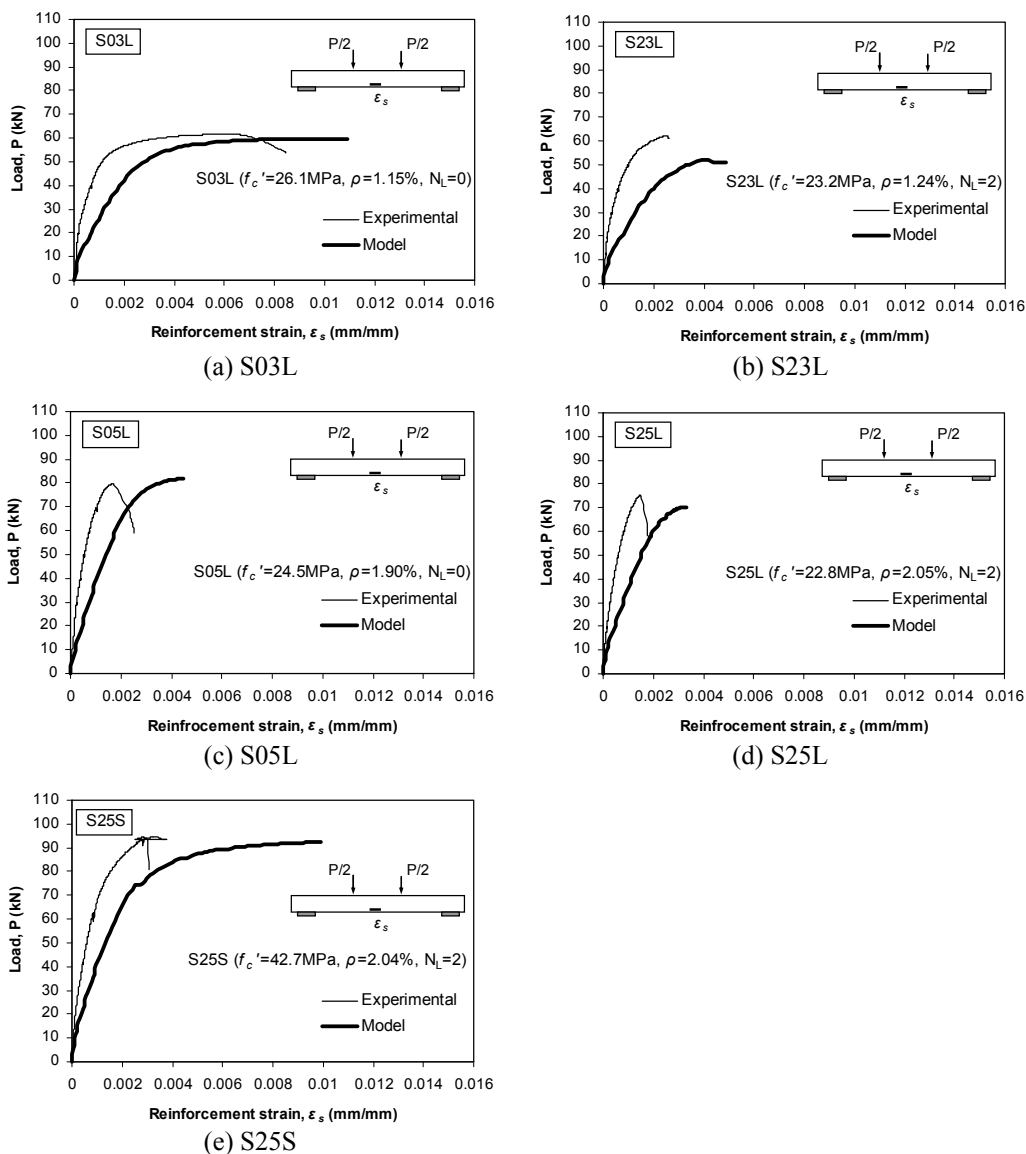


Figure 9.14- Measured and predicted load versus mid-span steel strain comparison

9.6.4 Comparison of Load-Deflection Response

Figure 9.15 shows a comparison between the model result and experimental values of load-deflection response at mid-span. The load-deflection response from the numerical model agreed well with the experimental data for most slabs. A good agreement with deflection in service load range of the experimental-to-model results were observed with a mean and CV of 0.90 and 8.4%, respectively. However, for some slabs (e.g., S03L, S23L), the stiffness predicted after about 15 kN was slightly lower than the experiment results. This was expected, due to the tension stiffening effect in the experimental slabs, as its effect was observed in load versus reinforcement strain response in Figure 9.14.

Table 9.5 shows that the experimental-to-predicted ultimate load exceeded 1.0 for most slabs and was slightly less than 1.0 for one slab (S05L). These indicate that the numerical model predicted the ultimate loads well with a mean and CV of 1.05 and 6.7%, respectively.

The analytical model also did a relatively good job of predicting the deflection corresponding to peak load for most slabs with a mean and CV of 0.86 and 9.3%, respectively. The measured deflections at peak load were 5% to 25% lower than the predicted deflections. However, this value was 43% higher than the predicted deflection for specimen S23L due to the premature failure of textile fabric in the model. Its effect can be seen in the moment-curvature response in Figure 9.12.

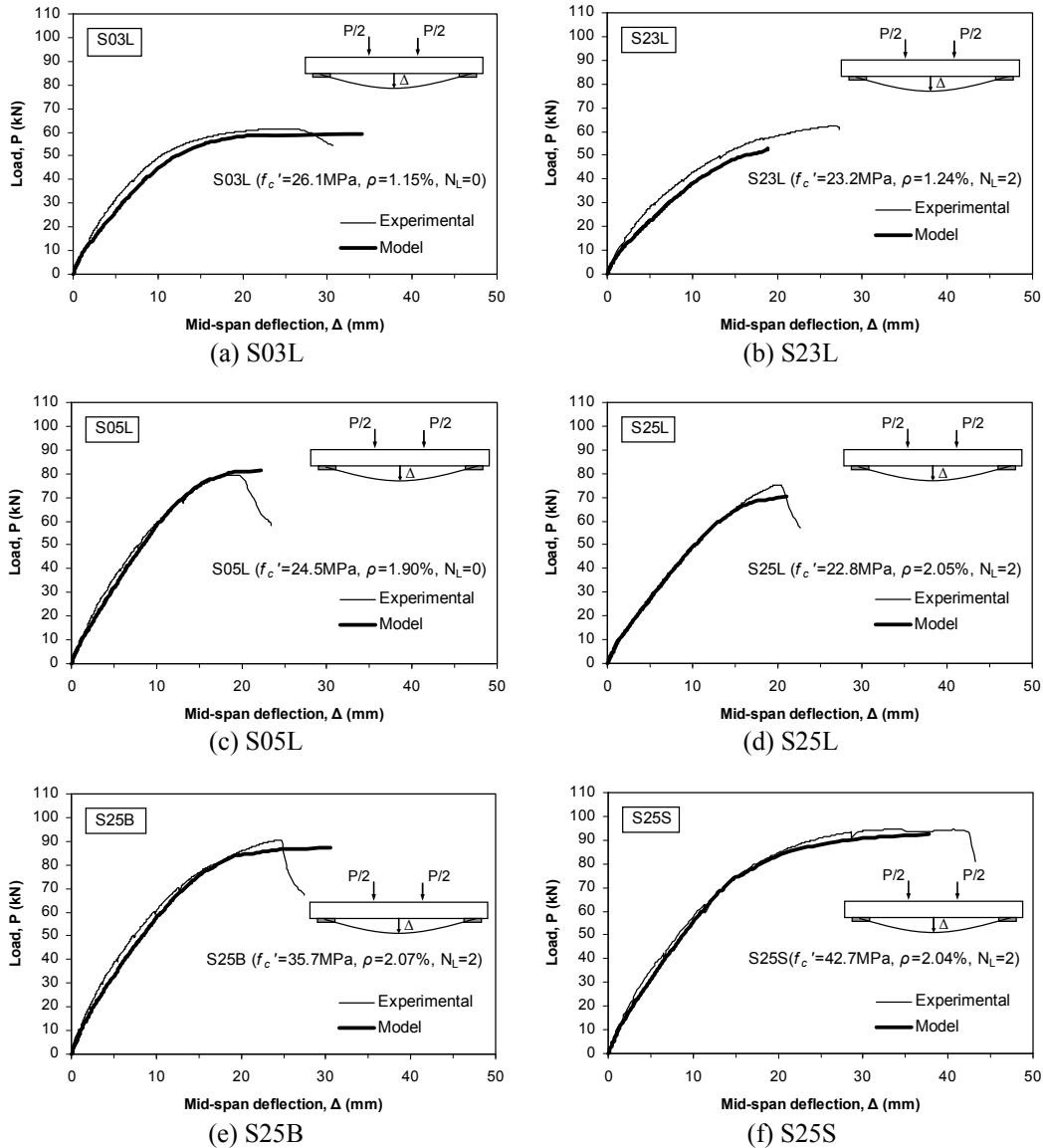


Figure 9.15- Measured and predicted mid-span load-deflection comparison

The failure modes obtained from the model was similar to test results for specimen S03L (see section 8.6.2). The failure occurred due to yielding of reinforcement (confirmed by steel stress at peak load = 520 MPa > $f_{sy} = 470 \text{ MPa}$) and crushing of concrete ($\epsilon_{cu} = 0.0055$).

Failure modes predicated by the model for specimen S23L however differed from the test result. This was due to premature failure of textile fabric in the model which controlled the slab capacity. As a result no crushing of concrete

($\epsilon_{cu}=0.0032$) or yielding of reinforcement (steel stress at peak load = 460 MPa) occurred unlike the test result reported in section 8.6.2.

The failure modes predicated by the model for slab specimens S05L and S25L was similar to experimental results. The failures occurred due to crushing of concrete (ϵ_{cu} for S05L and S25L was 0.0050 and 0.0058 respectively). However, no yielding of steel occurred in both cases (i.e., steel stress at peak load $< f_{sy}$).

The failure modes obtained from the model for specimen S05B was crushing of concrete ($\epsilon_{cu}= 0.0058$) similar to experimental results presented in section 8.6.2. The model result showed a yielding of steel reinforcements (steel stress at peak load = 499 MPa $> f_{sy} = 470$ MPa). However this couldn't be confirmed by the experimental results since strain gauges in S25B malfunctioned (see section 8.6.4.2).

The failure modes predicated by the model for slab specimen S05S was similar to experimental results. The failures occurred due to crushing of concrete ($\epsilon_{cu} = 0.0058$) and yielding of steel (steel stress at peak load = 515 MPa $> f_{sy} = 470$ MPa).

9.7 Parametric Study

A parametric study was carried out using the developed model to observe the effect of variation in ceramic concrete compressive strengths and steel reinforcement ratios on the moment-curvature response and ductility. The slab geometry was fixed, but f_c' and ρ were varied, as shown in Table 9.6. The concrete compressive strengths were similar to the strengths of S25L, S25B and S25S. Four different steel reinforcement ratios were considered (i.e., 0.77%, 1.15%, 1.54%, and 1.92%).

Table 9.6- Slab geometry and concrete material properties used for parametric study

Slab ID	Cross-section (mm)		d (mm)	Reinforcement			Concrete		
	b	h		Steel			f'_c (MPa)	ϵ_{co}	E_c (GPa)
				bar	A_s (mm ²)	ρ (%)			
SL1	200	150	130	2-10M	200	0.77	22.8	0.0028	10.4
SL2	200	150	130	3-10M	300	1.15	22.8	0.0028	10.4
SL3	200	150	130	4-10M	400	1.54	22.8	0.0028	10.4
SL4	200	150	130	5-10M	500	1.92	22.8	0.0028	10.4
SB1	200	150	130	2-10M	200	0.77	35.7	0.0038	13.1
SB2	200	150	130	3-10M	300	1.15	35.7	0.0038	13.1
SB3	200	150	130	4-10M	400	1.54	35.7	0.0038	13.1
SB4	200	150	130	5-10M	500	1.92	35.7	0.0038	13.1
SS1	200	150	130	2-10M	200	0.77	42.7	0.0042	12.1
SS2	200	150	130	3-10M	300	1.15	42.7	0.0042	12.1
SS3	200	150	130	4-10M	400	1.54	42.7	0.0042	12.1
SS4	200	150	130	5-10M	500	1.92	42.7	0.0042	12.1

9.7.1 Effect of f'_c and ρ on Moment-Curvature Response

The effect of f'_c on the model-predicted moment-curvature response of slabs with $\rho = 0.77\%$ and 1.92% but different f'_c is shown in Figure 9.16. For both reinforcement ratios, the moment-curvature responses were linear up to the cracking load point, after which the moment-curvature slope gradually reduced up to the yielding of reinforcements. Higher slopes were observed in this region when the f'_c increased due to higher E_c as described in Table 9.6. After yielding, all of the moment-curvature curves were nearly horizontal until the peak moment. This moment-curvature behaviour is similar to a response of typical Portland cement-based concrete. Figure 9.16 illustrates how the peak moment and the corresponding curvature at peak moment varied, depending on the f'_c . Both of these values increased as the f'_c increased. The increase in the peak moment is due to the presence of more concrete compression section to balance the tensile force when f'_c increased. In addition, increase in f'_c resulted in an increase in the internal couple lever arm between the compressive and tensile forces. An increase

in f_c' decreased the neutral axis depth at a given load level, as confirmed in section 9.7.2, thus increasing curvatures at the peak moment.

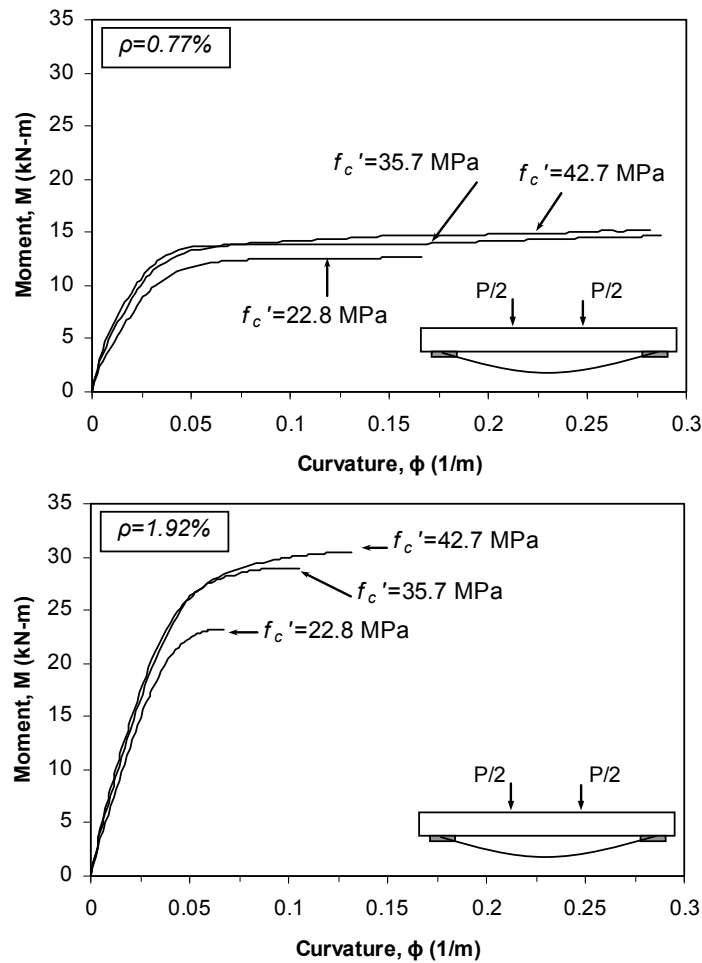


Figure 9.16- Effect of f_c' on moment-curvature response predicted by model

The effect of ρ on the moment-curvature response of slabs predicted by models for $f_c' = 22.8$ MPa, 35.7 MPa and 42.7 MPa and different ρ is shown in Figure 9.17. All moment-curvature responses were linear elastic up to the cracking load, similar to response of Portland cement-based concrete. After cracking, the moment-curvature responses were nonlinear, with slopes gradually reduced up to the yielding of reinforcements. Higher slopes were observed when ρ increased due to higher cracked moments of inertia. After the yielding of reinforcements, all of the curves were nearly horizontal up to the peak moment. As can be seen from Figure 9.17, the peak moment and the corresponding curvature were different, depending on ρ . The peak moment increased while the corresponding curvature

values decreased as ρ increased. The increase in reinforcing steel area (ρ) led to an increase in tensile force and thus an increase in the peak moment. An increase in ρ increased the neutral axis depth for a given load level, as confirmed in section 9.7.2 thus decreasing curvature.

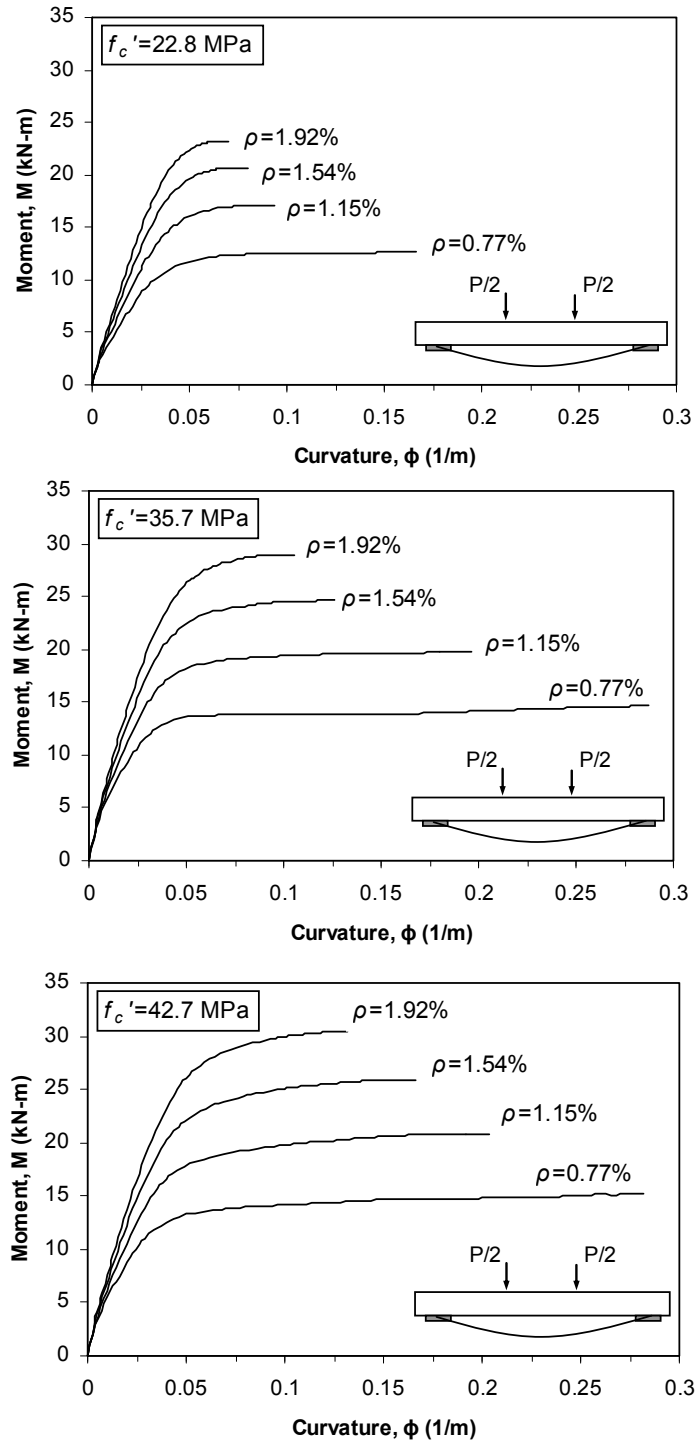
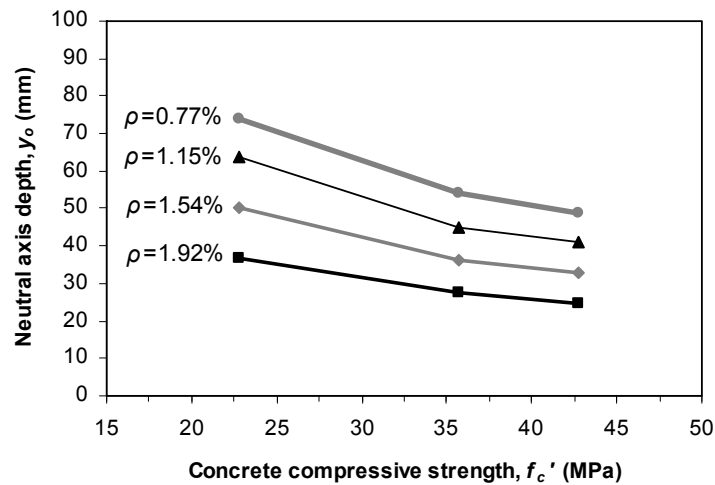


Figure 9.17- Effect of ρ on moment-curvature response predicted by model

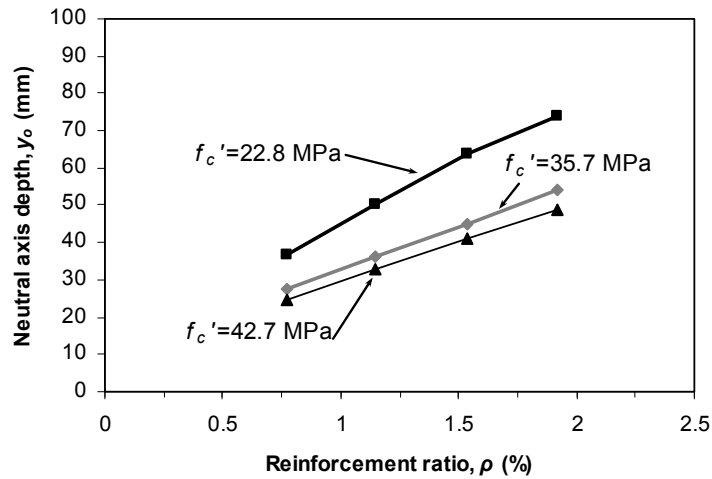
9.7.2 Effect of f_c' and ρ on Neutral Axis Depth

The effect of f_c' on the neutral axis depth at peak load is shown in Figure 9.18(a). The neutral axis depth decreased as the f_c' increased.

The effect of ρ on the neutral axis depth at peak load is shown in Figure 9.18(b). The neutral axes depth increased as the ρ increased, similar to Portland cement-based concrete.



(a) Effect of f_c' on neutral axis depth



(b) Effect of ρ on neutral axis depth

Figure 9.18- Effect of f_c' and ρ on neutral axis depth at peak load

9.7.3 Effect of f_c' and ρ on Curvature Ductility

As described in section 8.6.5, the curvature-ductility index (μ_c) is expressed as a ratio of the curvature at peak load (ϕ_u) to the curvature when the tension steel first

yields, ϕ_y . The effect of f_c' on μ_c predicted by the model for different ρ 's is shown in Figure 9.19. For slabs reinforced with $\rho=1.54\%$ and 1.92% , μ_c increased as f_c' increased. For relatively lower reinforcement ratio ($\rho=0.77\%$ and 1.15%), μ_c increases up to $f_c' = 35.7$ MPa and then decreased slightly up to $f_c' = 42.7$. This indicates that increasing concrete strength beyond some concrete compressive strength may not contribute to additional ductility in members with lower reinforcement ratios.

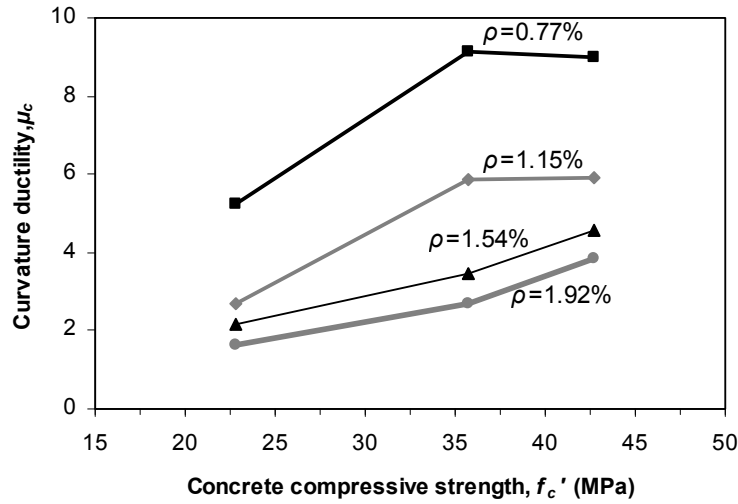


Figure 9.19- Effect of f_c' on μ_c

The effect of ρ on μ_c predicted by models for different f_c' is shown in Figure 9.20. It is observed that μ_c decreased as ρ increased, similar to Portland cement-based concrete. The reduction in curvature ductility was due to increases in neutral axis depth at failure when ρ increases, thus as peak load curvature decreases.

A minimum curvature ductility of 3 is considered to be adequate for ensuring ductile behaviour of reinforced concrete flexural members (e.g., Park and Paulay, 1975). Assuming similar minimum curvature ductility, Figure 9.20 illustrates that for slabs with $f_c' = 22.8$ MPa, ρ should not exceed 1.15% to satisfy an adequate ductility. Slabs with $f_c' = 35.7$ MPa and 42.7 MPa, can satisfy adequate ductility if reinforced up to $\rho = 2.0\%$.

Another way of ensuring ductility of flexural members is by limiting the neutral axis depth to a maximum of $0.45d$, where d is the effective depth (e.g., Mosley et al., 2007). For slabs analysed here where $d=130$ mm, this limit is equal to 58.5

mm. From Figure 9.18(b), it can be concluded that in slabs with $f_c' = 22.8$ MPa, ρ should not exceed 1.15% to satisfy adequate ductility, whereas, slabs with $f_c' = 35.7$ MPa and 42.7 MPa can satisfy adequate ductility if reinforced up to $\rho = 2.0\%$. These observations were similar to the minimum curvature ductility requirement.

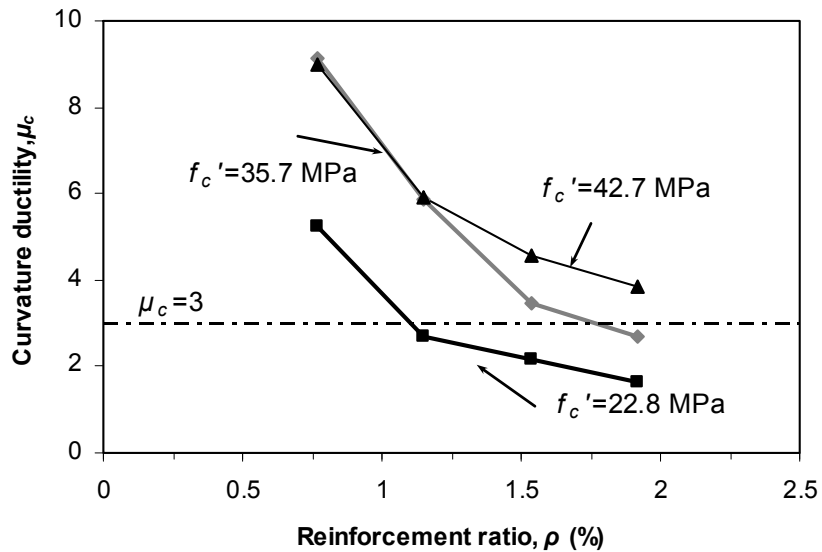


Figure 9.20- Effect of ρ on μ_c

9.8 Conclusions

This chapter presented a procedure used to develop a non-linear analytical model to investigate the flexural behaviour of GFRCC composite slabs. The model is based on the stress-strain relationships of constituent materials and the application of the compatibility of strains and equilibrium of forces. The proposed non-linear model was implemented using MATLAB® software. The model is used to analyze six slabs with similar cross-section configurations and test set-ups as slab specimens presented in Chapter 8. The moment-curvature response, load-deflection response, load versus strains in the steel reinforcement, and load versus strain in extreme concrete compression fibers were calculated and compared with the experimental results from Chapter 8. A numerical analysis was carried out to study the effect of variations in concrete strength and steel reinforcement ratio on moment-curvature response and curvature ductility. Based on the validation of the

proposed analytical model with the experimental results, the following conclusions can be drawn:

- The proposed model was successful in predicting the moment-curvature relationship.
- The concrete strains at mid-span top compression fibers predicted by the model were in good agreement with the experimental data.
- The reinforcement strain results at mid-span predicted by the model were higher than the experimental data. Hence, the tension stiffening effect should be included in future versions of the model to obtain improved agreement of predicted reinforcement strains with experimental results.
- The proposed model effectively predicted the load-deflection responses of GFRCC slabs reinforced with reinforcing steel and with or without textile reinforcements. It also showed the ability of estimating the ultimate load and corresponding deflections.
- The result of the numerical analysis showed that the curvature ductility increased as the longitudinal reinforcement ratio increased, similar to Portland cement-based concrete. Ductility also increased as the ceramic concrete strength increased up to a certain limit, and then it decreased.

9.9 References

- ACI Committee 213. (2009). Guide for Structural Lightweight-Aggregate Concrete (ACI 213R-03), ACI Manual of Concrete Practice (2009 Part 1). American Concrete Institute, Farmington Hills, MI, 24.
- Barros, J. A. O. and Figueiras, J. A. (1999). Flexural behavior of SFRC: Testing and modeling. *Journal of Materials in Civil Engineering, ASCE*, 11(4): 331–339.
- Bischoff, P. H. and Paixao, R. (2004). Tension stiffening and cracking of concrete reinforced with glass fiber reinforced polymer (GFRP) bars. *Canadian Journal of Civil Engineering*, 31(4): 579-588.

Chapter 9: Modeling the Flexural Behaviour of Reinforced Ceramic Concrete Slabs

- Bösche, A., Jesse F., Ortlepp, R., Weiland, S. and Curbach, M. (2008). Textile-reinforced concrete for flexural strength of RC-structures-Part 1: structural behaviour and design Model. Farmington Hills (MI, USA). ACI SP-251: 19-40.
- Canadian Standards Association. (2004). CSA A23.3-04: Design of Concrete Structures, Canadian Standards Association, Mississauga, Ontario, Canada, 1-52.
- Carreira, D. J. and Chu, K. H. (1985). Stress-strain relationship for plain concrete in compression. *ACI Journal*, 82(6): 797-804.
- Chapra, S. C. (2012). Applied numerical methods with MATLAB® for engineers and scientists. Third Edition, McGraw-Hill Inc., New York, 132-140.
- Collins, M. P. and Mitchell, D. (1997). Prestressed Concrete Structures. Prentice- Hall, Response Publications, Canada, 87-89 & 168-208.
- Ezeldine, A. S. and Balaguru, P. N. (1992). Normal and high strength fiber reinforced concrete under compression. *Journal of Materials in Civil Engineering, ASCE*, 4(4), 415-429.
- Fanella, D. A. and Naaman, A. E. (1985). Stress-strain properties of fiber reinforced mortar in compression. *ACI Journal*, 82(4): 475-483.
- Ghali, A. and Neville, A. A. M. (1989). Structural analysis, a unified classical and matrix approach. 3rd edition, Thomson Press Ltd. London, 232-233.
- Mansur, M. A., Chain, M. S. and Wee, T. H. (1999). Stress-strain relationship of high-strength fiber concrete in compression. *Journal of Materials in Civil Engineering, ASCE*, 11(1): 21-29.
- Mobasher, B. (2011). Mechanics of fiber and textile reinforced cement composites. CRC Press, 279-292.
- Mosley, B., Bungey, J. and Hulse R. (2007). Reinforced Concrete Design to Eurocode 2 . Palgrave Macmillan, N.Y., 62-63.
- Nataraja, M. C., Dhahg, N. and Gupta, A. P. (1999). Stress-strain curves for steel-fiber reinforced concrete under compression. *Cement and Concrete Composites*, 21: 383-390.
- Park, P. and Paulay, T. (1975). Reinforced concrete structures. John Wiley & Sons Inc., Canada, 37-41, 216-217, 237-238.

Chapter 9: Modeling the Flexural Behaviour of Reinforced Ceramic Concrete Slabs

RILEM TC 162-TDF. (2003). Test and design methods for steel fiber reinforced concrete, σ - ϵ design method. *Materials and Structures Journal*, 36: 560-567.

Popov, E. P., Nagarajan, S. and Lu, Z. A. (1978). Mechanics of materials. Prentice-Hall Inc., NJ, 135-138.

Stramandinoli, R. S. B. and Rovere, H. L. L. (2008). An efficient tension-stiffening model for nonlinear analysis of reinforced concrete members. *Engineering Structures*, 30: 2069–2080.

Vecchio, F. J. and Collins, M. P. (1986). The modified compression field theory for reinforced concrete elements subjected to shear. *ACI Journal*, 83(2): 219-231.

Conclusions and Recommendations

10.1 Summary

Magnesium potassium phosphate cement (MPPC) is a novel chemically bonded cement formed by the reaction of magnesium oxide and monopotassium phosphate. The aims of this study contained three themes: a) to develop a structural ceramic concrete made from MPPC binder and various aggregates, to examine the uniaxial tensile response of composite made of these ceramic concretes and glass textile reinforcements; (b) to develop an innovative ceramic composite material using the developed ceramic concretes, reinforcing steel and textile reinforcements; (c) to examine this composite for use of flexure-critical structural elements using experimental and analytical methods.

This research program was divided into two main parts: Material Development and Characterization, and Structural Application. Part I of this research project on Development and Characterization contained an experimental program that was divided into five phases. This experimental program contained trial mix design, mix and specimen preparation, and testing. In this part small size test specimens including cubes (50x50x50 mm and 100x100x100 mm), prisms (50x50x200 mm and 100x100x400 mm), and cylinder specimens (100x200 mm) were produced and tested.

In Phase I, the research developed and characterized MPPC binders that incorporate a high fly ash loading at up to 80% by mass of the binder. Two groups of mixes were prepared in this study. The first group of mixes comprised of MPPC binders. The second group of mixes comprised sand-cement mortars (SCM) made of MPPC binders and sand aggregates. The influence of the mix compositions on physical and mechanical properties of MPPC and SCM were examined.

In Phase II, this study developed and characterized the rheological and mechanical properties of lightweight ceramic concrete (LWCC) using the developed MPPC binder and various lightweight aggregates. Six groups of mixes were produced using combinations of coarse and fine lightweight expanded clay aggregates (LECA), fine LECA only, expanded slate, expanded shale coated, expanded shale crushed, and bottom ash aggregate. The primary aim of the study was to evaluate the influences of aggregate type, aggregate mass fraction and the water/binder mass ratio on the mechanical properties of LWCC. The mechanical properties such as the compressive strength, modulus of elasticity, flexural strength and direct shear strength were examined. The influence of aggregate type on the density and on the fresh properties including the slump and the setting time were also examined.

Phase III investigated the influence of chopped glass fibers on the mechanical and rheological properties of glass fiber reinforced ceramic concrete (GFRCC). Two different ceramic concrete matrices that contained either sand or lightweight expanded clay aggregates were studied. Fiber volume fractions between 0 and 2% were examined. The influence of fiber content and length on the mechanical properties including compressive strength, flexural strength and direct shear strength of GFRCC were investigated.

Phase IV investigated the load-bearing behaviour of textile reinforced ceramic concrete (TRCC) through uniaxial tensile testing. TRCCs with and without short glass fibers were considered. The axial tensile behaviour of TRCC was

determined using dog-bone shaped specimens containing up to two layers of glass textile reinforcement and short glass fibers at 0 or 1.5% by volume. Three ceramic concrete types that differed with aggregate types were used. The main aim of this investigation was to establish a relationship between axial load and axial deformation of TRCC.

Phase V examined a proof-of-concept study for a structural infill slab system using textile reinforced ceramic composites. Using ceramic concrete and textile reinforcements, small-scale specimens representing full-depth precast structural elements as well as partial-depth precast panels suitable for use as a stay-in-place formwork solution were produced and evaluated for strength and stiffness.

Part II of this research program on Structural Application contained two phases. In phase I, experimental study was conducted to study the flexural behaviour of six full-scale ceramic concrete composite slabs. In this phase many activities including formwork preparation, steel reinforcement cage preparation, mixing and casting of ceramic concrete, and testing were carried out. Innovative glass fiber reinforced lightweight ceramic composite slabs were developed using different configurations of ceramic concretes, longitudinal reinforcing steels and textile reinforcements. These composite slabs were made using unique concrete mix compositions and employed two types of construction (i.e. layered type and full depth type). The slab specimen had a depth of 150 mm, a width of 200 mm and overall length of 2200 mm. The different parameters varied were the ceramic concrete compressive strength, the longitudinal steel reinforcement ratio and the number of textile layers. The slabs were tested under four point bending with a span between supports was 1800 mm and between loading points was 600 mm. The slab behaviour including the load carrying capacity, failure modes, deformation and ductility as well as the crack development during loading were examined for potential application of these slabs as flexure-critical structural members.

In phase II, a numerical model was developed to study the flexural behaviour of the slabs. The experimental results were used to develop a model for the stress-strain responses of each constituent material. A non-linear analysis model was then developed based on these material constitutive equations and by applying the force equilibrium and strain compatibility conditions. The moment curvature relation was first determined using a layer-by-layer evaluation approach at each cross-section. To obtain the full-member load-deflection response the slab was first divided into small individual elements along the length. The load-deflection response at any load level is then obtained by integrating the curvature at cross-sections along the slab's length. The proposed model required iterative analysis and numerical integration at each stage of loading. To simplify the analysis, the model was then coded using MATLAB® software. The developed non-linear model was successfully validated using experimental results from the current study and was used in a parametric study to examine the effect of variation in ceramic concrete compressive strengths and steel reinforcement ratios on the moment-curvature response and ductility.

The summary of the main conclusions from this study and recommendations for future work are discussed in following sections.

10.2 Conclusions

10.2.1 Magnesium Potassium Phosphate Binder and Mortar

This study contained two phases. In the first phase, magnesium potassium phosphate cement (MPPC) binders were developed and characterized for rheological and mechanical properties. The second phase of the study investigated the mechanical properties of sand ceramic mortar (SCM) produced using the developed MPPC binders and sand aggregates. The following conclusions were drawn:

- The compressive strengths of both MPPC and SCM decreased as the water/binder ratio increased. Use of a w/b ratio of 0.20 resulted in good workability and mechanical properties.
- The compressive strength of MPPC and SCM were both influenced by the fly ash content and was a maximum when the fly ash loading was between 40% and 60%. Use of Class C fly ash resulted in higher compressive strengths of SCM compared to use of Class F fly ash.
- The compressive strength of SCM increased as the binder to sand mass ratio increased, regardless of the fly ash loading. The aggregate gradation influenced the mechanical properties of SCM, but this influence was less pronounced as the fly ash loading increased.
- B5 binder and M5 mortar containing 50% fly ash by weight of the binder were the strongest mixes produced, giving 28 day compressive strength of 36.6 MPa and 60.0 MPa, respectively. Early age strength gain was rapid with more than 72% of the 28-day strength within 24 hrs.

10.2.2 Mechanical Properties of LWCC

Lightweight ceramic concretes (LWCC) using different lightweight aggregates and MPPC binder were developed. The physical and mechanical properties of the LWCC were examined through laboratory testing. The following conclusions were drawn:

- The fresh properties of LWCC were influenced by the water/binder ratio and type of lightweight aggregate. Higher water/binder ratios resulted in increased slump flow but negligible influence on the setting time.
- Compressive strength of LWCC increased as the density increased. The 28-day compressive strengths and densities ranged from 17 to 36 MPa and 1600 to 1870 kg/m³ respectively, meeting the ACI 213 classification of structural lightweight concrete.

- The rate of compressive strength gain was very rapid with 65 to 90% of the 28-day strength attained within 3 days for most mixes.
- The compressive strength and density of LWCC both decreased with increases in the aggregate/binder ratio and in the water/binder ratio, regardless of the aggregate type.
- The modulus of elasticity of LWCC decreased as the water/binder ratio increases and increased with increasing compressive strength, regardless of the type of aggregates.
- The modulus of rupture increased with higher compressive strengths and decreased with larger water/binder ratios, regardless of the aggregate type.
- The direct shear strength of LWCC was found to increase with compressive strength and decrease for larger water/binder ratios, regardless of aggregate type.
- The coated expanded shale (i.e. Type B concrete) showed the most favourable properties among the aggregate types studied in terms of workability, compressive strength to density ratio, compressive strength and the modulus of elasticity.

10.2.3 Mechanical Properties of GFRCC

This study has examined the influence of chopped glass fibers on the mechanical and rheological properties of ceramic concrete. The following conclusions were drawn:

- Addition of glass fibers to a ceramic concrete matrix reduced the flow of the concrete. However the fibers had negligible effect on the densities of the hardened ceramic concrete, which were approximately 1800 kg/m³ and 2200 kg/m³ for mixes with LECA and sand aggregates respectively.

- For mixes with LECA aggregates, the compressive strength increased with increases in the glass fiber volume fraction, but the fibers had negligible effect on the modulus of elasticity. For ceramic concrete with sand aggregates, a marginal decrease in both the compressive strength and modulus of elasticity occurred for higher fiber dosages.
- The flexural strength of ceramic concrete increased with increases in the glass fiber volume fraction irrespective of the mix composition or fiber length. The flexural strengths of glass fiber reinforced ceramic concrete were 13-30% of the corresponding compressive strength.
- The direct shear strength of ceramic concrete increased with increase in glass fiber volume dosage irrespective of the mix composition and fiber length.
- The compression toughness index, flexural toughness and shear toughness of ceramic concrete showed a considerable increase with an increase in the fiber content. This was true regardless of the type of matrix or fiber length.
- The compression, flexure and shear strength results all indicated that the fiber failure mode was predominantly by fracture rather than pullout, even for the shortest fibers in use in this study.

10.2.4 Uniaxial Tensile Behaviour of Textile Reinforced Ceramic Concrete

In this study the direct tensile load-bearing behaviour of textile reinforced ceramic concrete dog-bone shaped specimens were examined. The influence of different parameters including the number of layers and the amount of chopped glass fibers were evaluated. The following conclusions were drawn:

- After 28 days, no significant changes were observed for the compressive strength, split tensile strength or flexural tensile strength of GFRCC.

- The direct tensile strength, flexural and splitting tensile strength of GFRCC all increased as the compressive strength increased.
- The direct tensile strength, splitting tensile strength and the flexural strength of GFRCC ranged from 4% to 7%, 13% to 16% and 15% to 20% of the corresponding cylinder compressive strength, respectively.
- For GFRCC, the ratios of the axial tensile strength to flexural tensile strength and to splitting tensile strength were found to be 0.15 to 0.40 and 0.25 to 0.50, respectively.
- Compared to plain samples, the addition of one layer of textile reinforcement to plain ceramic concrete samples resulted in the formation of multiple cracking, improved the post-cracking performance, and increased the axial tensile strength by a factor of 2 to 3 times.
- The addition of 1.5% by volume of short glass fibers increased the first-crack stress and the axial tensile strength value by a factor of 1.5 to 3 and 1.2 to 2, respectively for specimens with one layer of textile.
- Compared to samples with one layer textile reinforcement, the axial tensile strength value of TRCC specimens increased by 1.1 to 1.3 times, while the corresponding strain reduced by 0.2 to 0.5 times when two layers of textiles were used.

10.2.5 Flexural Behaviour of Reinforced Ceramic Concrete Slabs

This study included the casting and testing of six full-scale reinforced ceramic concrete slabs with different material and geometric parameters. The dimensions of all slab specimens were constant but parameters including ceramic concrete compressive strength, amount of steel reinforcement and the textile reinforcements were varied. The flexural behaviour of these slabs was investigated experimentally using four-point bending test. The load carrying capacity, failure modes, deformation, ductility, crack widths and cracking pattern

were of primary interest. Further, the flexural behaviour of all the six slabs were investigated using a non-linear analytical model developed in this study and the results compared with the experimental results. The model was based on the stress-strain relationships of constituent materials and applying compatibility of strains and equilibrium of forces. The model was implemented using MATLAB® software. The program was used to generate moment-curvature, load-deflection, load versus concrete compression fibers strain and load versus reinforcing steel strain curves at mid span for the six slab specimens. Based on the experimental and analytical results, the following conclusions were drawn:

- The overall load-deflection response of reinforced GFRCC slabs was similar to typical Portland cement based reinforced concrete slabs. The load-deflection behaviours were nearly linear up to concrete flexural cracking, followed by gradually decreasing slope up to yielding of reinforcement and then nearly horizontal response until failure depending on the amount of steel reinforcement.
- An increase in the ceramic concrete compressive strength or the amount of steel reinforcement increased the post-cracking stiffness and the peak load of GFRCC slabs.
- Increasing the ceramic concrete compressive strength or the amount of steel reinforcement had no trend with the service load deflection.
- For specimens whose steel bars yielded, the displacement and curvature ductility both increased when the ceramic concrete strength increased, and both decreased when the tension steel content increased.
- For the type and the number of textile layers considered in this study, addition of textile fabric had negligible effect on the ultimate load. However, it reduced the ultimate load deflection.

- The results indicated the crack type, crack pattern and flexural crack widths of reinforced ceramic concrete slab depend on the amount of tensile reinforcement, the concrete strength, and the type of cross-section used. In general, as the amount of steel bars increased, the crack width and crack spacing reduced. The service load crack widths of tested slabs were varied between 0.08 and 0.14 mm and this is within the maximum allowable limit specified in ACI 224R-01.
- At each stages of loading, a good correlation between the predicted results from the developed analytical model and the experimental data was observed for responses such as the load-deflection, the moment-curvature relationship and the load versus the concrete strains at mid-span top compression fiber. However, the model had a shortcoming of predicting the load versus reinforcement strains at mid-span.

10.3 Recommendations and Future Works

Based on the experimental and analytical results obtained from this study, the developed ceramic concrete showed the rheological and mechanical properties required for structural application. Further, the developed textile reinforced ceramic composite and reinforced ceramic composite slabs has a promising potentials to be used as structural material for the wide range of structural applications both for new structural elements and rehabilitation of structural members. An example of the structural applications includes building and bridge slabs, wall panels and stay-in-place formwork. However, to use it for structural application several additional studies are needed due to the limitation of the current study. The following are some of the recommendations identified for future work in the filed:

1. Further mix design study is needed to obtain wide range of strengths to come up with cost effective material.

2. The numbers of slab specimens studied are limited, additional slab tests are needed by varying various reinforcement amounts and concrete strength. This allows studying the ductility and the post peak behaviour of the slabs.
3. The examination of the tensile behaviour study of textile reinforced ceramic concrete is needed by using different number of layers of textiles and various textiles reinforcements having higher stiffness and strengths. This allows to optimize the amount and the type of textile reinforcements.
4. For layered type of construction, a detailed investigation of the shear behaviour at the interface between the main slab and the textile reinforced concrete layer is needed. This allows utilizing the composite properties of the two layers fully.
5. The effect of tension stiffening was not taken into account in analytical model in this study. This study is needed to refine the analytical model.
6. Since the ceramic composite slab is new composite material, the durability study (e.g., permeability and freeze-thaw resistance) of the slab under aggressive environment is needed to examine its performance for using it in field applications.

Bibliography

- ACI Committee 213 (2009). Guide for Structural Lightweight-Aggregate Concrete (ACI 213R-03). ACI manual of Concrete Practice (Part 1), American Concrete Institute, Farmington Hills, MI, 1-25.
- ACI Committee 224. (2008). Control of Cracking in Concrete Structures (ACI 224R-01). American Concrete Institute, Farmington Hills, MI, 19-20.
- ACI Committee 318. (2011). Building Code Requirements for Structural Concrete (ACI 318-08) and Commentary. American Concrete Institute, Farmington Hills, MI, 107-108.
- Advantages of Structural Lightweight Aggregate Concrete. Expanded Clay, Shale and Slate Institute, www.escsi.org. Last accessed on April, 2013.
- Ahmad, S. H. and Barker, R. (1991). Flexural Behavior of Reinforced High-Strength Lightweight Concrete Beams. *ACI Structural Journal*, 88(1): 69-77.
- Ahmad, S. H. and Batts, J. (1991). Flexural behavior of double reinforced high-strength lightweight concrete beams with web reinforcement. *ACI Structural Journal*, 88(3), 351-358.
- Ali, M. A. Majumdar, A. J. and Singh, B. (1975). Properties of glass fiber reinforced cement-the effect of fiber length and content. *Journal of Material Science*, 10: 1732-40.
- ASTM A370-11. (2011). Standard test methods and definitions for mechanical testing of steel products. ASTM International, West Conshohocken, PA.
- ASTM C 230/C 230M. (2008). Standard Specification for Flow Table for use in Tests of Hydraulic Cement. ASTM International, West Conshohocken, PA.
- ASTM C127. (2007). Standard test method for density, relative density (specific gravity), and absorption of coarse aggregate. ASTM International, West Conshohocken, PA.
- ASTM C136. (2006). Standard test method for sieve analysis of fine and coarse aggregate. ASTM International, West Conshohocken, PA.

Bibliography

- ASTM C143/C143M-10a. (2008). Standard test method for slump of hydraulic-cement concrete. ASTM International, West Conshohocken, PA.
- ASTM C1437. (2007). Standard Test Method for Flow of Hydraulic Cement Mortar. ASTM International, West Conshohocken, PA.
- ASTM C1609/C1609M. (2010). Standard test method for flexural performance of fiber-reinforced concrete (using beam with third-point loading). ASTM International, West Conshohocken, PA.
- ASTM C191 (2008). Standard test method for time of setting of hydraulic cement by vicat needle. ASTM International, West Conshohocken, PA.
- ASTM C39/C39M-09a (2009). Standard Test Method for Compressive Strength of Cylindrical Concrete Specimens. ASTM International, West Conshohocken, PA.
- ASTM C469-02e1. (2002). Standard Test Method for Static Modulus of Elasticity and Poisson's Ratio of Concrete in Compression. ASTM International, West Conshohocken, PA.
- ASTM C617 (2010). Practice for capping cylindrical concrete specimens. ASTM International, West Conshohocken, PA.
- ASTM C78 (2009). Standard Test Method for Flexural Strength of Concrete (Using Simple Beam with Third-Point Loading). ASTM International, West Conshohocken, PA.
- ASTM D6637. (2010). Standard test method for determining tensile properties of geogrids by the single or multi-rib tensile method. ASTM International, West Conshohocken, PA.
- Balaguru, P. N. and Shah S. P. (1992). Fiber reinforced cement composites. McGraw Hill Inc. Publishers, New York, 70-80.
- Bank, L. C., Malla, A. P., Oliva, M. G., Russell, J. S., Bentur, A. and Shapira, A. (2009). A model specification for fiber reinforced non-participating permanent formwork panels for concrete bridge deck construction. *Construction and Building Materials*, 23: 2664–2677
- Barhum, R. and Mechtcherine, V. (2012). Effect of short, dispersed glass and carbon fibres on the behaviour of textile-reinforced concrete under tensile loading. *Journal of Engineering Fracture Mechanics*, 92: 56-71.

Bibliography

- Barluenga, G. and Hernández-Olivares, F. (2007). Cracking control of concretes modified with short AR-glass fibers at early age. Experimental results on standard concrete and SCC. *Cement Concrete Research*, 37(12): 1624–38.
- Barros, J. A. O. and Figueiras, J. A. (1999). Flexural behavior of SFRC: Testing and modeling. *Journal of Materials in Civil Engineering, ASCE*, 11(4): 331–339.
- Bentur, A. and Mindess, S. (1990). Fibre reinforced cementitious composites. Elsevier Applied Science, London, 1-10, 31-41, 105-125, 189-204 & 390-393.
- Bischoff, P. H. and Paixao, R. (2004). Tension stiffening and cracking of concrete reinforced with glass fiber reinforced polymer (GFRP) bars. *Canadian Journal of Civil Engineering*, 31(4): 579-588.
- Biswas, M. (1986). Precast Bridge Deck Design Systems. *PCI Journal*, 31(2): 40-90.
- Bosche, A., Jesse, F., Ortlepp, R., Weiland, S. and Curbach, M. (2008). Textile-Reinforced Concrete for Flexural Strength of RC-Structures-Part 1: Structural Behaviour and Design Model. American Concrete Institute, Farmington Hills, MI, ACI SP-251: 19-40.
- Bramshuber, W., Koster, M., Hegger, J., Voss, S., Gries, T., Barle, M., Reinhardt, H. W. and Kruger, M. (2004). Integrated Formwork Elements Made of Textile Reinforced Concrete. American Concrete Institute, MI, ACI SP-224: 45-54.
- Brandt, A.M. (2008). Fibre reinforced cement-based (FRC) composites after over 40 years of development in building and civil engineering. *Journal of Composite Structures*, 86(1): 3-9.
- Bruckner, A., Ortlepp, R. and Curbach, M. (2006). Textile Reinforced Concrete for Strengthening in Bending and Shear. *Material and Structure Journal*, 39(8): 741-748.
- Bruckner, A., Ortlepp, R. and Curbach, M. (2008). Anchoring of shear strengthening for T-beams made of textile reinforced concrete (TRC). *Materials and Structures*, 41(2): 407–418.
- Butler, M., Mechtcherine, V. and Hempel, S. (2009). Experimental investigations on the durability of fibre–matrix interfaces in textile-reinforced concrete. *Cement and Concrete Composites*, 31: 221-231.
- Canadian Standards Association. (2004). CSA A23.3-04: Design of Concrete Structures. Canadian Standards Association, Mississauga, Ontario, Canada, 1-52.

Bibliography

- Carreira, D. J. and Chu, K. H. (1985). Stress-strain relationship for plain concrete in compression. *ACI Journal*, 82(6): 797-804.
- Chandra, S. and Berntsson, L. (2002). Lightweight aggregates concrete- Science, Technology and Application. Noyes Publications, New York, USA, 169-227 & 369-400.
- Chapra, S. C. (2012). Applied numerical methods with MATLAB® for engineers and scientists. Third Edition, McGraw-Hill Inc., New York, 132-140.
- Chi, J. M., Huang, R., Yang, C. C. and Chang J. J. (2003). Effect of aggregate properties on the strength and stiffness of lightweight concrete. *Cement and Concrete Composites*. 25(2): 197-205.
- Choi, Y. and Yuan, R. L. (2005). Experimental relationship between splitting tensile strength and compressive strength of GFRC and PFRC. *Cement and Concrete Research*, 35(8): 1587–1591.
- Collins, M. P. and Mitchell, D. (1997). Prestressed Concrete Structures. Prentice- Hall, Response Publications, Canada, 87-89 & 168-208.
- Correlated Solutions Inc. (2007). Vic-3D 2007 Testing Guide. www.correlatedsolutions.com. Last accessed April, 2013
- Correlated Solutions Inc. (2009). Vic-Snap 2009 and Vic-3D 2009. www.correlatedsolutions.com. Last accessed April, 2013
- Cuypers, H. (2002). Analysis and design of Sandwich Panels with Brittle Matrix Composite Faces for Building Applications. PhD thesis, Vrije Universiteit Brussel, 1-235.
- Ding, Z. and Li, Z. (2005a). High-early-strength magnesium phosphate cement with fly ash. *ACI Material Journal*, 102(6): 357-381.
- Ding, Z. and Li, Z. (2005b). Effect of aggregate and water content on the properties of magnesium phospho-silicate cement. *Cement and Concrete Composites*, 27(1): 11-18.
- Ezeldin, A. S. and Balaguru, P. N. (1992). Normal and high strength fiber-reinforced concrete under compression. *Journal of Material Civil Engineering*, 4(4): 415-29.
- Fanella, D. A. and Naaman, A. E. (1985). Stress–strain properties of fiber reinforced mortar in compression. *ACI Journal*, 82(4): 475–483.

Bibliography

- FIP Manual. (1983). FIP Manual of Lightweight Aggregate Concrete. Surrey University Press, London, 104-107.
- Gao, J., Sun, W. and Morino, K. (1997). Mechanical properties of steel fiber-reinforced, high-strength, lightweight concrete. *Cement Concrete Composite*, 19(4): 307–313.
- Ghali, A. and Neville, A. A. M. (1989). Structural analysis, a unified classical and matrix approach. 3rd edition, Thomson Press Ltd. London, 232-233.
- Hegger, J., Will, N., Bruckermann, S. and Voss, S. (2006). Loading-bearing behaviour and simulation of textile-reinforced concrete. *Materials and Structures Journal*, 39(8): 765-776.
- Hartig, J., Haußler-Combe, U. and Schicktanz, K. (2008). Influence of bond properties on the tensile behaviour of Textile Reinforced Concrete. *Cement & Concrete Composites*, 30(10): 898–906.
- Hegger, J., Schneider H., Voss, S., and Bergmann, I. (2008). Dimensioning and application of textile-reinforced concrete. American Concrete Institute, MI, ACI SP-250: 69-84.
- Hegger, J. and Voss, S. (2008). Investigations on the bearing behaviour and application potential of textile reinforced concrete. *Engineering Structures*, 30(7): 2050-2056.
- Heggar, J., Kulas, C. and Hortsmann, M. (2011). Realization of TRC facades with impregnated AR-glass textiles. *Key Engineering Materials*, 466: 121-130.
- Hegger, J., Kulas, C., Raupach, M. and Buttner, T. (2011). Tragverhalten und Dauerhaftigkeit einer schlanken Textilbetonbrücke. *Beton und Stahlbetonbau*, 106(2): 72- 80.
- Hegger, J., Kulas, C. and Horstmann, M. (2012). Spatial textile reinforcement structures for ventilated and sandwich facade elements. *Advances in Structural Engineering*, 15 (4): 665-675.
- Hinzen, M. and Brameshuber, W. (2009). Improvement of serviceability and strength of Textile Reinforced Concrete by using short fibres. Proceeding of 4th colloquium on textile reinforced structures (CTRS4), Dresden, 261–272.
- Jeong, S. and Wagh, A. (2003). Cementing the gap between ceramics, cement, and polymers. *Material Technology*, 3: 162-168.
- JSCE-SF6. (1990). Method of Test for Shear Strength of Steel Fiber reinforced concrete. Japan Society of Civil Engineering (JSCE), Tokyo, 67-69.

Bibliography

- Kantro, D. L. (1980). Influence of water-reducing admixtures on properties of cement paste-a miniature slump test. *Journal of Cement and Concrete and Aggregates*, 2(2): 95–102.
- Ke, Y., Beaucour, A. L., Ortola, S., Dumontent, H. and Cabrillac, R. (2009). Influence of volume fraction and characteristics of lightweight aggregates on the mechanical properties of concrete. *Construction and Building Materials*, 23(8): 2821-2828.
- Kim, D. J., Wille, K., Naaman, A. E. and El-Tawil, S. (2011). Strength dependent tensile behavior of strain hardening fiber reinforced concrete. In *Proceedings: High Performance Fiber Reinforced Cement Composites (HPFRCC-6)*, Ann Arbor, MI: 20-22.
- Lepenes, I., Meyer, C., Schorn, H. and Zastrau, B. (2007). Modeling of the Load Transfer Behavior of AR-Glass-Rovings in Textile Reinforced Concrete. American Concrete Institute, MI, ACI SP-244: 109-124.
- Li, Z. Ding, Z. and Zhang, Y. (2004). Development of sustainable cementitious materials. Proceedings of International Workshop on Sustainable Development and Concrete Technology, Beijing, China, 55–76.
- Li, Z. and Liang, W. (2011). Advanced concrete technology. Hoboken, NJ: John Wiley & Sons, 33-34 & 476-477.
- Lim, H. S., Wee, T. H., Mansur, M. A. and Kong, K. H. (2006). Flexural behaviour of reinforced lightweight aggregates concrete beam. *Proceeding of the 6th APSEC*. Kuala Lumpur, Malaysia, A68-82.
- Lim, H. S., Wee, T. H., Islam, M. R. and Mansur, M. A. (2011). Reinforced lightweight concrete beams in flexure. *ACI Structural Journal*, 108(1): 3-12.
- Lo, T., Tang, W.C. and Cui, H. Z. (2007). The effect of aggregate properties on lightweight concrete. *Building and Environment*, 42(8): 3025-3029.
- Majdzadeh, F. Soleimani, M. S. and Banthia, N. (2006). Shear strength of reinforced concrete beams with a fiber concrete matrix. *Canadian Journal of Civil Engineering*, 33(6): 726-734.
- Mansur, M. A., Chain, M. S. and Wee, T. H. (1999). Stress-strain relationship of high-strength fiber concrete in compression. *Journal of Materials in Civil Engineering, ASCE*, 11(1): 21-29.
- Mehta, P. K. (1986). Concrete structure, properties and materials: Prentice-hill, NJ, 42-68 & 238-242.

Bibliography

- Mirsayah, A. A. and Banthia, N. (2002). Shear strength of steel fiber-reinforced concrete. *ACI Materials Journal*, 99(5): 473-479.
- Mirza, F. A. and Soroushiand, P. (2002). Effects of alkali-resistant glass fiber reinforcement on crack and temperature resistance of lightweight concrete. *Cement and Concrete Composite*, 24(2): 223-227.
- Mobasher, B. (2011). Mechanics of fiber and textile reinforced cement composites. CRC Press, 14-15 & 279-292.
- Mosley, B., Bungey, J. and Hulse R. (2007). Reinforced Concrete Design to Eurocode 2. Palgrave Macmillan, N.Y., 62-63.
- Nataraja, M. C., Dhahg, N. and Gupta, A. P. (1999). Stress-strain curves for steel-fiber reinforced concrete under compression. *Cement and Concrete Composites*, 21: 383-390.
- Neville, A. M. (1996). Properties of concrete. John Wiley & Sons Ltd., New York. 529-545 & 580-600.
- Nilson, H., Darwin, D. and Dolan, C. W. (2004). Design of concrete structures. The McGraw-Hill companies, 38-39&68-69.
- Nippon Electric Glass America. <http://www.negamerica.com>. Last accessed on April, 2013.
- Obregon-Salinas, A. J., Rizkalla, S. H. and Zia, P. (2011). American Concrete Institute, MI, ACI SP275-17: 1-12.
- Orlowsky, J. and Raupach, M. (2006). Modelling the loss in strength of AR-glass fibres in textile-reinforced concrete. *Materials and Structures Journal*, 39(6): 635-643.
- Park, P. and Paulay, T. (1975). Reinforced concrete structures. John Wiley & Sons Inc, Canada, 37-41, 195-211, 216-217, 237-238 & 479-483.
- Peled, A. (2007). Confinement of damaged and non-damaged structural concrete with FRP and TRC sleeves. *ASCE Journal of Composite Construction*, 11(5): 514-522.
- Popov, E. P., Nagarajan, S. and Lu, Z. A. (1978). Mechanics of materials. Prentice-Hall Inc., NJ, 135-138.
- Qiao, F, Chau, C. K. and Li, Z. (2009). Property assessment of magnesium phosphate cement. *Key Engineering Material*, 400-402: 115-120.

Bibliography

- Qiao, F., Chau, C. K. and Li, Z. (2010). Property evaluation of magnesium phosphate cement mortar as patch repair material. *Construction and Building Materials*, 24: 695-700.
- Rashed, M. A and Mansur, M. A. (2005). Reinforced high-strength concrete beams in flexure. *ACI Structural Journal*, 102(3): 462-471.
- RILEM TC 162-TDF. (2003). Test and design methods for steel fiber reinforced concrete, σ - ϵ design method. *Materials and Structures Journal*, 36: 560-567.
- Roy, D. (1997). New strong cement materials: chemically bonded ceramics. *Science*, 235: 651–658.
- Short, A. and Kinniburgh, W. (1978). Light weight concrete. Applied science publication Ltd. London, 150-171.
- Singh, D., Wagh, A. S., and Jeong, S. Y. (2001). Pumpable/Injectable Phosphate-Bonded Ceramics. U.S. patent US 6,204,214, B1.
- Stramandinoli, R. S. B. and Rovere, H. L. L. (2008). An efficient tension-stiffening model for nonlinear analysis of reinforced concrete members. *Engineering Structures*, 30: 2069–2080.
- Swamy, R. N. and Mangat, P. S. (1974). A theory for the flexural strength of steel fiber reinforced concrete. *Cement and Concrete Research*, 42: 113-25.
- Swamy, R. N. and Lambert, G. H. (1984). Flexural behaviour of reinforced concrete beams made with fly ash coarse aggregates. *The International Journal of Cement Composites and Lightweight Concrete*, 6(3): 189-200.
- Tassew, S. T. and Lubell, A. S. (2010). Textile reinforced ceramic composite for structural infill slab application. Proceedings of 34th IABSE Symposium, Venice, Italy, A-0317, 1-8.
- Tassew, S. T., Mutsuddy, R., Bindiganavile, V. S. and Lubell, A. S. (2011). Drop Weight Impact Response of Glass Fiber Reinforced Ceramic Composites. In *Proceedings: High Performance Fiber Reinforced Cement Composites (HPFRCC-6)*, Ann Arbor, MI: 289-296.
- Tassew, S. T. and Lubell, A. S. (2012). Mechanical properties of lightweight ceramic concrete. *Materials and Structures Journal*, 45(4): 561-574.
- Triantafyllou, T. C. and Papanicolaou, C. G. (2005). Textile reinforced mortar (TRM) versus FRP as strengthening material of concrete structures. American Concrete Institute, Farmington Hills, MI, ACI SP-230: 99-118.

Bibliography

- Vecchio, F. J. and Collins, M. P. (1986). The modified compression field theory for reinforced concrete elements subjected to shear. *ACI Journal*, 83(2): 219-231.
- Wagh, A. S., Jeong, S. Y, and Singh, D. (1997). High-strength ceramic (cement) using industrial by-product and slag. *Proceeding of International Conference on High-Strength Concrete*, Kona, HI.
- Wagh, A. S. and Jeong, S. Y. (1998). Method of waste stabilization via chemically bonded phosphate ceramics. U.S. Patent No. 5,830,815.
- Wagh, A. S. (2004). Chemically bonded phosphate ceramics: Twenty-first century material with diverse applications. Elsevier Ltd., Amsterdam. 1-283.
- Weibull, W. (1939). The phenomenon of rupture in solids. *Proceedings of Royal Swedish Institute of Engineering Research*, Stockholm, 151:1-45.
- Wu, C. H., Kan, Y. C., Huang, C. H., Yen, T. and Chen, L. H. (2011). Flexural behaviour and size effect of full scale reinforced lightweight concrete beam. *Journal of Marine Science and Technology*, 19(2): 132-140.
- Yang, Q. and Wu, X. (1999). Factors influencing properties of phosphate cement-based binder for rapid repair of concrete. *Cement and Concrete Research*, 29(3): 389-396.

Tables and Plots

A.1 Introduction

Additional plots of experimental test results that were not included in each chapter and summary of key test results are provided in this Appendix. The test results from Chapters 3 to 8 are presented in sections A.2, A.3, A.4, A.5, A.6 and A.7, respectively.

A.2 Magnesium Potassium Phosphate Cement and Mortar

Table A.2.1- Density of magnesium potassium phosphate cement (MPPC) binder for different fly ash loading and water binder ratio (MPa)

Mix		w/b=0.16	w/b=0.18	w/b=0.20	w/b=0.22	w/b=0.24	w/b=0.26
BC4		1718	1755	1900	1818	1787	1823
		1761	1772	1851	1842	1825	1813
		1752	1768	1912	1835	1786	1810
	AVG	1744	1765	1887	1832	1799	1815
	CV (%)	1.3	0.5	1.7	0.7	1.2	0.4
BC5		1695	1771	1797	1805	1769	1764
		1728	1801	1827	1815	1784	1766
		1700	1793	1809	1802	1768	1756
	AVG	1707	1788	1811	1807	1774	1762
	CV (%)	1.0	0.8	0.8	0.4	0.5	0.3
BC6		-	1735	1753	1756	1706	1673
		-	1763	1717	1758	1745	1705
		-	1746	1702	1733	1733	1685
	AVG	-	1748	1724	1749	1728	1688
	CV (%)	-	0.8	1.5	0.8	1.2	1.0
BC7		-	1648	1716	1652	1642	1603
		-	1645	1699	1640	1636	1601
		-	1648	1662	1643	1640	1625
	AVG	-	1647	1692	1645	1639	1610
	CV (%)	-	0.1	1.6	0.4	0.2	0.8
BC8		-	1538	1591	1566	1511	1528
		-	1562	1615	1587	1561	1509
		-	1563	1593	1599	1499	1481
	AVG	-	1554	1599	1584	1524	1506
	CV (%)	-	0.9	0.8	1.0	2.1	1.6

Appendix A: Tables and Plots

Table A.2.2- 7 day cube compressive strength of MPPC binder for different fly ash loading and water binder (MPa)

Mix		w/b=0.16	w/b=0.18	w/b=0.20	w/b=0.22	w/b=0.24	w/b=0.26
BC4		16.7	22.8	24.2	26.8	20.1	31.1
		22.0	23.0	35.2	26.5	31.1	27.8
		18.1	25.9	26.5	36.0	22.7	32.4
	AVG	18.9	23.9	28.6	29.7	24.6	30.4
	CV (%)	14.4	7.3	20.3	18.2	23.2	7.9
BC5		20.9	31.2	37.6	22.9	24.7	25.5
		28.9	29.1	43.2	31.2	19.0	19.8
		20.9	30.2	28.0	25.5	32.0	21.5
	AVG	23.6	29.1	36.3	26.5	25.2	22.2
	CV (%)	19.2	3.4	21.3	16.1	25.9	13.1
BC6		-	31.1	30.3	27.9	20.0	13.5
		-	24.4	37.3	32.6	20.6	11.5
		-	26.6	30.2	24.2	26.7	12.2
	AVG	-	24.4	32.6	28.2	22.4	12.4
	CV (%)	-	12.6	12.5	14.9	16.5	8.4
BC7		-	18.8	14.3	11.6	4.2	3.1
		-	17.9	16.3	10.9	4.7	3.0
		-	22.9	14.9	9.7	5.1	2.8
	AVG	-	17.9	15.2	10.7	4.7	3.0
	CV (%)	-	13.4	6.9	8.8	9.7	6.3
BC8		-	8.3	5.1	3.8	1.8	0.9
		-	7.9	5.9	4.1	2.2	2.1
		-	9.8	5.3	3.5	2.5	1.4
	AVG	-	7.9	5.4	3.8	2.2	1.4
	CV (%)	-	11.3	7.0	7.1	17.9	41.4

Table A.2.3- Cube compressive strength of MPPC binder (MPa)

Mix		2 hr	7 hr	1 day	3 day	7 day	28 day	56 day
B5		5.6	8.8	23.4	30.4	34.5	32.0	49.3
		6.0	14.4	22.5	32.0	40.8	35.6	43.0
		4.8	-	34.2	33.4	30.9	42.2	40.4
	AVG	5.5	11.4	26.7	31.9	35.4	36.6	44.2
	CV (%)	11.2	-	24.4	4.7	14.2	14.2	10.4
B7		-	5.0	9.0	13.4	14.3	17.2	30.3
		-	6.0	8.6	16.0	16.3	19.4	17.6
		-	4.6	9.8	11.8	14.9	25.1	23.8
	AVG	-	5.2	9.13	13.7	15.2	20.6	23.9
	CV (%)	-	13.9	6.7	15.4	6.9	19.9	26.5

Table A.2.4- Density of sand ceramic mortar (MPa)

Mix		b/S=1.00	b/S=1.50	b/S=2.00	b/S=2.50	b/S=3.00
MC51		2200	2096	2060	2027	2014
		2197	2092	2063	2017	2013
		2234	2094	2068	2022	2008
	AVG	2210	2094	2064	2022	2012
	CV (%)	0.9	0.1	0.2	0.3	0.2
MC52		2070	2048	2022	2005	2022
		2062	2032	2035	2020	2003
		2120	2060	2021	2019	1989
	AVG	2084	2047	2026	2014	2005
	CV (%)	1.5	0.7	0.4	0.4	0.8
MC71		2082	2037	1975	1937	1878
		2058	2001	1972	1945	1888
		2082	2006	1952	1933	1887
	AVG	2074	2015	1966	1938	1884
	CV (%)	0.7	1.0	0.6	0.3	0.3
MC72		1961	1882	1921	1843	1843
		2000	1882	1921	1843	1843
		2000	1843	1882	1843	1843
	AVG	1987	1869	1908	1843	1843
	CV (%)	1.1	1.2	1.2	0.0	0.0

Table A.2.5- 7 day cube compressive strength of sand ceramic mortar (MPa)

Mix		$b/S=1.00$	$b/S=1.50$	$b/S=2.00$	$b/S=2.50$	$b/S=3.00$
MC51		38.4	33.1	39.0	32.3	37.6
		37.2	38.8	40.4	55.4	45.0
		38.4	44.6	42.0	42.0	51.3
	AVG	38.0	38.8	40.5	43.2	44.6
	CV (%)	1.8	14.8	3.7	26.9	15.3
MC52		29.9	35.2	34.7	53.7	45.7
		45.1	52.3	40.0	40.2	45.1
		32.5	42.1	51.9	43.4	59.8
	AVG	35.8	43.2	42.2	45.7	50.2
	CV (%)	22.8	19.8	20.9	15.4	16.5
MC71		21.2	14.7	15.4	18.8	13.7
		22.0	21.8	15.4	17.2	14.5
		18.2	18.0	19.2	16.2	18.8
	AVG	20.5	18.2	16.7	17.4	15.6
	CV (%)	9.7	19.6	13.0	7.5	17.7
MC72		14.1	16.8	19.0	21.0	19.4
		17.8	19.2	19.8	16.2	16.4
		15.6	18.0	23.6	19.4	18.6
	AVG	15.8	18.0	20.8	18.9	18.2
	CV (%)	11.9	6.6	11.7	12.8	8.5

Table A.2.6- Cube compressive strength of sand ceramic mortar (MPa)

Mix		2 hr	7 hr	1 day	3 day	7 day	28 day
M51		13.5	36.4	53.7	53.7	54.9	59.4
		18.8	30.5	43.0	58.8	63.6	71.3
		13.7	36.4	42.0	48.3	58.2	63.2
	AVG	15.3	32.7	46.2	53.6	58.9	64.6
	CV (%)	19.8	9.9	14.0	9.8	7.5	9.4
M52		8.9	26.9	48.7	50.1	53.7	56.7
		8.3	23.0	39.8	57.4	62.9	67.5
		10.1	26.9	39.8	43.6	54.5	52.9
	AVG	9.1	24.3	42.8	50.4	57.0	59.0
	CV (%)	10.0	9.4	12.0	13.8	9.0	12.8
M53		7.9	34.7	46.0	45.5	51.9	53.1
		8.5	31.7	37.3	43.8	48.7	61.6
		9.3	34.7	43.3	46.7	51.1	47.7
	AVG	8.6	33.9	42.2	45.3	50.6	54.1
	CV (%)	8.1	5.8	10.6	3.3	3.3	12.9
M71		-	5.5	9.5	9.9	18.0	26.7
		-	4.8	7.1	12.1	21.8	28.1
		-	5.5	8.5	9.7	14.7	25.9
	AVG	-	5.1	8.4	10.6	18.2	26.9
	CV (%)	-	7.7	14.4	12.6	19.6	4.2
M72		-	4.8	7.9	8.3	15.8	24.6
		-	3.6	7.1	8.7	23.0	27.7
		-	4.8	6.3	8.5	15.2	25.3
	AVG	-	4.1	7.1	8.5	18.0	25.9
	CV (%)	-	14.8	11.1	2.3	23.8	6.4
M73		-	8.7	11.9	11.3	17.0	24.6
		-	7.1	10.3	13.3	18.6	32.1
		-	8.7	11.3	10.9	17.2	27.7
	AVG	-	7.0	11.2	11.8	17.6	28.1
	CV (%)	-	25.9	7.2	10.9	5.0	13.4

Table A.2.7- Cube compressive strength of ceramic mortar with class F fly ash (MPa)

Mix		3 day	7 day	28 day	Mix		3 day	7 day	28 day
M51		43.8	48.7	65.3	M53		41.2	50.7	51.5
		54.3	52.5	52.7			39.6	41.4	44.6
		46.5	48.7	58.2			41.2	50.7	45.7
	AVG	48.2	49.3	58.7		AVG	40.7	42.2	47.3
	CV (%)	11.3	5.9	10.8		CV (%)	2.2	19.1	7.8
M71		14.5	15.2	25.1	M53		6.7	16.2	22.4
		17.0	18.4	27.7			13.9	15.4	25.5
		15.4	15.8	25.5			10.3	14.7	23.8
	AVG	15.6	16.5	26.1		AVG	10.3	15.4	23.9
	CV (%)	8.3	10.2	5.3		CV (%)	34.6	5.1	6.6

Table A.2.8- 28 day properties of binder and ceramic (MPa)

Mix		$f_{c,b}$	$f_{r,b}$	Mix		$f_{c,m}$	$f_{r,m}$
B5		58.2	2.4	M51		57.3	4.0
		47.5	2.4			64.8	4.1
		37.1	2.4			-	4.1
	AVG	47.6	2.4		AVG	61.0	4.1
	CV (%)	22.2	1.0		CV (%)	8.7	1.4
B7		25.3	1.9	M52		56.9	3.4
		25.6	1.4			-	3.6
		25.9	1.2			-	3.6
	AVG	25.6	1.5		AVG	-	3.6
	CV (%)	1.2	22.6		CV (%)	-	3.0
				M53		55.2	3.2
						57.9	3.3
						-	3.2
	AVG				AVG	56.6	3.2
	CV (%)				CV (%)	3.4	0.4

A.3 Lightweight Ceramic Concrete

The physical properties of each aggregate used in this study are given in Table A.3.1.

Table A.3.1- Physical properties of lightweight aggregates







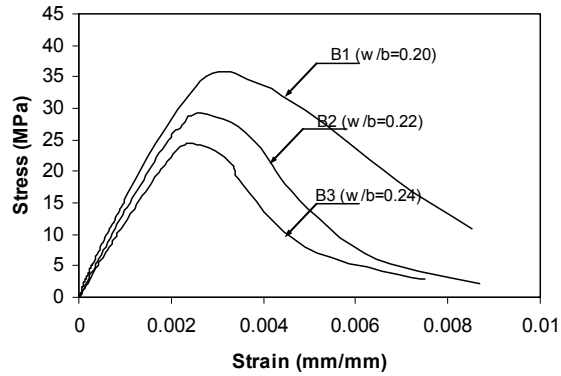
Aggregate Type		Aggregate Properties	
Fine expanded clay (FL)		Specific Gravity (dry)	1.49
		Water absorption (%)	10.3
		Max. Size (mm)	2.5
		Fineness modulus	2.97
Coarse expanded clay (CL)		Specific Gravity (dry)	0.995
		Water absorption (%)	24.4
		Max. Size (mm)	10
		Fineness modulus	5.86
Coated expanded shale (BCO)		Specific Gravity (dry)	1.58
		Water absorption (%)	14.6
		Max. Size (mm)	2.5
		Fineness modulus	3.74

Table A.3.4 continued...

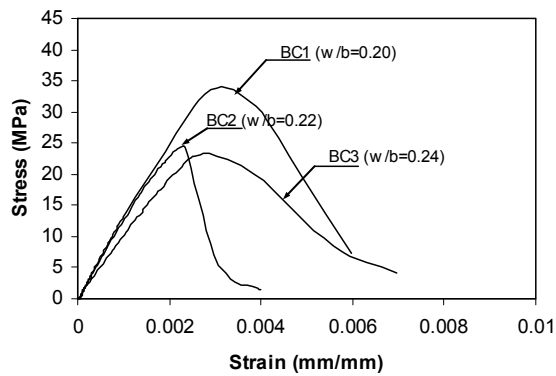
Aggregate Type		Aggregate Properties	
Crushed expanded shale (BCR)		Specific Gravity (dry)	1.69
		Water absorption (%)	7.6
		Max. Size (mm)	2.5
		Fineness modulus	2.80
Expanded slate (ST)		Specific Gravity (dry)	1.76
		Water absorption (%)	3.2
		Max. Size (mm)	5
		Fineness modulus	3.26
Bottom ash (BAA)		Specific Gravity (dry)	1.65
		Water absorption (%)	0.80
		Max. Size (mm)	5
		Fineness modulus	2.68

Cylinder Test

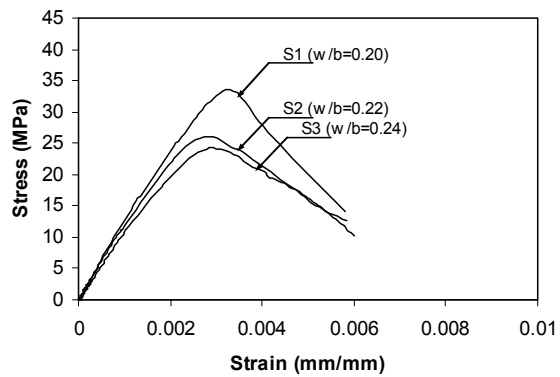
The uniaxial cylinder compressive stress-strain response of LWCC containing different lightweight aggregates at 28 days is given in Figure A.3.1.



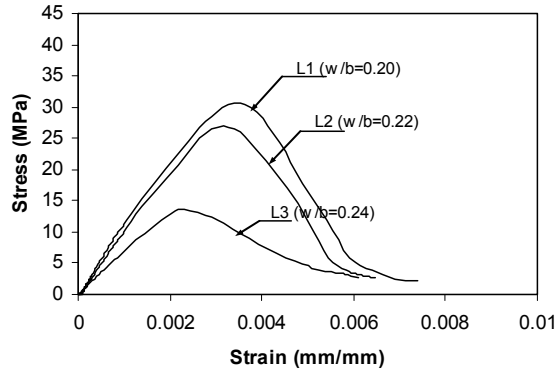
(a) B ceramic concrete



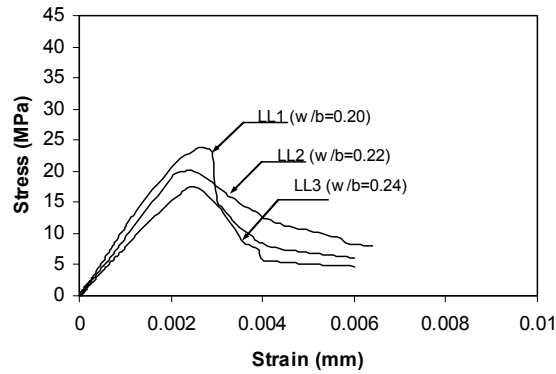
(b) BC ceramic concrete



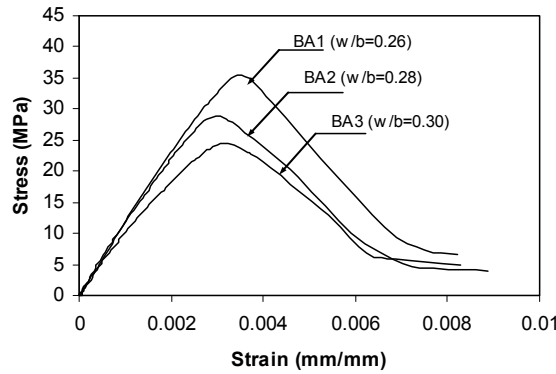
(c) S ceramic concrete



(d) L ceramic concrete



(e) LL ceramic concrete

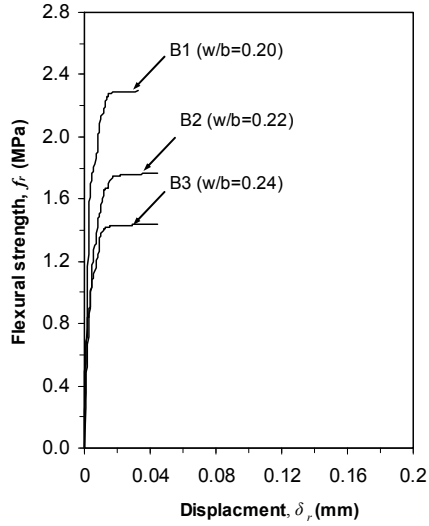


(f) BA ceramic concrete

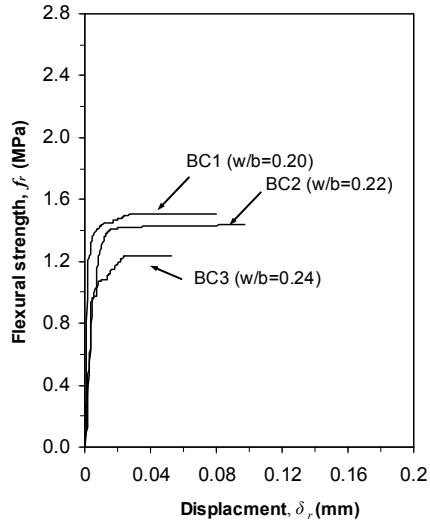
Figure A.3.1- Stress-strain response of different LWCC

Flexure Test

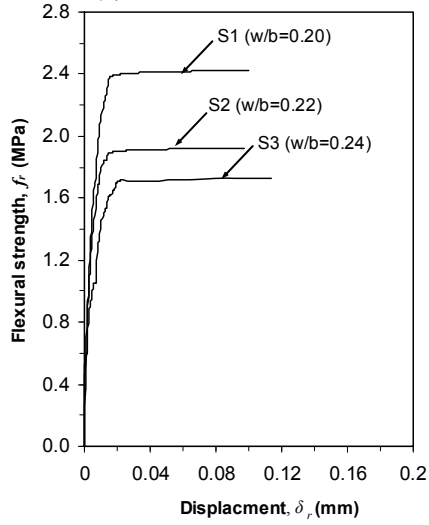
Flexural strength of ceramic concrete made with different types of lightweight aggregates tested at 28 days is shown in Figure A.3.2.



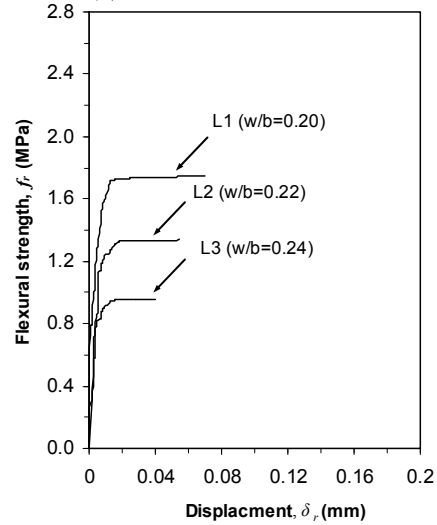
(a) B ceramic concrete



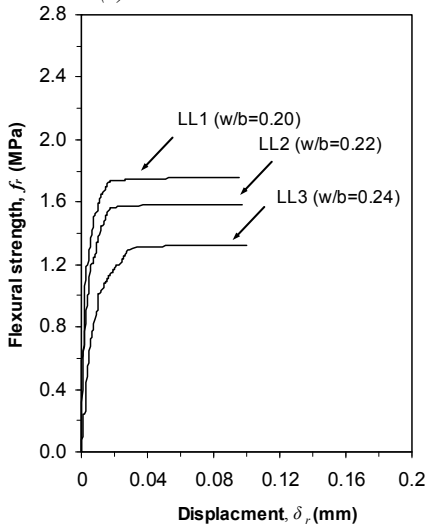
(b) BC ceramic concrete



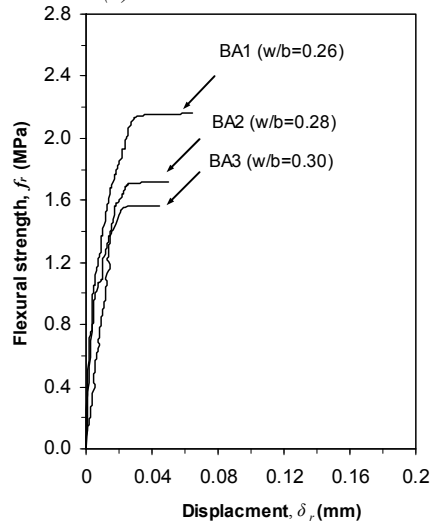
(c) S ceramic concrete



(d) L ceramic concrete



(e) LL ceramic concrete



(f) BA ceramic concrete

Figure A.3.2- Flexural strength of different LWCC

Shear Test

Shear strength of ceramic concrete made with different types of lightweight aggregates tested at 28 days is shown in Figure A.3.3.

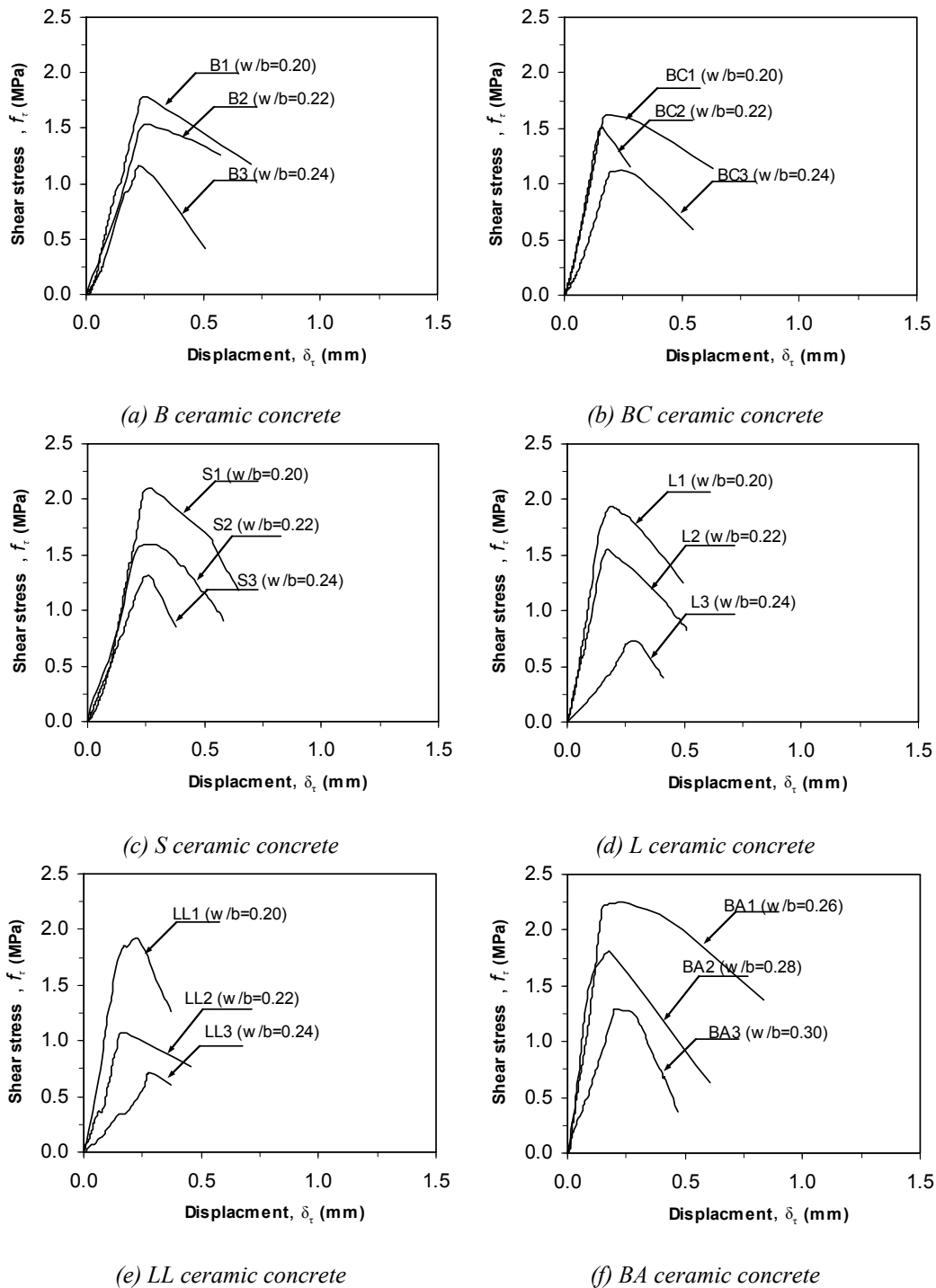


Figure A.3.3- Shear strength of different light weight ceramic concrete

Appendix A: Tables and Plots

Table A.3.2- Density of lightweight ceramic concrete (kg/m^3)

Mix type		Density, ρ		
		w/b=0.20	w/b=0.22	w/b=0.24
B		1814	1752	1739
		1781	1725	1677
		1792	1758	1691
	AVG	1795	1745	1702
	CV (%)	0.9	1.0	1.9
BC		1834	1821	1756
		1856	1804	1758
		1860	1793	1737
	AVG	1850	1806	1750
	CV (%)	0.8	1.0	0.7
S		1864	1843	1819
		1888	1819	1786
		1840	1816	1837
	AVG	1864	1826	1814
	CV (%)	1.3	1.0	1.4
L		1739	1699	1662
		1782	1683	1630
		1766	1736	1654
	AVG	1762	1706	1649
	CV (%)	1.2	1.6	1.0
LL		1660	1701	1606
		1658	1681	1600
		1764	1677	1584
	AVG	1694	1686	1597
	CV (%)	3.6	0.8	0.7

Mix type		Water to binder ratio		
		w/b=0.26	w/b=0.28	w/b=0.30
BA		1740	1786	1753
		1739	1751	1714
		1779	1744	1702
	AVG	1753	1761	1723
	CV (%)	1.3	1.3	1.5

Table A.3.3- Density of lightweight ceramic concrete (kg/m³)

Mix type		Aggregate to binder ratio		
		0.50	0.67	1.0
B		1844	1814	1763
		1808	1781	1730
		1808	1792	1757
	AVG	1820	1795	1750
	CV (%)	1.1	0.9	1.0
BC		1857	1834	1756
		1839	1856	1762
		1859	1860	1798
	AVG	1852	1850	1772
S		1882	1864	1854
		1850	1888	1839
		1897	1840	1832
	AVG	1876	1864	1842
	CV (%)	1.3	1.3	0.6
L		1830	1739	1718
		1770	1782	1734
		1774	1766	1746
	AVG	1791	1762	1733
	CV (%)	1.9	1.2	0.8
Mix Type		Aggregate to binder ratio		
		0.44	0.54	0.64
LL		1696	1606	1532
		1656	1600	1552
		1640	1584	1664
	AVG	1664	1597	1583
	CV (%)	1.7	0.7	4.5

Table A.3.3 continued...

Mix type		Aggregate to binder ratio		
		0.5	0.67	1
BA		1812	1806	1740
		1815	1745	1739
		1749	1815	1779
	AVG	1792	1789	1753
	CV (%)	2.1	2.1	1.3

Table A.3.4- Cube compressive strength of lightweight ceramic concrete with different water binder ratios (MPa)

Mix type	w/b=0.20			w/b=0.22			w/b=0.24			
	3 day	7 day	28 day	3 day	7 day	28 day	3 day	7 day	28 day	
B		23.4	27.7	32.9	24.1	28.8	25.7	21.7	27.8	24.2
		30.5	31.5	37.6	22.7	28.2	31.0	18.6	20.6	29.5
		26.5	27.0	30.5	24.1	24.0	29.0	19.3	16.8	23.1
	AVG	26.8	28.7	33.7	22.3	27.0	28.5	19.9	21.7	25.6
	CV (%)	13.3	8.4	10.78	9.0	9.7	9.3	8.1	25.7	13.4
BC		21.8	26.2	26.5	19.0	23.7	23.9	17.7	20.6	21.3
		27.7	26.5	35.8	23.8	20.8	24.7	14.9	15.2	26.6
		24.6	26.6	30.0	19.0	21.8	28.4	14.6	17.2	25.0
	AVG	24.7	26.4	30.8	20.7	22.1	25.7	15.7	17.7	24.3
	CV (%)	12.0	0.8	15.3	12.8	6.7	9.4	10.7	15.5	11.1
S		24.0	23.9	34.7	22.8	19.1	34.2	21.6	18.7	27.5
		30.0	29.5	40.0	17.2	22.8	37.8	17.6	21.0	33.8
		22.8	26.0	41.3	22.8	18.6	28.6	16.6	19.6	29.0
	AVG	25.6	26.5	38.7	18.8	20.2	33.6	18.6	19.8	30.1
	CV (%)	15.1	10.7	9.0	18.5	11.4	13.8	14.2	5.9	10.9
L		21.4	23.2	32.6	18.2	21.2	21.8	14.2	18.0	21.4
		24.0	19.4	31.5	16.7	21.0	29.2	16.9	17.2	20.4
		20.0	24.0	33.6	18.2	20.4	25.1	13.1	19.2	25.1
	AVG	21.8	22.2	32.6	17.3	20.9	25.4	14.7	18.1	22.3
	CV (%)	9.3	11.1	3.2	4.6	2.0	14.6	13.3	5.6	11.1
LL		25.4	25.2	27.4	21.6	20.4	21.9	16.6	20.2	20.8
		23.0	25.4	26.2	23.4	24.8	26.0	19.8	18.7	19.2
		22.1	22.0	25.1	21.6	20.4	18.8	15.3	17.8	23.2
	AVG	23.5	24.2	26.2	21.7	21.9	22.2	17.2	18.9	21.1
	CV (%)	7.3	7.9	4.4	7.9	11.6	16.2	13.5	6.4	9.6

Appendix A: Tables and Plots

Table A.3.4 continued...

Mix type	Water to binder ratio									
	w/b=0.26			w/b=0.28			w/b=0.30			
	3 day	7 day	28 day	3 day	7 day	28 day	3 day	7 day	28 day	
BA		23.8	28.2	28.2	26.8	28.0	31.2	26.1	22.8	30.0
		25.6	31.4	38.0	27.3	30.4	29.2	23.4	25.0	27.9
		26.0	27.2	33.4	26.8	28.0	29.0	19.8	26.4	21.7
	AVG	27.4	28.9	33.2	26.7	28.8	29.8	23.1	24.7	26.5
	CV (%)	4.7	7.6	14.8	2.5	4.8	4.1	13.7	7.3	16.3

Table A.3.5- Cube compressive strengths of light weight ceramic concrete with different aggregate to binder ratios (MPa)

Mix type		Aggregate to binder ratio					
		0.50		0.67		1.0	
		7 day	28 day	7 day	28 day	7 day	28 day
B		33.0	37.2	31.5	32.9	22.2	23.6
		34.8	35.6	27.0	37.6	27.6	30.8
		29.2	37.2	27.7	30.5	24.5	23.8
	AVG	32.3	36.2	28.7	33.7	24.8	26.1
	CV (%)	8.8	2.4	8.4	10.8	10.9	15.7
BC		32.2	34.9	26.5	26.5	20.2	24.6
		34.0	32.4	26.6	35.8	23.2	26.6
		26.4	34.9	26.2	30.0	21.8	25.0
	AVG	30.9	32.3	26.4	30.8	21.7	25.4
	CV (%)	12.9	8.2	0.8	15.3	6.9	4.2
S		32.2	41.1	29.5	34.7	21.8	27.8
		37.2	35.8	26.0	40.0	23.3	34.0
		29.2	41.1	23.9	41.3	21.4	31.4
	AVG	32.9	36.0	26.5	38.7	22.2	31.1
	CV (%)	12.3	13.9	10.7	9.0	4.5	10.0
L		21.6	33.0	19.4	32.6	17.4	18.8
		28.9	25.2	24.0	31.5	18.8	27.6
		27.6	33.0	23.2	33.6	19.4	20.0
	AVG	26.0	27.1	22.2	32.6	18.5	22.1
	CV (%)	15.0	19.2	11.1	3.2	5.5	21.6

Appendix A: Tables and Plots

Table A.3.5 continued...

Mix type		Aggregate to binder ratio					
		0.44		0.54		0.64	
		7 day	28 day	7 day	28 day	7 day	28 day
LL		21.0	23.0	18.7	20.8	13.6	22.0
		20.4	22.0	17.8	19.2	15.2	19.0
		21.2	23.0	20.2	23.2	17.6	16.8
	AVG	20.9	22.4	18.9	21.1	15.5	19.3
	CV (%)	2.0	2.4	6.4	9.6	13.0	13.5

Mix type		Aggregate to binder ratio					
		0.25		0.33		0.50	
		7 day	28 day	7 day	28 day	7 day	28 day
BA		29.9	44.1	36.7	39.4	27.2	28.2
		38.4	39.6	29.5	37.4	31.4	38.0
		24.6	44.1	31.6	35.4	28.2	33.4
	AVG	31.0	39.4	32.6	37.4	28.9	33.2
	CV (%)	22.5	12.3	11.4	5.3	7.6	14.8

A.4 Textile Reinforced Ceramic Concrete Panels

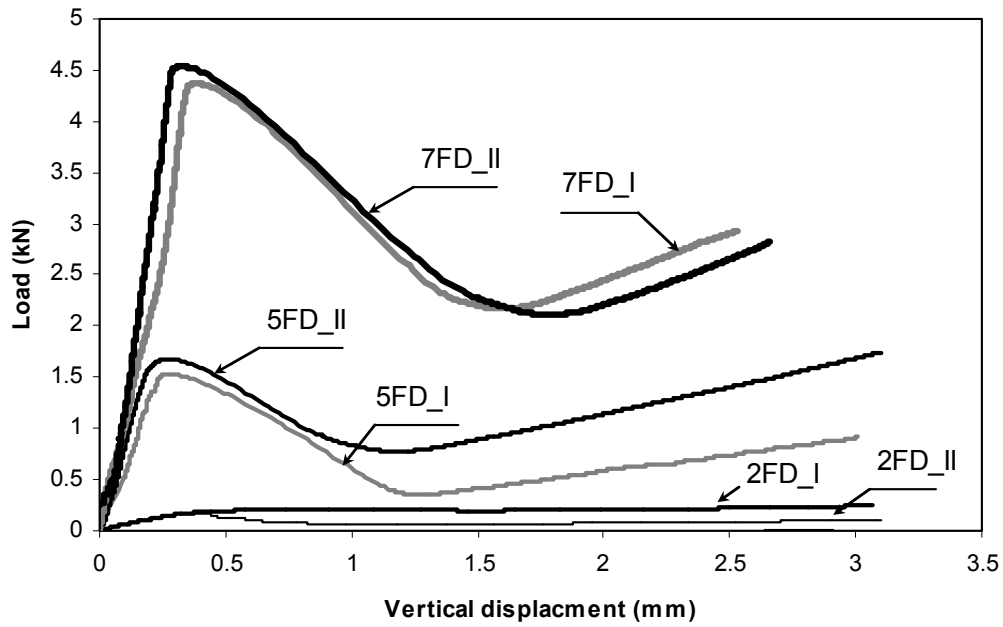


Figure A.4.1- Load-deflection response of full depth panels

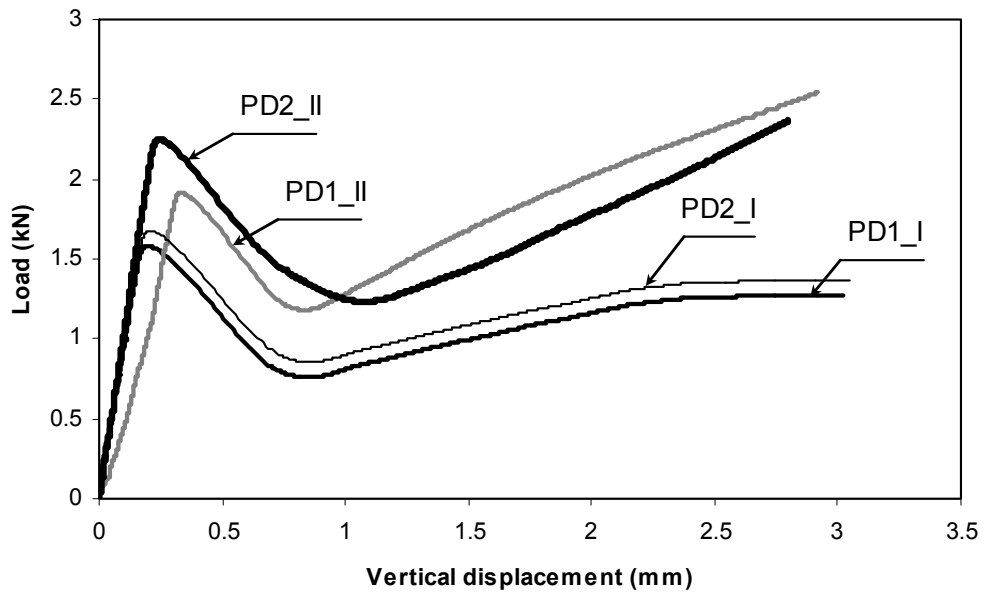


Figure A.4.2- Load-deflection response of partial depth precast panels

A.5 Glass Fiber Reinforced Ceramic Concrete

Cube Compression Response

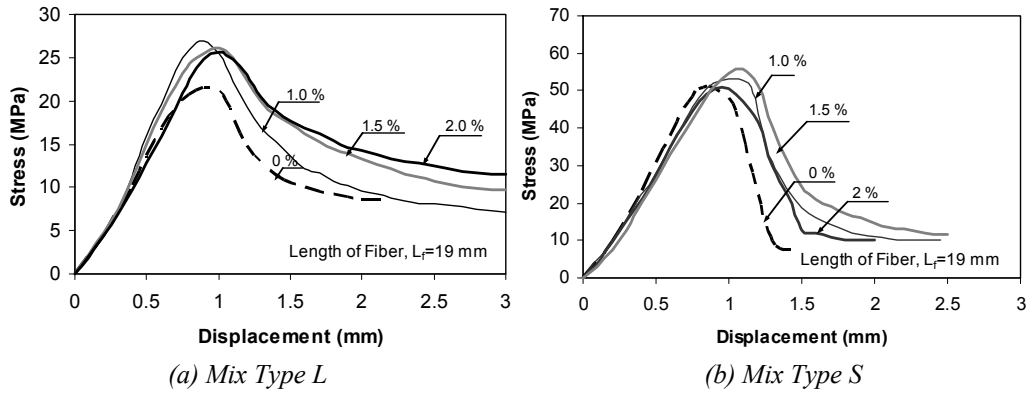


Figure A.5.1- Influence of fiber volume fraction on cube compressive stress to displacement relationship of cube samples

Cylinder Compression Response

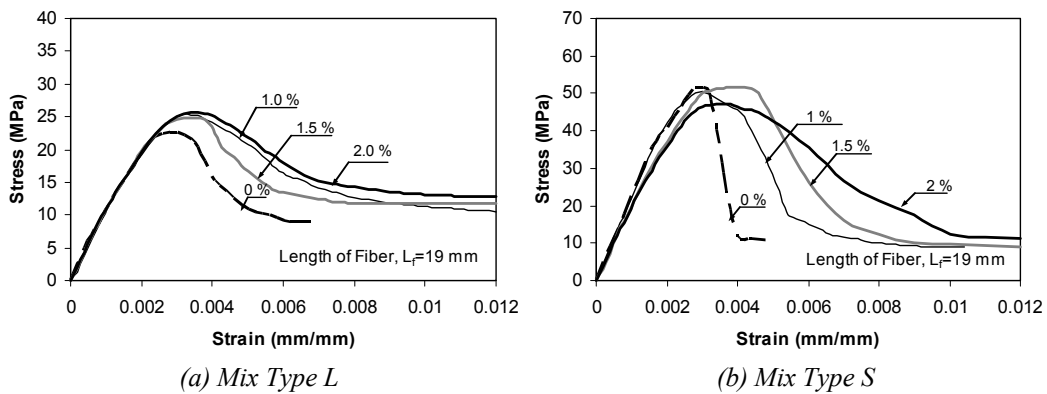


Figure A.5.2- Influence of fiber volume fraction on cylinder compressive stress-strain relation

Flexure Response

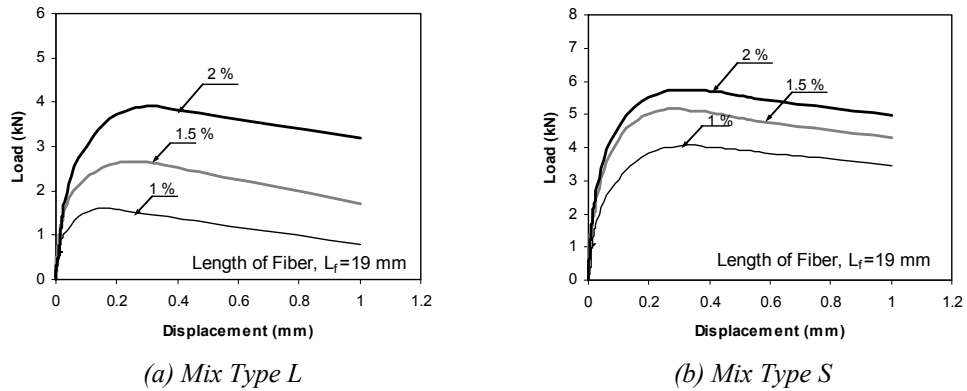


Figure A.5.3- Influence of fiber volume fraction on load-displacement under flexure

Shear Response

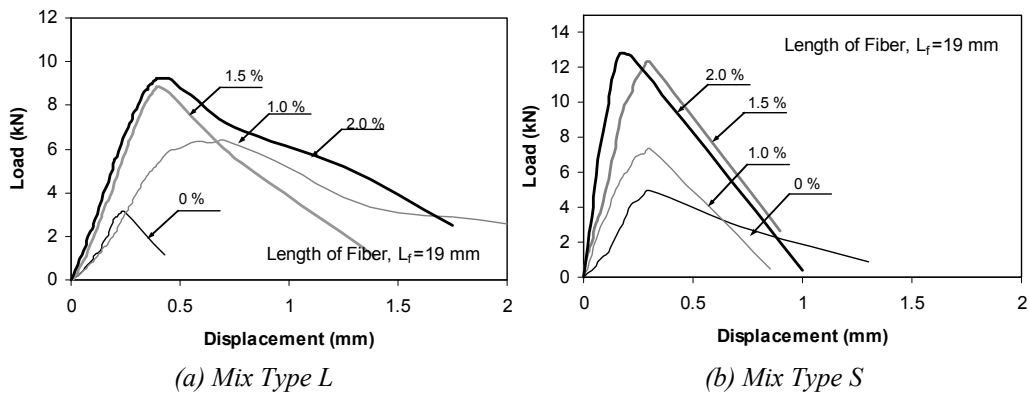


Figure A.5.4- Influence of fiber volume fraction on load-displacement under shear

Table A.5.1- Density of mix type L ceramic concrete (kg/m³)

Mix Type	Series	Density, ρ					CV (%)
		Prism specimen 1	Prism specimen 2	Cylinder specimen	Cube specimen	AVG	
L	LL0	1784	1832	1803	1783	1799	1.83
		1788	1860	1729	1777		
		1830	1798	1809	1792		
	LL11	1788	1836	1799	1794	1810	1.46
		1826	1846	1787	1842		
		1810	1840	1789	1769		
	LL12	1794	1880	1808	1798	1816	1.79
		1786	1874	1790	1795		
		1840	1826	1800	1797		
	LL13	1774	1766	1797	1813	1797	0.95
		1802	1818	1810	1820		
		1782	1790	1801	1792		
	LL21	1782	1742	1814	1805	1801	1.30
		1832	1786	1798	1809		
		1822	1814	1795	1811		
	LL22	1808	1776	1792	1821	1809	0.98
		1826	1796	1795	1823		
		1836	1812	1800	1826		
	LL23	1778	1842	1804	1812	1818	1.10
		1828	1808	1823	1818		
		1850	1830	1795	1825		

Table A.5.2- Density of mix type S ceramic concrete (kg/m³)

Mix Type	Series	Density, ρ					CV (%)
		Prism specimen 1	Prism specimen 2	Cylinder specimen	Cube specimen	AVG	
S	S0	2212	2220	2196	2195.4	2201	1.27
		2180	2236	2184	2162		
		2250	2224	2182	2165		
	S11	2172	2162	2086	2167	2176	2.00
		2130	2216	2171	2208		
		2150	2226	2179	2243		
	S12	2202	2218	2163	2147	2190	1.58
		2206	2230	2183	2129		
		2248	2196	2188	2165		
	S13	2084	2156	2157	2174	2151	1.72
		2156	2162	2165	2174		
		2188	2178	2068	2148		
	S21	2174	2172	2178	2159	2159	0.90
		2116	2144	2180	2157		
		2138	2158	2180	2157		
	S22	2178	2156	2174	2194	2179	1.45
		2204	2228	2185	2177		
		2194	2188	2096	2177		
	S23	2148	2188	2186	2186	2179	0.93
		2174	2188	2175	2191		
		2132	2208	2187	2185		

Table A.5.3- Cube compressive, cylinder compressive, flexure and shear strengths test results of mix type L ceramic concrete (MPa)

Mix type		f_{cu} (MPa)	f_c' (MPa)	f_r (MPa)	f_τ (MPa)
L	LL0	21.5	24.5	1.1	1.7
		21.6	23.8	1.0	1.8
		23.3	25.6	1.3	-
	AVG	22.1	24.7	1.1	1.8
	CV (%)	4.5	3.7	9.6	4.5
	LL11	25.4	25.0	4.3	3.8
		25.9	27.8	4.1	4.1
		26.5	25.8	3.5	3.8
	AVG	25.9	26.2	3.9	3.9
	CV (%)	2.0	5.6	11.0	4.1
	LL12	24.3	24.7	6.9	2.8
		27.7	26.9	4.8	5.0
		31.5	24.2	3.1	4.2
	AVG	27.8	25.3	4.9	4.0
	CV (%)	12.9	5.8	38.9	28.1
	LL13	28.9	25.6	7.3	3.7
		24.4	26.8	8.4	5.1
		26.4	26.7	7.1	3.0
	AVG	26.6	26.4	7.6	4.0
	CV (%)	8.4	2.4	9.3	27.2
	LL21	28.4	27.4	3.1	4.0
		28.2	26.4	3.1	3.3
		24.7	22.4	3.0	-
	AVG	27.1	25.4	3.1	3.7
	CV (%)	7.7	10.4	1.5	12.8
	LL22	27.2	24.5	4.4	4.5
		25.5	25.5	5.7	5.4
		26.2	24.8	5.0	3.8
	AVG	26.3	24.9	5.0	4.6
	CV (%)	3.3	2.2	12.7	12.7
LL23	25.1	26.7	5.3	5.7	
	26.6	25.8	8.7	4.6	
	25.1	24.8	8.4	-	
AVG	25.6	25.7	7.5	5.2	
CV (%)	3.4	3.6	25.3	15.4	

Table A.5.4- Cube compressive, cylinder compressive, flexure and shear strengths test results of mix type S ceramic concrete (MPa)

Mix type		f_{cu} (MPa)	f_c' (MPa)	f_r (MPa)	f_τ (MPa)
S	S0	50.6	31.9	2.3	3.4
		46.7	64.5	2.4	2.7
		54.2	59.3	1.5	2.2
	AVG	50.5	51.9	2.1	2.8
	CV (%)	7.5	33.7	23.5	21.4
	S11	55.7	51.6	6.1	4.5
		54.2	55.2	5.2	7.0
		57.8	52.3	4.9	6.4
	AVG	55.9	53.0	5.4	6.0
	CV (%)	3.2	3.6	10.9	21.8
	S12	58.1	48.9	9.3	6.6
		54.5	57.6	9.5	7.5
		57.4	56.7	8.4	5.9
	AVG	56.6	54.4	9.0	6.6
	CV (%)	3.4	8.8	6.5	12.0
	S13	54.8	53.2	10.0	8.6
		58.2	52.0	11.0	7.3
		59.1	48.8	9.5	6.8
	AVG	57.3	51.4	10.2	7.6
	CV (%)	4.0	4.5	7.6	12.3
	S21	53.9	50.4	8.4	3.7
		53.7	54.2	6.9	4.0
		53.8	53.2	0.0	4.6
	AVG	53.8	52.6	7.7	4.1
	CV (%)	0.3	3.7	14.4	11.7
	S22	45.2	56.7	11.0	6.0
		56.5	54.3	8.4	7.7
		-	49.1	9.9	-
	AVG	50.8	53.3	9.8	6.9
	CV (%)	15.7	7.3	13.8	16.9
S23	55.3	47.6	11.5	7.1	
	54.5	47.9	10.6	6.0	
	57.2	50.2	10.3	8.0	
AVG	55.7	48.6	10.8	7.0	
CV (%)	2.5	2.9	6.0	14.4	

A.6 Uniaxial Tensile Behaviour of Textile Reinforced Ceramic Concrete

Prisms Flexure Stress-displacement Curves

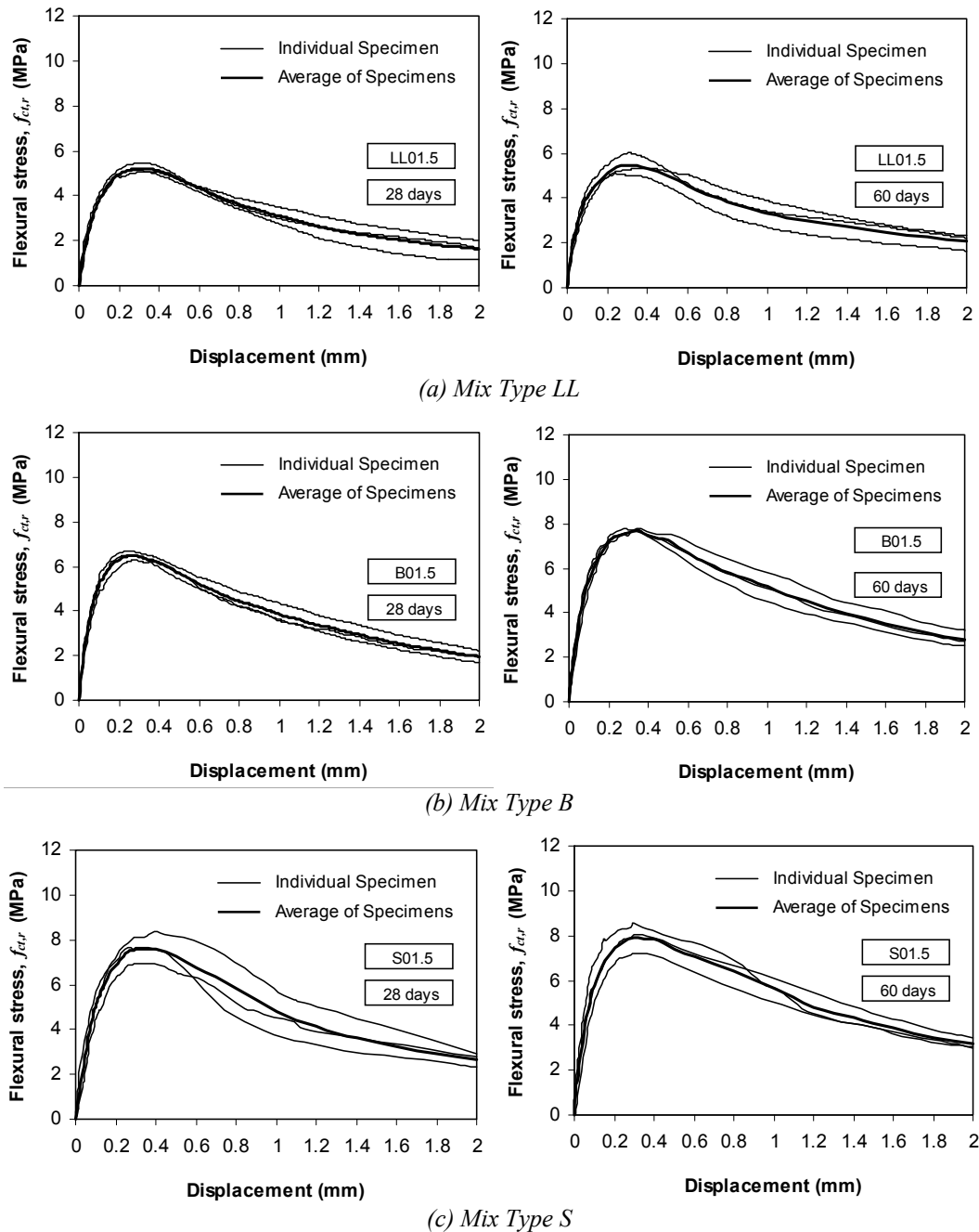
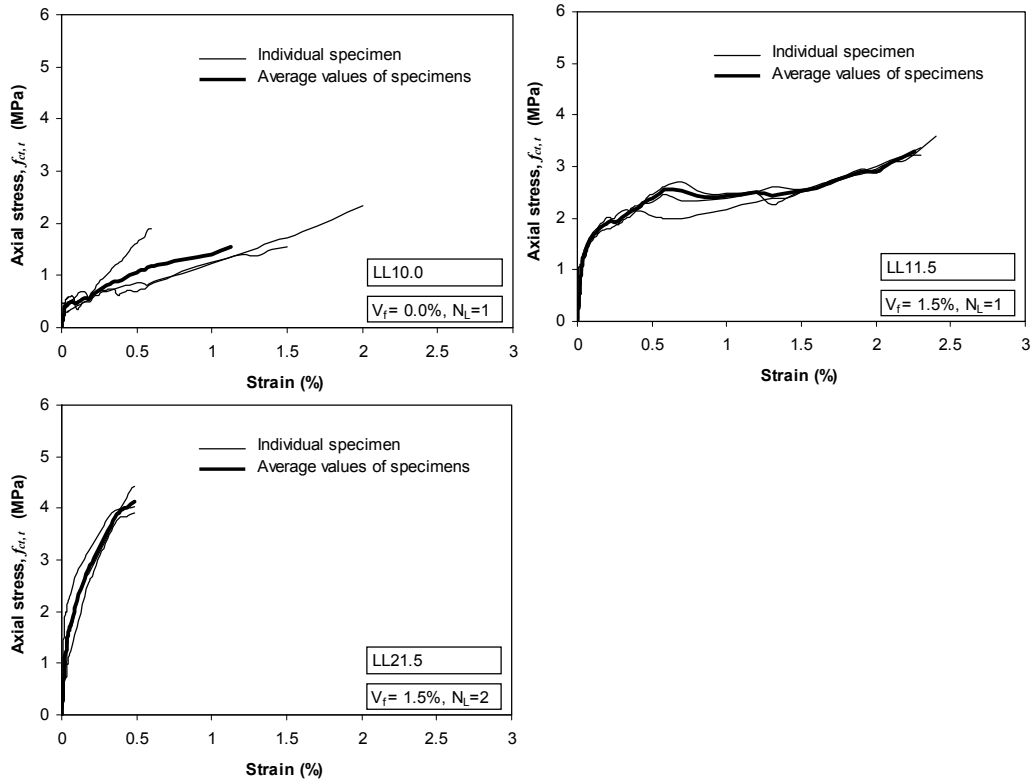
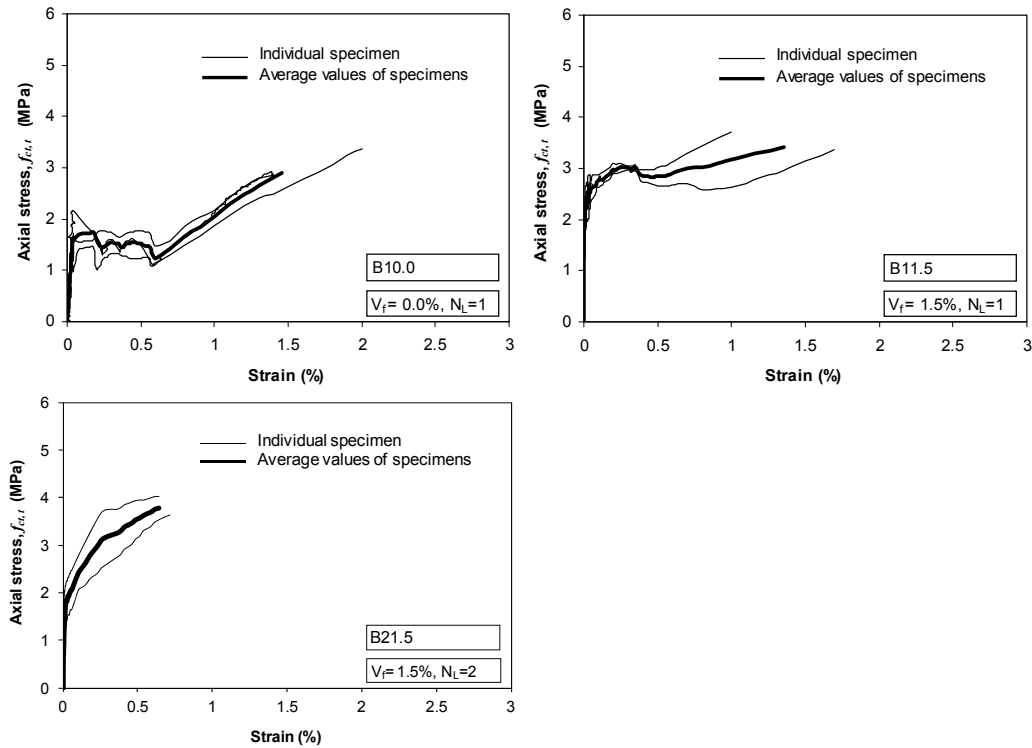


Figure A.6.1-Flexure stress-displacement curves of glass fiber reinforced ceramic concrete obtained from prism specimens

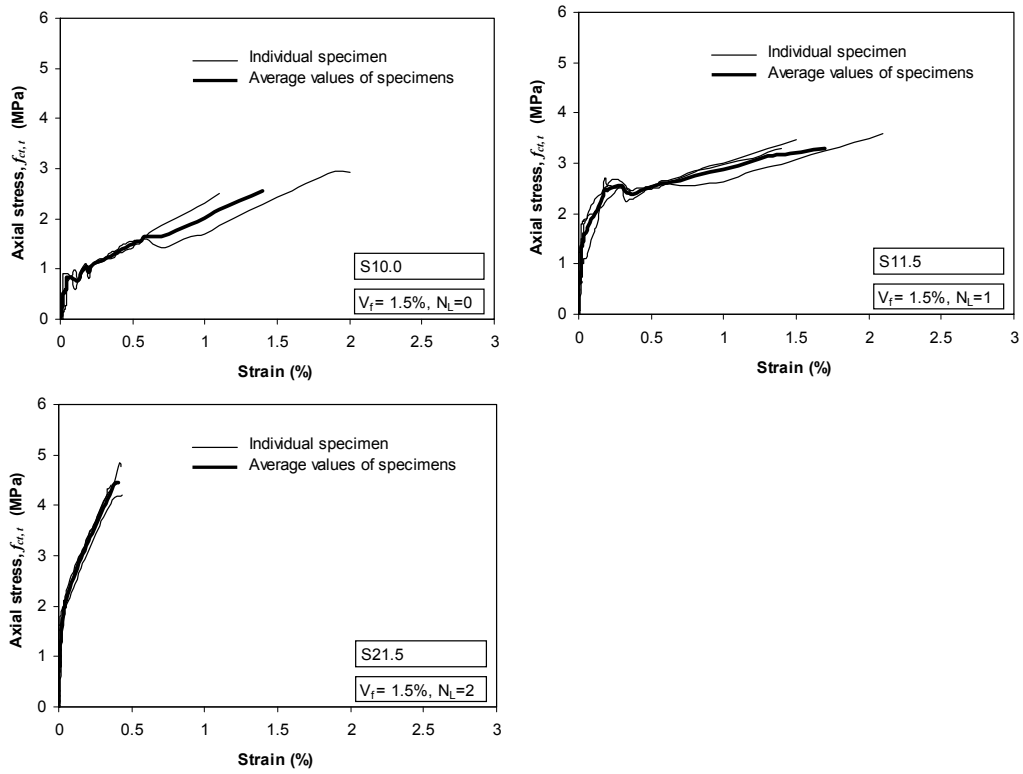
Dog-bone Uniaxial Tensile Stress-strain Curves



(a) Mix Type LL



(b) Mix Type B



(c) Mix Type S

Figure A.6.2- Axial stress-strain response of textile reinforced ceramic concrete obtained from dog-bone shaped specimens

Table A.6.1- Density of glass fiber reinforced ceramic concrete (kg/m^3)

Mix Type	Age (Days)	Density, ρ			CV (%)
		Prism specimen	Cylinder specimen	AVG	
LL01.5	28	1785	1779	1792	3.47
		1738	1782		
		1752	1814		
	60	1733	1824	1831	8.57
		1724	1830		
		1725	1840		
B01.5	28	1922	1951	1957	1.62
		1926	1981		
		1941	1940		
	60	1941	2033	2032	8.03
		1979	2045		
		1948	2016		
S01.5	28	2134	2209	2216	3.52
		2149	2228		
		2160	2212		
	60	2151	2156	2191	4.78
		2171	2201		
		2160	2216		

Table A.6.2- Cube compressie strength (f_{cu}) of ceramic concrete at 28 days

Group	Series	Cube specimen			AVG	CV (%)
LL	LL00.0	30.1	27.4	25.8	27.8	7.86
	LL01.5	29.3	30.5	27.2	29.0	5.81
	LL10.0	28.6	25.8	25.9	26.8	5.96
	LL11.5	27.5	28.7	27.3	27.8	2.64
	LL21.5	29.3	26.2	29.3	28.3	6.29
B	B00.0	45.7	44.8	-	45.2	1.41
	B01.5	45.8	42.1	46.0	44.6	4.90
	B10.0	37.4	40.8	35.8	38.0	6.73
	B11.5	43.1	40.8	44.9	42.9	4.76
	B21.5	44.8	45.9	44.2	45.0	1.89
S	S00.0	43.7	-	43.8	43.7	0.19
	S01.5	49.7	53.7	53.1	52.2	4.15
	S10.0	52.4	47.0	57.8	52.4	10.31
	S11.5	54.4	48.4	50.4	51.1	5.98
	S21.5	46.6	45.3	46.3	46.1	1.54

Table A.6.3- Cylinder compressive strength ($f_{c,t}$), Flexural strength ($f_{c,r}$) and Splitting tensile strength ($f_{c,st}$) of glass fiber reinforced ceramic concrete

Mix type	Age		f_c' (MPa)	$f_{c,r}$ (MPa)	$f_{c,st}$ (MPa)
LL01.5	28 day		26.5	5.5	4.5
			28.3	5.1	4.4
			27.0	5.1	3.9
		AVG	27.2	5.2	4.3
		CV(%)	3.47	4.06	8.03
	60 day		27.9	5.1	4.2
			28.4	6.0	3.8
			27.5	5.4	3.9
		AVG	27.9	5.5	4.0
		CV(%)	1.62	8.57	4.78
B01.5	28 day		41.6	6.3	5.6
			40.6	6.5	5.6
			41.4	6.7	5.2
		AVG	41.2	6.5	5.5
		CV(%)	1.28	3.09	4.46
	60 day		36.4	7.8	4.9
			40.1	7.6	5.3
			-	7.8	5.5
		AVG	38.3	7.8	5.2
		CV(%)	6.84	1.30	6.34
S01.5	28 day		45.1	8.5	5.6
			42.9	7.7	7.2
			45.1	7.3	6.9
		AVG	44.3	7.8	6.6
		CV(%)	2.90	7.52	12.53
	60 day		47.7	7.2	5.85
			43.4	8.0	6.03
			43.6	8.5	7.03
		AVG	44.9	7.9	6.30
		CV(%)	5.42	8.61	10.07

Table A.6.4- Axial tensile strength, $f_{ct, t}$ from dog-bone specimens (MPa)

Mix Type	Series	$f_{ct, t}$ (MPa)			AVG	CV (%)
LL	LL00.0	0.6	0.5	0.8	0.6	26.02
	LL01.5	1.5	1.1	-	1.3	18.95
	LL10.0	1.9	-	1.3	1.6	24.63
	LL11.5	3.4	3.2	3.6	3.4	5.53
	LL21.5	4.4	4.0	3.9	4.1	6.31
B	B00.0	1.0	1.0	-	1.0	5.89
	B01.5	2.7	-	2.7	2.7	0.73
	B10.0	2.9	2.8	3.4	3.0	9.09
	B11.5	3.1	3.7	3.1	3.3	10.35
	B21.5	3.6	4.0	3.2	3.6	11.49
S	S00.0	1.2	1.2	1.2	1.2	1.86
	S01.5	1.7	2.0	1.7	1.8	9.72
	S10.0	2.9	2.5	-	2.7	11.70
	S11.5	3.5	3.6	3.3	3.5	4.33
	S21.5	4.8	4.7	4.4	4.6	4.82

Bare Textile Reinforcement Tensile Test Results

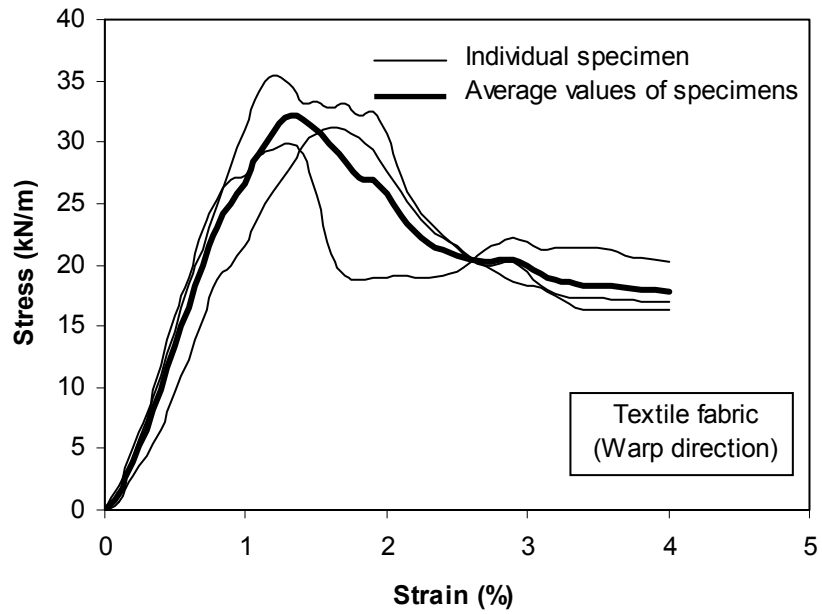


Figure A.6.3- Tensile stress-strain curve for bare textile fabric

Table A.6.5- Tensile test result for bare textile along warp direction

		Peak tensile stress (kN/m)	Tensile strain at peak stress (%)	Modulus of elasticity (kN/mm)
Textile fabric		31.0	1.6	30400
		35.0	1.2	35100
		30.0	1.3	35700
	AVG	32.0	1.37	33700
	CV(%)	8.96	15.30	8.70

A.7 Reinforced Ceramic Concrete Slabs

A.7.1 Material Test Results

Ceramic Concrete Compression Test Results

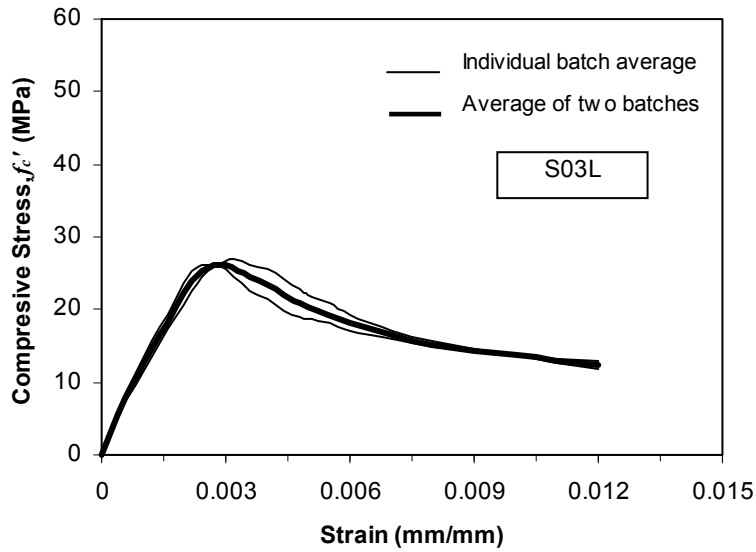


Figure A.7.1- Compressive stress-strain curves for specimen S03L

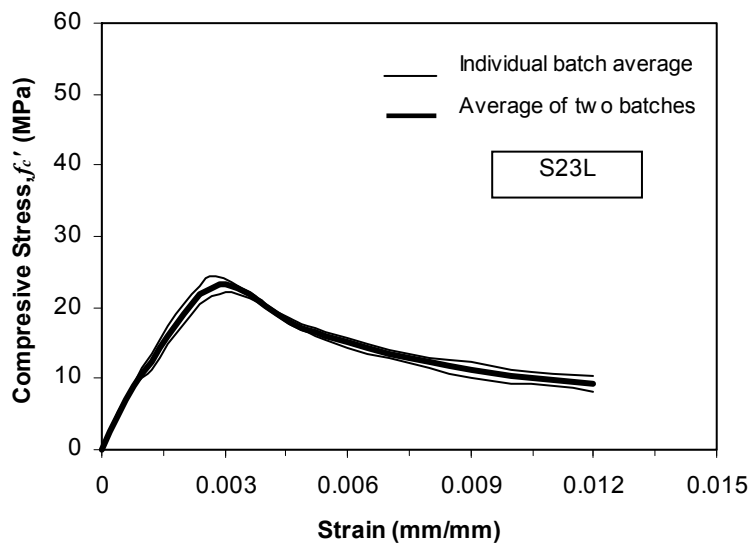


Figure A.7.2- Compressive stress-strain curves for specimen S23L

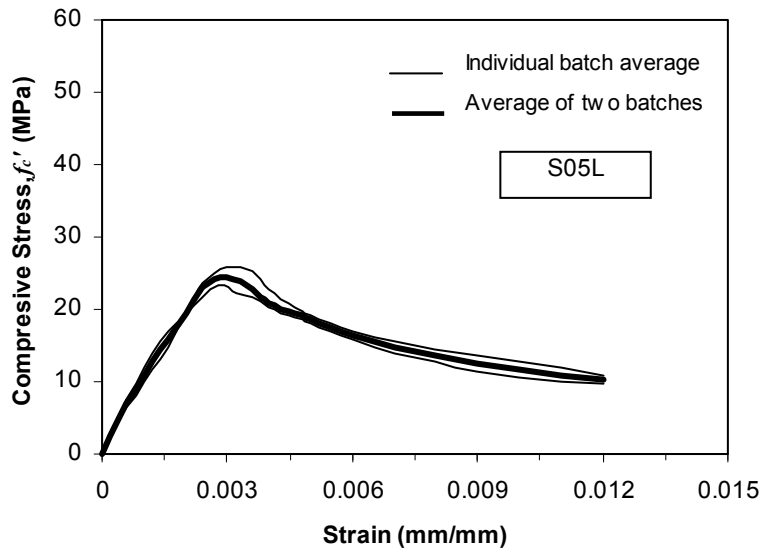


Figure A.7.3- Compressive stress-strain curves for specimen S05L

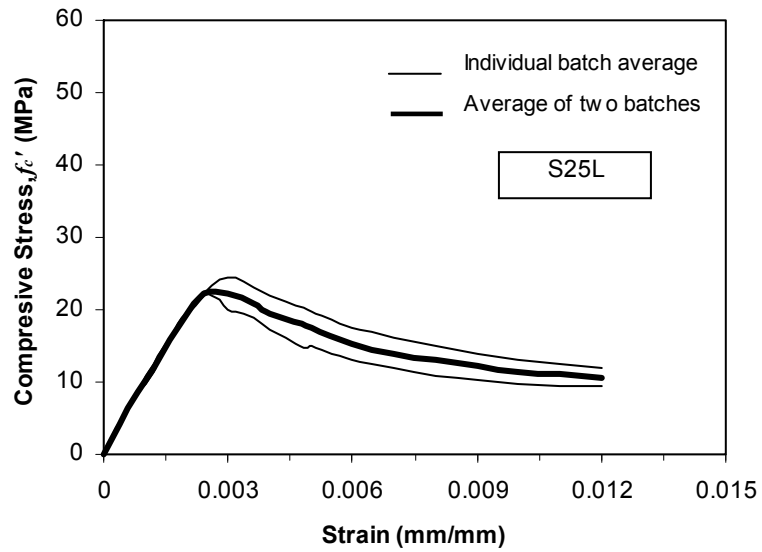


Figure A.7.4- Compressive stress-strain curves for specimen S25L

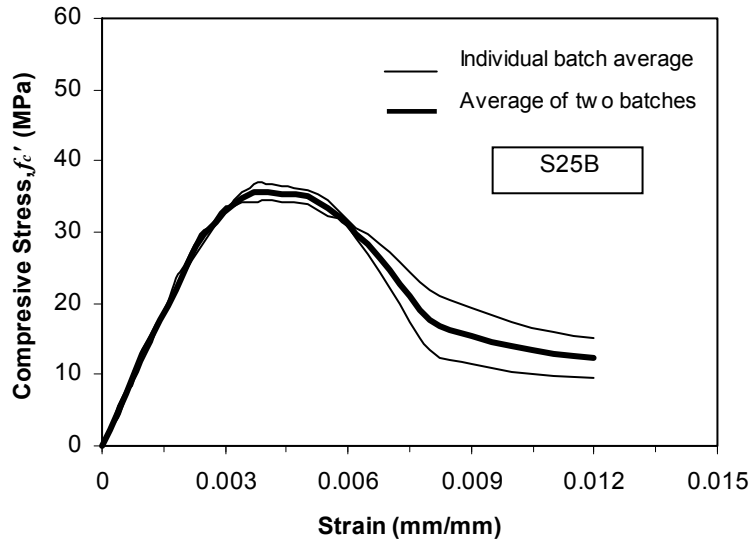


Figure A.7.5- Compressive stress-strain curves for specimen S25B

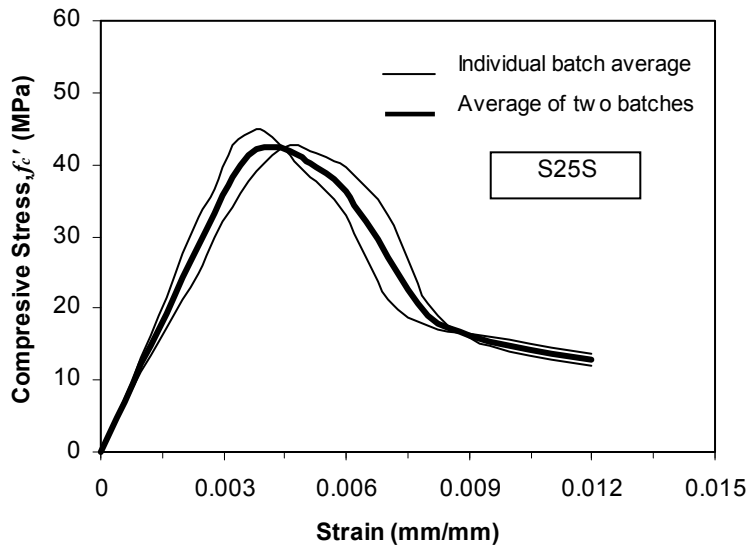


Figure A.7.6- Compressive stress-strain curves for specimen S25S

Table A.7.1- Compression test result for glass fiber reinforced ceramic concrete

Slab ID	Mix batch		f_c' (MPa)	ϵ_c' (mm/mm)	E_c (GPa)
S03L	I		26.9	0.0024	14.8
			26.7	0.0030	9.7
			27.4	0.0032	11.2
		AVG	27.0	0.0029	11.9
		CV (%)	1.32	14.52	21.8
	II		26.8	0.0024	14.4
			27.0	0.0030	13.5
			25.9	0.0024	14.3
		AVG	26.6	0.0026	14.1
		CV (%)	2.23	13.32	3.64
S23L	I		24.8	0.0028	9.6
			26.5	0.0028	12.7
			22.7	0.0030	13.0
		AVG	24.7	0.0029	11.7
		CV (%)	7.66	4.03	15.79
	II		22.0	0.0030	12.0
			23.4	0.0030	10.0
			22.4	0.0036	9.8
		AVG	22.6	0.0032	10.6
		CV (%)	3.09	10.83	11.64
S05L	I		22.0	0.0024	8.9
			24.2	0.0036	9.0
			27.1	0.0030	12.5
		AVG	24.4	0.0030	10.1
		CV (%)	10.39	20.00	20.04
	II		25.4	0.0028	12.1
			26.0	0.0032	12.8
			26.6	0.0030	11.6
		AVG	26.0	0.0030	12.1
		CV (%)	2.34	6.67	5.13

Table A.7.1 continued...

S25L	I		22.8	0.0026	7.8
			23.3	0.0032	9.5
			22.7	0.0024	10.6
		AVG	22.9	0.0027	9.3
		CV (%)	1.52	15.23	15.18
	II		24.7	0.003	13.3
			24.3	0.0032	10.7
			25.6	0.0038	8.5
		AVG	24.8	0.0033	10.8
		CV (%)	2.71	12.49	21.89
S25B	I		36.5	0.0038	15.2
			36.0	0.0048	11.7
			40.3	0.0038	11.9
		AVG	37.6	0.0041	12.9
		CV (%)	6.14	13.97	15.03
	II		36.0	0.0030	15.5
			34.9	0.0042	9.1
			35.2	0.0040	15.3
		AVG	35.3	0.0037	13.3
		CV (%)	1.63	17.22	27.35
S25S	I		43.7	0.0055	10.6
			43.7	0.0060	10.2
			43.9	0.0046	11.4
		AVG	43.8	0.0054	10.8
		CV (%)	0.30	13.22	5.62
	II		45.8	0.0036	13.1
			45.5	0.0038	15.1
			46.9	0.0042	12.9
		AVG	46.1	0.0039	13.7
		CV (%)	1.52	7.90	8.71

Steel Reinforcement Uniaxial Tensile Test Results

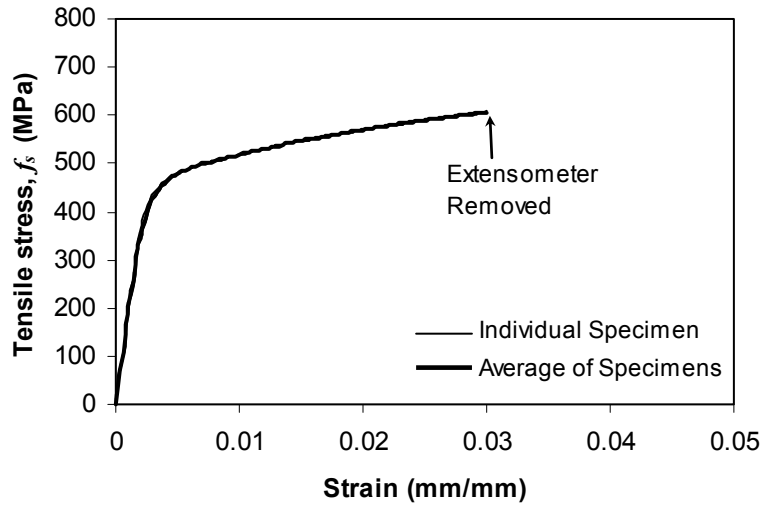


Figure A.7.7- Tensile stress-strain curve of reinforcing steel

Table A.7.2- Reinforcing steel coupon test results

Bar designation	Area (mm ²)		f_y (MPa)	ϵ_{ys} (mm/mm)	E_s (GPa)	f_{us} (MPa)	ϵ_{us} (mm/mm)
10 M	100		470	0.0024	199	683	0.17
			471	0.0023	202	681	0.18
			468	0.0024	194	644	0.18
		AVG	470	0.0024	198	669	0.17
		CV (%)	0.33	2.44	2.04	3.28	4.41

A.7.2 Slab Specimens Experimental Results

A.7.2.1 Specimen S03L

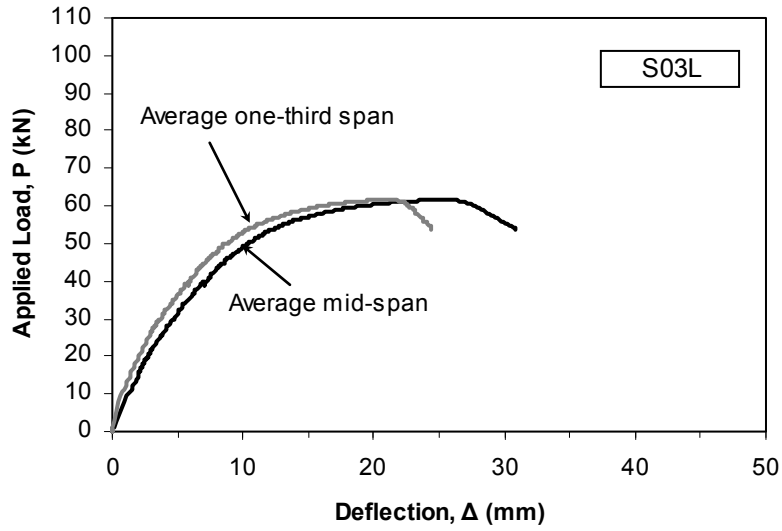


Figure A.7.8- Load-deflection response of specimen S03L

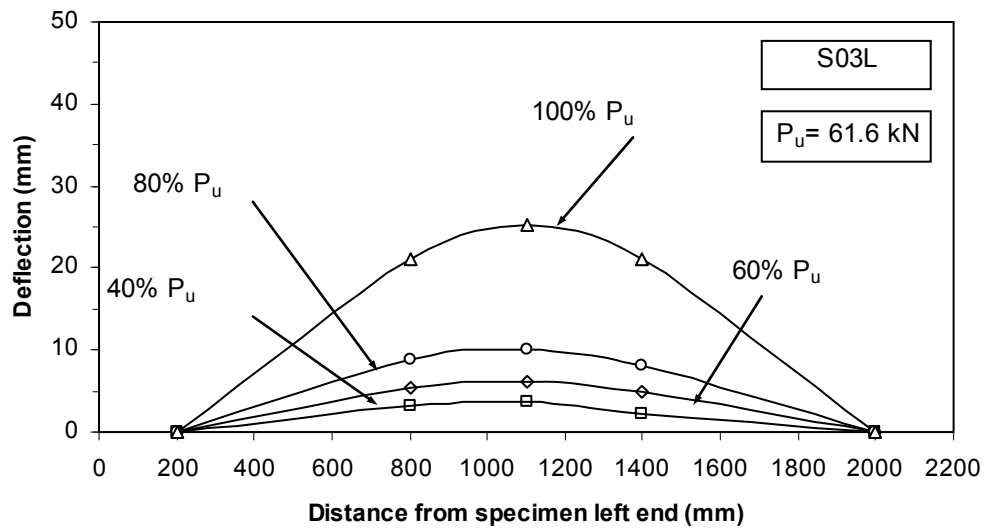


Figure A.7.9- Deflection profile of specimen S03L at various load stages

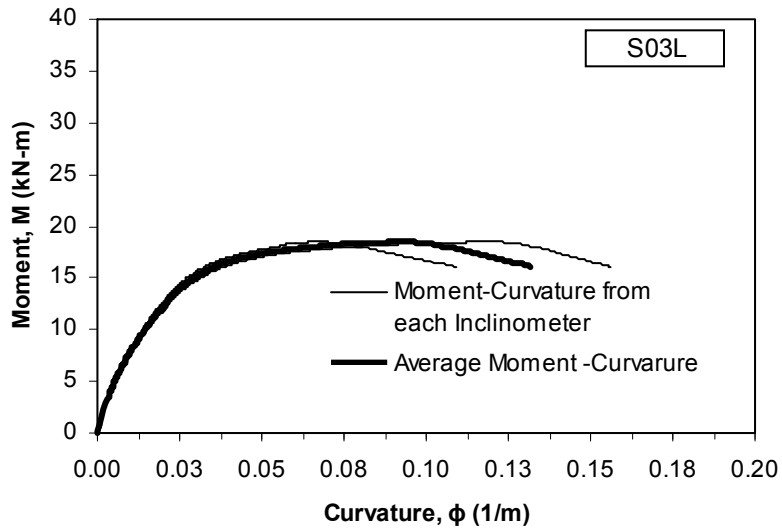


Figure A.7.10- Moment-curvature response of specimen S03L

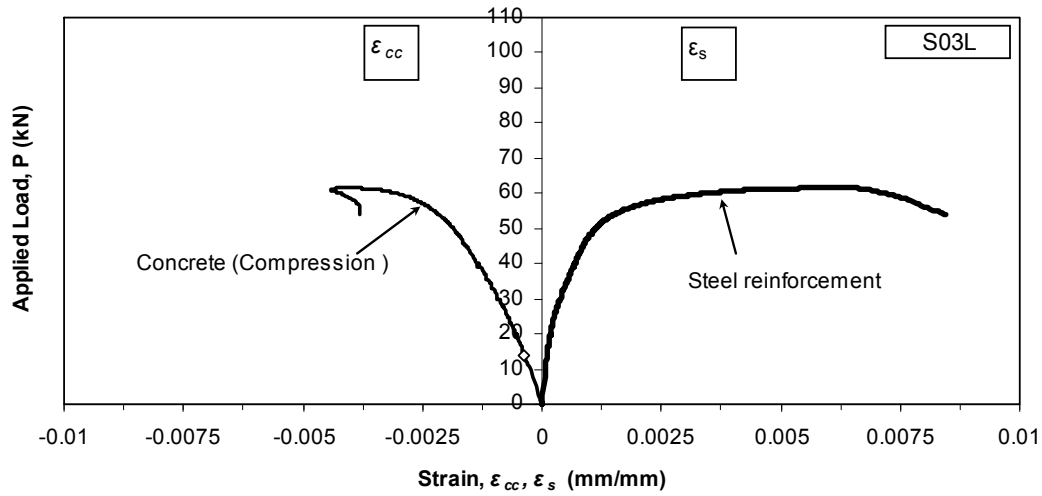


Figure A.11- Load-strain curves of specimen S03L

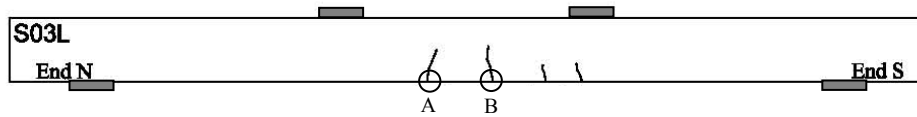
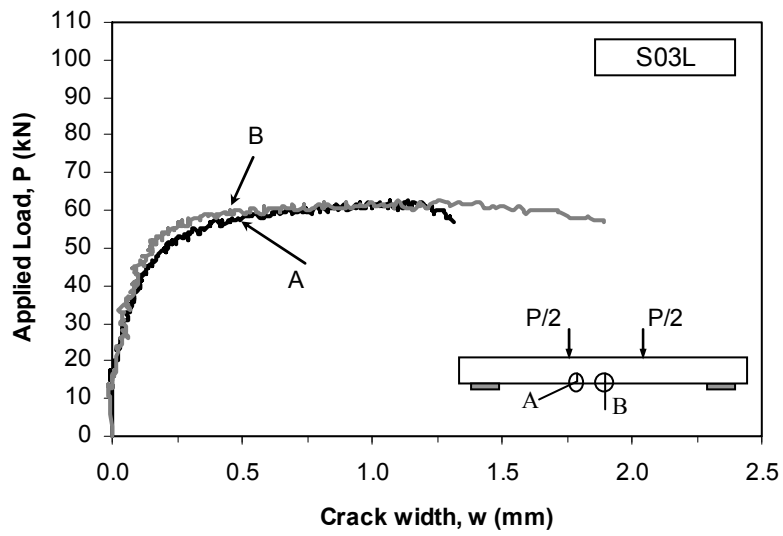


Figure A.7.12- Load-crack width curves of specimen S03L at different locations

A.7.2.2 Specimen S23L

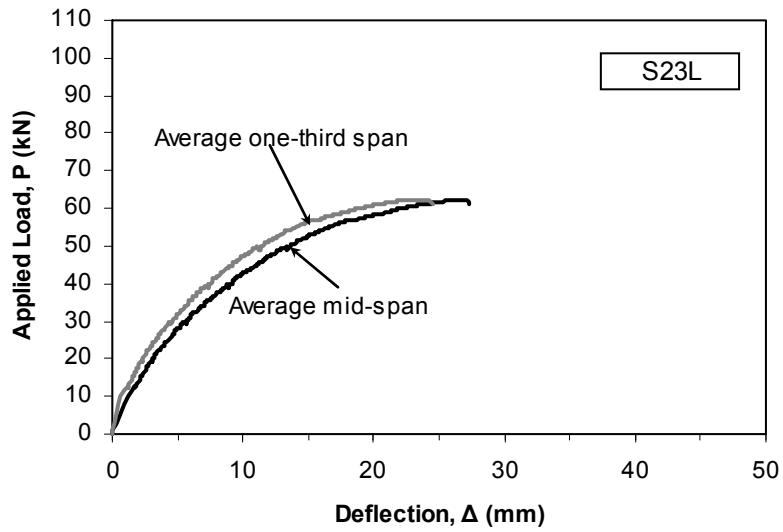


Figure A.7.13- Load-deflection response of specimen S23L

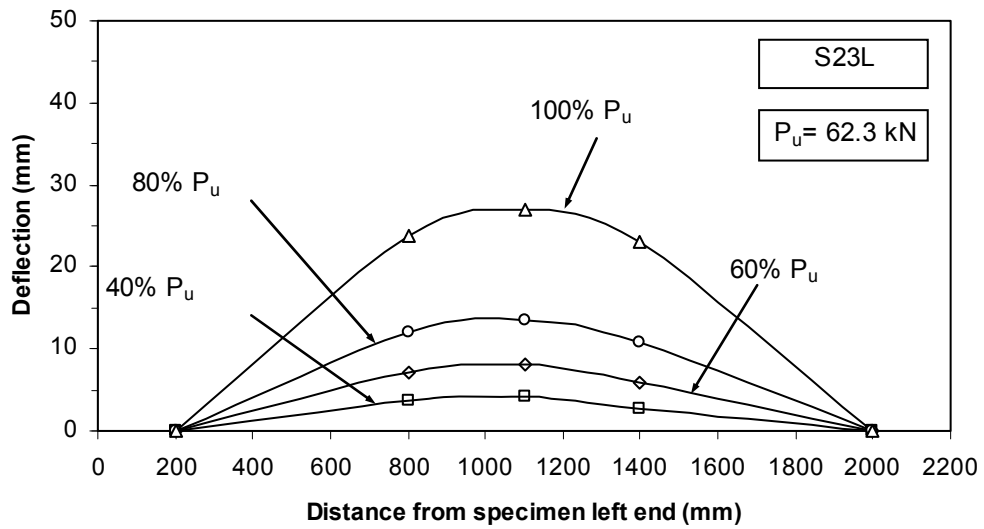


Figure A.7.14- Deflection profile of specimen S23L at various load stages

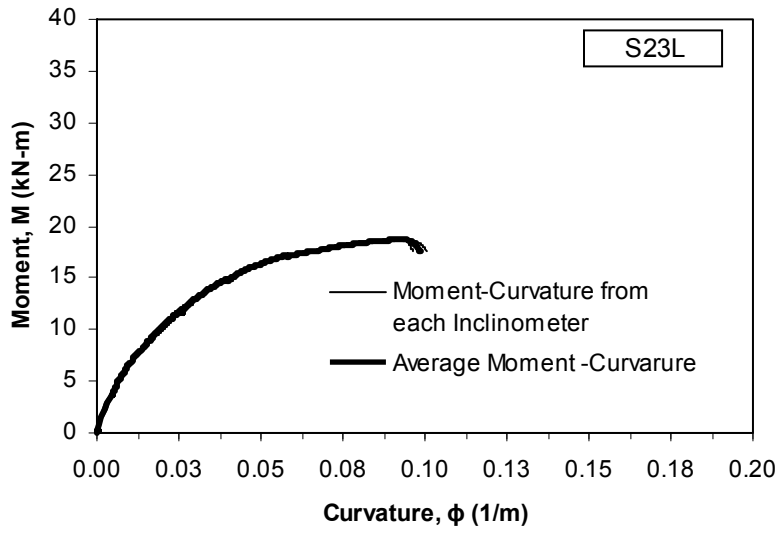


Figure A.7.15- Moment-curvature response of specimen S23L

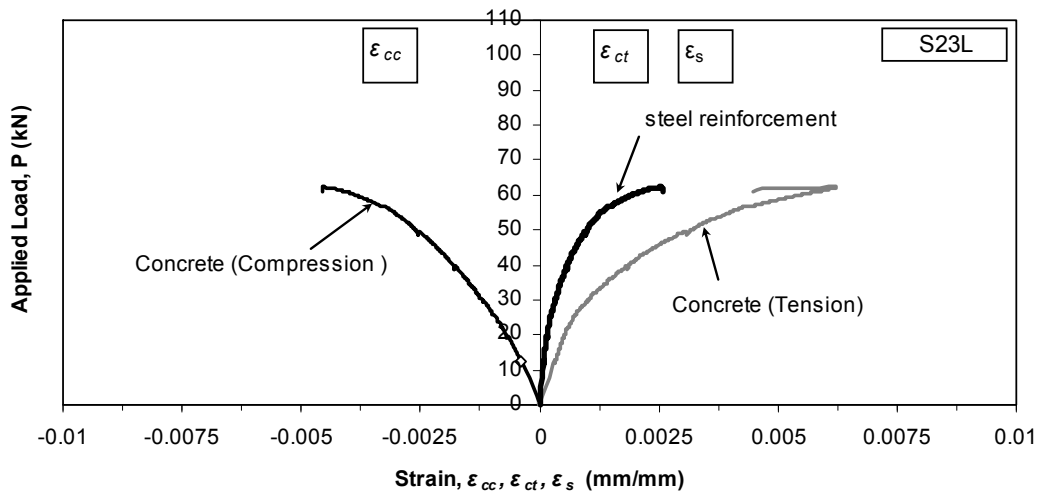


Figure A.7.16- Load-strain curves of specimen S23L

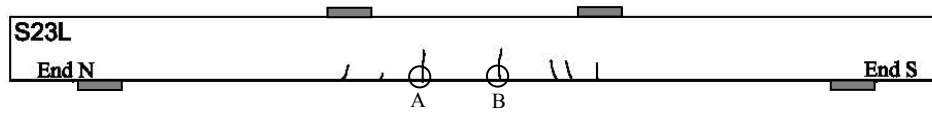
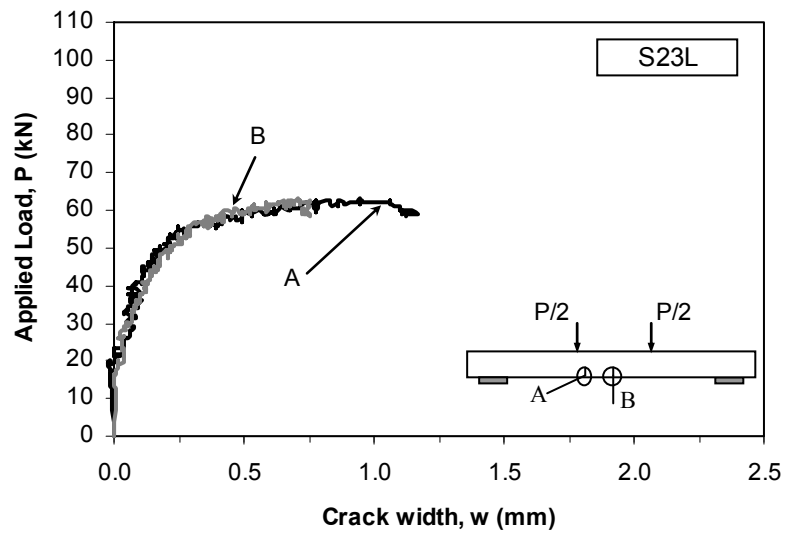


Figure A.7.17- Load-crack width curves of S23L at different locations

A.7.2.3 Specimen S05L

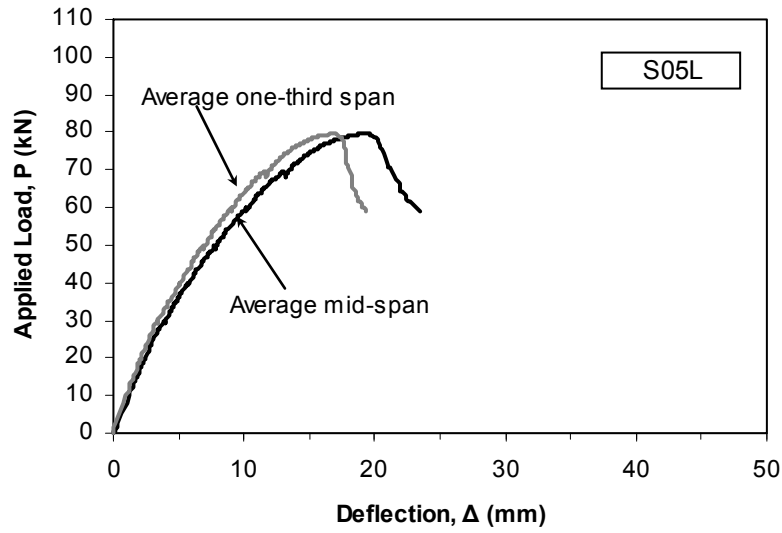


Figure A.7.18- Load-deflection response of specimen S05L

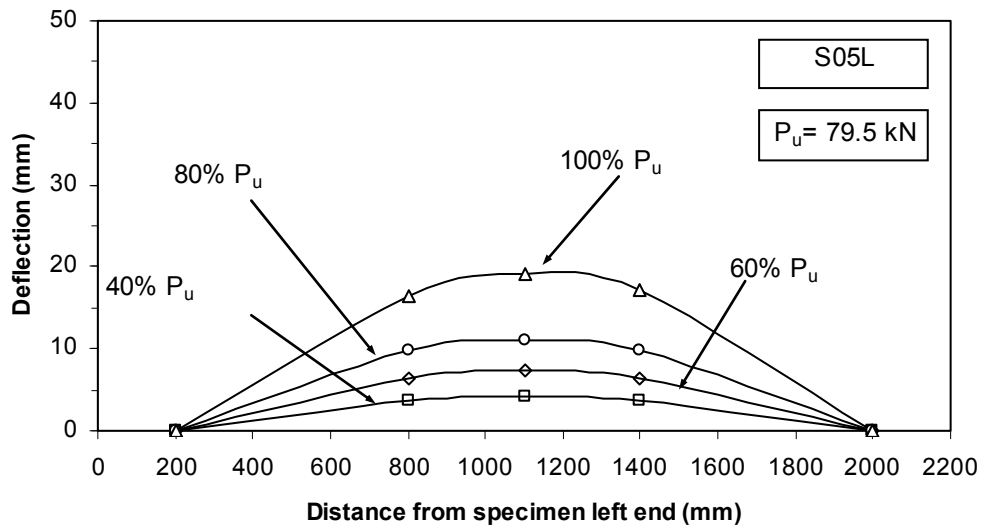


Figure A.7.19- Deflection profile of specimen S05L at various load stages

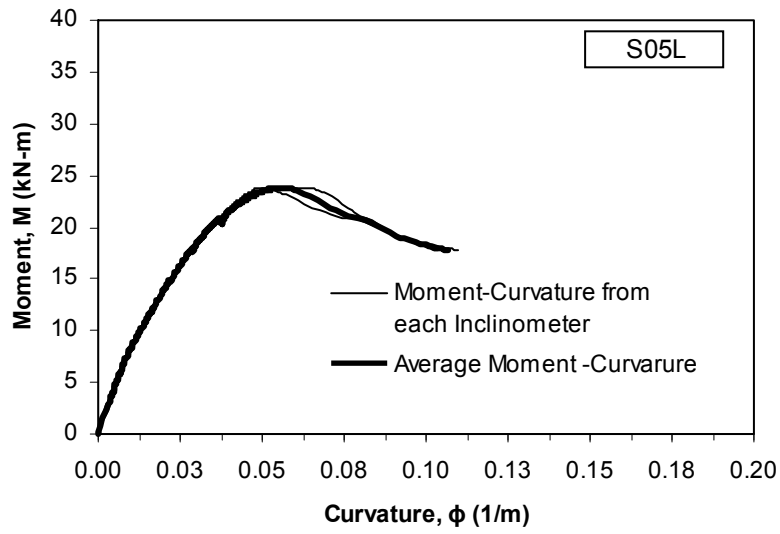


Figure A.7.20- Moment-curvature response of specimen S05L

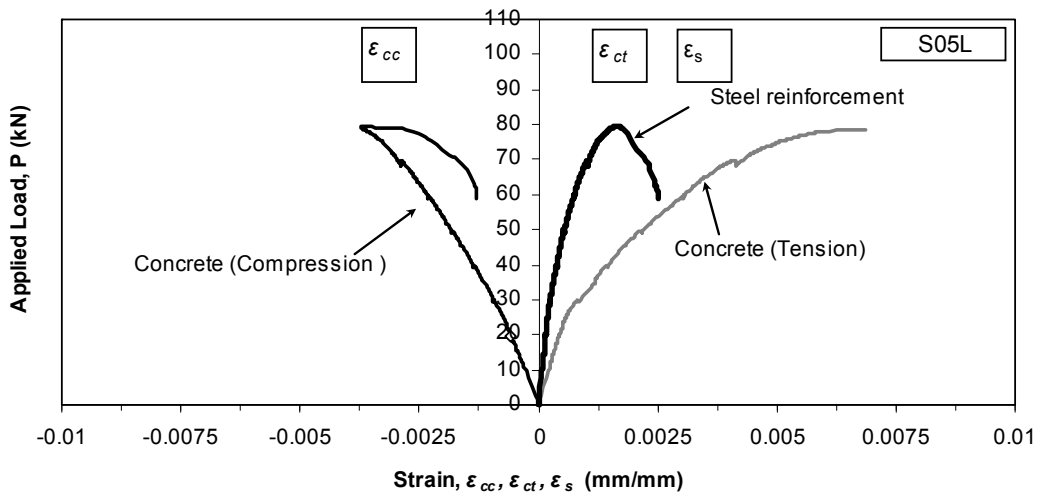


Figure A.7.21- Load-strain curves of specimen S05L

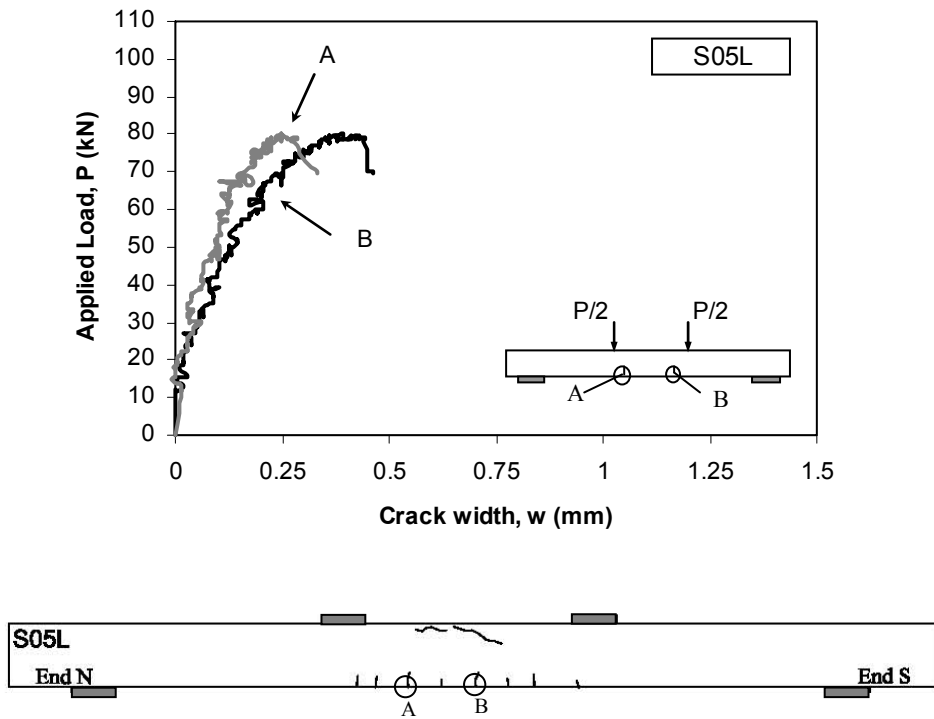


Figure A.7.22- Load-crack width curves of S05L at different locations

A.7.2.4 Specimen S25L

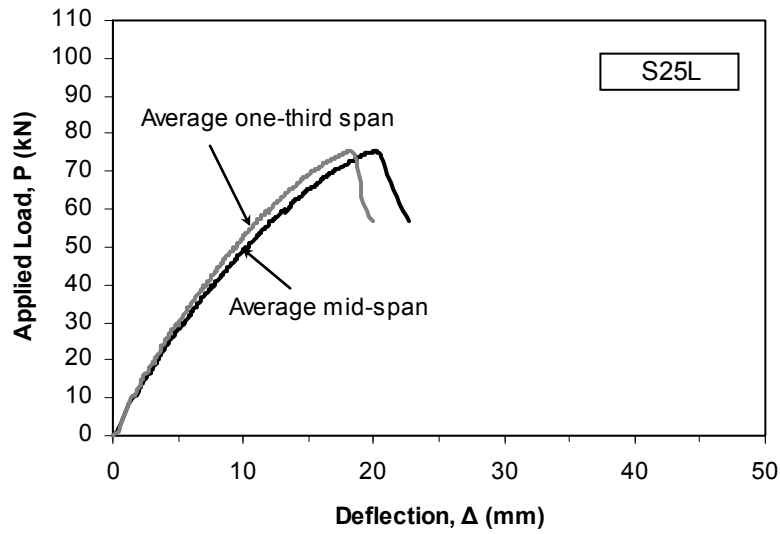


Figure A.7.23- Load-deflection response of specimen S25L

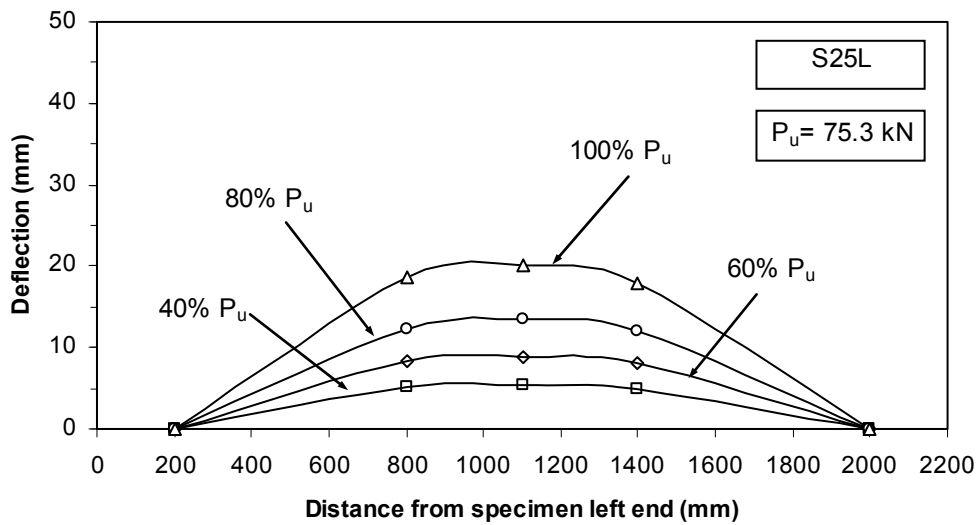


Figure A.7.24- Deflection profile of specimen S25L at various load stages

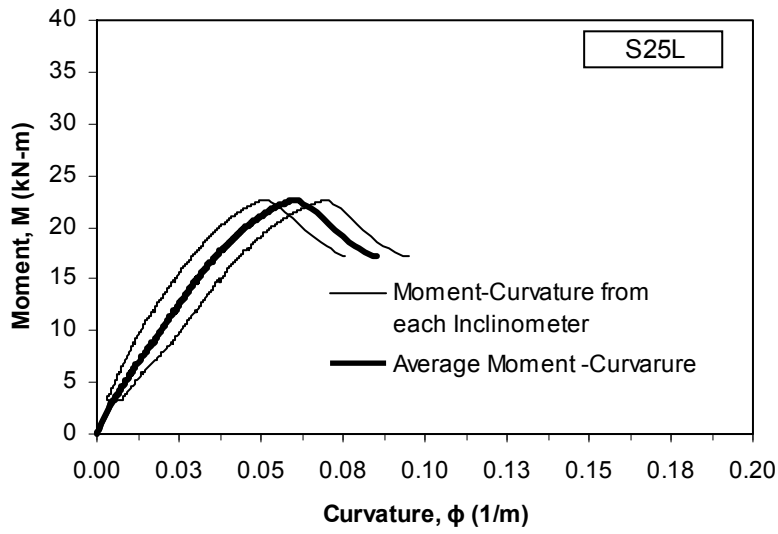


Figure A.7.25- Moment-curvature response of specimen S25L

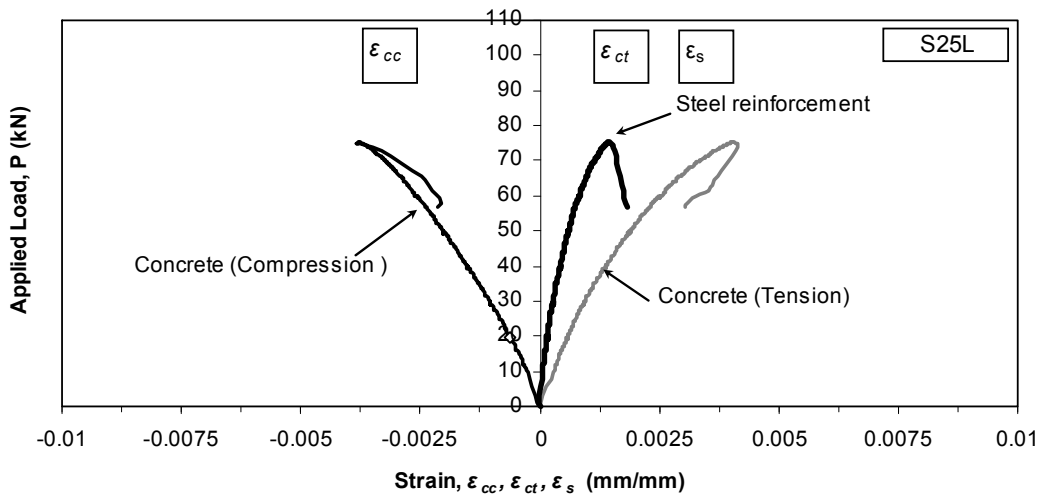


Figure A.7.26- Load-strain curves of specimen S25L

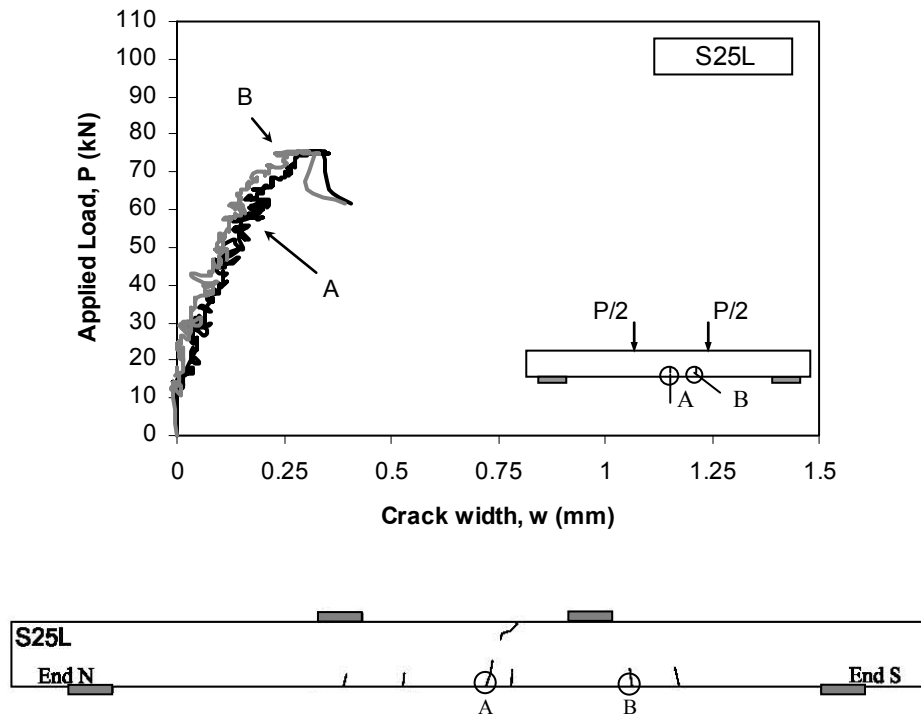


Figure A.7.27- Load-crack width curves of S25L at different locations

A.7.2.5 Specimen S25B

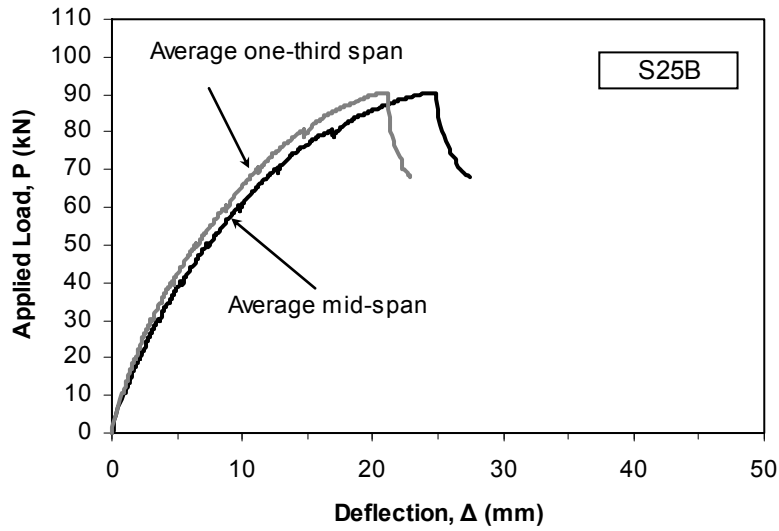


Figure A.7.28- Load-deflection response of specimen S25B

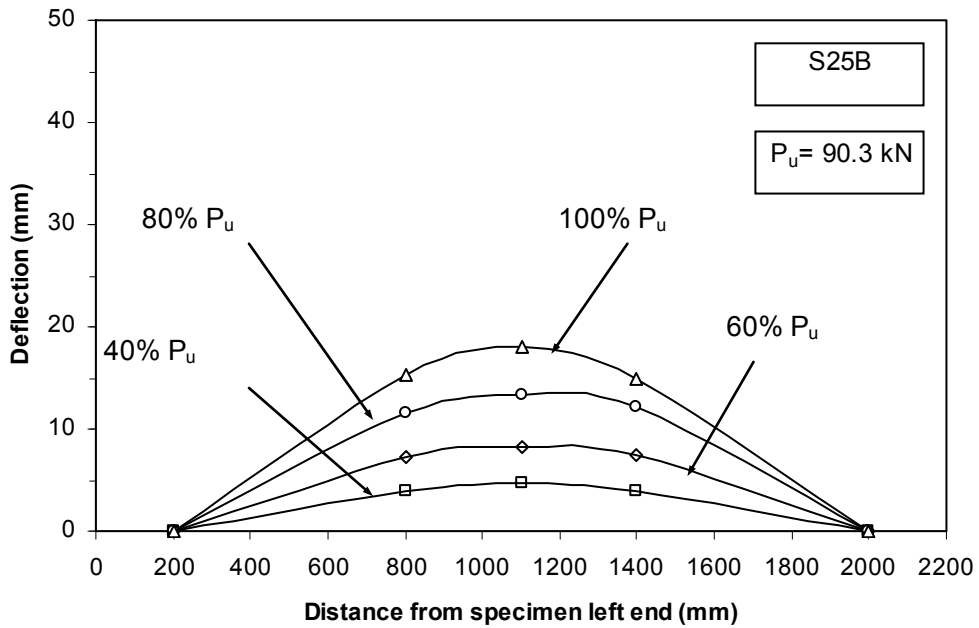


Figure A.7.29- Deflection profile of specimen S25B at various load stages

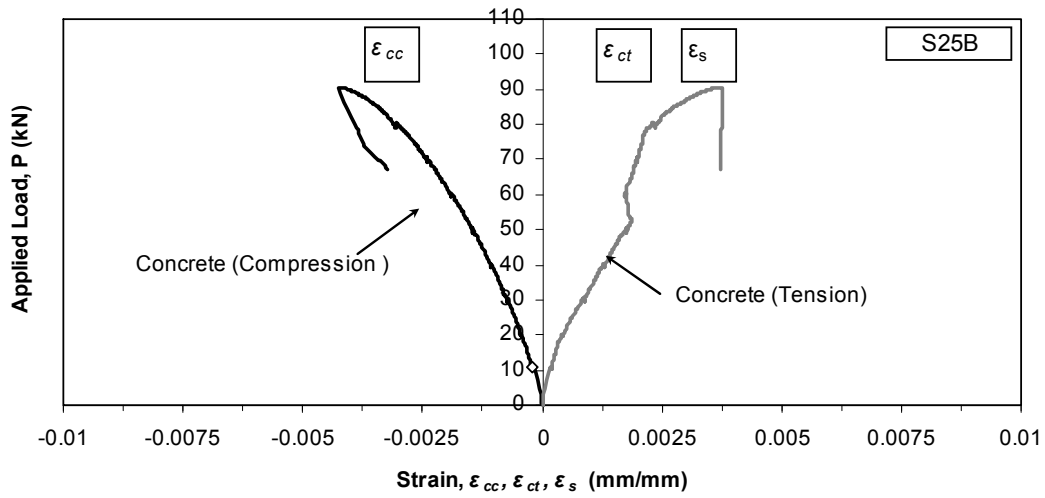


Figure A.7.30- Load-strain curves of specimen S25B

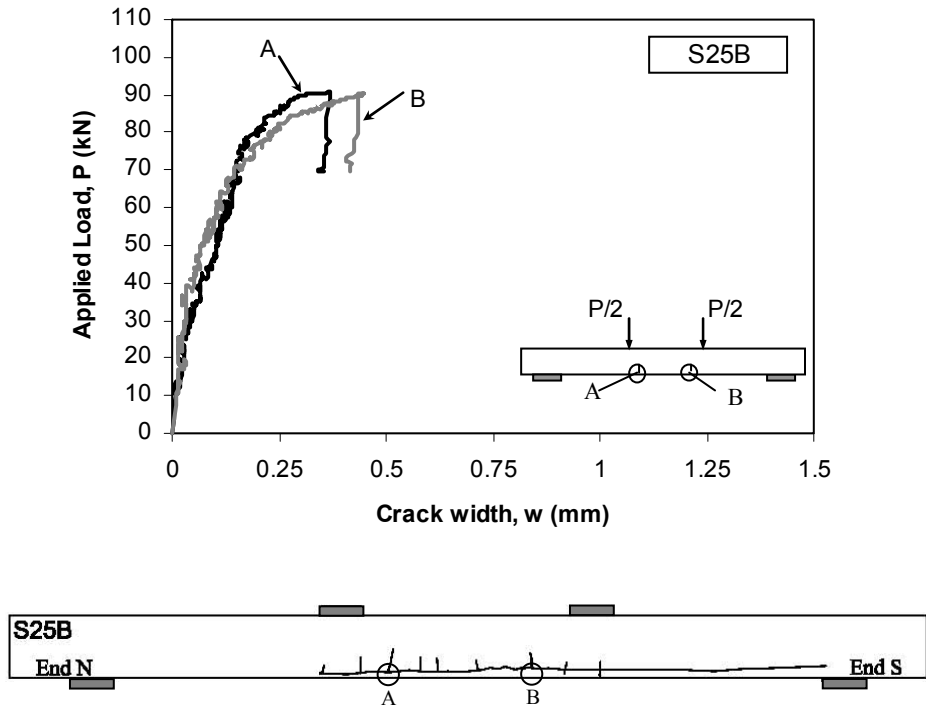


Figure A.7.31- Load-crack width curves of S25B at different locations

A.7.2.6 Specimen S25S

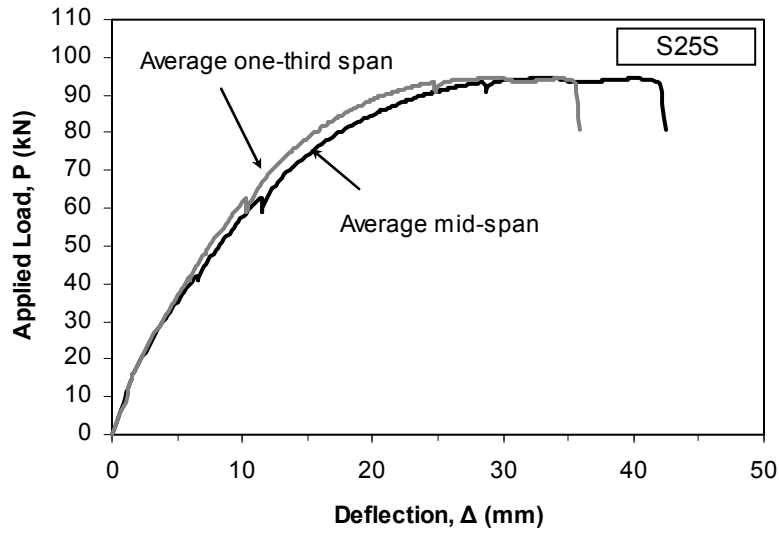


Figure A.7.32- Load-deflection response of specimen S25S

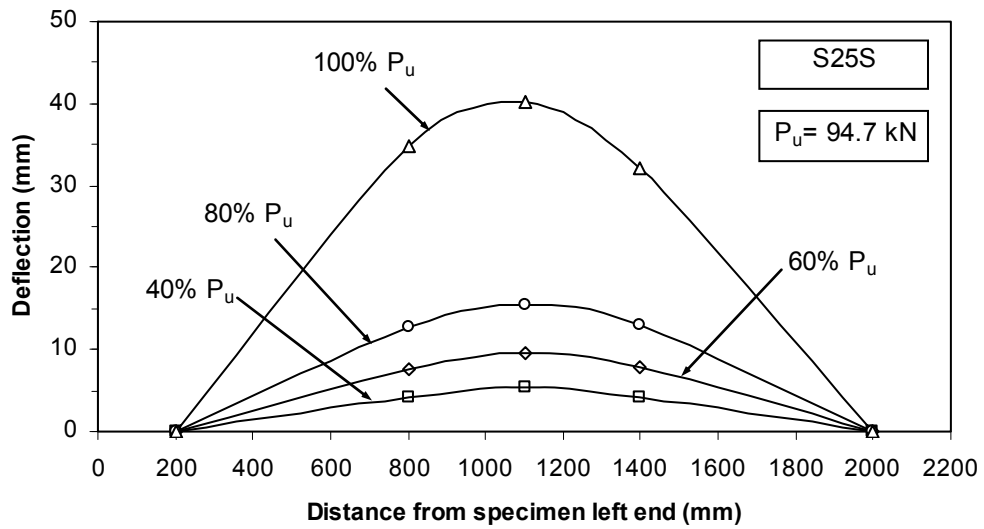


Figure A.7.33- Deflection profile of specimen S25S at various load stages

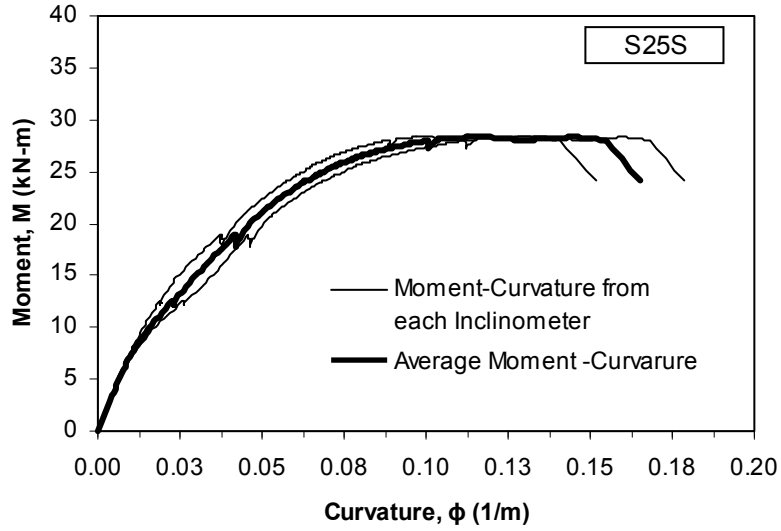


Figure A.7.34- Moment-curvature response of specimen S25S

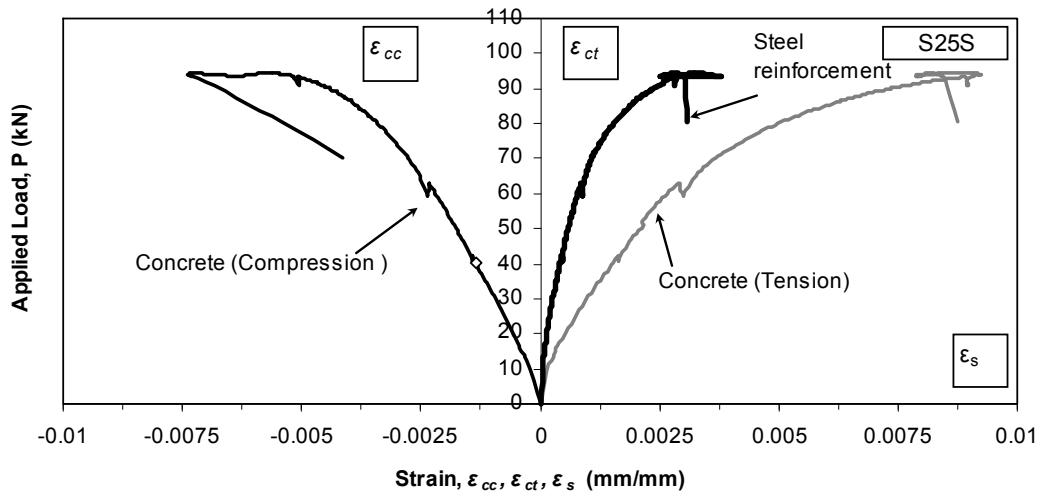


Figure A.7.35- Load-strain curves of specimen S25S

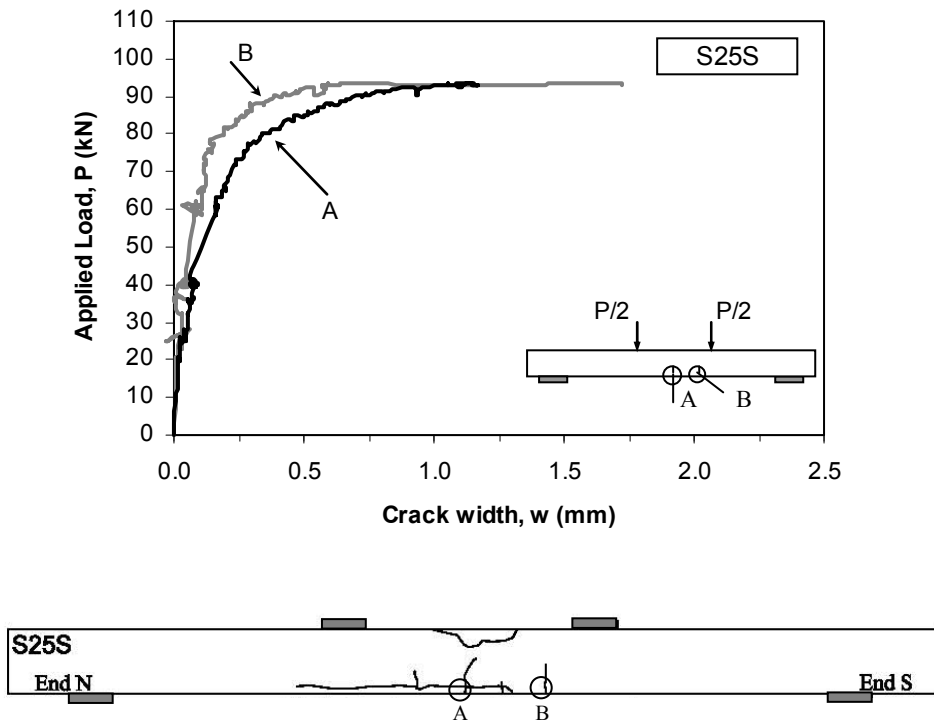


Figure A.7.36- Load-crack width curves of S25S at different locations